

Charge-density-wave ordering in three-dimensional metallic compounds

Von der Universität Bayreuth
zur Erlangung des Grades eines
Doktors der Naturwissenschaften (Dr. rer. nat.)
genehmigte Abhandlung

von
Sitaram Ramakrishnan
aus Mumbai, Indien

1. Gutachter: Prof. dr. Sander van Smaalen
2. Gutachter: Prof. Dr. rer. nat. Thomas Doert

Tag der Einreichung: 26.03.2020

Tag des Kolloquiums: 24.06.2020

Do or do not. There is no try.

Contents

Abstract	7
Kurzfassung	9
1 Introduction	11
1.1 Theoretical background	12
1.1.1 Brief description of phase transitions	12
1.1.2 Description of the Charge-density-wave (CDW) phase transition	14
1.1.3 Twinning	22
1.2 Overview of the results	26
1.2.1 CDW behaviour in CuV_2S_4	26
1.2.2 Interplay of CDW, antiferromagnetism and disorder in $\text{Er}_2\text{Ir}_3\text{Si}_5$	27
1.2.3 Properties of disordered $\text{Ni}_{0.89}\text{V}_{2.11}\text{Se}_4$	29
1.3 Outlook	30
2 Analysis of single-crystal X-ray diffraction data of twinned and modulated crystals in EVAL15	33
2.1 Experimental details and instrumental parameters	34
2.2 Initial set-up of the data	34
2.3 Integration of diffraction data of CuV_2S_4	36
2.4 Refining lattice parameters of CuV_2S_4 post integration	44
2.5 Absorption correction for CuV_2S_4	44
2.6 Integration of diffraction data of $\text{Er}_2\text{Ir}_3\text{Si}_5$	45
2.7 Refining lattice parameters of $\text{Er}_2\text{Ir}_3\text{Si}_5$ post integration	50
2.8 Absorption correction for $\text{Er}_2\text{Ir}_3\text{Si}_5$	51
3 Charge-density-wave and lock-in transitions of CuV_2S_4	53
3.1 Introduction	54
3.2 Experimental	56
3.2.1 Synthesis and X-ray diffraction	56
3.2.2 Physical properties	57
3.3 Results	60

3.3.1	Structural phase transitions	60
3.3.2	Diffraction symmetry and lattice distortion	66
3.3.3	Crystal structures of the CDW and lock-in states	69
3.3.4	Vanadium clusters in the CDW state	71
3.4	Conclusions	74
3.5	Acknowledgments	76
4	Unusual charge density wave transition and absence of magnetic ordering in $\text{Er}_2\text{Ir}_3\text{Si}_5$	77
5	Unusual magnetic behavior of crystalline $\text{Ni}_{0.89}\text{V}_{2.11}\text{Se}_4$ with site disorder	87
5.1	Introduction	88
5.2	Results and discussion	89
5.3	Conclusions	95
5.4	Methods	96
5.4.1	Crystal growth	96
5.4.2	Chemical composition	96
5.4.3	Physical properties measurements	96
5.5	Acknowledgements	97
	Appendix A: Structure refinements and models of CuV_2S_4	99
	Appendix B: Structure refinements and models of $\text{Er}_2\text{Ir}_3\text{Si}_5$	127
	Bibliography	149
	List of publications	163
	Acknowledgements	165
	Declaration	167

Abstract

The Charge-density-wave (CDW) is a static modulation of the density of conduction electrons which is accompanied by a periodic distortion of the lattice. Although CDW mechanisms have been established in one-dimensional (1D) and two-dimensional (2D) systems, the driving force behind the CDW remains an enigma for three-dimensional (3D) systems. This thesis reports on two 3D systems, CuV_2S_4 and $\text{Er}_2\text{Ir}_3\text{Si}_5$, with the purpose of explaining the mechanism for the formation of the CDW. Detailed investigations are presented of phase transitions of the compounds CuV_2S_4 and $\text{Er}_2\text{Ir}_3\text{Si}_5$, using physical property measurements of single-crystals and single-crystal X-ray diffraction (SXRD). Another compound, $\text{Ni}_{0.89}\text{V}_{2.11}\text{Se}_4$ with Ni/V disorder is also presented in the thesis.

Earlier studies report that CuV_2S_4 undergoes an incommensurate CDW phase transition at 90 K and a second phase transition at 50 K. Upon the analysis of the SXRD data below 90 K, we observe incommensurate superlattice reflections at positions $\mathbf{q} = (\sigma, \sigma, 0)$, with $\sigma = 3/4 + \delta$. Moreover, there is a distortion of the lattice, where the symmetry lowers from cubic $Fd\bar{3}m$ to orthorhombic $Imm2$, which is in agreement with the previous work. Below 50 K, the symmetry remained orthorhombic $Imm2$, however, we found the nature of the 50 K phase transition to be a lock-in transition towards a threefold superstructure. The lock-in transition occurs only on annealed crystals. As-grown (without annealing) crystals, on other hand, suffer from lattice defects, and as a result, they do not undergo the 50 K phase transition. Instead, the σ component of the modulation wave vector \mathbf{q} decreases and passes the rational value of $3/4$, but never reaches $2/3$. From the analysis of the SXRD data, we have established a superspace model for the crystal structure of the CDW phase suggesting that the formation of extended 3D clusters of Vanadium atoms is at the origin of the CDW.

At room temperature, $\text{R}_2\text{Ir}_3\text{Si}_5$ ($\text{R} = \text{Lu}, \text{Er}, \text{Ho}$) is orthorhombic $Ibam$. A previous study by Electron diffraction (ED) of $\text{Lu}_2\text{Ir}_3\text{Si}_5$ revealed the presence of incommensurate superlattice reflections at $\mathbf{q} = (-\sigma, 2\sigma, \sigma)$, with $\sigma = 0.23 \sim 0.25$, associated with a CDW phase transition below 140 K. From studies of the physical properties (2 to 300 K) of a single-crystal of $\text{Er}_2\text{Ir}_3\text{Si}_5$ we have concluded the CDW in the material is a first-order phase transition. The analysis of the SXRD data below 150 K, shows the presence of incommensurate superlattice reflections at positions

$\mathbf{q} = (1/4-\delta, 1/2-\delta, 1/4-\delta)$ accompanied by a strong monoclinic distortion of the lattice. However, we find that triclinic symmetry $I\bar{1}$ provides a better fit to the model compared to monoclinic symmetry. Our analysis of the crystal structure shows that the CDW resides on the zigzag chains of Iridium atoms. What makes this CDW unusual is that, firstly, it is an incommensurate first-order transition accompanied by a monoclinic lattice distortion, and secondly, from the magnetic susceptibility measurements, we observe that there is a strong coupling between the CDW and magnetism, as the Er^{3+} moments are influenced by the CDW. We also show that in the high-quality single-crystal, the magnetic ordering of the compound is suppressed to at least 0.1 K. However, previous studies report that in a polycrystal of $\text{Er}_2\text{Ir}_3\text{Si}_5$ the antiferromagnetic ordering is observed around 2.1 K. This seems to suggest that disorder in the polycrystal brings back the antiferromagnetism at the expense of the CDW transition.

According to the literature, polycrystalline NiV_2Se_4 is reported to be a CDW system at 165 K. We sought to investigate the CDW in the material, however, the attempts to synthesize single crystals of NiV_2Se_4 led to Ni deficient material with Ni/V site disorder, resulting in $\text{Ni}_{0.89}\text{V}_{2.11}\text{Se}_4$. By studying temperature-dependent structural and bulk properties of $\text{Ni}_{0.89}\text{V}_{2.11}\text{Se}_4$, we report a possible Non-Fermi-liquid (NFL) to a Fermi-liquid (FL) transition at ambient pressure. The electrical resistivity (ρ) shows metallic behavior with a broad anomaly around 150-200 K. $\rho(T)$ is found to exhibit an anomalous $T^{3/2}$ dependence which is a strong indication of NFL, and below 15 K it exhibits a T^2 dependence down to 1.5 K, meaning that the FL behaviour is recovered below 15 K. From the analysis of the SXRD data at 100 K, we observed no superlattice reflections and no change to the structure as it remained monoclinic $I2/m$, indicating the absence of a CDW phase transition. The presence of magnetic fluctuations and quenched disorder on the Ni/V sites could be the cause of NFL to FL transition, given that stoichiometric NiV_2Se_4 is claimed to be a non-magnetic CDW system. Synthesis of a stoichiometric NiV_2Se_4 without the disorder is necessary to investigate the possibility of a CDW phase transition, and it is being undertaken.

Kurzfassung

Die Ladungsdichtewelle (charge-density-wave, CDW) ist eine statische Modulation der Leitungselektronendichte, kombiniert mit einer periodischen Verzerrung des Gitters. Auch wenn die CDW-Mechanismen für eindimensionale (1D) und zweidimensionale (2D) Systeme etabliert sind, so ist die treibende Kraft für dreidimensionale (3D) Systeme noch immer nicht ganz verstanden. Mit der vorliegenden Doktorarbeit soll anhand der 3D Systeme CuV_2S_4 und $\text{Er}_2\text{Ir}_3\text{Si}_5$ zur Klärung des Bildungsmechanismus der CDW beigetragen werden. Für genaue Untersuchungen der Phasenumwandlungen in den Verbindungen CuV_2S_4 und $\text{Er}_2\text{Ir}_3\text{Si}_5$ werden Messungen physikalischer Eigenschaften und Einkristallröntgenstrahlbeugung (single-crystal X-ray diffraction, SXRD) durchgeführt. Eine weitere Verbindung, $\text{Ni}_{0,89}\text{V}_{2,11}\text{Se}_4$ mit Ni/V Lagenfehlordnung, wird in dieser Doktorarbeit ebenfalls diskutiert.

Frühere Untersuchungen zeigen, dass CuV_2S_4 eine inkommensurable CDW Phasenumwandlung bei 90 K und eine zweite Phasenumwandlung bei 50 K hat. Die Auswertung der SXRD-Daten unterhalb von 90 K zeigt inkommensurable Überstruktureflektive auf den Lagen $\mathbf{q} = (\sigma, \sigma, 0)$, mit $\sigma = 3/4 + \delta$. Darüberhinaus ist das Gitter verzerrt, wodurch sich die Symmetrie von kubisch $Fd\bar{3}m$ nach orthorhombisch $Imm2$ verringert, wie es auch in früheren Arbeiten berichtet wird. Unterhalb von 50 K verbleibt die Symmetrie orthorhombisch $Imm2$, wir charakterisieren diese Umwandlung als eine "Lock-in"-Phasenumwandlung hin zu einer dreifachen Überstruktur. Diese Lock-in-Phasenumwandlung tritt aber nur bei getemperten Kristallen auf. Unbehandelte Kristalle (ohne Tempern) leiden unter Gitterbaufehlern, die diese zweite Phasenumwandlung bei 50 K verhindern. Stattdessen verkleinert sich die σ -Komponente des Modulationswellenvektors \mathbf{q} weiter, wobei der rationale Wert $3/4$ zwar unterschritten, aber der ebenfalls rationale Wert $2/3$ nicht errreicht wird. Basierend auf der Auswertung der SXRD-Daten haben wir ein Superraummodell der Kristallstruktur der CDW-Phase aufgestellt und schlagen die Bildung von ausgedehnten 3D Clustern der Vanadiumatome als Ursache der CDW vor.

Bei Zimmertemperatur ist die Symmetrie von $\text{R}_2\text{Ir}_3\text{Si}_5$ ($\text{R} = \text{Lu}, \text{Er}, \text{Ho}$) orthorhombisch $Ibam$. Frühere Untersuchungen mittels Elektronenbeugung (electron diffraction, ED) an $\text{Lu}_2\text{Ir}_3\text{Si}_5$ zeigen inkommensurable Überstruktureflektive auf den Lagen $\mathbf{q} = (-\sigma, 2\sigma, \sigma)$, mit $\sigma = 0,23 \sim 0,25$, verbunden mit einer CDW-

Phasenumwandlung unterhalb 140 K. Basierend auf Untersuchungen der physikalischen Eigenschaften (von 2 bis 300 K) an einem Einkristall von $\text{Er}_2\text{Ir}_3\text{Si}_5$ schlagen wir vor, dass die CDW in dieser Verbindung eine Phasenumwandlung erster Ordnung ist. Die Auswertung der SXR-Daten unterhalb 150 K ergeben inkommensurable Überstrukturreflexe auf den Lagen $\mathbf{q} = (1/4-\delta, 1/2-\delta, 1/4-\delta)$, zusammen mit einer starken monoklinen Verzerrung des Gitters. Weitere Untersuchungen zeigen jedoch, dass ein Strukturmodell mit trikliner Symmetrie $I\bar{1}$ einen besseren Fit an die Daten ergibt, als ein Strukturmodell mit monokliner Symmetrie. Unseren Datenauswertungen folgend liegt die CDW auf den Zig-Zag-Ketten der Iridium-Atome. Diese CDW ist sehr ungewöhnlich. Einerseits stellt sie eine inkommensurable Umwandlung erster Ordnung mit monokliner Gitterverzerrung dar. Andererseits zeigt die Messung der magnetischen Suszeptibilität eine starke Kopplung zwischen der CDW und Magnetismus, da die Er^{3+} Momente durch die CDW beeinflusst werden. Wir zeigen auch, dass die magnetische Ordnung in Einkristallen hoher Qualität zumindest bis 0,1 K unterdrückt wird. Frühere Untersuchungen berichten jedoch, dass in polykristallinem $\text{Er}_2\text{Ir}_3\text{Si}_5$ antiferromagnetische Ordnung bei etwa 2,1 K beobachtet wird. Dies scheint nahezuzeigen, dass Fehlordnung im polykristallinen Material antiferromagnetische Ordnung auf Kosten der CDW-Umwandlung zurückbringt.

In der Literatur wird polykristallines NiV_2Se_4 als CDW-System bei 165 K behandelt. Wir wollten deshalb die CDW in diesem Material untersuchen. Jeder Versuch, Einkristalle von NiV_2Se_4 zu züchten, endete in der Ni-armen Verbindung $\text{Ni}_{0,89}\text{V}_{2,11}\text{Se}_4$ mit einer Ni/V-Lagenfehlordnung. Mittels Untersuchungen temperaturabhängiger struktureller und Volumeneigenschaften von $\text{Ni}_{0,89}\text{V}_{2,11}\text{Se}_4$ berichten wir eine mögliche Umwandlung von einer Nicht-Fermi-Flüssigkeit (non-Fermi-liquid, NFL) zu einer Fermi-Flüssigkeit (Fermi-liquid, FL) bei Umgebungsdruck. Die elektrische Widerstand (ρ) zeigt metallisches Verhalten mit einer ausgeprägten Anomalie bei etwa 150-200 K. $\rho(T)$ folgt einer anomalen $T^{3/2}$ -Abhängigkeit als starkes Indiz einer NFL, und unterhalb 15 K bis 1,5 K einer T^2 -Abhängigkeit, was bedeutet, dass das FL-Verhalten unterhalb 15 K wiederhergestellt ist. In der Auswertung der SXR-Daten bei 100 K können keine Überstrukturreflexe und keine Änderung der Struktur gefunden werden, die Symmetrie bleibt monoklin $I2/m$. Dies deutet auf eine Abwesenheit der CDW-Phasenumwandlung hin. Das Vorhandensein magnetischer Fluktuationen und abgeschreckter Fehlordnung auf den Ni/V-Lagen könnte die Ursache der NFL nach FL-Umwandlung sein, unter der Annahme, dass das stoichiometrische NiV_2Se_4 ein nicht-magnetisches CDW-System darstellt. Die Synthese von stoichiometrischem NiV_2Se_4 ohne Fehlordnung ist notwendig für die Untersuchung einer möglichen CDW-Phasenumwandlung und wird zur Zeit durchgeführt.

Chapter 1

Introduction

The free-electron theory also known as the Drude-Sommerfeld model [1] along with the periodic potential of the lattice became successful in explaining the electronic conduction mechanism in metals, semiconductors, and insulators. However, there exist states of matter, such as superconductivity or charge density wave ordering, that cannot be explained by the above mentioned model. It is now well established that both superconductivity (SC) and charge density wave ordering (CDW) can only be described by theories which take electron-phonon interactions into account. Both SC and CDW have continued to be in the forefront of condensed matter research [2]. CDW was predicted to occur in a material whose crystal structure has one dimensional (1D) character, where one observes a static modulation of the density of conduction electrons which is accompanied by a periodic distortion of the lattice [3].

However, in reality, 1D crystals do not exist as matter occupies a finite volume in space. It is possible for a crystal structure to contain a chain of strongly bonded atoms that is weakly coupled to the other atomic chains in the network. This could arise due to the predominant overlap of the wave functions of the atomic orbitals in one direction and a very small overlap in the other two directions. Such 1D conduction bands composed of parallel metallic chains that interact weakly between them and also with the network of other atoms can be present in 3D crystals. So one can realize electronic conduction in 1D while phonons see a 3D crystal. Although the CDW formation has been established in lower-dimensional compounds (quasi 1D or 2D crystal structures), the current understanding of the CDW in real 3D systems (where there are no distinct 1D conduction bands) is not fully developed. We aim to elucidate the mechanism for the formation of the CDW in two of these 3D systems, namely CuV_2S_4 and $\text{Er}_2\text{Ir}_3\text{Si}_5$, through the means of X-ray diffraction, resistivity, heat capacity and magnetic susceptibility measurements. Our studies reveal the observation of atypical CDWs in both compounds which are sensitive to lattice disorder.

1.1 Theoretical background

In the first part of the chapter, we present the theoretical background relevant to the understanding of phase transitions with a particular emphasis on CDW mechanisms. We also present the theory of twinning of crystals, since twinning turned to be a major issue for both CuV_2S_4 and $\text{Er}_2\text{Ir}_3\text{Si}_5$.

1.1.1 Brief description of phase transitions

Matter exists in different states. A change of state brought out by variation of an external parameter, such as pressure, temperature or an applied field, is called a phase transition. Phase transitions result in changes in some physical properties of the material and it may involve a change of its crystal structure. In fact, the changes in the properties or the change in the structure are the usual way that a phase transition is established. Simple forms of phase transitions are transformations between solids, liquids, and gases. The six types of phase changes are melting (solid to liquid), freezing (liquid to solid), vaporization (liquid to gas), condensation (gas to liquid), sublimation (solid to gas) and deposition (gas to solid) [4]. Figure 1.1 shows a flow chart describing the transitions between different phases.

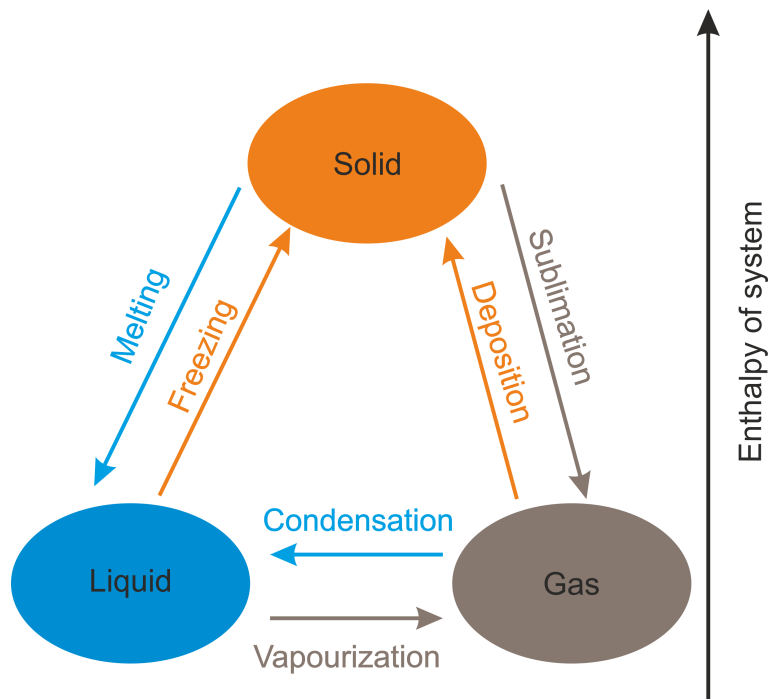


Figure 1.1: Flow chart showing the transitions between different phase changes of matter.

Phase transitions can be broadly classified into first-order and second-order phase transitions. This classification can be understood using the Gibbs free energy (G) of a pure system [5], whose differential is defined as

$$dG = -SdT + VdP + \mu dN \quad (1.1)$$

where S , T , V and P are entropy, temperature, volume and pressure. μ is the chemical potential of the system and N is the number of particles (or moles). The order of the lowest derivative of the Gibbs free energy (G) showing a discontinuity at the phase transition by definition is the order of a phase transition. For the first-order phase transition, the derivative of G is discontinuous which implies the entropy $S = -(dG/dT)_P$ and the volume $V = (dG/dP)_T$ are discontinuous at the phase transition. Since the first-order transition allows the coexistence of two phases with different entropies S_1 and S_2 at an equilibrium temperature T_0 , the system must therefore absorb or release heat and that is known as the latent heat $\Delta Q_L = T_0(S_2 - S_1)$. The classic example of this case is ice melting to water where the latent heat is 0.336 MJ/kg. A second-order phase transition is characterized by discontinuity in the second derivative of the Gibbs free energy. For instance, the heat capacity at constant pressure $C_P = T(dS/dT)_P = -T(d^2G/dT^2)_P$, thermal expansion $\alpha = (1/V)(dV/dT)_P = (1/V)(d^2G/dVdT)_P$ show discontinuous change at a second-order phase transition.

Unlike the first-order phase transition, there is no latent involved in the second-order phase transition. Moreover, thermal hysteresis observed in the physical properties at the first-order phase transition is absent in the second-order phase transition. Second-order phase transitions can be realized in a system which exhibits spontaneous magnetization like ferromagnetism shown by a permanent magnet or perfect diamagnetism by superconductors, etc. These phase transitions are not always induced by modification of atomic or molecular arrangements but by modification of electronic properties. On the other hand, Ferroelectricity and CDW require a subtle change in the crystal structure.

The ideal CDW transition is a second-order phase transition and that has been seen in traditional CDW systems, such as NbSe_3 and $\text{K}_{0.3}\text{MoO}_3$ [6, 7], where the bulk transport and magnetic properties do not show hysteresis at the CDW transition. However, there are a number of cases where one observes thermal hysteresis (due to significant contribution from phonons) of bulk physical properties near the CDW transition similar to those observed in CuV_2S_4 and $\text{Er}_2\text{Ir}_3\text{Si}_5$ which will be discussed in the next section.

1.1.2 Description of the Charge-density-wave (CDW) phase transition

Transition metal compounds have always been a focus in condensed matter physics research. In general, the richness of exotic physical properties is based on one essential part of the electronic structure, namely, the partially occupied d shell of the transition metal ions. However, there are some exceptions to this conjecture such as the CDW observed in low-dimensional organic salts like TTF-TCNQ [8], etc. The spatial extent of the d orbital lies between those delocalized Bloch states of s orbitals, as they occur in the alkali metals, and the f electrons of rare-earth elements which are very close to the atomic nucleus. The small but non-negligible overlap between neighbouring d orbitals leads to significant correlation effects in the many-particle system of the valence electrons.

It is exactly these correlation effects that are the origin of a plethora of phase transitions that occur in transition metal compounds. One of the important phase transitions which arises due to such correlations is the charge density wave (CDW) transition [9]. The CDW phenomena have been observed in low dimensional systems (1D, 2D) and higher dimensional systems (3D). However, the theoretical description of the CDW phase transition presents great challenges and still has unresolved issues for 3D systems [10].

The CDW phase transition can occur by means of different mechanisms, depending on the material. One mechanism is Fermi surface nesting (FSN) in solids which have low dimensional structures. The energy of such a solid is lowered by a lattice distortion, because the concomitant strain energy is more than compensated by the reduction in electronic energy. Figure 1.2 shows two parallel pieces of a Fermi surface, where each point on the fermi surface is connected by the nesting vector \mathbf{q} to a point on the opposing surface. In a one dimensional system there is complete nesting. The associated phonon energy of the nesting vector is considerably reduced and leads to phonon softening. In some cases, the phonon energy is reduced to zero causing a distortion of the lattice. This was explained by Walter Kohn and known as the 'Kohn anomaly' [10, 11].

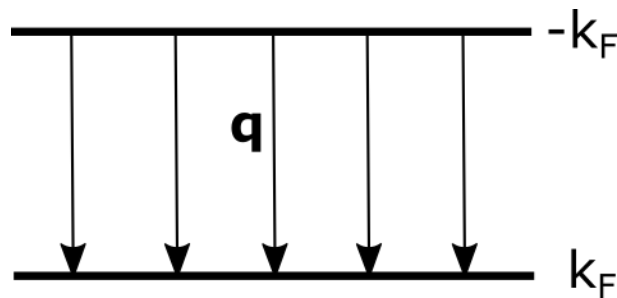


Figure 1.2: FSN in 1D system.

Other mechanisms for forming a CDW include electron-phonon coupling (EPC) [12] and another form of (CDW) order which has been shown to compete and co-exist with superconductivity in underdoped cuprate superconductors known as charge-ordering (CO) [10, 13].

For a one-dimensional solid Peierls [14] proposed that the system is susceptible to a periodic lattice distortion that can lower the total energy. He assumed that every atom in the chain contributes one electron to the band, such that the band is half filled as shown in Figure 1.3.

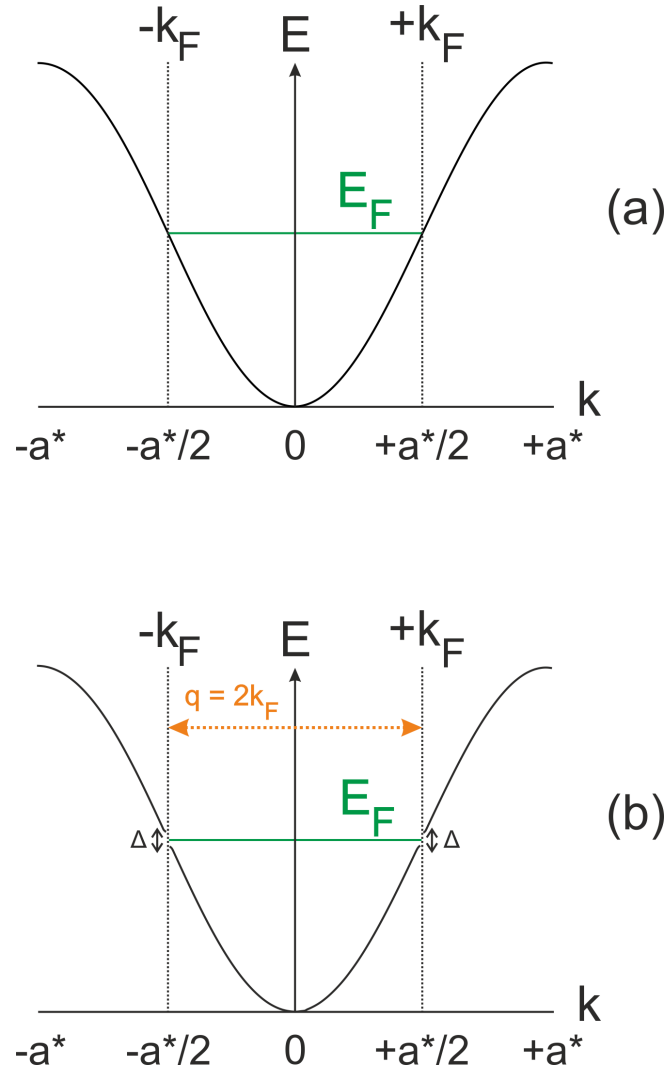


Figure 1.3: (a) Band structure of a periodic 1D system. (b) Band structure of a distorted 1D system.

In Figure 1.3, the boundary of the first Brillouin zone is described by $\pm\mathbf{a}^*$ where the crystal is periodic. \mathbf{k}_F is the Fermi vector which is a fraction of the basis vector of the reciprocal space. In this case, \mathbf{k}_F is $\mathbf{a}^*/2$. The electronic charge density is of periodic form, being maximum in the vicinity of the ion cores. Now if one displaces every second atom by the same amount, it results in a doubling of the period from a to $2a$ to the lattice in direct space, as shown in Figure 1.4.

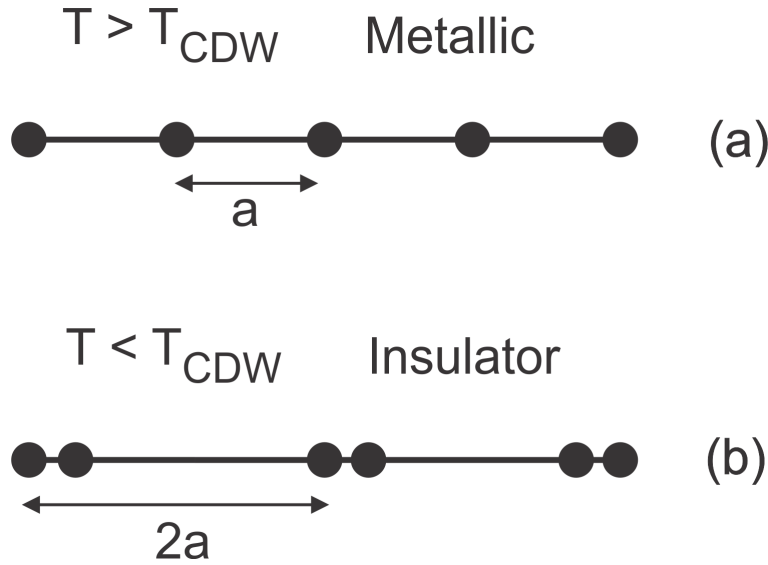


Figure 1.4: Peierls distortion of a 1D lattice.

The CDW transition causes a shift in the electronic energy that leads to an opening of a gap Δ at $\pm\mathbf{k}_F$. The occupied electron states at $\pm\mathbf{k}_F$ are shifted downwards, whereas the empty electron states are shifted upwards as shown in Figure 1.3, which leads to a decrease in the energy of the electrons. The formation of the nesting vectors depends on the geometry of the Fermi surface that results in the formation of a CDW state.

The modulation with wavevector $\mathbf{q} = 2\mathbf{k}_F$ will modify the Fermi surface by creating gaps at these nested positions. The 'gain' by creating energy gaps overcome the energy cost arising from the strain associated with the periodic lattice distortion, thus allowing the formation of a CDW. In other words, a structural change will occur when the CDW formation is accompanied by ion displacements that stabilize the charge density wave. However, the wavevector of a CDW is determined by the Fermi surface and is therefore not necessarily an integral fraction of a reciprocal lattice vector of the undistorted parent phase. Consequently, an incommensurate phase may result [15], which is considered to have lost its translational symmetry. Since a CDW is accompanied by a lattice distortion, diffraction techniques (electron, neutron, X-ray) can be used to reveal satellite reflections appearing near the Bragg

reflections of the parent phase as a consequence of the new superlattice associated with the formation of the CDW. These satellites are separated from the associated Bragg reflections by a reciprocal lattice vector determined by the CDW wavevector. Figure 1.5 shows sketches of a diffraction pattern showing the commensurate and incommensurate phases.

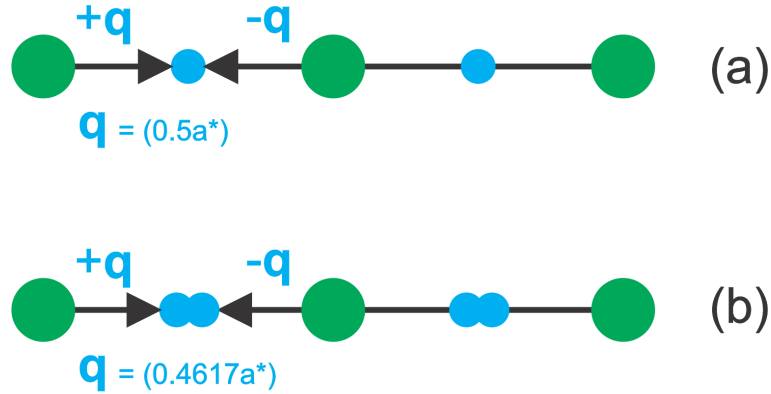


Figure 1.5: Sketch showing the commensurate (a) and incommensurate (b) phases. Large green circles indicate main reflections, small blue circles indicate satellites.

The incommensurate state described in 1.5 (b) may not actually correspond to the lowest possible energy state and, accordingly, the CDW or the lattice may undergo a further distortion that makes the two commensurate in which case the CDW wavevector is an integral fraction of the underlying lattice. The commensurate state is usually referred to as a 'lock-in' state. Thus, there can be two-phase changes associated with a CDW formation: the incommensurate transition (usually second-order) and the incommensurate-to-commensurate transformation (usually first-order).

While no material is strictly 1D, a number of inorganic materials form very anisotropic crystals, which leads to strongly anisotropic electronic structures. Initial research was focused on quasi-linear compounds like NbSe_3 [6] which is a layered material, composed of weakly bonded neighbouring planes. Its units, which consist of a triangular prism of chalcogen ions with metallic ion in the center, form infinite chains, which are held together with Nb-Se bonds. Figure 1.6 shows **a,c**- plane of NbSe_3 .

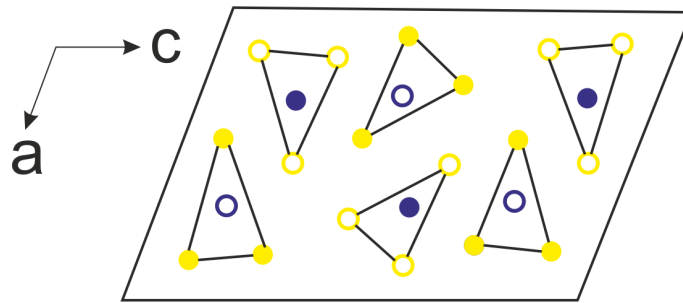


Figure 1.6: Projection of the \mathbf{a}, \mathbf{c} -plane of NbSe_3 . Dark blue circles indicate Niobium (Nb) atoms and yellow circles indicate Selenium (Se) atoms. Filled circles are atoms at $y = 0$, and open circles are atoms at $y = 0.5$. (Atomic coordinates from [16].)

Another group of such materials are transition metal bronzes, for example, ternary Molybdenum oxide of formula $\text{A}_{0.3}\text{MoO}_3$, where A is K, Rb or Tl [7]. These materials also form long chains, composed of clusters of MoO_6 octahedra, separated with alkali ions. The common property of these materials is their high band anisotropy. There is a strong overlap of d orbitals along the chain direction, but no d - d overlap in perpendicular direction. Consequently, these materials are good conductors in the direction of chains while perpendicular electrical conductivity is 1-3 orders of magnitude smaller. Figure 1.7 shows the crystal structure of $\text{K}_{0.3}\text{MoO}_3$.

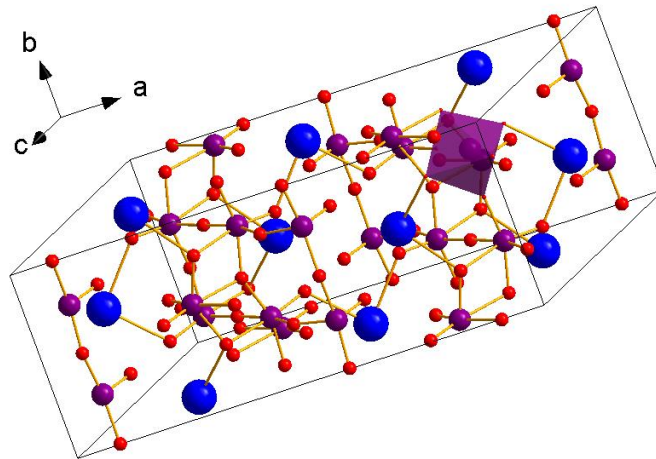


Figure 1.7: Crystal structure of $\text{K}_{0.3}\text{MoO}_3$. Dark blue spheres correspond to Potassium (K), purple spheres correspond to Molybdenum (Mo) atoms and red spheres correspond to Oxygen (O) atoms. Purple octahedron shows the Mo atom surrounded by six O atoms. (Drawn with Diamond software [17] with atomic coordinates from [18].)

Another large group of highly anisotropic compounds are transition metal dichalcogenides, which are composed of weakly bound layers of MX_2 [19]. They have recently been getting more attention due to advances in scanning probe microscopy and preparation techniques [10]. In a layered quasi-2D material 2H-NbSe_2 , the classic and the most studied CDW system, a large number of studies [20] have shown that the observed charge ordering phase transition cannot be understood within the Peierls scenario. Most importantly, angle-resolved photo-emission spectroscopy measurements do not show any sign of FSN [20]. Moreover, the measured resistivity as a function of temperature showed no change at the CDW transition temperature [21], indicating there is no metal–insulator transition associated with the structural transition. Apparently, the origin of the CDW in this system is not driven by FSN. Instead, it has been postulated that CDW phases are dictated by the \mathbf{q} -dependent electron–phonon coupling (EPC) [22]. One may argue that both FSN and EPC are forms of electron–lattice interaction, involving excitations of electrons from filled to empty states. However, they should be distinguished because FSN involves elastic scattering, whereas EPC involves inelastic scattering from the lattice [20]. Figure 1.8 shows the crystal structure of 2H-NbSe_2 .

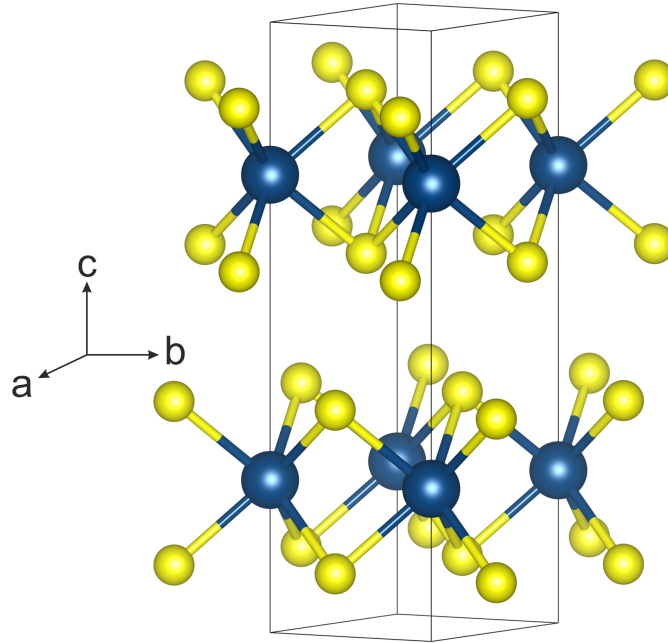


Figure 1.8: Crystal structure of 2H-NbSe_2 . Blue spheres correspond to Niobium (Nb) atoms and yellow spheres correspond to Selenium (Se) atoms. (Drawn with Vesta software [23] with atomic coordinates from [24].)

The CDW transitions have been reported in a number of compounds that have 3D crystal structures. Some of them include trivalent rare earth and divalent atoms such as $R_5Ir_4Si_{10}$ [25], $Lu_2Ir_3Si_5$ [26, 27], RTe_2 [28], RTe_3 [29], and $M_3T_4Sn_{13}$ ($M = Ca, Sr$; $T = Ir, Rh$) [30]. The crystal structures of these compounds have either quasi-1D chains or quasi-2D planes with strong inter-chain or inter-planar interactions. Multiple CDW transitions were observed both in $R_5Ir_4Si_{10}$ and $R_2Ir_3Si_5$ instead of a single CDW transition [25]. Further strong inter-chain or inter-planar interactions lead to first order characteristics (hysteresis in the temperature dependencies of resistivity, susceptibility near the T_{CDW}) of the CDW transition, unlike the usual CDW phase transition, which is a second-order phase transition. There is also a significant contribution from the phonons due to phonon softening at the phase transition. This causes large entropy change at the phase transition resulting in a strong CDW system [25]. Understanding of the CDW in these systems is far from complete as compared to those of low-dimensional CDW systems. In order to get a clear picture, one needs direct measurements of electronic structure using angle-resolved photo-emission (ARES), phonon dispersion (using inelastic neutron scattering) of these materials, direct bandgap measurements of the CDW using optical conductivity or STM (scanning tunneling microscope) measurements and X-ray diffraction studies of the periodic lattice distortion.

In this thesis we have investigated two 3D CDW compounds; CuV_2S_4 and $Er_2Ir_3Si_5$. CuV_2S_4 is a spinel described by the cubic space group $Fd\bar{3}m$ at room temperature [31]. Figure 1.9 shows the spinel structure of CuV_2S_4 .

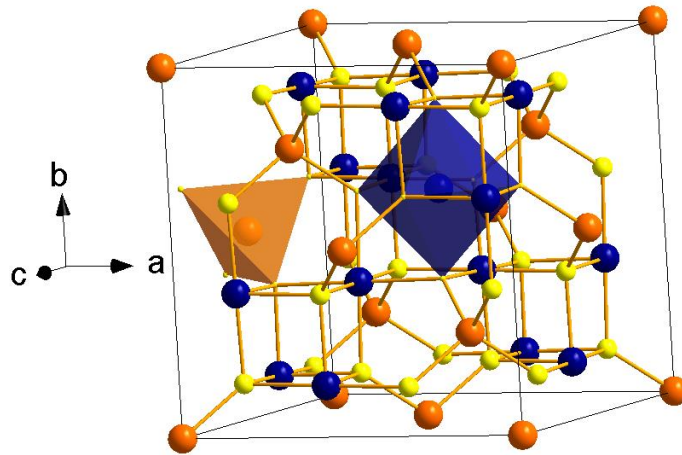


Figure 1.9: Crystal structure of CuV_2S_4 . Cu atoms are orange spheres, V are blue spheres and S are yellow spheres. The Cu atoms are surrounded by four neighbouring S atoms forming tetrahedra and the V atoms are surrounded by six S atoms forming the octahedra. (Drawn with Diamond software [17].)

Upon cooling the compound down to 90 K, superlattice reflections appear in the $\mathbf{a}^*\mathbf{b}^*$ plane at incommensurate positions at $(3/4 + \delta, 3/4 + \delta, 0)$. A lowering of symmetry is also observed from $Fd\bar{3}m$ to orthorhombic $Imm2$ [32]. The symmetry remains orthorhombic $Imm2$, however, locks to a 3-fold superstructure upon cooling it down to 50 K. The observation of CDW in CuV_2S_4 can only be considered as atypical since its structure has no clear low dimensional (1D or 2D) features. The origin of the CDW prior to the present study remained unclear. By doing detailed refinement and analysis of the structure of high-quality single crystals of CuV_2S_4 , it is shown that the formation of extended vanadium clusters is at the origin of the CDW.

$\text{Er}_2\text{Ir}_3\text{Si}_5$ belongs to the family of $\text{R}_2\text{Ir}_3\text{Si}_5$ ($\text{R} = \text{Lu}, \text{Ho}, \text{Er}, \text{Dy}, \text{etc.}$). It adopts the $\text{U}_2\text{Ir}_3\text{Si}_5$ structure type at room temperature described by the space group $Ibam$. Figure 1.10 shows two projections of the structure.

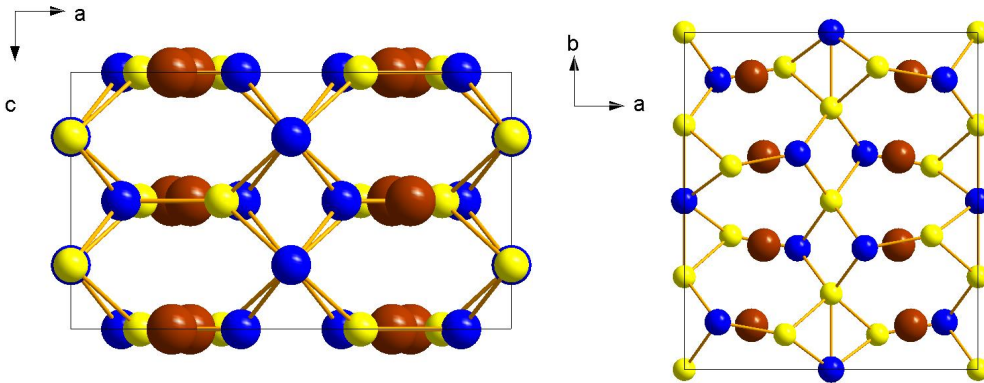


Figure 1.10: Crystal structure of $\text{Er}_2\text{Ir}_3\text{Si}_5$ at room temperature. Projections along \mathbf{a}, \mathbf{c} and \mathbf{a}, \mathbf{b} -planes. Brown spheres correspond to Erbium (Er) atoms, blue spheres correspond to Iridium (Ir) atoms and yellow spheres correspond to Silicon (Si) atoms. (Drawn with Diamond software [17].)

$\text{Er}_2\text{Ir}_3\text{Si}_5$ undergoes an incommensurate CDW transition with CDW wavevector $\mathbf{q} = (0.25 - \delta, 0.5 - \delta, 0.25 - \delta)$. A lowering of the symmetry was observed from $Ibam$ to $I\bar{1}$. However, unlike CuV_2S_4 , the phase transition is of first-order indicated by hysteresis loop from our physical property measurements which is also in agreement with the previous literature [33, 34]. The structure of $\text{Er}_2\text{Ir}_3\text{Si}_5$ also has no low-dimensional features similar to those of CuV_2S_4 . From our analysis of the structure, it is seen that CDW resides on the chain of Iridium atoms.

1.1.3 Twinning

The twinning of crystals is defined as 'regular aggregates consisting of individual crystals of the same species joined together in some definite mutual orientation' by *Giacovazzo et al.* [35]. The relation between the domains of the twinned crystal is the 'twin law' which is a set of operations relating the twin components to each other by rotation, mirror or inversion.

Twins can be broadly classified as growth twins, deformation twins and transformation twins. Growth twins may occur due to accidents during the synthesis of the crystal which disrupts or influences a change in the lattice thereby creating a new crystal in different direction on the face of the parent crystal. The twin components have different orientation and share some of the lattice points. Such crystals can easily be identified under the microscope. There is a chance that growth twinning can be avoided for some materials if one carefully controls the thermodynamic conditions. Figure 1.11 shows a growth twin of a quartz crystal.



Figure 1.11: Crystal twinning by growth (Japan twin) as seen in a quartz crystal (Reproduced from Rob Lavinsky [36].)

Deformation twins occur by relieving the strain induced by some applied stress.

Transformation twins occur as a result of phase transitions, whereby the symmetry of the crystal structure reduces from a higher to a lower one, and the two are related by group-subgroup relations. The lost symmetry operators act as a twin law to describe the relation of the lower symmetry twin domains with the parent domain. Such type of twins can be understood by studying the diffraction pattern. Both CuV_2S_4 and $\text{Er}_2\text{Ir}_3\text{Si}_5$ are twinned as a result of the lowering of symmetry after undergoing the CDW phase transitions. Twinning in both these compounds

presents a challenge to solve the crystal structure as it also modulated. Figure 1.12 shows a diffraction pattern of $\text{Er}_2\text{Ir}_3\text{Si}_5$ where both main and satellite reflections are split as a result of twinning which leads to complications while solving the crystal structure.

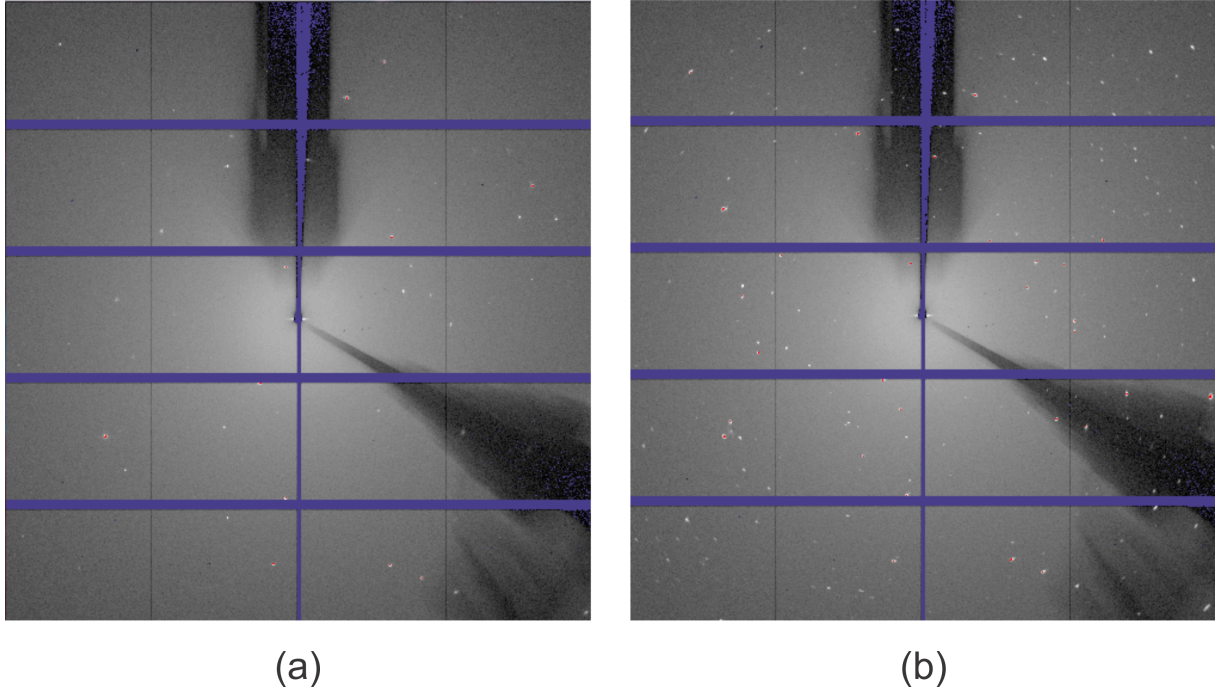


Figure 1.12: (a) Diffraction of $\text{Er}_2\text{Ir}_3\text{Si}_5$ at 200 K. Sample is not twinned above the phase transition. (b) Diffraction of $\text{Er}_2\text{Ir}_3\text{Si}_5$ at 75 K. One can see many split peaks and a lot more reflections compared to 200 K. Sample becomes twinned after the phase transition. (Both images are image no. 1 with attenuator 0.)

From the diffraction pattern of twinned crystals, we can observe merohedral, pseudo-merohedral and non-merohedral twins. The point groups of the crystal lattices $\bar{1}$ (triclinic), $2/m$ (monoclinic), mmm (orthorhombic), $4/mmm$ (tetragonal), $\bar{3}m$ (rhombohedral), $6/mmm$ (hexagonal) and $m\bar{3}m$ (cubic) are known as the holohedral point groups. If the twin law belongs to the point group which is essentially a subgroup of the above mentioned holohedral point groups, then it is referred to as a twin by merohedry. For example, the holohedry of the cubic lattice is $m\bar{3}m$; the low-symmetry cubic structure might belong to pointgroups 23, $m\bar{3}$, 432 or $\bar{4}3m$. This would categorize into merohedral twins [37]. In such type of twinning, the lattices of the twin components undergo complete overlap in direct and reciprocal space. From the diffraction pattern of such crystals, one cannot distinguish between the peaks from the different twin domains. One may, however, notice a change in the intensity of the reflections before and after the phase transition.

Pseudo-merohedral twinning is said to occur when 'the lattice of the individual has a metric close to that of a higher holohedry' [38]. The lattices of the twin domains do not directly coincide with each other as there is a slight deviation between the lattices. The degree of deviation is described by ω known as the twin obliquity [38]. From the diffraction pattern, one can see that not all the reflections from the domains undergo complete overlapping as some of them are partially overlapped. A simple example is a pseudo-monoclinic system where the symmetry, in reality, is actually triclinic as two out of the three of the axial angles are close to 90 deg. The twin law that describes the relation between such cases is one of the lost symmetry operators from the 'pseudo-higher' Laue class. A more complex example of such a twinning is CuV_2S_4 . This compound goes from cubic $Fd\bar{3}m$ down to orthorhombic $Imm2$ resulting in 12 twelve twin domains, related by the lost symmetry operations like the 3-fold rotation along the body diagonal, 4-fold rotation parallel to the c axis, mirror planes and loss of inversion center as $Imm2$ is a non-centrosymmetric space group. For CuV_2S_4 the main reflections approximately coincide with each other. The superlattice reflections are separate and not shared belonging to each individual domain respectively.

There exists another type of twinning known as the non-merohedral twinning where the lattices do not coincide in certain planes of direct and reciprocal space. Looking at the diffraction pattern one can see many more diffraction spots from the twinned crystal compared to the untwinned one (See Figure 1.12). The split reflections would require a different orientation matrix to index them the reflections do not overlap in certain planes of the reciprocal space. An example of a such case is one of the compounds $\text{Er}_2\text{Ir}_3\text{Si}_5$ which we have found the twin relation [37] to be:

$$Q = \begin{pmatrix} 1 & 0 & 0 \\ 0 & -1 & 0 \\ (2c \cos \beta)/a & 0 & -1 \end{pmatrix} \quad (1.2)$$

The system is pseudo-monoclinic where $\beta \neq 90$ deg and as a result, the element $(2c \cos \beta)/a$ from the matrix Q in equation 1.2 is non-zero. Therefore, the twin law is a not 2 fold rotation parallel to the a axis but rather derived from the temperature-dependent lattice parameters. If one transforms the (h, k, l) as given in equation 1.2, it is seen that for increasing value of l , the splitting is larger and if l is 0 then there is no splitting. Meaning that the $hk0$ plane is common between the two domains. In this case of non-merohedral twinning, Figure 1.13 (a) shows a regular orthorhombic lattice before the phase transition and 1.13 (b) shows a twinned monoclinic lattice after the phase transition.

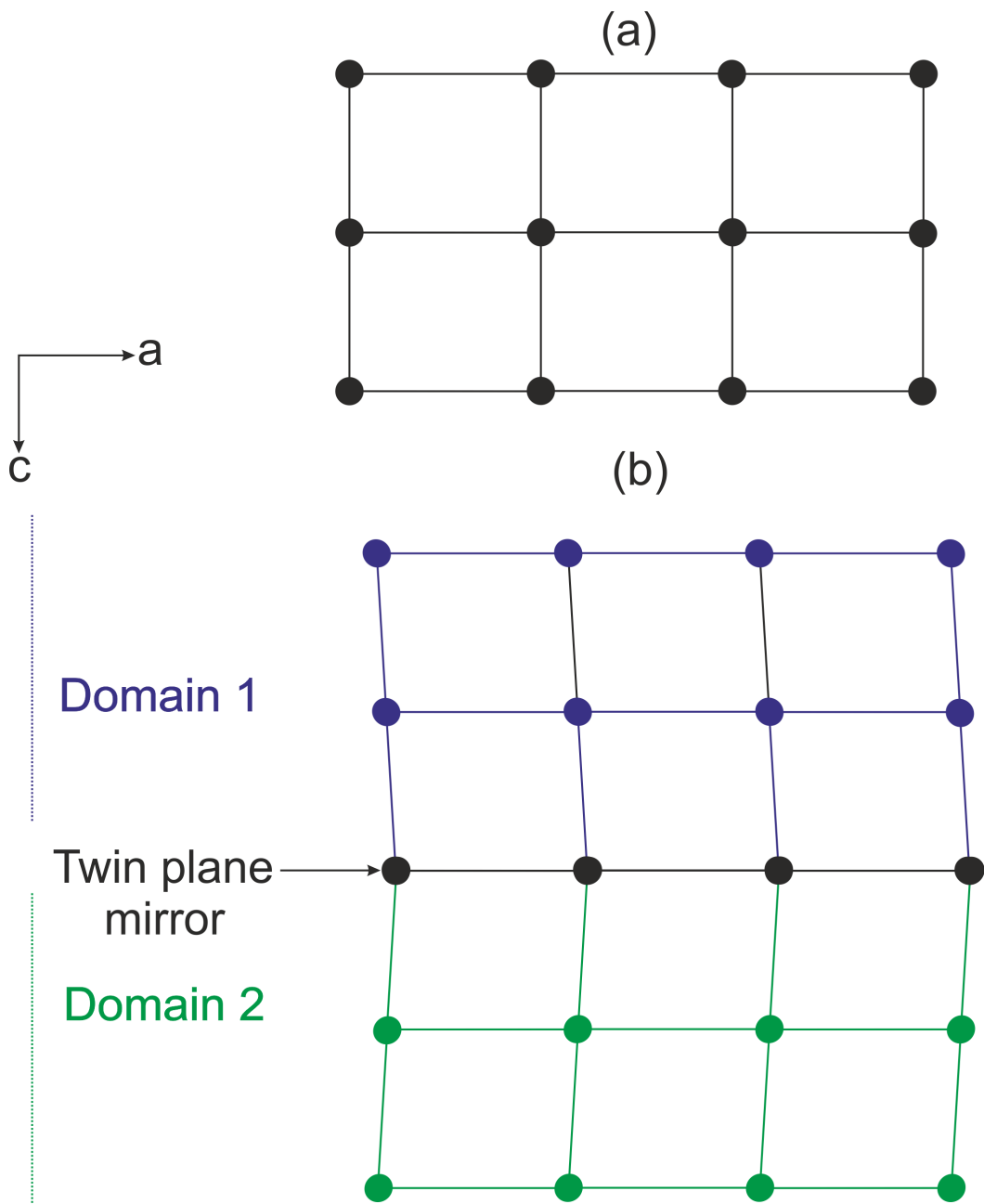


Figure 1.13: a) Shows a regular lattice. (b) Twinned crystal where the two domains are separated by a boundary.

1.2 Overview of the results

In the second part of this chapter, major results from the previous investigations of the compounds CuV_2S_4 , $\text{Er}_2\text{Ir}_3\text{Si}_5$ and $\text{Ni}_{0.89}\text{V}_{2.11}\text{Se}_4$ are presented in the context of the present work.

1.2.1 CDW behaviour in CuV_2S_4

CuV_2S_4 was studied through the means of resistivity, magnetic susceptibility and NMR experiments, where a phase transition was reported to occur below 100 K [39, 40]. Further investigation was done by Fleming *et al.* in 1981 [31], where he reported two CDW transitions at 90 K and 50 K based on his analysis through X-ray diffraction and physical property measurements. At 90 K, He observed the presence of superlattice reflections at $\mathbf{q} = (\sigma, \sigma, 0)$, with $\sigma = 1/4 - \delta$. Upon cooling the crystal down to 50 K, the wavevector remains in the $\mathbf{a}^*\mathbf{b}^*$ plane, but the sigma component (σ) of the wavevector \mathbf{q} changes to $1/3$. The compound was also studied by Okada *et al.* [41] in 2004 where he did a PXRd of the sample and reported that symmetry of the crystal reduces from cubic to tetragonal. Okada *et al.* also performed magnetic susceptibility and resistivity measurements where he found the anomalies at 90 K and 50 K which is in agreement with what Fleming had found. In 2012 Kawaguchi *et al.* [32] studied the nature of CDW in CuV_2S_4 by powder X-ray diffraction and found that symmetry of CuV_2S_4 below 90 K to be orthorhombic $Imm2$. He also observed that at 70 K, the superlattice reflections were at positions $(3/4 - \delta, 3/4 - \delta, 0)$, which is in agreement with Fleming. However, on cooling the crystal down to 20 K the wavevector remained as $(3/4 - \delta, 3/4 - \delta, 0)$ and did not reach $(1/3, 1/3, 0)$.

Our main motivation to study the spinel CuV_2S_4 is to understand the nature of the CDW at 90 K phase transition as well as the low-temperature transition around 50 K. Moreover, we report on the role of the disorder in the CDW in CuV_2S_4 by conducting single-crystal X-ray diffraction (SXRd) measurements and measurements of bulk electronic properties on as-grown and annealed crystals [42].

Upon analysis of the SXRd data from both as-grown and annealed crystals, we observe that the 90 K phase transition is an incommensurate CDW where the symmetry of the crystal reduces from cubic $Fd\bar{3}m$ to orthorhombic $Imm2$ with the appearance of superlattice reflections at incommensurate positions $\mathbf{q} = (3/4 + \delta, 3/4 + \delta, 0)$ which is agreement with [32]. Although annealing the crystal does not change the symmetry of the crystal, the temperature at which the CDW transition occurs is close to 90 K which is consistent with the literature. However, for the as-grown crystals the CDW transition occurs at a much lower temperature, at 84 K.

The 50 K phase transition never quite occurred in the as-grown crystals as the

sigma component (σ) of the wavevector \mathbf{q} continued to reduce passing through the rational value of $3/4$ but did not reach $(2/3, 2/3, 0)$. There was one exception for a crystal upon cooling it down to 4.2 K the satellites are present both in positions $(3/4+\delta, 3/4+\delta, 0)$ and $(2/3+\delta, 2/3+\delta, 0)$ with respect to the main reflections resulting in a mixture of both 90 K and 50 K phases. However, the annealed crystals could undergo the 50 K phase transition albeit with significant time up to four hours. The 50 K phase transition is found to be a lock-in transition towards a 3-fold superstructure.

On comparison of the physical properties of both as-grown crystals and annealed crystals, we find that the residual resistivity ratio ($\rho(300\text{ K})/\rho(4.2\text{ K})$) increases by almost a factor of four as compared to the as-grown crystal. The most, revealing effect is the absence of the phase transition at 50 K in the heat capacity data of as-grown crystal even though it exhibits the high-temperature CDW transition at 87 K. On the other hand, one observes both transitions at 90 K and 56 K for the annealed crystal. In addition, anomalies in the magnetic susceptibility are found to appear sharper for the annealed crystal as compared to the as-grown one.

Our conclusion based on this is that the properties of the annealed crystal are different from that of the as-grown crystal as certain lattice defects inhibit the as-grown crystals from undergoing the phase transition at 50 K and also affect the phase transition at 90 K by causing it to happen at a much lower temperature. The crystal structure model from both annealed and as-grown crystals that we present significantly differs from that proposed by Kawaguchi *et al.* [32], as we not only observed the dimerization of the V1 chains but also have found a major distortion of the average positions of the V2 chains resulting in a dimerization of about 0.18 Å. Based on our analysis we deem 3D clusters of Vanadium atoms to be the key role in the formation of the CDW in CuV_2S_4 .

1.2.2 Interplay of CDW, antiferromagnetism and disorder in $\text{Er}_2\text{Ir}_3\text{Si}_5$

One of the more interesting features of the CDW is how it competes with other phase transitions namely superconducting and magnetic ordering. $\text{Er}_2\text{Ir}_3\text{Si}_5$ at room temperature crystallizes in the orthorhombic *Ibam*, $\text{U}_2\text{Co}_3\text{Si}_5$ structure type [43].

In 2012 Padam *et al.* [33] investigated polycrystalline $\text{Er}_2\text{Ir}_3\text{Si}_5$ through X-ray diffraction and resistivity measurements where a first-order phase transition at 150 K was reported. Resistivity measurements were carried out on single crystal $\text{Er}_2\text{Ir}_3\text{Si}_5$ by Lalngilneia *et al.* [34] who was able to reproduce the phase transition at around 160 K. The hysteresis in the resistivity data indicates that it is a first-order phase transition. More importantly on a direct comparison with measurements from both Padam and Lalngilneia we see that phase transition is unusually sharp with the single-crystal by Lalngilneia *et al.* whereas the polycrystal by Padam *et al.* is

broader. This could be attributed to the crystalline disorder in lower quality polycrystal which has affects the CDW.

We studied $\text{Er}_2\text{Ir}_3\text{Si}_5$ through the means of SXRD and physical property measurements. From the analysis of the SXRD data at 75 K, we report the presence of satellite reflections at $\mathbf{q} = (0.2495(2), 0.4973(1), 0.2483(1))$ at 75 K which is similar to the wavevector \mathbf{q} reported by Lee *et al.* for $\text{Lu}_2\text{Ir}_3\text{Si}_5$ [44]. We also observed from the lattice parameters that at 75K, one of the axial angles β is $91.695(2)$ deg indicating a monoclinic distortion. However, it became evident that the crystal structure model provides a better fit with triclinic symmetry $I\bar{1}$ over monoclinic symmetry. Moreover, it is seen that the incommensurate CDW resides on the zigzag chains of the Iridium atoms along the c axis where there is a strong modulation along the zigzag chain of Ir1, with one distance nearly constant at 3.76 \AA , and the other distance varying between 3.1 and 3.8 \AA . Figure 1.14 shows a t -plot which is a tool in superspace capable of describing any quantity derived from the structural parameters [45] and in this case the variation of the interatomic distances d (\AA) between atoms Ir1a and Ir1b is analyzed.

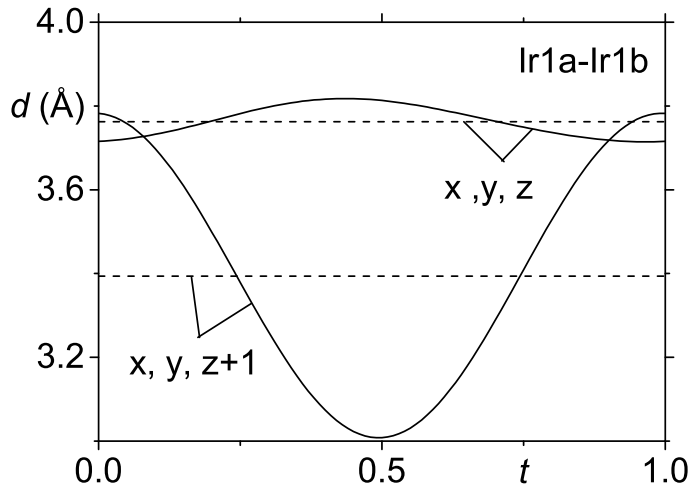


Figure 1.14: t -Plot of the interatomic distances d (\AA) between atoms Ir1a and Ir1b (x, y, z) and between Ir1a and Ir1b at ($x, y, z+1$) for the crystal structure at $T = 75$ K. Dashed lines give the distances in the basic structure, with values of $3.763(6)$ and $3.390(6) \text{ \AA}$.

In addition to the unusual nature of the CDW transition, the bulk electronic properties of $\text{Er}_2\text{Ir}_3\text{Si}_5$ crystal are anomalous in nature. The unique nature of the CDW is that it somehow influences the local magnetic moments Er^{3+} ions imply-

ing a strong coupling between the CDW and magnetism even in the paramagnetic state. This has not been observed in any system which displays multiple phase transition that includes a CDW ordering. The temperature dependence of the resistivity measurements shows that for the single-crystal, the transition is unusually sharp.

Just like CuV_2S_4 , the CDW in $\text{Er}_2\text{Ir}_3\text{Si}_5$ is also very sensitive to disorder and defects. Tests were done on a high-quality single crystal, where the magnetic order is suppressed down to at least 0.1 K. However, in the polycrystalline material the disorder broadens the CDW transition, where one observes the appearance of antiferromagnetic ordering of Er^{3+} moments at 2.1 K, as reported in [46]. This clearly suggests the underlying CDW transition and the magnetic ordering of Er^{3+} moments are strongly coupled in $\text{Er}_2\text{Ir}_3\text{Si}_5$ unlike the case of $\text{Er}_5\text{Ir}_4\text{Si}_{10}$ [47].

1.2.3 Properties of disordered $\text{Ni}_{0.89}\text{V}_{2.11}\text{Se}_4$

A study on polycrystalline NiV_2S_4 has indicated a CDW transition at 165 K [48], while another study on NiV_2Se_4 reported a small anomaly in the resistivity around 160 K [49].

We wanted to study the nature of the phase transition of NiV_2Se_4 in its single crystalline form. However, our attempts to grow single crystal of NiV_2Se_4 resulted in a Ni deficient crystal. It crystallizes in the monoclinic Cr_3S_4 structure type with space group $I2/m$ [49]. From the resistivity measurements, we have found that a single crystal of composition $(\text{Ni}_{0.894(6)}\text{V}_{0.106})\text{V}_2\text{Se}_4$ exhibits a broad anomaly around 150-200 K. All properties, including low-temperature X-ray diffraction data, are in agreement with the absence of the CDW phase transition down to $T = 2$ K. We suspect that the CDW is suppressed due to the Ni/V disorder. Figure 1.15 shows the crystal structure of $\text{Ni}_{0.89}\text{V}_{2.11}\text{Se}_4$.

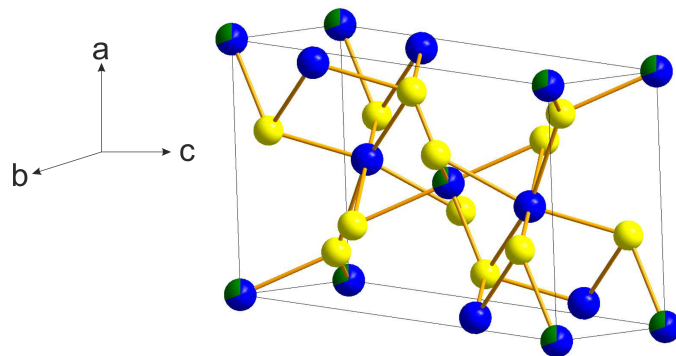


Figure 1.15: Crystal structure of $\text{Ni}_{0.89}\text{V}_{2.11}\text{Se}_4$. Yellow spheres correspond to Selenium (Se) atoms, blue spheres correspond to Vanadium (V) and the mixed colours of spheres, green and blue correspond to the mixed site Nickel/Vanadium (Ni/V). (Drawn with Diamond software [17].)

The temperature dependence of the electrical resistivity varies as $T^{3/2}$ which indicates that $\text{Ni}_{0.89}\text{V}_{2.11}\text{Se}_4$ is in a non-Fermi-liquid state for 15–150 K. Since below 15 K, the resistivity changes to T^2 dependence suggesting Fermi-liquid behavior is recovered below 15 K. These features, together with deviations from Curie-Weiss behavior of the magnetic susceptibility below 150 K can be explained by the gradual build-up of antiferromagnetic fluctuations upon cooling. Isothermal magnetization curves confirm the absence of bulk magnetic order down to 2 K but suggest a strong build-up of antiferromagnetic correlations.

We think that $\text{Ni}_{0.89}\text{V}_{2.11}\text{Se}_4$ exhibits an unusual Non-Fermi-liquid to a Fermi-liquid transition under ambient pressure. This could be due to the presence of magnetic fluctuations (borderline magnetism of Ni) and quenched disorder on the Ni/V sites. However, the results presented are preliminary and one needs more detailed study to establish that the observed features are due to Non-Fermi-liquid to Fermi-liquid transition in $\text{Ni}_{0.89}\text{V}_{2.11}\text{Se}_4$.

1.3 Outlook

In this thesis we have presented the 3D CDW crystal structures of CuV_2S_4 and $\text{Er}_2\text{Ir}_3\text{Si}_5$ and discussed the physical properties. However, there are still some unresolved issues and open questions. Namely, the strongly correlated nature of CuV_2S_4 is not understood. In particular, the origin of relatively large Sommerfeld coefficient ($\gamma \approx 35 \text{ mJ mol}^{-1} \text{ K}^{-2}$) and the T^2 dependence of resistivity at low temperatures is still not resolved. Previous studies also indicate the unusual properties of CuV_2S_4 are due to 3d states of Vanadium in the lattice. One has to perform neutron scattering as well as photoemission measurements on high-quality single crystals of CuV_2S_4 to establish whether spin fluctuations or strong electron-phonon interaction is the reason for unusual Fermi liquid properties of CuV_2S_4 . If the latter hypothesis is to be believed, CuV_2S_4 should exhibit superconductivity (SC) at low temperatures. However, we did not find SC in our annealed high-quality crystal down 10 mK.

For $\text{Er}_2\text{Ir}_3\text{Si}_5$ one needs to perform neutron scattering on crystals of varying disorder in $\text{Er}_2\text{Ir}_3\text{Si}_5$ to understand the absence of bulk magnetic ordering in a well ordered crystal of $\text{Er}_2\text{Ir}_3\text{Si}_5$. In addition, one needs to perform synchrotron studies to see whether the CDW state survives in the disordered crystals which show bulk magnetic ordering at low temperatures. Also, detailed band structure calculations and photoemission measurements have to be done to understand why CDW affects the local moments on Er^{3+} in $\text{Er}_2\text{Ir}_3\text{Si}_5$.

Finally, we observed unconventional temperature dependence of bulk properties like resistivity, susceptibility and specific heat in Ni deficient single crystal of NiV_2Se_4 . Polycrystalline NiV_2Se_4 was reported as a CDW system around 160 K. We did not observe a CDW transition in our crystal $\text{Ni}_{0.89}\text{V}_{2.11}\text{Se}_4$ down to 4.2 K.

However, the low-temperature behaviour of bulk properties implies that the system is not a Fermi liquid. More investigations (both bulk and microscopic), in particular on a stoichiometric crystal of NiV_2Se_4 are needed to understand the unusual nature of the bulk properties of this system.

Chapter 2

Analysis of single-crystal X-ray diffraction data of twinned and modulated crystals in EVAL15

This chapter deals with strategies employed in treating single-crystal X-ray diffraction (SXR) data of CuV_2S_4 and $\text{Er}_2\text{Ir}_3\text{Si}_5$, which are both twinned and modulated after the phase transition. The method used here is not straightforward due to the limitations of the software employed for data processing. While it is possible to index and integrate the data as a twin with modulation in EVAL15 [50], the problem lies during the absorption correction with SADABS [51] which cannot handle twins with an incommensurate modulation. As a result, an alternative approach was taken to handle the data. The basic principle is that in EVAL15 we could index and integrate the data with one *rmat* file which has the orientation matrix describing the positions of the main reflections. After which we append the \mathbf{q} vectors describing the positions of the satellites with respect to the main reflections. In order to distinguish the satellites from the different domains, we have to apply the twin law to the \mathbf{q} vector and transform it accordingly. \mathbf{q} vector combinations are also used from which EVAL15 can employ linear combinations to generate other \mathbf{q} vectors. After integrating in (3+n)D we sort out the satellite reflections into their respective domains and reduce it to (3+1)D with a small Fortran-95 program.

The idea behind this procedure is that for CuV_2S_4 almost all main reflections are shared by all the twin domains, whereas each satellite reflection belongs to a single twin domain and is not shared. The method is explained in Section 2.3. For $\text{Er}_2\text{Ir}_3\text{Si}_5$ the situation becomes more complex as the main reflections are also split but a similar strategy is described in Section 2.6.

2.1 Experimental details and instrumental parameters

The single crystal X-ray diffraction (SXRD) of CuV_2S_4 was measured at two beamlines. Firstly on a one circle diffractometer with Eulerian geometry using a Pilatus 2M area detector at BM01 of the SNBL beamline in ESRF Grenoble [52] in 2015. Secondly on a four-circle Eulerian diffractometer using a Marccd 165 detector in experimental hutch 2 (EH2) of the P24 beamline in PETRA III Hamburg in 2018. CuV_2S_4 is reported to show two phase transitions, one at 90 K and the other at 50 K [31].

Another material $\text{Er}_2\text{Ir}_3\text{Si}_5$ was also measured at P24 beamline in PETRA III Hamburg in 2019 to investigate the structural phase transition of 150 K [33, 34]. Table 2.1 shows the instrumental parameters used for the experiments.

Table 2.1: Instrumental parameters of SNBL BM01 ESRF and P24 PETRA III DESY.

Beamline	BM01 SNBL ESRF	P24 PETRA III DESY	P24 PETRA III DESY
Compound	CuV_2S_4	CuV_2S_4	$\text{Er}_2\text{Ir}_3\text{Si}_5$
Detector	Pilatus 2M	MarCCD165	Pilatus 1M CdTe
Pointsperad gamma	1	0.9	1
Beam size (h*v) (μm) ²	350 * 320	400 * 400	400 * 400
Diffractometer	KUMA KM6-CH	4-circle Huber diffractometer	4-circle Huber diffractometer
Exposure time (s)	0.1	1	1
Crystal to detector distance (mm)	146	90	110
Vertical position of detector (mm)	80	-	-
$2\theta_{offset}$ (deg)	0	0	0
χ (deg)	0	-60	-60
Rotation per image (deg)	0.1	1	1
No. of frames per run	3640	362	362
Wavelengths used Å	0.67760	0.495935	0.499940

2.2 Initial set-up of the data

For the data collected at beamline BM01 SNBL ESRF, each run has 3640 image files with a 0.1 deg rotation per image. As EVAL15 cannot handle the processing of thousands of images, we binned the 3640 images to 364 images with 1 deg rotation per image using the SNBL toolbox [52]. The data was collected on a Pilatus 2M area detector (see table 2.1 for details).

The Pilatus detectors are manufactured by the company DECTRIS, they function on the principle of hybrid photon counting (HPC) [53, 54]. They consist of semiconductor sensors such as Silicon or Cadmium Telluride. On the basis of the photoelectric effect of the semiconductor sensors, the detected X-rays are converted to electrical signals, where the electrical signals are counted by the sensors. They are well known for their for the large dynamic range and absence of background

noise. The Pilatus detector is made up of several multichip modules which is an amalgamation of several integrated circuits, semiconducting components, etc.

The image produced by the Pilatus detector is a crystallographic binary file format (*cbf*) [55]. The header information regarding the instrumental parameters used in the experiment is appended to the binary file, which is read in VIEW a program within EVAL15 as shown in Figure 2.1.

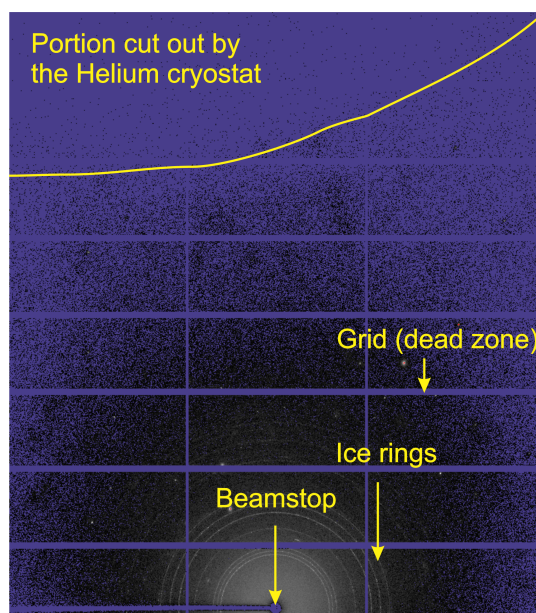


Figure 2.1: Frame no. 1 of the 4.2 K data collected on the Pilatus 2M area detector at ESRF, showing the ice problem. (Header information is given in Table 2.1)

From VIEW we study the frames and can ascertain whether the data is of sufficient quality for further processing, thus it is imperative that we should check all the frames in the run in order to avoid processing empty or damaged frames. For example, in Figure 2.1 we see that the data is unusable due to the development of ice rings as we could not be able to find the appropriate unit cell with good indexing. Notice the grid which is the spacing between the modules, the dead pixels in the grid have been excluded from the indexing and integration procedures.

We also used the MarCCD165 detector at beamline P24 PETRA III DESY Hamburg to collect data. The MarCCD 165 is manufactured by the company RAYONIX. The MarCCD is equipped with 165 mm diameter detector head, and typically with 4 ccd sensor chips. The detector is cooled to a temperature of about -70 deg Celcius so as to lower background noise. The images produced by them are of *mccd* format which can also be read in VIEW in EVAL15. Typically the header information regarding the instrumental parameters is not included with image file, and as a result

we had to include it manually in the *view.init* file which is a text file that is read by VIEW. Figure 2.2 shows the mccd image of the CuV_2S_4 at 80 K.

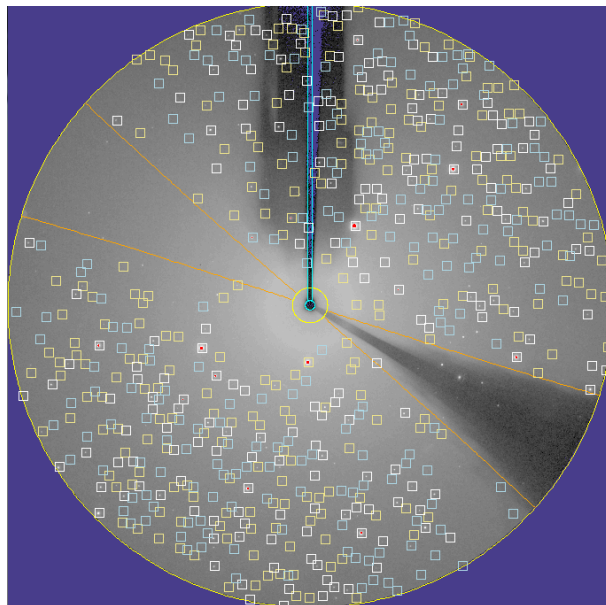


Figure 2.2: Image of the 80 K data collected using MarCCD165 as seen in VIEW, EVAL15. The squares are boxes created by EVAL15 around each calculated reflection position. (Header information is given in Table 2.1)

Along with *view.init*, it is important to also have the *goniostat.vic* file which holds the information regarding the geometry of the goniometer. Each temperature consists of two or three runs with varying attenuation filter factors to capture both strong main and weak satellite reflections, it is advisable to process the images of the different runs together for a single temperature.

2.3 Integration of diffraction data of CuV_2S_4

For CuV_2S_4 we observe that below 90 K the main reflections are surrounded by the satellite reflections of first order at incommensurate positions close to $(3/4, 3/4, 0)$ and at commensurate positions $(2/3, 2/3, 0)$ below 55 K. Almost all the main reflections are shared by all the domains whereas the satellite reflections belong to each domain separately and are not shared. Meaning that we have some main reflections which undergo a small splitting. EVAL15 can handle such reflections whose splitting is smaller than the width of the reflection by obtaining an integrated intensity which is a sum of the intensities from the domains. However, the splitting

is large for the satellites such that EVAL15 can only obtain the integrated intensity for one domain. Figure 2.3 shows the diffraction sketch of CuV_2S_4 at 83 K.

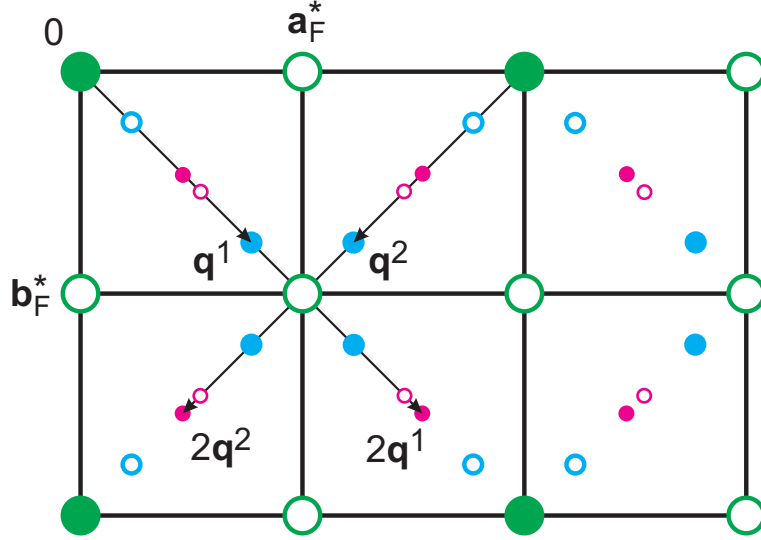


Figure 2.3: Schematic representation of the $(\mathbf{a}_F^*, \mathbf{b}_F^*)$ plane of the diffraction pattern of incommensurate CuV_2S_4 below T_{CDW} . Open circles indicate the positions of reflections that are extinct due to the F centering. Positions of second-order satellites are indicated, but these reflections have not been observed.

Due to limitations of SADABS [51] which cannot handle twinned incommensurate for absorption correction, an alternate approach was taken where all reflections have been indexed using six integers (h, k, l, m, n, p) on a F -centered pseudo cubic lattice with point symmetry $\bar{1}$ with three modulation wave vectors $(\mathbf{q}^2, \mathbf{q}^4, \mathbf{q}^5)$ selected from Table 2.2.

Table 2.2: Six modulation wave vectors describing the twelve satellite reflections at positions $\pm\mathbf{q}^j$ around the main reflections. The domain number gives the assignment to the orthorhombic domain.

q.no.	Modulation wavevector, \mathbf{q}	Domain.no
\mathbf{q}^1	$(\sigma, \sigma, 0)$	1
\mathbf{q}^2	$(-\sigma, \sigma, 0)$	2
\mathbf{q}^3	$(\sigma, 0, \sigma)$	3
\mathbf{q}^4	$(-\sigma, 0, \sigma)$	4
\mathbf{q}^5	$(0, \sigma, \sigma)$	5
\mathbf{q}^6	$(0, -\sigma, \sigma)$	6

Along with the orientation matrix describing the positions of the main reflec-

tions we append the chosen wavevectors ($\mathbf{q}^2, \mathbf{q}^4, \mathbf{q}^5$) to describe the other three modulation wave vectors ($\mathbf{q}^1, \mathbf{q}^3, \mathbf{q}^6$) by linear combination.

$$\begin{aligned}\mathbf{q}^1 &= \mathbf{q}^5 - \mathbf{q}^4 = (\sigma \mathbf{a}_F^* + \sigma \mathbf{b}_F^* + 0 \mathbf{c}_F^*) \\ \mathbf{q}^3 &= \mathbf{q}^5 - \mathbf{q}^2 = (\sigma \mathbf{a}_F^* + 0 \mathbf{b}_F^* + \sigma \mathbf{c}_F^*) \\ \mathbf{q}^6 &= \mathbf{q}^4 - \mathbf{q}^2 = (0 \mathbf{a}_F^* - \sigma \mathbf{b}_F^* + \sigma \mathbf{c}_F^*)\end{aligned}\tag{2.1}$$

The six modulation wave vectors have also been sorted in their respective orthorhombic twin domains.

In order to successfully index and integrate we must also understand the relation between the twin domains. The relation is a twin law which essentially is a 3 x 3 matrix 'Q'. Before we explore the relations we present the basic formulae in relating the atomic coordinates, reflection indices and basis vectors of direct and reciprocal space between the twin domains.

Important formulae

Atomic coordinates:

$$\begin{pmatrix} x' \\ y' \\ z' \end{pmatrix} = Q \begin{pmatrix} x \\ y \\ z \end{pmatrix}\tag{2.2}$$

Reflection indices:

$$\begin{pmatrix} h' \\ k' \\ l' \end{pmatrix} = Q^{-1,t} \begin{pmatrix} h \\ k \\ l \end{pmatrix}\tag{2.3}$$

Basis vectors of direct space:

$$\begin{pmatrix} \mathbf{a}' \\ \mathbf{b}' \\ \mathbf{c}' \end{pmatrix} = Q^{-1,t} \begin{pmatrix} \mathbf{a} \\ \mathbf{b} \\ \mathbf{c} \end{pmatrix}\tag{2.4}$$

Basis vectors of reciprocal space:

$$\begin{pmatrix} \mathbf{a}^{*'} \\ \mathbf{b}^{*'} \\ \mathbf{c}^{*'} \end{pmatrix} = Q \begin{pmatrix} \mathbf{a}^* \\ \mathbf{b}^* \\ \mathbf{c}^* \end{pmatrix}\tag{2.5}$$

Now that the formulae have been listed we use them to explain the relations between the domains.

Domain 1

As we consider domain 1 as a reference point or 'parent'. The relation to itself is

described the Identity given by: $Q = \begin{pmatrix} 1 & 0 & 0 \\ 0 & 1 & 0 \\ 0 & 0 & 1 \end{pmatrix}$

In this specific case, $Q = Q^{-1} = Q^t = Q^{-1,t}$ which renders no change to the atomic coordinates, reflection indices and basis vectors of direct and reciprocal space.

Domain 2

$$Q = Q^{-1,t} = \begin{pmatrix} 0 & 1 & 0 \\ -1 & 0 & 0 \\ 0 & 0 & 1 \end{pmatrix} \text{ and } Q^{-1} = Q^t = \begin{pmatrix} 0 & -1 & 0 \\ 1 & 0 & 0 \\ 0 & 0 & 1 \end{pmatrix}$$

This is $+270^\circ$ rotation about $[001]$ direction.

$$\begin{pmatrix} x' \\ y' \\ z' \end{pmatrix} = Q \begin{pmatrix} x \\ y \\ z \end{pmatrix} = \begin{pmatrix} y \\ -x \\ z \end{pmatrix} \quad (2.6)$$

$$\begin{pmatrix} h' \\ k' \\ l' \end{pmatrix} = Q^{-1,t} \begin{pmatrix} h \\ k \\ l \end{pmatrix} = \begin{pmatrix} k \\ -h \\ l \end{pmatrix} \quad (2.7)$$

$$\begin{pmatrix} \mathbf{a}' \\ \mathbf{b}' \\ \mathbf{c}' \end{pmatrix} = Q^{-1,t} \begin{pmatrix} \mathbf{a} \\ \mathbf{b} \\ \mathbf{c} \end{pmatrix} = \begin{pmatrix} \mathbf{b} \\ -\mathbf{a} \\ \mathbf{c} \end{pmatrix} \quad (2.8)$$

$$\begin{pmatrix} \mathbf{a}^{*'} \\ \mathbf{b}^{*'} \\ \mathbf{c}^{*'} \end{pmatrix} = Q \begin{pmatrix} \mathbf{a}^* \\ \mathbf{b}^* \\ \mathbf{c}^* \end{pmatrix} = \begin{pmatrix} \mathbf{b}^* \\ -\mathbf{a}^* \\ \mathbf{c}^* \end{pmatrix} \quad (2.9)$$

Domain 3

$$Q = Q^{-1,t} = \begin{pmatrix} 0 & 0 & 1 \\ 1 & 0 & 0 \\ 0 & 1 & 0 \end{pmatrix} \text{ and } Q^{-1} = Q^t = \begin{pmatrix} 0 & 1 & 0 \\ 0 & 0 & 1 \\ 1 & 0 & 0 \end{pmatrix}$$

This is $+120^\circ$ rotation about $[111]$ direction.

$$\begin{pmatrix} x' \\ y' \\ z' \end{pmatrix} = Q \begin{pmatrix} x \\ y \\ z \end{pmatrix} = \begin{pmatrix} z \\ x \\ y \end{pmatrix} \quad (2.10)$$

$$\begin{pmatrix} h' \\ k' \\ l' \end{pmatrix} = Q^{-1,t} \begin{pmatrix} h \\ k \\ l \end{pmatrix} = \begin{pmatrix} l \\ h \\ k \end{pmatrix} \quad (2.11)$$

$$\begin{pmatrix} \mathbf{a}' \\ \mathbf{b}' \\ \mathbf{c}' \end{pmatrix} = Q^{-1,t} \begin{pmatrix} \mathbf{a} \\ \mathbf{b} \\ \mathbf{c} \end{pmatrix} = \begin{pmatrix} \mathbf{c} \\ \mathbf{a} \\ \mathbf{b} \end{pmatrix} \quad (2.12)$$

$$\begin{pmatrix} \mathbf{a}^{*'} \\ \mathbf{b}^{*'} \\ \mathbf{c}^{*'} \end{pmatrix} = Q \begin{pmatrix} \mathbf{a}^* \\ \mathbf{b}^* \\ \mathbf{c}^* \end{pmatrix} = \begin{pmatrix} \mathbf{c}^* \\ \mathbf{a}^* \\ \mathbf{b}^* \end{pmatrix} \quad (2.13)$$

Domain 4

$$Q^{-1} = Q^t = Q^{-1,t} = Q = \begin{pmatrix} -1 & 0 & 0 \\ 0 & 0 & 1 \\ 0 & 1 & 0 \end{pmatrix}$$

This is $+180^\circ$ rotation about $[011]$ direction.

$$\begin{pmatrix} x' \\ y' \\ z' \end{pmatrix} = Q \begin{pmatrix} x \\ y \\ z \end{pmatrix} = \begin{pmatrix} -x \\ z \\ y \end{pmatrix} \quad (2.14)$$

$$\begin{pmatrix} h' \\ k' \\ l' \end{pmatrix} = Q^{-1,t} \begin{pmatrix} h \\ k \\ l \end{pmatrix} = \begin{pmatrix} -h \\ l \\ k \end{pmatrix} \quad (2.15)$$

$$\begin{pmatrix} \mathbf{a}' \\ \mathbf{b}' \\ \mathbf{c}' \end{pmatrix} = Q^{-1,t} \begin{pmatrix} \mathbf{a} \\ \mathbf{b} \\ \mathbf{c} \end{pmatrix} = \begin{pmatrix} -\mathbf{a} \\ \mathbf{c} \\ \mathbf{b} \end{pmatrix} \quad (2.16)$$

$$\begin{pmatrix} \mathbf{a}^{*'} \\ \mathbf{b}^{*'} \\ \mathbf{c}^{*'} \end{pmatrix} = Q \begin{pmatrix} \mathbf{a}^* \\ \mathbf{b}^* \\ \mathbf{c}^* \end{pmatrix} = \begin{pmatrix} -\mathbf{a}^* \\ \mathbf{c}^* \\ \mathbf{b}^* \end{pmatrix} \quad (2.17)$$

Domain 5

$$Q = Q^{-1,t} = \begin{pmatrix} 0 & 1 & 0 \\ 0 & 0 & 1 \\ 1 & 0 & 0 \end{pmatrix} \text{ and } Q^{-1} = Q^t = \begin{pmatrix} 0 & 0 & 1 \\ 1 & 0 & 0 \\ 0 & 1 & 0 \end{pmatrix}$$

This is -120° rotation about $[111]$ direction.

$$\begin{pmatrix} x' \\ y' \\ z' \end{pmatrix} = Q \begin{pmatrix} x \\ y \\ z \end{pmatrix} = \begin{pmatrix} y \\ z \\ x \end{pmatrix} \quad (2.18)$$

$$\begin{pmatrix} h' \\ k' \\ l' \end{pmatrix} = Q^{-1,t} \begin{pmatrix} h \\ k \\ l \end{pmatrix} = \begin{pmatrix} k \\ l \\ h \end{pmatrix} \quad (2.19)$$

$$\begin{pmatrix} \mathbf{a}' \\ \mathbf{b}' \\ \mathbf{c}' \end{pmatrix} = Q^{-1,t} \begin{pmatrix} \mathbf{a} \\ \mathbf{b} \\ \mathbf{c} \end{pmatrix} = \begin{pmatrix} \mathbf{b} \\ \mathbf{c} \\ \mathbf{a} \end{pmatrix} \quad (2.20)$$

$$\begin{pmatrix} \mathbf{a}^{*'} \\ \mathbf{b}^{*'} \\ \mathbf{c}^{*'} \end{pmatrix} = Q \begin{pmatrix} \mathbf{a}^* \\ \mathbf{b}^* \\ \mathbf{c}^* \end{pmatrix} = \begin{pmatrix} \mathbf{b}^* \\ \mathbf{c}^* \\ \mathbf{a}^* \end{pmatrix} \quad (2.21)$$

Domain 6

$$Q^{-1} = Q^t = Q^{-1,t} = Q = \begin{pmatrix} 0 & 0 & 1 \\ 0 & -1 & 0 \\ 1 & 0 & 0 \end{pmatrix}$$

This is $+180^\circ$ rotation about $[101]$ direction.

$$\begin{pmatrix} x' \\ y' \\ z' \end{pmatrix} = Q \begin{pmatrix} x \\ y \\ z \end{pmatrix} = \begin{pmatrix} z \\ -y \\ x \end{pmatrix} \quad (2.22)$$

$$\begin{pmatrix} h' \\ k' \\ l' \end{pmatrix} = Q^{-1,t} \begin{pmatrix} h \\ k \\ l \end{pmatrix} = \begin{pmatrix} l \\ -k \\ h \end{pmatrix} \quad (2.23)$$

$$\begin{pmatrix} \mathbf{a}' \\ \mathbf{b}' \\ \mathbf{c}' \end{pmatrix} = Q^{-1,t} \begin{pmatrix} \mathbf{a} \\ \mathbf{b} \\ \mathbf{c} \end{pmatrix} = \begin{pmatrix} \mathbf{c} \\ -\mathbf{b} \\ \mathbf{a} \end{pmatrix} \quad (2.24)$$

$$\begin{pmatrix} \mathbf{a}^{*'} \\ \mathbf{b}^{*'} \\ \mathbf{c}^{*'} \end{pmatrix} = Q \begin{pmatrix} \mathbf{a}^* \\ \mathbf{b}^* \\ \mathbf{c}^* \end{pmatrix} = \begin{pmatrix} \mathbf{c}^* \\ -\mathbf{b}^* \\ \mathbf{a}^* \end{pmatrix} \quad (2.25)$$

Now that we have presented the relations between the different domains, there is still a question to be answered on how it occurs. The twinning happens due to the loss of symmetry. The crystal at room temperature is cubic $Fd\bar{3}m$. As the symmetry of the lattice is reduced from cubic to tetragonal, the characteristic feature of the cubic symmetry, the threefold rotation along the body diagonal is lost and can be used as a twin law to describe the three tetragonal twin domains with each domain having two modulation wave vectors. The symmetry is further lowered from tetragonal to orthorhombic. Upon doing so the fourfold rotation parallel the c

axis is lost. Each of the three tetragonal twin domains is split into two orthorhombic domains, a total of six orthorhombic twin domains having one \mathbf{q} vector each. Figure 2.4 shows a flowchart describing the symmetry loss.

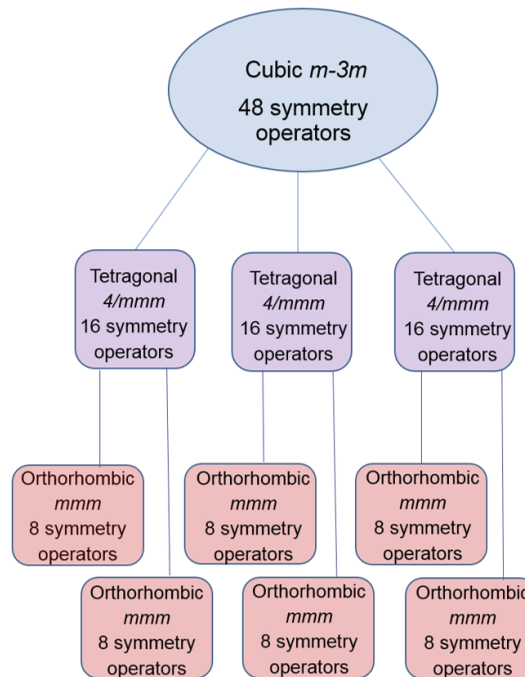


Figure 2.4: Flow chart showing the reduction in symmetry.

As the symmetry lowers to orthorhombic, the mirror planes perpendicular to the a and b axis are lost, the mirror planes perpendicular to the diagonals are preserved, and an I centered lattice can be obtained as indicated in Figure 2.5.

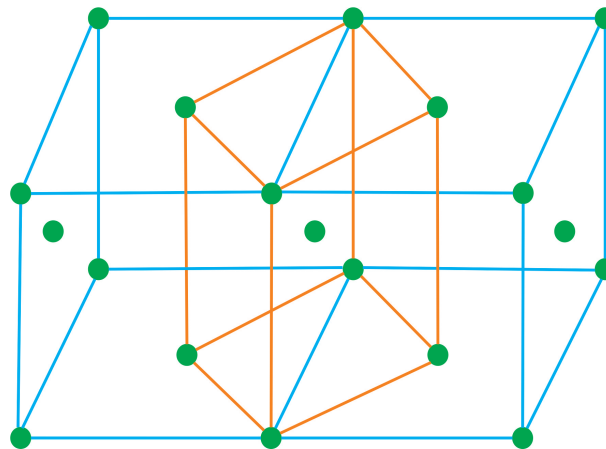


Figure 2.5: I-center cell obtained from F-center.

However, we wish to preserve the F centered setting as it is easier to compare the structure at room and low temperatures and also the twin laws for the domains are mathematically more complex for the I-center. Details regarding the relation between F and I center are discussed in Section A1 in Appendix A: Structure refinements and models of CuV_2S_4 .

Integrated intensities are obtained for main reflections $(h, k, l, 0, 0, 0)$ and for first order satellites (h, k, l, m, n, p) where the values of m, n, p are listed in Table 2.3. The absorption corrected was determined by SADABS [51]. Point symmetry $\bar{1}$ has been used for the calculations, this is the minimum symmetry of the diffraction pattern where the 6 twin domains have unequal volume. SADABS is incapable of handling incommensurate data that is twinned. Hence we integrated one domain with three modulation wave vectors and later split it into 6 domains using an external Fortran-95 program. Using the program we have transformed (h, k, l, m, n, p) to (h', k', l', m') , we have transformed also the reflection indices for the six twin domains.

Table 2.3: Indexing of the twelve satellite reflections surrounding one main reflection. Information is given for (i) the cubic indexing (h, k, l, m, n, p) and (ii) the orthorhombic indexing (h, k, l, m') .

Sr.no	m, n, p	Modulation wavevector, \mathbf{q}	Type	Domain No.	m'
1	1 0 0	$(-\sigma, \sigma, 0)$	\mathbf{q}^2	2	1
2	0 1 0	$(-\sigma, 0, \sigma)$	\mathbf{q}^4	4	1
3	0 0 1	$(0, \sigma, \sigma)$	\mathbf{q}^5	5	1
4	-1 0 0	$(\sigma, -\sigma, 0)$	$-\mathbf{q}^2$	2	-1
5	0 -1 0	$(\sigma, 0, -\sigma)$	$-\mathbf{q}^4$	4	-1
6	0 0 -1	$(0, -\sigma, -\sigma)$	$-\mathbf{q}^5$	5	-1
7	1 -1 0	$(0, \sigma, -\sigma)$	$-\mathbf{q}^6$	6	-1
8	0 1 -1	$(-\sigma, -\sigma, 0)$	$-\mathbf{q}^1$	1	-1
9	1 0 -1	$(-\sigma, 0, -\sigma)$	$-\mathbf{q}^3$	3	-1
10	-1 1 0	$(0, -\sigma, \sigma)$	\mathbf{q}^6	6	1
11	0 -1 1	$(\sigma, \sigma, 0)$	\mathbf{q}^1	1	1
12	-1 0 1	$(\sigma, 0, \sigma)$	\mathbf{q}^3	3	1

Table 2.3 shows the sorting of the satellite reflections into their respective twin domains and their subsequent reduction from (3+3)D to (3+1)D. We have used $\mathbf{q}^2 \mathbf{q}^4 \mathbf{q}^5$ in the *rmat* file with 12 \mathbf{q} vector combinations from Tables 2.2 and 2.3. $(m * \mathbf{q}^2) + (n * \mathbf{q}^4) + (p * \mathbf{q}^5)$ will give us \mathbf{q} .

2.4 Refining lattice parameters of CuV_2S_4 post integration

As mentioned in Section 2.3, some of the main reflections of CuV_2S_4 undergo a small splitting. However, the splitting is smaller than the width of the reflections, such that EVAL15 obtains an integrated intensity that is the sum of the intensities of the domains. The satellite reflections, on the other hand, are completely split, belong to a single twin domain and are not shared. In order to tackle the problem of indexing and integrating the satellites we must apply the twin law. But this time rather taking one orientation matrix with different \mathbf{q} . We use another approach to get accurate lattice parameters for CuV_2S_4 , where we integrate the data as a twin with six *rmat* files each having one orientation matrix each for one domain. We apply the twin law to each of the orientation matrices but not the wavevector, thereby integrating in (3+1)D which happens to be the standard approach if SADABS could handle it. After processing in ANY we generate a peak file where the strongest reflections are stored after removal of weak reflections with which the refinement is done in PEAKREF. Constraints are used in the specific case of CuV_2S_4 , where $a = b$ and $\alpha = \beta = 90$ deg. The results are shown for one temperature in Table 2.4.

Table 2.4: Accurate lattice parameters of CuV_2S_4 at 83 K. Notice that γ is not 90 deg. This is because we preserved the F-center during indexing and integration. Details regarding the transformation from F to I are given in Section A1 in Appendix A: Structure refinements and models of CuV_2S_4 .

a (Å)	9.7741(3)
c (Å)	9.7591(5)
γ °	89.960(2)
σ of \mathbf{q}	0.7629(2)
V (Å ³)	932.29(7)

2.5 Absorption correction for CuV_2S_4

After integration, the *final.y* file produced by EVAL15 is read in the program ANY, where 3 to 5% of the reflections are rejected as outliers. After which the reflection files which can be imported for absorption correction in SADABS with triclinic Laue group $\bar{1}$. The *hk6* file created was processed by Fortran-95 program to reduce it from (3+3)D to (3+1)D and also to sort out the reflections of different domains such that each *hk6* file will have only the satellites belonging to a single domain. After running Fortran-95 program, we had one *hk6* file for the main reflections and six *hk6* for the satellites. All the files were later imported in Jana 2006 [56] for structure refinement

and analysis.

2.6 Integration of diffraction data of $\text{Er}_2\text{Ir}_3\text{Si}_5$

Compared to CuV_2S_4 , the integration of diffraction data of $\text{Er}_2\text{Ir}_3\text{Si}_5$ is more complex. At 130 K and below we have observed that the main reflections are surrounded by weaker superlattice reflections of first order, moreover it is observed that the twinning results in the splitting of both main reflections and satellites. Figure 2.6 shows a diffraction sketch of $\text{Er}_2\text{Ir}_3\text{Si}_5$ at 20 K.

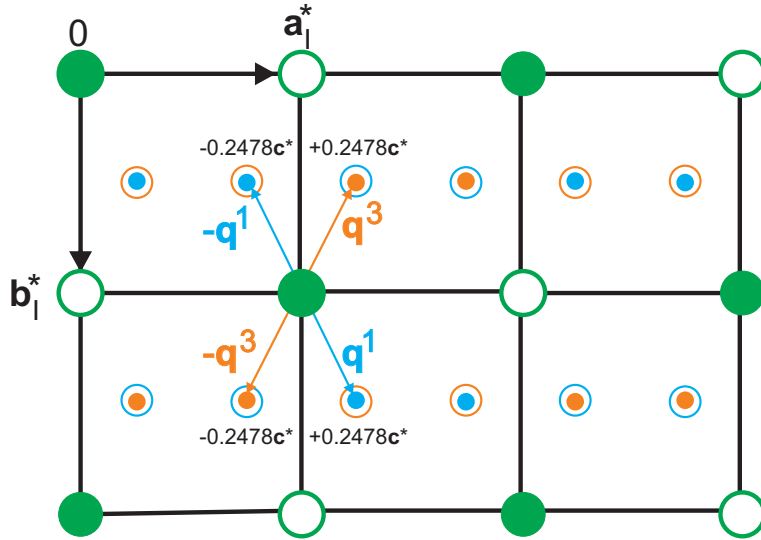


Figure 2.6: Sketch of the $(\mathbf{a}_I^*, \mathbf{b}_I^*)$ reciprocal lattice plane of $\text{Er}_2\text{Ir}_3\text{Si}_5$ in the triclinic phase at 20 K. Green circles are the main reflections, blue circles are the \mathbf{q}^1 satellites, and orange circles indicate the \mathbf{q}^3 satellites. Main reflections are in the plane of the drawing, while satellite reflections are projected onto it. Open circles indicate systematic absences.

Integrating the data was not straightforward as SADABS does not allow to simultaneously handle twinning and an incommensurate modulation.

For integration and absorption correction of the intensities of Bragg reflections, we therefore had to index and integrate main reflections of domain 1 and domain 3 with the satellites belonging separately to domain 1 and domain 3 in (h, k, l, m, n) on an I-centered lattice. Domain 1 and domain 3 are related by a mirror plane perpendicular to the b axis where the main reflections are shared between the two domains and the satellites are not. Thus in addition to the main reflections, we have chosen:

$$\begin{aligned}
\mathbf{q}^1 &= (\sigma_1 \mathbf{a}_I^* + \sigma_2 \mathbf{b}_I^* + \sigma_3 \mathbf{c}_I^*) \\
\mathbf{q}^3 &= (\sigma_1 \mathbf{a}_I^* - \sigma_2 \mathbf{b}_I^* + \sigma_3 \mathbf{c}_I^*)
\end{aligned}
\tag{2.26}$$

where \mathbf{q}^1 and \mathbf{q}^3 are wavevectors of domain 1 and domain 3 respectively, describing the positions of the superlattice reflections with respect to the main reflections belonging both to domain 1 and domain 3.

Similarly to handle the split main reflections and its corresponding satellites that arises due to the non-merohedral twinning a second independent integration in (h, k, l, m, n) was done for the main reflections of domain 2 and domain 4 with the satellites reflections that belong to domains 2 and 4 separately. Domain 2 and domain 4 are also related by the mirror plane perpendicular to the b axis. Thus if we index the main reflections of domain 2 and domain 4 we have:

$$\begin{aligned}
\mathbf{q}^2 &= (\sigma_1 \mathbf{a}_{II}^* + \sigma_2 \mathbf{b}_{II}^* + \sigma_3 \mathbf{c}_{II}^*) \\
\mathbf{q}^4 &= (\sigma_1 \mathbf{a}_{II}^* - \sigma_2 \mathbf{b}_{II}^* + \sigma_3 \mathbf{c}_{II}^*)
\end{aligned}
\tag{2.27}$$

where \mathbf{q}^2 and \mathbf{q}^4 are independent wavevectors of domain 2 and domain 4 describing the positions of the superlattice reflections with respect to the main reflections belonging both to domain 2 and domain 4.

Accordingly, all Bragg reflections can be indexed by five integer indices (h, k, l, m, n) with respect to

$$\{\mathbf{a}_I^*, \mathbf{b}_I^*, \mathbf{c}_I^*, \mathbf{q}^1, \mathbf{q}^3\}. \tag{2.28}$$

$$\{\mathbf{a}_{II}^*, \mathbf{b}_{II}^*, \mathbf{c}_{II}^*, \mathbf{q}^2, \mathbf{q}^4\}. \tag{2.29}$$

Table 2.5 shows the wavevector combinations and which domain it belongs to. After integrating and absorption correction as (h, k, l, m, n) , the reflection file was reduced to (h, k, l, m') using a Fortran-95 program. Using SADABS equivalent reflections for computation of scaling and absorption correction have been defined by point symmetry $\bar{1}$, as this is the symmetry of the diffraction pattern. Table 2.6 shows the results after integrating the data as (3+2)D.

Table 2.5: Indexing of the four satellite reflections surrounding one main reflection that belongs both to domain 1 and domain 3. Information is given for (i) the indexing (h, k, l, m, n) and (ii) the indexing (h, k, l, m') . The principle of indexing and integrating is the same for the reflections of domain 2 and domain 4.

m, n	Modulation wavevector, q	Type	Domain No	m'
1 0	$(\sigma_1, \sigma_2, \sigma_3)$	\mathbf{q}^1	1	1
0 1	$(\sigma_1, -\sigma_2, \sigma_3)$	\mathbf{q}^3	3	1
-1 0	$(-\sigma_1, -\sigma_2, -\sigma_3)$	$-\mathbf{q}^1$	1	-1
0 -1	$(-\sigma_1, \sigma_2, -\sigma_3)$	$-\mathbf{q}^3$	3	-1

Table 2.6: ANY and SADABS results for 3+2 integration for both domains at 75 K. Three different runs with different attenuators have been integrated together to capture both strong main reflections and weak satellite reflections.

Domain + sat	Domain1(main+sat)+Domain3(sat)	Domain2(main+sat)+Domain4(sat)
Reflections (ANY)	85828	85445
Reflections (SADABS)	16075	15994
Measured main	3206	3156
Measured sat	6438(D1) and 6431(D3)	6416(D2) and 6422(D4)
R_{int} % (SADABS) Attenuator 24	0.1211	0.2477
R_{int} % (SADABS) Attenuator 10	0.0605	0.0663
R_{int} % (SADABS) Attenuator 0	0.0601	0.0580

When it comes to the case of partially overlapped reflections EVAL15 is rather unpredictable. In the sense that, EVAL15 could integrate the two intensities as a sum or simply integrate only one intensity from the twin domain, as a result they are unreliable. Thus we excluded the partially overlapped reflections in Jana 2006 [56]. The reflections with difference in theta smaller than “Maximal angular difference for twin overlap” are treated as fully overlapped; the reflections with theta difference larger than “Minimal angular difference for full separation” are treated as fully separated; the reflections between the limits are discarded. The limits should be adjusted carefully not to discard too many reflections. From Table 2.7 the values $L1 = 0.1$ and $L2 = 0.27$ have been chosen.

Table 2.7: Refinement results from Jana 2006 of the 75 K data attenuator 0 with 155 parameters Maximal angular difference for twin overlap” (L1 in the table) and “Minimal angular difference for full separation” (L2 in the table).

$R_F(\text{main})\%$	$R_F(\text{sat})\%$	wR(all)%	Unique main (obs/all)	Unique sat(obs/all)	Comments	L1	L2
5.94	6.84	7.90	1022/1572	1097/13042	D1(main) + all sat	0.1	0.1
5.72	5.20	6.66	769/1249	1025/12496	D1(main) + all sat	0.1	0.27
6.08	8.02	7.46	1022/0	1097/0	D1(main) + all sat	0.1	0.1
5.74	5.21	6.33	769/0	1025/0	D1(main) + all sat	0.1	0.27
14.15	8.03	20.21	866/1513	1097/13042	D2(main)+ all sat	0.1	0.1
5.84	5.23	6.64	1022/1572	720/6527	D1(main) + D1 and D3(sat)	0.1	0.1
14.36	12.81	21.13	866/1513	377/6515	D2(main)+ D2 and D4(sat)	0.1	0.1
9.40	7.23	16.17	1839/2997	1097/13042	All	0.1	0.1
6.51	5.27	7.68	1190/2098	966/11521	All No NPD	0.1	0.4
6.56	5.24	7.94	1395/2394	979/11892	All No NPD	0.1	0.35
6.56	5.22	7.94	1395/2394	1002/12220	All No NPD	0.1	0.3
6.56	5.28	7.96	1395/2394	1025/12496	All No NPD	0.1	0.27
6.62	5.28	7.78	1395/0	1025/0	All	0.1	0.27
7.64	5.50	11.16	1623/2691	1025/12496	All	0.1	0.26
7.64	5.50	11.16	1623/2691	1025/12496	All	0.1	0.25

For a detailed description of the procedure please refer to Section B5 in Appendix B: Structure refinements and models of $\text{Er}_2\text{Ir}_3\text{Si}_5$.

Another important case is that of understanding the relation between the twin domains which is crucial to index and integrate the data. We describe the relation between the different twin domains. The formulae used are described in Section 2.3.

Domain 1

As we consider domain 1 as a reference point or ‘parent’. The relation to itself is described the Identity given by: $Q = \begin{pmatrix} 1 & 0 & 0 \\ 0 & 1 & 0 \\ 0 & 0 & 1 \end{pmatrix}$

In this specific case, $Q = Q^{-1} = Q^t = Q^{-1,t}$ which renders no change to the atomic coordinates, reflection indices and basis vectors of direct and reciprocal space.

Domain 2

$$Q = Q^{-1} = \begin{pmatrix} 1 & 0 & 0 \\ 0 & -1 & 0 \\ -0.0359 & 0 & -1 \end{pmatrix} \text{ and } Q^t = Q^{-1,t} = \begin{pmatrix} 1 & 0 & -0.0359 \\ 0 & -1 & 0 \\ 0 & 0 & -1 \end{pmatrix}$$

$$\begin{pmatrix} x' \\ y' \\ z' \end{pmatrix} = Q \begin{pmatrix} x \\ y \\ z \end{pmatrix} = \begin{pmatrix} x \\ -y \\ -0.0359x - z \end{pmatrix} \quad (2.30)$$

$$\begin{pmatrix} h' \\ k' \\ l' \end{pmatrix} = Q^{-1,t} \begin{pmatrix} h \\ k \\ l \end{pmatrix} = \begin{pmatrix} h - 0.0359l \\ -k \\ -l \end{pmatrix} \quad (2.31)$$

$$\begin{pmatrix} \mathbf{a}' \\ \mathbf{b}' \\ \mathbf{c}' \end{pmatrix} = Q^{-1,t} \begin{pmatrix} \mathbf{a} \\ \mathbf{b} \\ \mathbf{c} \end{pmatrix} = \begin{pmatrix} \mathbf{a} - 0.0359\mathbf{c} \\ -\mathbf{b} \\ -\mathbf{c} \end{pmatrix} \quad (2.32)$$

$$\begin{pmatrix} \mathbf{a}^{*'} \\ \mathbf{b}^{*'} \\ \mathbf{c}^{*'} \end{pmatrix} = Q \begin{pmatrix} \mathbf{a}^* \\ \mathbf{b}^* \\ \mathbf{c}^* \end{pmatrix} = \begin{pmatrix} \mathbf{a}^* \\ -\mathbf{b}^* \\ -0.0359\mathbf{a}^* - \mathbf{c}^* \end{pmatrix} \quad (2.33)$$

Domain 3

$$Q^{-1} = Q^t = Q^{-1,t} = Q = \begin{pmatrix} 1 & 0 & 0 \\ 0 & -1 & 0 \\ 0 & 0 & 1 \end{pmatrix}$$

$$\begin{pmatrix} x' \\ y' \\ z' \end{pmatrix} = Q \begin{pmatrix} x \\ y \\ z \end{pmatrix} = \begin{pmatrix} x \\ -y \\ z \end{pmatrix} \quad (2.34)$$

$$\begin{pmatrix} h' \\ k' \\ l' \end{pmatrix} = Q^{-1,t} \begin{pmatrix} h \\ k \\ l \end{pmatrix} = \begin{pmatrix} h \\ -k \\ l \end{pmatrix} \quad (2.35)$$

$$\begin{pmatrix} \mathbf{a}' \\ \mathbf{b}' \\ \mathbf{c}' \end{pmatrix} = Q^{-1,t} \begin{pmatrix} \mathbf{a} \\ \mathbf{b} \\ \mathbf{c} \end{pmatrix} = \begin{pmatrix} \mathbf{a} \\ -\mathbf{b} \\ \mathbf{c} \end{pmatrix} \quad (2.36)$$

$$\begin{pmatrix} \mathbf{a}^{*'} \\ \mathbf{b}^{*'} \\ \mathbf{c}^{*'} \end{pmatrix} = Q \begin{pmatrix} \mathbf{a}^* \\ \mathbf{b}^* \\ \mathbf{c}^* \end{pmatrix} = \begin{pmatrix} \mathbf{a}^* \\ -\mathbf{b}^* \\ \mathbf{c}^* \end{pmatrix} \quad (2.37)$$

Domain 4

$$Q = Q^{-1} = \begin{pmatrix} 1 & 0 & 0 \\ 0 & 1 & 0 \\ -0.0359 & 0 & -1 \end{pmatrix} \text{ and } Q^t = Q^{-1,t} = \begin{pmatrix} 1 & 0 & -0.0359 \\ 0 & 1 & 0 \\ 0 & 0 & -1 \end{pmatrix}$$

$$\begin{pmatrix} x' \\ y' \\ z' \end{pmatrix} = Q \begin{pmatrix} x \\ y \\ z \end{pmatrix} = \begin{pmatrix} x \\ y \\ -0.0359x - z \end{pmatrix} \quad (2.38)$$

$$\begin{pmatrix} h' \\ k' \\ l' \end{pmatrix} = Q^{-1,t} \begin{pmatrix} h \\ k \\ l \end{pmatrix} = \begin{pmatrix} h - 0.0359l \\ k \\ -l \end{pmatrix} \quad (2.39)$$

$$\begin{pmatrix} \mathbf{a}' \\ \mathbf{b}' \\ \mathbf{c}' \end{pmatrix} = Q^{-1,t} \begin{pmatrix} \mathbf{a} \\ \mathbf{b} \\ \mathbf{c} \end{pmatrix} = \begin{pmatrix} \mathbf{a} - \mathbf{0.0359c} \\ \mathbf{b} \\ -\mathbf{c} \end{pmatrix} \quad (2.40)$$

$$\begin{pmatrix} \mathbf{a}^{*'} \\ \mathbf{b}^{*'} \\ \mathbf{c}^{*'} \end{pmatrix} = Q \begin{pmatrix} \mathbf{a}^* \\ \mathbf{b}^* \\ \mathbf{c}^* \end{pmatrix} = \begin{pmatrix} \mathbf{a}^* \\ \mathbf{b}^* \\ -\mathbf{0.0359a}^* - \mathbf{c}^* \end{pmatrix} \quad (2.41)$$

After we present the different relations to better understand the twin laws, we describe how it happens by lowering of symmetry. The crystal starts out at room temperature as Orthorhombic *Ibam*. After undergoing the phase transition below 150 K it becomes either monoclinic or triclinic twinned. Triclinic symmetry is favoured due to the R_{int} of the monoclinic symmetry of the integrated satellite intensities to be rather large at 0.49, whereas with the triclinic symmetry is around 0.05. Also during the refinement of the wavevector the σ_2 component of the wavevector should be 0.5 however upon refinement, it always refined close to 0.4972(2) breaking monoclinic symmetry. These results and comparisons are discussed in more detail in Table B5 in Appendix B: Structure refinements and models of $\text{Er}_2\text{Ir}_3\text{Si}_5$.

2.7 Refining lattice parameters of $\text{Er}_2\text{Ir}_3\text{Si}_5$ post integration

As mentioned in Section 2.6 for $\text{Er}_2\text{Ir}_3\text{Si}_5$ some of reflections undergo a large splitting such that EVAL15 would need another orientation matrix to describe the positions of the reflections from the other twin domain. In order to solve the problem, we integrated the data twice in (3+2)D. However, for the acquiring accurate lattice parameters, we use another approach, where we integrate the data as a twin with four *rmat* files each having one orientation matrix each for one domain. We apply the twin law to each of the orientation matrices but not the wavevector, thereby integrating in (3+1)D. After processing in ANY we generate a peak file where the strongest reflections are stored after removal of weak reflections with which the refinement is done in PEAKREF. Constraints are not used in the case of $\text{Er}_2\text{Ir}_3\text{Si}_5$ as it is triclinic $I\bar{1}$, The results are shown for one such temperature in Table 2.8. Each temperature consists of several runs with different filter factors, the images of the runs have been processed together as a single set.

Table 2.8: Accurate lattice parameters of $\text{Er}_2\text{Ir}_3\text{Si}_5$ at 75 K.

a (Å)	9.8494(3)
b (Å)	11.4863(3)
c (Å)	5.7268(2)
α°	90.079(1)
β°	91.695(2)
γ°	90.051(1)
Wavevector \mathbf{q}	(0.2495(2), 0.4973(1), 0.2483(1))
V (Å ³)	647.60(5)

2.8 Absorption correction for $\text{Er}_2\text{Ir}_3\text{Si}_5$

For each temperature, we integrated the different runs with varying filter factors together. However, we had to integrate the data twice to deal with the problem of twinning as discussed in Section 2.6. As a result, we acquired two *final.y* files produced by EVAL15 which are read separately in ANY where 3 to 5% of the reflections are rejected as outliers. After which the reflection files which can be imported for absorption correction in SADABS with triclinic Laue group $\bar{1}$. Two sets of *hk6* files created in (3+2)D was processed in Fortran-95 to reduce it from (3+2)D to (3+1)D and also to sort out the reflections. After running Fortran-95 program we have six *hk6* files, two files for the main reflections which are completely split and four files for the satellite reflections. All the files were imported in Jana 2006 [56] for structure refinement and analysis. The common reflections between the domains were not suppressed and used for scaling.

Chapter 3

Charge-density-wave and lock-in transitions of CuV_2S_4

1

The three-dimensional charge-density-wave compound CuV_2S_4 is known to undergo phase transitions at ~ 91 K and ~ 50 K. Employing single-crystal X-ray diffraction on an annealed crystal, we confirm the formation of an incommensurate CDW at $T_{CDW} \approx 91$ K, and we establish the nature of the transition at $T_{lock-in} \approx 50$ K as a lock-in transition towards a threefold superstructure. As-grown crystals develop the same incommensurate CDW as the annealed crystal does, but they fail to go through the lock-in transition.

Instead, the length of the modulation wave vector continues to decrease down to low temperatures in as-grown crystals. These findings are corroborated by distinct temperature dependencies of the electrical resistivity, magnetic susceptibility and specific heat measured on as-grown and annealed crystals. A superspace model for the crystal structure of the incommensurate CDW suggests that the formation of extended vanadium clusters is at the origin of the CDW. In the lock-in phase short and long V–V distances persist, but clusters now percolate the entire crystal.

The lowering towards orthorhombic symmetry appears to be responsible for the precise pattern of short and long V–V distances. However, the orthorhombic lattice distortion is nearly zero for the annealed crystal, while it is visible for the as-grown material, again suggesting the role of lattice defects in the latter.

¹This chapter has been published as: Sitaram Ramakrishnan, Andreas Schönleber, Christian B. Hübschle, Claudio Eisele, Achim M. Schaller, Toms Rekis, Nguyen Hai An Bui, Florian Feulner, Sander van Smaalen, Biplab Bag, Srinivasan Ramakrishnan, Martin Tolkiehn, and Carsten Paulmann. Charge-density-wave and lock-in transitions of CuV_2S_4 . *Phys. Rev. B* **99**, 195140 (2019)

3.1 Introduction

Historically, charge-density waves (CDWs) have been associated with instabilities of quasi-one-dimensional (1D) metals [3, 2]. The latter compounds feature parallel chains of atoms or molecules in their crystal structures, while the electrical conductivity is much higher along this unique direction than perpendicular to it. The CDW is stabilized by Fermi surface nesting (FSN) between co-planar sections of the Fermi surface. The wave vector \mathbf{q} responsible for the FSN characterizes a wave-like variation of the valence electron density as well as a periodic lattice distortion (PLD) of the atoms.

Depending on the filling of the valence band, \mathbf{q} may be commensurate or incommensurate with the periodicities of the underlying lattice. Ideally, FSN involves the entire Fermi surface and the phase transition between the normal state and the CDW state is a metal-insulator transition, like it has been observed for blue bronze, $\text{K}_{0.3}\text{MoO}_3$ [57].

In most compounds only a finite fraction of the Fermi surface is nested, and the CDW transition causes an anomalous increase of the electrical resistivity upon cooling through the transition, like it has been found in NbSe_3 [58]. FSN as the origin of the CDW transition has been criticized by Johannes & Mazin (2008) [59]. Instead, they proposed \mathbf{q} -dependent electron-phonon coupling (EPC) to be the deciding interaction. It is now recognized that there can exist several disparate mechanisms for CDW formation, applicable in different compounds, which include FSN, EPC, orbital order and charge ordering [20, 60].

CDW instabilities have been recognized to develop in three-dimensional (3D) materials, which lack a clear anisotropy of their electrical conductivities and their crystal structures, but which involve strong electronic correlations [9]. Materials of this kind include $R_5\text{Ir}_4\text{Si}_{10}$, where R is a rare earth element [61], $R\text{NiC}_2$ [62, 63, 64, 65], $R_3\text{Co}_4\text{Sn}_{13}$ [66], $\text{Sr}_3\text{Ir}_4\text{Sn}_{13}$ [67, 68], and NiV_2S_4 [48]. Recent interest in CDW materials is motivated by the interplay between CDW, superconductivity and magnetic order.

The competition between CDWs and superconductivity was experimentally demonstrated through the observation of enhanced superconductivity upon suppression of the CDW, for example, as achieved by pressure in $\text{Lu}_5\text{Ir}_4\text{Si}_{10}$ [69], and by chemical doping in Cu_xTiSe_2 ($x \approx 0.05$) [70]. CuV_2S_4 is a prototypic 3D material, since its spinel structure has cubic symmetry $Fd\bar{3}m$ and thus lacks anisotropy of its electrical resistivity by principle. Yet, it shows CDW transitions at ~ 91 K and ~ 50 K. Furthermore, low-temperature behavior of the specific heat and magnetic susceptibility have suggested the presence of strong electron correlations [71, 42].

This makes CuV_2S_4 unique among the CDW materials. However, unlike other CDW materials, there is conflicting information on the low-temperature phase diagram. The initial report by Fleming *et al.* [31] proposed a CDW phase transition

at $T_{CDW} = 90$ K and a first-order phase transition at $T_{c2} = 50$ K with a hysteresis of $\Delta T = 10$ K. Single-crystal X-ray diffraction (SXR) by Fleming *et al.* [31] indicated the development of an incommensurate CDW at T_{CDW} with modulation wave vector $\mathbf{q} = (\frac{3}{4} + \delta)(1, 1, 0)$ and a temperature dependent incommensurability δ between 0.015 and zero [72].

At $T = 75$ K the modulation became commensurate ($\delta = 0$), while the 50 K transition involved a change of \mathbf{q} towards a different incommensurate value $\mathbf{q}' = (\frac{2}{3} + \delta')(1, 1, 0)$ with $\delta' \approx 0.01$ [31]. Subsequent work confirmed two phase transitions, albeit at different $T_{CDW} = 91.5$ K and $T_{c2} = 56$ K with a hysteresis of only 4 K [41]. Specific heat data resulted in $T_{CDW} = 92$ K and $T_{c2} = 58$ K [73]. Based on X-ray powder diffraction (XRPD), Okada *et al.* [41] discovered a tetragonal lattice distortion at all temperatures below 90 K. More recently, again using XRPD, Kawaguchi *et al.* [32] determined the modulated structure of the incommensurate CDW at 70 K, employing the orthorhombic superspace group $Imm2(0\sigma_o0)$ and modulation wave vector $\mathbf{q} = (\frac{3}{4} + \delta)(1, 1, 0)$ with $\delta = -0.0109$ (negative) [32]. An orthorhombic lattice distortion is in agreement with the number of six domains in the CDW phase as observed by electron diffraction [74]. However, Kawaguchi *et al.* [32] report the diffraction to be equal at 20 and 70 K, thus failing to see any structural effects of the phase transition at 50 K. Horny *et al.* [75, 42] have shown that the phase transitions of CuV_2S_4 depend on the history of the sample, which they attributed to the presence of disorder in various degrees. Good-quality samples with a reproducible behavior can be obtained by annealing previously synthesized single crystals at 723 K for several days [42].

Here we report the results of SXR experiments on as-grown and annealed CuV_2S_4 . For an annealed single crystal we find that the phase transition at T_{CDW} involves the development of a CDW with $\mathbf{q} = (\frac{3}{4} + \delta)(1, 1, 0)$ and a temperature-dependent incommensurability δ . The 50 K transition is identified as a lock-in transition towards $\mathbf{q}_c = \frac{2}{3}(1, 1, 0)$. The modulated structure is refined against SXR, employing the same orthorhombic superspace group as used in [32].

However, modulation amplitudes are different for some atoms than their values obtained from Rietveld refinement against XRPD [32]. We can reproduce all the previously observed behavior in the present SXR experiments on as-grown single crystals, including the absence of phase transitions in some crystals and different temperature dependencies of the modulation satellite reflections in other crystals.

The present models for the CDW and lock-in phases are discussed in view of other highly correlated CDW materials and of the band structure of CuV_2S_4 .

3.2 Experimental

3.2.1 Synthesis and X-ray diffraction

Microcrystalline CuV_2S_4 was prepared by direct reaction of the elements according to procedures discussed by Horny [42]. An evacuated and sealed quartz-glass ampoule containing a stoichiometric mixture of copper (381.2 mg; 99.999 % purity; Alfa Aesar), vanadium (635.8 mg; 99.5 %; Aldrich) and sulfur (769.6 mg; 99.998 %; Alfa Aesar), including 4% excess of vanadium, was slowly heated to and then kept at 1153 K for 120 hours. Subsequently, the ampoule was cooled down to 293 K over 8 hours.

Single crystals were grown by vapour transport in evacuated quartz-glass ampoules, employing 110 mg of previously synthesized microcrystalline powder together with 5 mg/cm^3 iodine as transport agent [42]. After slow heating, the ampoule was kept for 96 hours in a gradient of 1063 K / 1003 K, with the educt at the hotter side. Single crystals of CuV_2S_4 grew in the colder half of the ampoule with sizes of up to 0.2 mm. Different experiments led to crystals of different sizes, but never larger than 2 mm. Attempts to grow single crystals in a gradient of 1093 / 1033 K—favorably discussed in the literature [42]—resulted in the formation of single crystals of almost exclusively Cu_3VS_4 [76]. Employing an exact stoichiometric mixture or an excess of sulfur also increases the amount of Cu_3VS_4 that is formed at the product side. Crystals of suitable sizes for SXRD were taken from one batch.

They were annealed for 48 hours at 723 K in an evacuated quartz-glass ampoule [42]. One annealed crystal of good quality—crystal A—was used for the SXRD experiment at beamline P24 of the synchrotron PETRA III at DESY in Hamburg, Germany. SXRD was measured on a four-circle diffractometer with a MARCCD detector, employing monochromatic radiation of wave length $\lambda_{P24} = 0.495935 \text{ \AA}$. The temperature of the sample was set at selected values between 20 and 250 K with a CRYOCOOL open-flow cryostat, employing helium as cryo gas.

As-grown single crystals from different batches were extensively tested by SXRD on a MAR345 image plate diffractometer with monochromatized $\text{Ag-K}\alpha$ radiation ($\lambda = 0.5608 \text{ \AA}$) from a rotating anode source. Several crystals of suitable sizes (smaller than 0.2 mm) were obtained, which were of excellent quality (all peaks indexed with the cubic lattice; narrow Bragg reflections). The quality of annealed and as-grown single crystals cannot be distinguished on the basis of these criteria. Temperature dependent SXRD was measured on several as-grown single crystals at the Swiss-Norwegian Beamlines (SNBL) of the European Synchrotron Radiation Facility (ESRF) in Grenoble [52].

A one-circle diffractometer was used together with a PILATUS 2M detector placed perpendicular to the beam, employing monochromatic radiation of wave length $\lambda_{SNBL} = 0.67760 \text{ \AA}$. In a first experiment crystal B was cooled with a nitro-

gen open-flow cryostat toward temperatures between 80 and 300 K. In particular, diffraction was measured at 1 K intervals between 80 and 95 K, encompassing the CDW transition. In a second experiment, an open-flow helium cryostat was used to cool the samples at temperatures between 4.2 and 45 K [77]. This setup was prone to the formation of ice around the samples. Ice formation prevented some data sets to be indexed, while reliable values for integrated intensities of Bragg reflections could not be obtained for several more data sets, even though reliable values for the lattice parameters and modulation wave vector were obtained. Useable data were thus obtained at six temperatures for crystal C, at eight temperatures for crystal D, and at a single temperature for crystal E.

3.2.2 Physical properties

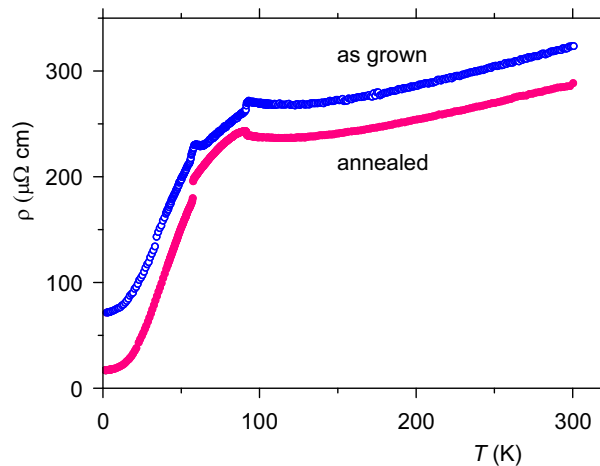


Figure 3.1: Temperature dependence (2–300 K) of the electrical resistivity (ρ) of CuV_2S_4 , as measured on an as-grown crystal (blue open circles) and on the same crystal after annealing (filled red dots).

Physical properties and their dependence on temperature have been measured on a large, bar-shaped single crystal of CuV_2S_4 : crystal P from batch KK216. Properties were initially measured on the as-grown crystal P. Subsequently, crystal P was annealed for one week at 723 K. Properties were again measured, then producing values for the annealed state. The electrical resistivity was measured at temperatures from 2 to 300 K, employing a laboratory-built set-up at the Tata Institute of Fundamental Research (TIFR) in Mumbai. Ohmic contacts have been made using conductive Silver paste and Gold wires (40 μm diameter) for the standard four-probe technique configuration to measure resistivity. Electrical resistivity was measured

using a LR-700 (Linear Research, USA) AC bridge with 5 mA current operating at a frequency of 16 Hz.

The electrical resistivities of both the as-grown and annealed states of crystal P reveal anomalies at ~ 91 and ~ 56 K, *i.e.* at both transitions (Fig. 3.1). These anomalies are sharper and more pronounced in the annealed state, in agreement with better quality of the latter state.

The resistivity is smaller for the annealed state by an amount of $35.1 \mu\Omega \text{ cm}$ at room temperature and by an amount of $54.6 \mu\Omega \text{ cm}$ at low temperatures. This indicates that annealing removes much of the defects, indeed. The excellent quality of the crystal in the annealed state also shows up in the residual resistance ratio (RRR; $\rho_{300\text{K}}/\rho_{4.2\text{K}}$) being equal to 16.5, which is comparable to the best reported values [42], and being substantially larger than 4.5 for the as-grown crystal.

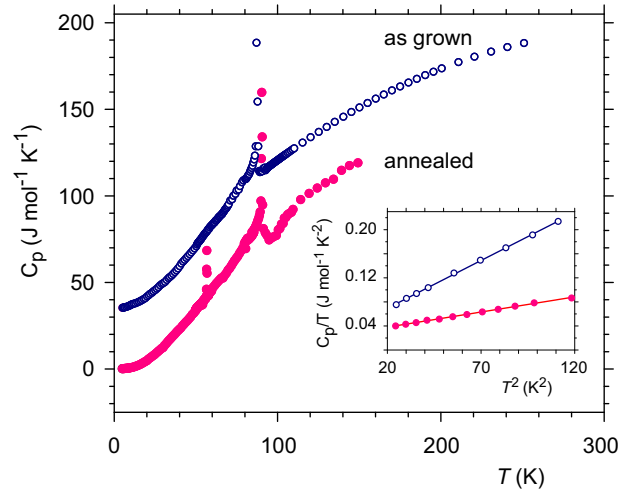


Figure 3.2: Temperature dependence (5–250 K) of the specific heat (C_p) of CuV_2S_4 , as measured on an as-grown crystal (blue open circles) and on the same crystal after annealing (red filled dots). Data for the as-grown crystal have been offset by $35 \text{ J mol}^{-1} \text{ K}^{-1}$. The inset shows C_p/T at low temperatures. The linear fit resulted in $\gamma_{asg} = 37.6(9)$ and $\gamma_{ann} = 28.0(4) \text{ mJ mol}^{-1} \text{ K}^{-2}$ for the as-grown and annealed samples, respectively.

The heat capacity (C_p) was measured by the thermal relaxation method using a Physical Property Measuring unit (PPMS, Quantum Design, USA). Data on the as-grown state were collected for 5–250 K. The annealed crystal P was measured for 5–150 K. $C_p(T)$ of the annealed crystal exhibits anomalies at $T_{CDW} = 90.37$ K and $T_{c2} = 56.68$ K, whereas $C_p(T)$ of the as-grown state has an anomaly at

$T_{CDW} = 87.08$ K only (Fig. 3.2). Clearly, the sharp feature at lower temperature is related to the lock-in transition as observed by the X-ray measurements. The low temperature heat-capacity coefficient, γ , is found to be in good agreement with the value reported earlier (Fig. 3.2) [31, 75, 42].

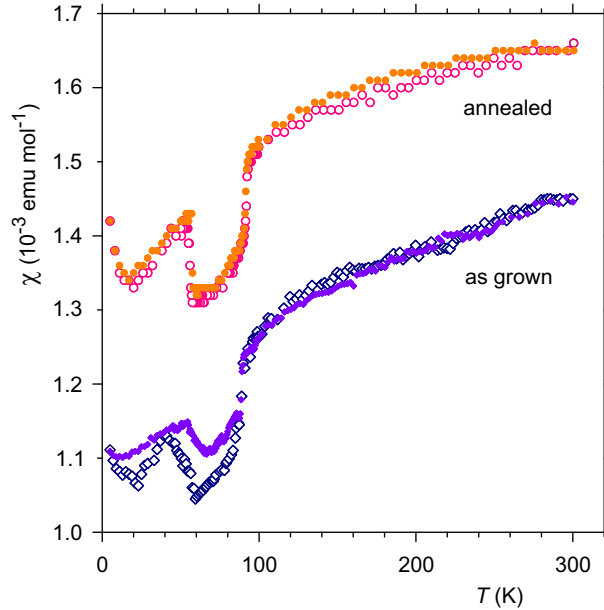


Figure 3.3: Temperature dependence (5–300 K) of the magnetic susceptibility (χ) of CuV_2S_4 . Measured on an annealed crystal upon cooling (red open circles) and heating (orange filled dots), and measured on an as-grown crystal upon cooling (blue open diamonds) and heating (violet filled diamonds).

This again implies that the crystal is of very good quality. The magnetic susceptibility (χ) was measured with a commercial SQUID magnetometer (MPMS 7, Quantum Design, USA) in the temperature range 5–300 K. Data were collected while cooling of the sample and again while heating of the sample, both for the as-grown and annealed state. Anomalies in $\chi(T)$ are found for both transitions in all four curves, while transitions appear sharper for the annealed state (Fig. 3.3). The values of the susceptibility and the temperature dependence behaviour are very similar to the previous reports [31, 75, 42].

3.3 Results

3.3.1 Structural phase transitions

Table 3.1: Temperature dependence of the lattice parameters a_F , c_F and γ_F , the volume V of the unit cell, and the component σ of the modulation wave vector $\mathbf{q} = (\sigma, \sigma, 0)$ for crystal A (annealed). See Section A1 in the Appendix for the F -centered setting of F -centered cubic and I -centered orthorhombic lattices.

T (K)	a_F (Å)	c_F (Å)	γ_F (deg)	σ	V (Å ³)
20	9.7592 (3)	9.7576 (4)	89.993 (2)	0.6733 (3)	929.32 (6)
40	9.7743 (4)	9.7726 (5)	90.012 (3)	0.6702 (4)	933.63 (8)
60	9.7728 (14)	9.7738 (13)	89.996 (4)	0.7370 (3)	933.48 (26)
80	9.7711 (4)	9.7664 (4)	89.987 (2)	0.7517 (2)	932.44 (8)
90	9.7762 (2)	9.7736 (4)	89.984 (2)	0.7595 (3)	933.48 (26)
250	9.8023 (5)		cubic lattice		941.87 (15)

Based on anomalies observed in the temperature dependencies of transport properties, magnetic properties and thermodynamic properties, Okada *et al.* [41] have identified two phase transitions for CuV_2S_4 , at temperatures of $T_{CDW} = 91.5$ K and $T_{c2} = 56$ K, respectively. These results are in agreement with the present data on the annealed state, for which we have observed anomalies in the temperature dependencies of the electrical resistivity (Fig. 3.1), specific heat (Fig. 3.2) and magnetic susceptibility (Fig. 3.3) at both transitions. The sharpest anomalies are found for the specific heat, resulting in transition temperatures $T_{CDW} = 90.37$ K and $T_{c2} = T_{lock-in} = 56.68$ K. The up-turn of the resistivity at T_{CDW} , the smaller value of the magnetic susceptibility in the CDW state and the λ -shaped anomaly in the specific heat are all in agreement with a CDW transition at T_{CDW} . Employing an annealed single crystal, we could correlate these transitions with the development of an incommensurate CDW below T_{CDW} and a lock-in transition at $T_{c2} = T_{lock-in}$ (Table 3.1). The present diffraction data do not give accurate values for the transition temperatures, but they are in agreement with values obtained from transport properties. The components of the modulation wave vectors at 20 and 40 K seem to deviate from $2/3$.

However, structure refinements (see below) show that a threefold supercell model gives a substantially better fit to the diffraction data than a model with an incommensurate modulation does, thus providing definite evidence for the commensurate

character of the modulation in the lock-in phase below T_{c2} . These features place the behavior of CuV_2S_4 on par with many other aperiodic crystals, where an incommensurate phase transition is followed by a lock-in transition at lower temperatures. Unique to CuV_2S_4 is the sluggish character of the lock-in transition. Upon initial cooling from 80 K to 20 K it took about four hours at 20 K for the transition towards the commensurate phase to complete. For the as-grown crystal P, anomalies in the temperature dependencies of the electrical resistivity (Fig. 3.1) and magnetic susceptibility (Fig. 3.3) are again found at both transitions. However, they appear broadened and less pronounced, especially for the lock-in transition. The temperature dependence of the specific heat has a sharp anomaly at $T_{CDW}^{asgr} = 87.08$ K (Fig. 3.2), which value is 3.3 K lower than for the annealed state.

The specific heat of the as-grown crystal P does not reveal any anomaly at the lock-in transition, suggesting that as-grown material does not proceed through the lock-in transition. These results are corroborated by diffraction experiments. The SXRD experiment on crystal B (not annealed) revealed the CDW transition to take place at 84.5 ± 0.5 K (Table 3.2).

Table 3.2: Temperature dependence of the lattice parameters a_F , c_F and γ_F , the volume V of the unit cell, and the component σ of the modulation wave vector $\mathbf{q} = (\sigma, \sigma, 0)$ for crystal B (as-grown). See Section A1 in the Appendix for the F -centered setting of F -centered cubic and I -centered orthorhombic lattices.

T (K)	a_F (Å)	c_F (Å)	γ_F (deg)	σ	V (Å ³)
80	9.7749(3)	9.7588(5)	89.945(3)	0.7625(2)	932.45(8)
81	9.7748(3)	9.7596(4)	89.961(3)	0.7622(2)	932.50(7)
82	9.7742(3)	9.7596(5)	89.958(3)	0.7625(2)	932.38(8)
83	9.7741(3)	9.7591(5)	89.960(2)	0.7629(2)	932.29(7)
84	9.7715(4)	9.7587(5)	89.959(3)	0.7659(2)	931.79(10)
85	9.7667(4)	9.7654(5)	89.994(3)	-	931.50(7)
87	9.7666(4)	9.7669(5)	90.002(4)	-	931.64(8)
88	9.7680(3)	9.7659(5)	89.994(3)	-	931.81(7)
89	9.7670(2)	9.7653(4)	89.981(3)	-	931.54(5)
91	9.7653(3)	9.7635(5)	89.987(4)	-	931.06(7)
92	9.7650(3)	9.7631(4)	90.003(4)	-	930.96(6)
93	9.7643(3)	9.7636(5)	89.988(3)	-	930.87(8)
94	9.7656(4)	9.7630(4)	89.996(3)	-	931.08(8)
95	9.7655(3)	9.7643(5)	90.009(4)	-	931.19(7)

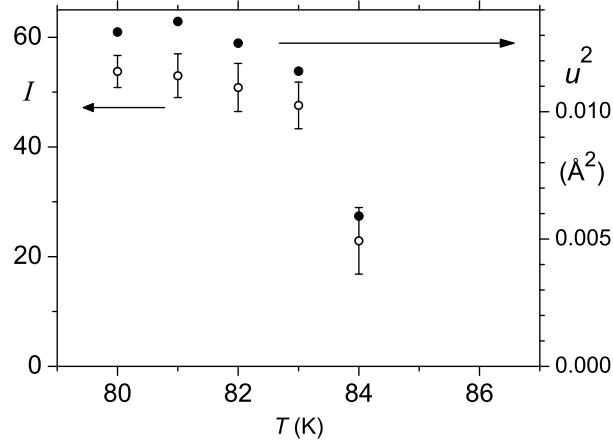


Figure 3.4: Temperature dependence near the CDW transition of the Intensity (I) of the satellite Bragg reflection $(10, 12, 0, -1)$ (open circles; left scale), and square of the magnitude (u) of the modulation amplitude of atom V1 (filled circles; right scale), as determined for crystal B. Notice the perfect scaling between these two quantities. The satellite intensity and modulation are zero for 85 K and higher temperatures.

The intensities of the satellite reflections as well as the magnitudes of the major modulation amplitudes of the refined structure models are in agreement with a second order phase transition, although there are too few data points close to T_{CDW} for the determination of a critical exponent (Fig. 3.4). The transition of as-grown crystals is at a substantially lower temperature than the transition of annealed crystal A, where we have found by SXRD that the CDW phase exists at 90 K. It appears that as-grown material goes into an undercooled state of the periodic phase, despite that the CDW transition is of second order. The transition is inhibited by the 'disorder' proposed by Horny *et al.* [75]. The lock-in transition at about 50 K has been observed upon initial cooling of as-grown crystal C. At $T = 4.2$ K, satellite reflections appeared that could be described by the commensurate modulation wave vector with $\sigma = \frac{2}{3}$, while the original set of incommensurate satellite reflections remained (Table 3.3).

Table 3.3: Temperature dependence of the lattice parameters a_F , c_F and γ_F , the volume V of the unit cell, and the component σ of the modulation wave vector $\mathbf{q} = (\sigma, \sigma, 0)$ for crystals C, D and E (as-grown). See Section A1 in the Appendix for the F -centered setting of F -centered cubic and I -centered orthorhombic lattices.

T (K)	a_F (Å)	c_F (Å)	γ_F (deg)	σ	V (Å ³)
Crystal C					
4.2 ^a	9.7746(3)	9.7752(4)	89.999(3)	0.6593(8)	933.96(7)
				0.7598(7)	
4.4 ^b	9.7672(4)	9.7660(6)	89.989(4)	0.7290(5)	931.54(10)
25 ^c	9.7754(4)	9.7705(4)	89.978(4)	0.7496(6)	933.12(6)
35 ^{b,d}	9.7759(4)	9.7991(4)	89.989(4)	0.7532(6)	934.57(9)
35 ^{c,d}	9.7739(4)	9.7785(5)	89.979(3)	0.7561(5)	933.69(9)
39 ^{c,e}	9.7745(6)	9.7702(8)	89.959(4)	0.7585(4)	933.45(14)
Crystal D					
5 ^a	9.7697(4)	9.7627(4)	89.987(2)	0.7289(3)	931.82(6)
5 ^{b,d}	9.7644(3)	9.7612(4)	89.988(3)	0.7278(4)	930.66(7)
8 ^{c,d}	9.7642(4)	9.7614(3)	89.985(4)	0.7253(3)	930.91(9)
11 ^{c,d}	9.7674(2)	9.7656(4)	89.998(4)	0.7234(2)	931.66(2)
16 ^b	9.7718(4)	9.7702(3)	89.981(3)	0.7476(3)	932.93(8)
20 ^{a,e}	9.7710(3)	9.7710(4)	89.986(4)	0.7586(3)	933.13(9)
30 ^{c,d}	9.7779(4)	9.7792(5)	89.984(4)	0.7489(3)	934.96(9)
35 ^a	9.7796(4)	9.7641(5)	89.949(2)	0.7511(1)	933.85(7)
Crystal E					
45 ^d	9.7701(3)	9.7704(3)	90.003(3)	0.7508 (2)	932.60(6)

^aFirst cooling; ^bSecond cooling; ^cThird cooling; ^dStructure refinements not possible, because the formation of ice prevented the determination of intensities of Bragg reflections; ^eToo few satellite reflections for refinement of the modulated structure.

This observation showed that the lock-in transition has proceeded in only part of crystal C. Heating toward 35 K restored the incommensurate state, while subsequent cooling, as well as cooling of crystals D and E, never produced the commensurate state. Instead, we observe a decrease in the length of the incommensurate modulation wave vector towards lower temperatures (Fig. 3.5).

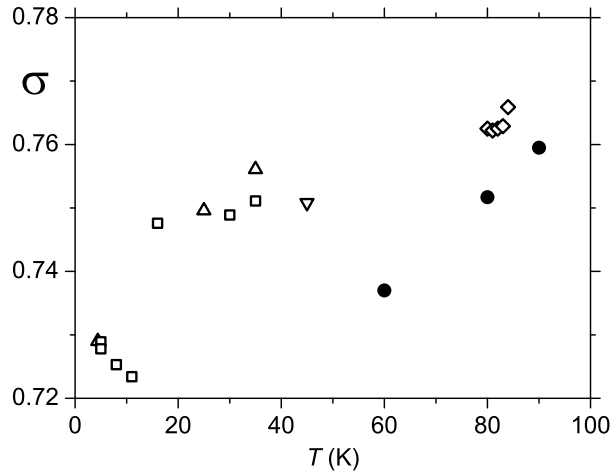


Figure 3.5: Temperature dependence of the incommensurate component σ of the modulation wave vector. Filled circles for crystal A (annealed). Open symbols for as-grown crystals, B (diamonds), C (up triangles), D (squares) and E (down triangle).

Together, these results can be explained by modifications to the CDW state of as-grown crystals, which take place around the temperature of the lock-in transition, but that fail to develop long-range order. That is, the lock-in transition as such does not take place in as-grown crystals, despite anomalies observed in the temperature dependencies of the electrical resistivity, $\rho(T)$, and the magnetic susceptibility, $\chi(T)$. For the annealed crystal, the incommensurate component σ goes through the rational value $\frac{3}{4}$ upon cooling through about 80 K (Table 3.1). For the as-grown crystals, the behaviour is not exactly reproducible, but the component σ again passes $\frac{3}{4}$, with a tendency towards a value of 0.725 at very low temperatures (Table 3.3). These observations are in agreement with Kawaguchi *et al.* [32], who reported to have observed the same modulated crystal structures at 70 and 20 K. Furthermore, they might explain the results of Fleming *et al.* [31], who found a presumed lock-in transition at 75 K towards the commensurate value $\frac{3}{4}$.

Here it is noticed that modulation wave vector $\mathbf{q}_c = (\frac{2}{3}, \frac{2}{3}, 0)$ describes a threefold superstructure, because $3\mathbf{q}_c = (2, 2, 0)$ is a reciprocal lattice vector of the basic lattice, while $\mathbf{q} = (\frac{3}{4}, \frac{3}{4}, 0)$ describes an eightfold superstructure, because $4\mathbf{q} = (3, 3, 0)$ is a forbidden reciprocal point of the F -centered lattice, and only $8\mathbf{q}$ is a reciprocal lattice vector. Apparently, an eightfold supercell relation is of too high order for inducing a lock-in transition towards the value $\frac{3}{4}$.

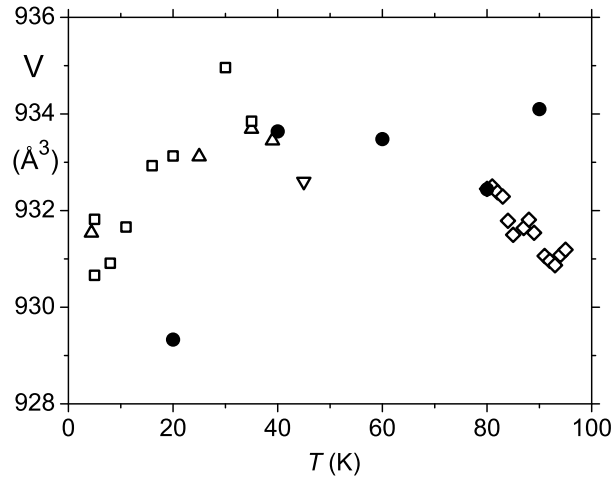


Figure 3.6: Temperature dependence of the volume of the F -centered unit cell. Filled circles for crystal A (annealed). Open symbols for as-grown crystals, B (diamonds), C (up triangles), D (squares) and E (down triangle).

3.3.2 Diffraction symmetry and lattice distortion

One of the open questions is the symmetry of the CDW phase, where the possibility must be considered, that the development of the modulation is accompanied by a lowering of the point symmetry of crystal structure. The cubic space group $Fd\bar{3}m$ (No. 227 [78]) has the maximum tetragonal subgroup $I4_1/amd$ (No. 141), the latter which has the orthorhombic subgroups $Fddd$ (No. 70) and $Imma$ (No. 74). Kawaguchi *et al.* [32] established non-centrosymmetric $Imm2$ symmetry for the incommensurate CDW phase, with superspace group $Imm2(\sigma 0 0)000$ (No. 44.1.12.4; standard setting $I2mm(0 0 \sigma)000$ [79]).

The present SXRD data allow for further tests of the lattice symmetry. In particular, the cubic lattice is approximately preserved in the CDW phase, because there is no obvious splitting of main reflections. Up to twelve satellite reflections around each main reflection can be described by six symmetry equivalent modulation wave vectors (Tables A3 and A4 in the Appendix). A tetragonal CDW structure would involve four of the twelve satellite reflections that are described by two modulation wave vectors. (Fig. 3.7).

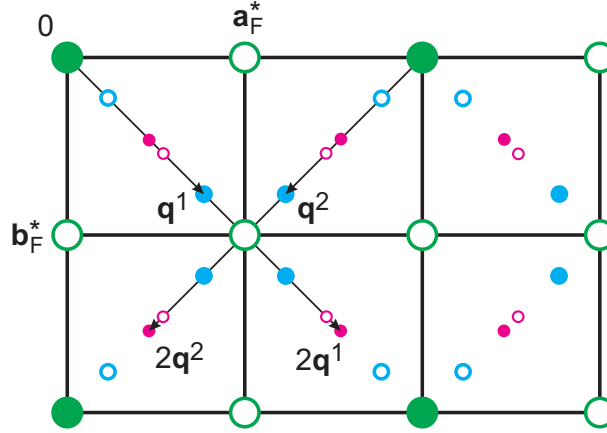


Figure 3.7: Schematic representation of the $(\mathbf{a}_F^*, \mathbf{b}_F^*)$ plane of the diffraction pattern of incommensurate CuV_2S_4 below T_{CDW} . Open circles indicate the positions of reflections that are extinct due to the F centering. Positions of second-order satellites are indicated, but these reflections have not been observed.

The other satellite reflections then are due to threefold twinning. Three domains exist, with the tetragonal fourfold axis along one of \mathbf{a}_F , \mathbf{b}_F and \mathbf{c}_F of the F -centered unit cell, respectively. The point symmetry of the main Bragg reflections of such a twinned crystal is orthorhombic mmm , whereby the mirror planes refer to mirror planes perpendicular to the coordinate axes of the F -centered unit cell. However, satellites from different domains are completely separated, so that the full $4/mmm$ symmetry would apply to them. Averaging the diffraction data according to these symmetries resulted in $R_{int} = 0.487$ for the satellite reflections, which provides definite proof that the CDW phase does not have tetragonal symmetry nor orthorhombic $Fddd$ symmetry (Table A5 in the Appendix). Orthorhombic $Imm2$ symmetry refers to mirror planes perpendicular to the face diagonals of the F -centered unit cell and a twofold axis along the coordinate axis \mathbf{c}_F . Sixfold twinning combined with inversion twinning results in diffraction symmetry $\bar{1}$ of the overlapping main Bragg reflections.

Each of the six pairs of satellite reflections at $\pm \mathbf{q}^j$ ($j = 1, \dots, 6$) has contributions from a pair of inversion domains (Tables A3 and A4 in the Appendix). Since Friedel's law is valid in good approximation, satellite reflections should have mmm symmetry referring to the I -centered lattice. Averaging according to this symmetry resulted in $R_{int} = 0.104$ for the satellite reflections, while $R_\sigma = 0.117$ (R_σ is the average of the standard uncertainty divided by the intensity). These values show that orthorhombic symmetry according to $Immm$ is fulfilled within the accuracy of

the data (Table A5 in the Appendix).

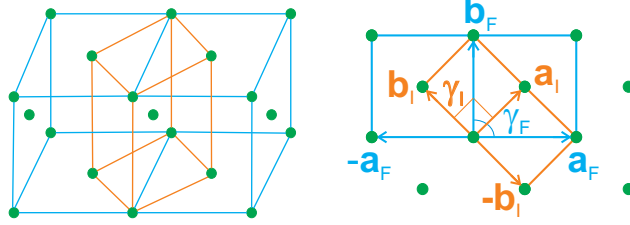


Figure 3.8: Relation between the F -centered (blue) and I -centered (orange) unit cells for the pseudo-cubic F -centered lattice.

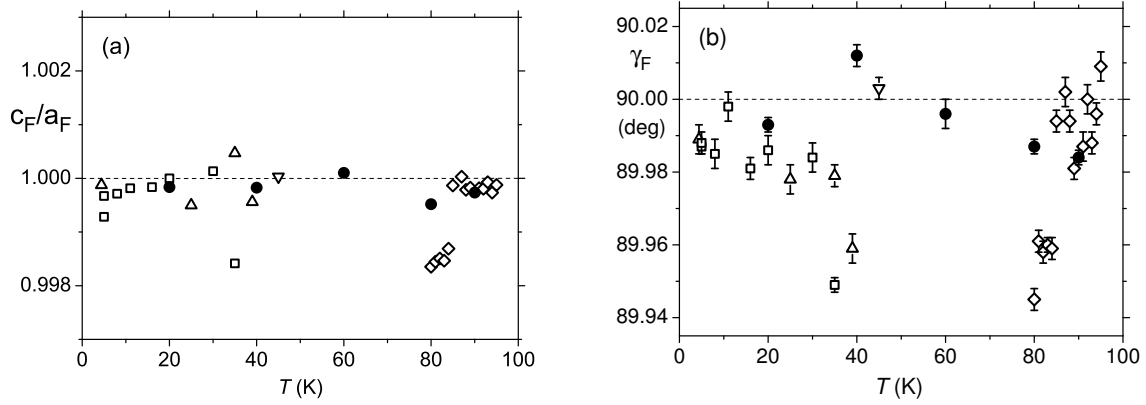


Figure 3.9: Temperature dependence of (a) Ratio c_F/a_F of the lattice parameters a_F and c_F , and (b) the lattice parameter γ_F . Both refer to the F -centered setting of the I -centered tetragonal or orthorhombic lattices. Filled circles for crystal A (annealed). Open symbols for as-grown crystals, B (diamonds), C (up triangles), D (squares) and E (down triangle).

The F -centered unit cell (lattice parameters $a_F = b_F \neq c_F$ and $\alpha_F = \beta_F = \gamma_F = 90$ deg) is a valid alternate setting for the I -centered tetragonal lattice with $a_I = b_I = a_F/\sqrt{2}$ and $c_I = c_F$ (Fig. 3.8) [80]. It is noticed here that a F -centered unit cell can also be chosen for the I -centered orthorhombic lattice. The orthorhombic distortion, $a_I \neq b_I$, of the I -centered unit cell is reflected in the F -centered unit cell by $\gamma_F \neq 90$ deg, while $a_F = b_F = \sqrt{a_I^2 + b_I^2}$, $c_F = c_I$ and $\alpha_F = \beta_F$ remain 90 deg (see Section A1 in the Appendix). The ratio $\frac{c_F}{a_F}$ thus is a good measure for the tetragonal lattice distortion, while γ_F is a good measure for the orthorhombic distortion (Fig. 3.9). The ratio $\frac{c_F}{a_F}$ varies irregularly over the different samples B–E. For crystal B, $\frac{c_F}{a_F} \approx 1$ for the cubic phase, while it is ~ 0.998

in the CDW phase. The latter values are comparable to those of Kawaguchi *et al.* [32] and Okada *et al.* [41] at 70 K. These values suggest that previous work has studied as-grown crystalline material. Okada *et al.* [41] have reported an increasing distortion on decreasing temperature.

We find different behavior for the as-grown crystals C–E, which have lattice distortions smaller than that of crystal B [Fig. 3.9(a)]. These disparate behaviors are again in agreement with samples in non-equilibrium states, where lattice defects may depend on the precise thermal history of each sample. Further support for this interpretation comes from crystal A (annealed), for which we have obtained values within the range $0.9995 < \frac{c_F}{a_F} < 1.0001$. Apparently, the tetragonal lattice distortion (which is part of the orthorhombic distortion) is much smaller for equilibrium crystals than for the disordered crystals. The magnitude of this small distortion cannot be reliably extracted from our experiments. A similar picture is obtained for the second part of the orthorhombic distortion, which is described by γ_F .

The largest distortion is obtained for crystal B [Fig. 3.9(b)], with the value of $\gamma_F \approx 89.95$ deg equal to the values obtained by Kawaguchi *et al.* [32]. Okada *et al.* [41] report $a_F = b_F$ and c_F and conclude towards a tetragonal lattice for 8–90 K. However, they do not report the value of γ_F , and might have mistakenly considered any deviations from 90 deg as inaccuracies of their analysis instead of being the orthorhombic distortion towards the *I*-centered lattice. The present data on as-grown crystals C–E suggest a decrease of the orthorhombic distortion upon cooling, whereas the annealed crystal A has nearly zero orthorhombic distortion, which apparently is the signature of equilibrated material.

3.3.3 Crystal structures of the CDW and lock-in states

The cubic spinel structure has been confirmed for annealed crystal A at 250 K and for as-grown crystal B at 95 K. Structure refinements with the software Jana2006 [56] gave an excellent fit to the diffraction data (Details in the Appendix). A good fit to the diffraction data of the incommensurate CDW phase could only be achieved for superspace symmetry $Imm2(\sigma 0 0)$, in agreement with the observed diffraction symmetry (Section 3.3.2). Employing single-harmonic modulation functions (Eq. A8 in the Appendix), a good fit has been obtained to both main reflections and satellite reflections of crystal A at temperatures of 60, 80 and 90 K (Tables A2 and A6 in the Appendix), of crystal B at 80–85 K, of crystal C at 4.4 and 25 K and of

crystal D at 5, 16 and 35 K (Tables A12–A15 in the Appendix). Structure models are similar between different crystals A–D, while a tendency is observed towards larger modulation amplitudes at lower temperatures. This result implies that annealed and as-grown material reach the same CDW state at low temperatures.

Accordingly, the present analysis will be concentrated on the results for crystal A (annealed) at 80 K. The present modulation functions bear a great similarity to the first-order harmonics reported by Kawaguchi *et al.* [32], especially when considering the large standard uncertainties of ~ 0.015 Å for the latter Rietveld refinements against XRPD data [32].

The present refinements against SXRD data have resulted in much lower standard uncertainties (Table A10 in the Appendix). Kawaguchi *et al.* [32] also report modulation amplitudes of second harmonic, which are of larger magnitude than first-order harmonics. The largest amplitude is $B_{2,x} = B_{2,y} = 0.13(1)$ Å for atom V1. Amplitudes of this large magnitude should have led to strong second-order satellite reflections, which we do not observe. The second harmonic reported in [32] thus should be considered as an artifact of the Rietveld refinement. Second-order harmonics have been successfully introduced into the present refinements against SXRD data, despite the missing second-order satellites. However, resulting amplitudes are insignificant in view of their large standard uncertainties. Therefore, we propose modulation functions consisting of solely first-order harmonics as the final model.

Another major discrepancy between Kawaguchi’s *et al.* [32] model and the present model is that we find a significant orthorhombic distortion of the basic structure, especially for atom V2, while it is zero for atom V1. This structural feature has important consequences for understanding the CDW phase (see Section 3.3.4 below). The structure of the lock-in phase has been determined for crystal A at 20 and 40 K. The lock-in phase is described by the same superspace symmetry $Imm2(\sigma 00)$ as applies to the incommensurate CDW. Structure refinements of the modulated structure against SXRD data resulted in a fit that is much better for the commensurate model than for an incommensurate model (Tables A6 and A7 in the Appendix).

3.3.4 Vanadium clusters in the CDW state

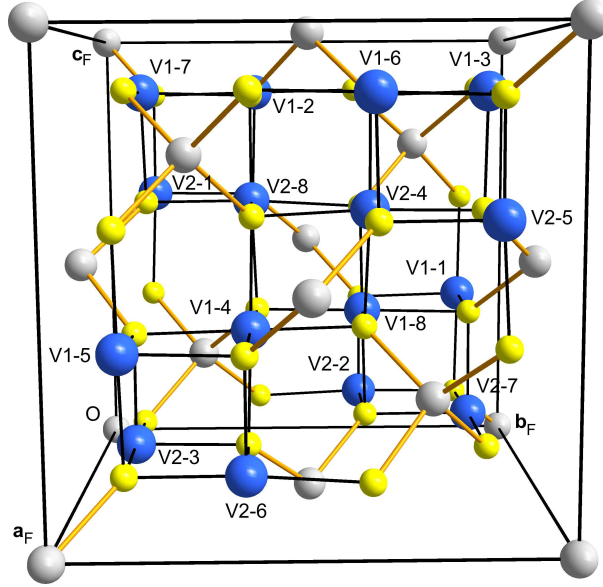


Figure 3.10: Perspective view of the crystal structure of CuV_2S_4 . The basis vectors of the F -centered unit cell are indicated as \mathbf{a}_F , \mathbf{b}_F and $\mathbf{c}_F = \mathbf{c}_I$. Labels V1-1, V2-1 and other labels indicate atoms equivalent by symmetry to V1 and V2, respectively. Blue is vanadium, gray is copper and yellow is sulfur.

Band-structure calculations have shown that the Fermi level in CuV_2S_4 is mainly composed of $3d$ states of vanadium [81, 82]. Therefore, it is a reasonable assumption that the origin of the CDW will be related to the modulation of the vanadium atoms. This idea is reinforced by the fact that the largest modulation amplitudes are the displacements of vanadium (Table A10). Furthermore, all short distances between metal atoms are between vanadium atoms, while copper atoms have isolated positions farther away from any other metal atom.

The orthorhombic crystal structure of CuV_2S_4 contains chains of V2 atoms along $\mathbf{a}_F + \mathbf{b}_F$ (the orthorhombic axis \mathbf{a}_I) and chains of V1 atoms along $-\mathbf{a}_F + \mathbf{b}_F$ (the orthorhombic axis \mathbf{b}_I ; see Fig. 3.10 and Section A1 in the Appendix). The modulation wave vector is parallel \mathbf{a}_I , *i.e.* along the V2 chains. The model by Kawaguchi *et al.* [32] involves dimerization of the V1 chains, while the incommensurate modulation of the interatomic distances along the V2 chains does not display clear features.

It was thus proposed that the CDW is a commensurate CDW on the V1 chains, while inter-chain interactions would be responsible for the incommensurability of

the modulation, in analogy to the situation for SmNiC_2 [83]. The present structure model again involves dimerization of the V1 chains, albeit with double the period than in [32], since the present model does not involve second-order harmonics (Fig. 3.11).

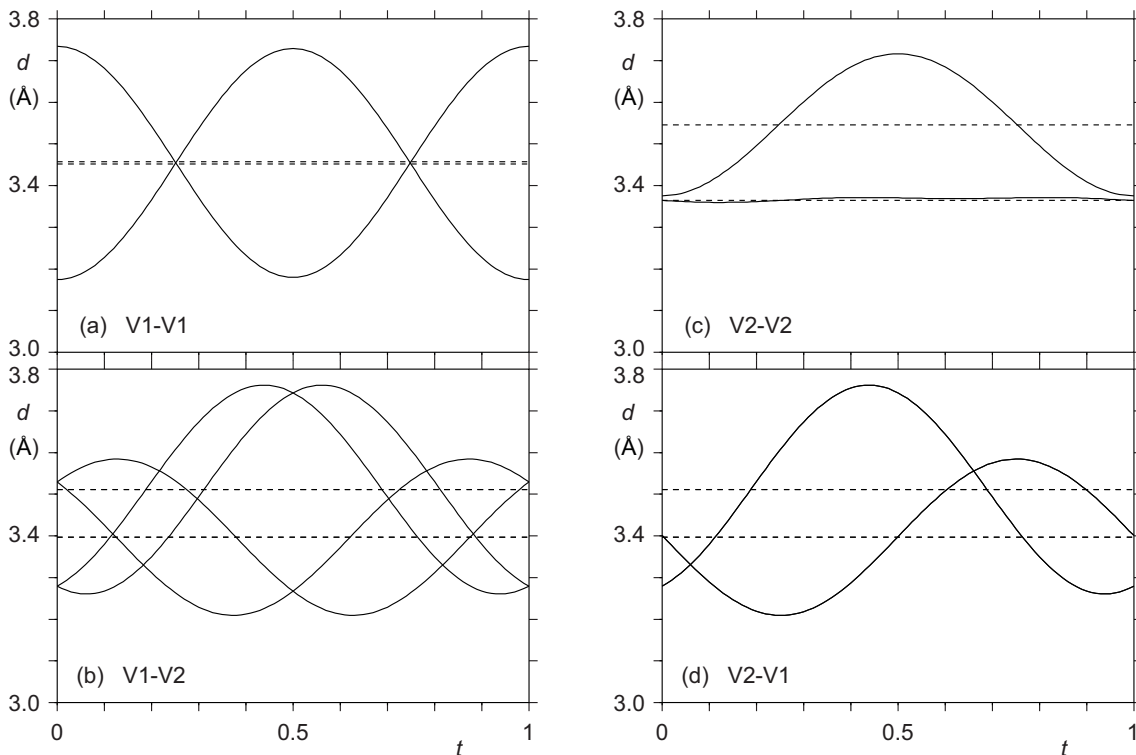


Figure 3.11: t -Plot of interatomic distances between one V atom and its six surrounding V atoms for the incommensurate CDW state of crystal A at 80 K. Horizontal dashed lines indicate distances for the basic structure. (a),(b) central atom is V1 at $(1/8, -1/8, 3/8)$, which is part of V-atom chains along $-\mathbf{a}_F + \mathbf{b}_F$, $\mathbf{b}_F + \mathbf{c}_F$ and $-\mathbf{a}_F + \mathbf{c}_F$. (c),(d) central atom is V2 at $(1/8, 1/8, 5/8)$, which is part of V-atom chains along $\mathbf{a}_F + \mathbf{b}_F$, $\mathbf{b}_F + \mathbf{c}_F$ and $\mathbf{a}_F + \mathbf{c}_F$.

We have presently found a major distortion of the average positions of the V2 atoms, a feature not present in the model in [32], and resulting in a dimerization of the basic structure of the V2 chains by 0.18 Å. Furthermore, the phase shift of the modulation between consecutive atoms along the V2 chain of $\sigma/2 \approx 0.375$ results in a V2 chain containing dimers and trimers, and there is no compelling evidence favoring a CDW on the V1 chains. An important difference between the cubic spinel structure and orthorhombic SmNiC_2 is that the latter contains chains of Ni

atoms along a single orthorhombic axis, while the spinel structure contains chains of V atoms along the six equivalent directions $\pm\mathbf{a}_F + \mathbf{b}_F$, $\pm\mathbf{a}_F + \mathbf{c}_F$ and $\pm\mathbf{b}_F + \mathbf{c}_F$. Referring to the F -centered setting of the orthorhombic $Imm2$ structure, each V1 atom is at the intersection of the V1 chain along $-\mathbf{a}_F + \mathbf{b}_F$, and two chains composed of alternating V1 and V2 atoms. For one V1 atom, these mixed chains are along $\mathbf{b}_F + \mathbf{c}_F$ and $-\mathbf{a}_F + \mathbf{c}_F$. The orthorhombic symmetry then implies that a second, symmetry equivalent V1 atom is at the intersection of the V1 chain and two V1–V2 mixed chains, along $-\mathbf{b}_F + \mathbf{c}_F$ and $\mathbf{a}_F + \mathbf{c}_F$. Similarly, each V2 atom is at the intersection of the V2 chain along $\mathbf{a}_F + \mathbf{b}_F$, and two V2–V1 mixed chains, along $\mathbf{b}_F + \mathbf{c}_F$ and $\mathbf{a}_F + \mathbf{c}_F$. A second, symmetry equivalent V2 atom is at the intersection of the V2 chain and two V2–V1 mixed chains, along $-\mathbf{b}_F + \mathbf{c}_F$ and $-\mathbf{a}_F + \mathbf{c}_F$. t -Plots of V–V interatomic distances then indicate that large modulations and short distances also involve V1–V2 contacts (Fig. 3.11). Depending on t , extended clusters of vanadium atoms are formed, which are eventually interrupted by long distances due to the incommensurability of the modulation. Accordingly, we propose that the formation of 3D clusters is at the basis of the CDW in CuV_2S_4 .

Modulation amplitudes for the lock-in state are similar to but distinctly different than those for the incommensurate CDW phase. The distortion of the basic structure is much smaller for the lock-in state than for the incommensurate CDW. On the other hand, the commensurability determines that values of the modulation functions are physically relevant for only three values of their arguments. In the present structure models those are the values of t equal to $\frac{1}{6}$, $\frac{1}{2}$ and $\frac{5}{6}$ (vertical dashed lines in Fig. 3.12).

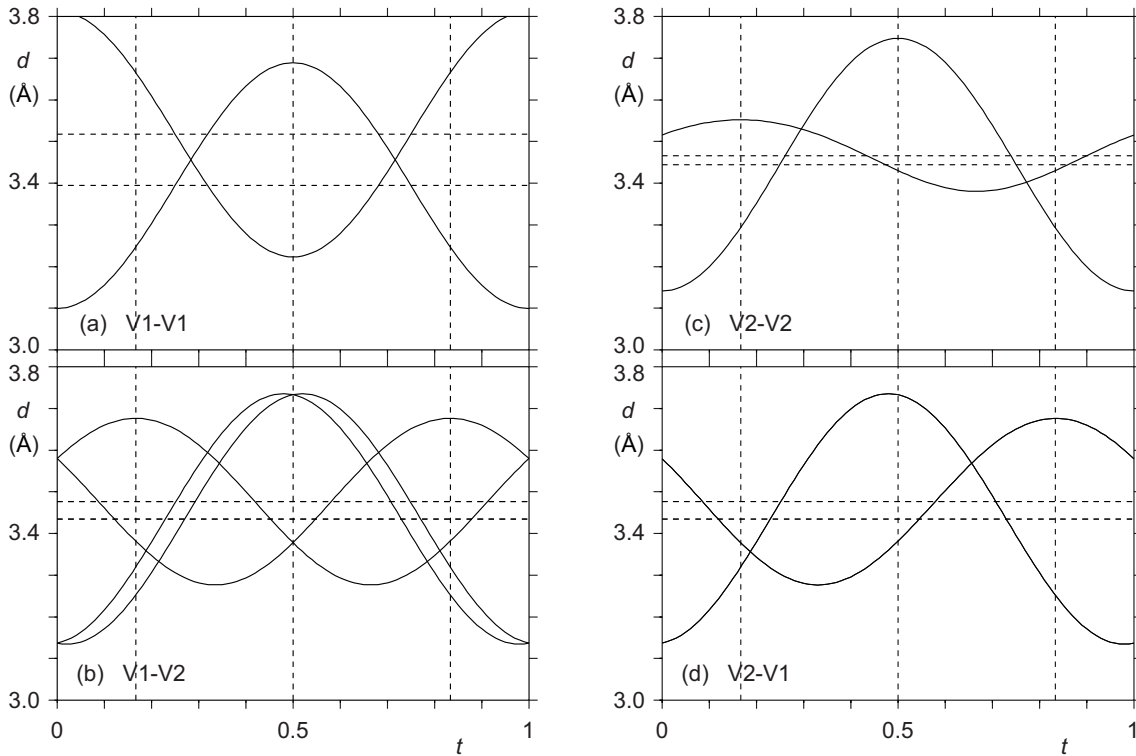


Figure 3.12: t -Plot of interatomic distances between one V atom and its six surrounding V atoms for the commensurately modulated structure of the lock-in state of crystal A at 40 K. The threefold superstructure involves distances and atomic positions at t -values of $\frac{1}{6}$, $\frac{1}{2}$ and $\frac{5}{6}$, indicated by vertical dashed lines. Horizontal dashed lines indicate distances for the basic structure. (a),(b) central atom is V1 at $(\frac{1}{8}, -\frac{1}{8}, \frac{3}{8})$. (c),(d) central atom is V2 at $(\frac{1}{8}, \frac{1}{8}, \frac{5}{8})$. Distances are shown between the same atoms as have been used for Fig. 3.11.

Similar to the incommensurate structure, the lock-in state is characterized by extended clusters defined by short interatomic V–V distances.

3.4 Conclusions

CuV_2S_4 possesses the cubic spinel structure at room temperature. We have established that the formation of an incommensurate CDW state at $T_{CDW} \approx 91$ K is followed by a lock-in transition towards a threefold superstructure at $T_{lock-in} \approx 50$ K. The phase transitions critically depend on the thermal history of the sample. As-grown samples are supposed to suffer from disorder and other lattice defects

[75, 42]. These defects do not show up in the diffraction of the spinel structure, but they are responsible for a suppression by a few K of T_{CDW} (Section 3.3.1). Despite the presence of anomalies around $T_{lock-in}$ in the temperature dependencies of the electrical resistivity and magnetic susceptibility of an as-grown crystal, corresponding superlattice reflections have not been observed in SXRD. It is worthwhile to recall that the temperature dependence of the heat capacity does not exhibit an anomaly for the lock-in transition in the as-grown crystal, as well (Fig. 3.2). This implies that long-range order of the lock-in phase does not develop in as-grown material, but requires annealed crystals. Instead, the length of the incommensurate CDW wave vector continues to decrease towards the lowest temperatures in as-grown crystals (Fig. 3.5). Both as-grown and annealed material transform into the same, incommensurate CDW state, as it is evidenced by the structure models at low temperatures for both types of crystal.

The orthorhombic superspace symmetry of the CDW state is the same as proposed by Kawaguchi *et al.* [32]. However, structural parameters of the present models are much more accurate than those of the Rietveld refinement [32], and the present structure models are significantly different than that in [32]. Largest modulation amplitudes and shortest interatomic distances between metal atoms are found for vanadium atoms. They suggest that formation of the CDW is governed by the vanadium atoms, in agreement with band-structure calculations for the spinel phase, that indicate $3d$ vanadium states at the Fermi level [81, 82]. The incommensurate CDW state can be characterized by the formation of extended vanadium clusters, that are interrupted by long V–V distances due to the incommensurability.

In the lock-in phase, a connected path of short V–V distances percolates throughout the crystal in all directions. The lowering towards orthorhombic symmetry appears to be responsible for the precise pattern of modulations and short and long V–V distances. The actual orthorhombic lattice distortion—visible for some as-grown material—is nearly zero within standard uncertainties for the annealed crystal (Fig. 3.9).

3.5 Acknowledgments

Single crystals of CuV_2S_4 have been synthesized by Kerstin Küsspert at the Laboratory of Crystallography in Bayreuth. We thank Mariia Anurova for assistance with initial diffraction experiments. We thank Dmitry Chernyshov (SNBL) for assistance with the synchrotron experiments at beam line BM01 of the SNBL at the ESRF in Grenoble, France. This research has been funded by the Deutsche Forschungsgemeinschaft (DFG, German Research Foundation)—265092781, and the Alexander-von-Humboldt Foundation within their research-group linkage program.

Chapter 4

Unusual charge density wave transition and absence of magnetic ordering in $\text{Er}_2\text{Ir}_3\text{Si}_5$

1

The first-order charge-density-wave (CDW) phase transition of $\text{Er}_2\text{Ir}_3\text{Si}_5$ is characterized by crystal structure analysis, and electrical resistivity, magnetic susceptibility and specific heat measurements. The incommensurate CDW is accompanied by a strong lattice distortion, from which it is shown that the CDW resides on zigzag chains of iridium atoms.

The CDW transition affects the magnitude of the local magnetic moments on Er^{3+} , implying strong coupling between CDW and magnetism. This could account for the observation, that magnetic order is suppressed down to at least 0.1 K in the high-quality single crystal presently studied. Any disorder in the crystallinity, like in ceramic material, broadens and suppresses the CDW transition, while magnetic order appears at 2.1 K.

The study of competing phase transitions is one of the frontier areas of condensed matter physics [65]. A large number of investigations have been made to understand the competition between and coexistence of local-moment magnetism, superconductivity, giant magnetoresistance and charge-density-wave (CDW) ordering in both inorganic and organic compounds. Many of these materials possess one-dimensional (1D) or two-dimensional (2D) crystal structures [84, 85, 86, 87]. The low dimensionality of these compounds is central to the exotic ground states exhibited by these

¹This chapter has been published as: Sitaram Ramakrishnan, Andreas Schönleber, Toms Rekis, Natalija van Well, Leila Noohinejad, Sander van Smaalen, Martin Tolkiehn, Carsten Paulmann Biplob Bag, Arumugam Thamizhavel, Dilip Pal and Srinivasan Ramakrishnan. Unusual charge density wave transition and absence of magnetic ordering in $\text{Er}_2\text{Ir}_3\text{Si}_5$. *Phys. Rev. B* **101**, 060101(R) (2020)

compounds.

In contrast to these low-dimensional compounds, CDWs seem to occur in several compounds with complex three-dimensional (3D) structures. Crystal structures of these compounds do not show obvious 1D or 2D features, while their electrical conductivity is only weakly anisotropic. These materials include the element uranium [88], the rare earth (R) containing compounds $R\text{Te}_3$ [29], $R\text{Te}_2$ [28], $R\text{NiC}_2$ [89, 63, 90, 65], $R_5\text{Ir}_4\text{Si}_{10}$ [25] and $R_2\text{Ir}_3\text{Si}_5$ [26, 91, 44] as well as CuV_2S_4 [31].

Usually one observes coexistence of the CDW with magnetism or superconductivity in the above mentioned systems. However, in recently discovered $R\text{NiC}_2$ [92, 90], the CDW competes with magnetism and in the extreme case ferromagnetic order destroys the CDW in SmNiC_2 [93, 89, 83], suggesting strong coupling of the rare-earth spins to the CDW in this series. Even in the series $R\text{NiC}_2$, where R is a magnetic rare earth element, the normal state magnetic susceptibility is unaffected by the CDW transition.

Nonmagnetic $\text{Lu}_2\text{Ir}_3\text{Si}_5$ becomes superconducting below $T_{sc} = 3.5$ K, and it undergoes a first-order CDW transition between 150 and 200 K, which is governed by strong electron–phonon coupling [26].

Kuo *et al.* [91] established these transitions in their polycrystalline sample at temperatures of 5.5 K and 110–160 K, respectively. A lowering of the transition temperature of the presumed CDW transition with a concomitant increase of the superconducting transition is strong evidence for involvement of the Fermi surface in the CDW transition and thus for the CDW character of this transition [91]. Furthermore, sample-dependent transition temperatures indicate a sensitive dependence of the transition on intrinsic disorder or lattice defects, which is again in agreement with the CDW character of this transition. The second characteristic of the CDW state is the presence of a periodic lattice distortion (PLD). Lee *et al.* [44] have discovered incommensurate satellite reflections in the electron diffraction of $\text{Lu}_2\text{Ir}_3\text{Si}_5$ measured at temperatures below T_{CDW} , which indicate an incommensurate PLD/CDW with modulation wave vector $\mathbf{q} = \delta (\bar{1} 2 1)$ and $\delta = 0.23\text{--}0.25$.

A signature of possible CDW transitions was not found for polycrystalline samples of the other compounds $R_2\text{Ir}_3\text{Si}_5$ [46], except for a broad anomaly in the electrical resistivity of $\text{Er}_2\text{Ir}_3\text{Si}_5$ [33].

Unlike the polycrystalline material, a single crystal of $\text{Er}_2\text{Ir}_3\text{Si}_5$ showed very sharp anomalies with a clear hysteresis in the temperature dependencies of the electrical resistivity and magnetic susceptibility [34].

Here we show that the incommensurate CDW is accompanied by a structural transition, resulting in a lowering of the crystal symmetry from orthorhombic to triclinic. Evidence for the involvement of the Ir atoms in CDW formation is obtained from a detailed description of the incommensurate crystal structure of the CDW state.

We show that magnetic ordering is suppressed in single crystals, while a previous

report has found $T_N = 2.2$ K for polycrystalline $\text{Er}_2\text{Ir}_3\text{Si}_5$, where the CDW transition is suppressed [46]. Cooling through the CDW transitions leads to an increased magnetic susceptibility, while $\text{Er}_2\text{Ir}_3\text{Si}_5$ remains paramagnetic, making it a unique CDW system where there is strong coupling of the Er spins to CDW ordering.

Single crystals of $\text{Er}_2\text{Ir}_3\text{Si}_5$ were grown in a tetra-arc furnace from a stoichiometric mixture of the elements, employing a modified Czochralski technique. The purity of the reactants was 99.99% for Er and Ir, and 99.999% for silicon.

The 2–3–5 stoichiometry was established by energy-dispersive X-ray analysis (EDAX). X-ray diffraction confirmed the expected lattice parameters. A small part of the as-grown single crystal was crushed, and a piece of $0.05 \times 0.08 \times 0.06$ mm³ was selected for single-crystal X-ray diffraction. Diffraction experiments were performed at Beamline P24 of PETRA-III extension at DESY in Hamburg, employing radiation of a wave length of 0.49994 Å. The temperature of the specimen was controlled by a CRYOCOOL open-flow helium gas cryostat. Complete data sets of intensities of Bragg reflections were measured at temperatures of 20, 75 and 130 K (CDW phase) and 150 and 200 K (normal phase). The crystallographic orientation of the as-grown single crystal was determined by the back-scattering Laue diffraction method, employing the Orient Express software [94]. The observed sharp Bragg reflections provided independent evidence for the single crystalline nature of the sample. Small bars of required orientations were cut off the oriented crystal by a wire saw and used for transport and magnetization measurements.

The electrical resistivity was measured by the four-point method along the \mathbf{c} direction of an oriented single crystal. Electrical contacts were applied by gluing gold wires (40 μm diameter) with silver paste to the crystal surface. The electrical resistivity was measured with a custom built setup based on a LR-700 (Linear Research, USA) AC bridge, operating with a current of 5 mA at a frequency of 16 Hz. Resistivity data were measured for temperatures between 1.5 and 300 K with a cooling and heating rate of 1 K/min (Fig. 4.1).

A very sharp anomaly is observed, that starts at $T = 150$ K and reaches a maximum at 149 K, while cooling. Upon heating, the anomaly starts at $T = 166$ K and reaches a minimum value at 168 K. It signifies the opening of a gap in the electronic density of states over a major fraction of the Fermi surface, in agreement with a charge-density wave (CDW) transition. The hysteresis of 17.0 K and the sharpness of the transition indicate a first-order CDW transition. A similarly sharp transition has been observed for single crystals of $\text{Lu}_2\text{Ir}_3\text{Si}_5$ [27], as well as for the commensurate CDW in $\text{Lu}_5\text{Ir}_4\text{Si}_{10}$ [95], suggestive of a similar mechanism for CDW formation in these compounds. A much more gradual transition, but still with hysteresis, has been observed for ceramic samples of $\text{Lu}_2\text{Ir}_3\text{Si}_5$ and $\text{Er}_2\text{Ir}_3\text{Si}_5$ [46, 26, 91].

The sensitivity of the CDW transition for crystal defects furthermore follows from the electrical resistivity measured on single crystals of $\text{Er}_2\text{Ir}_3\text{Si}_5$ of less good

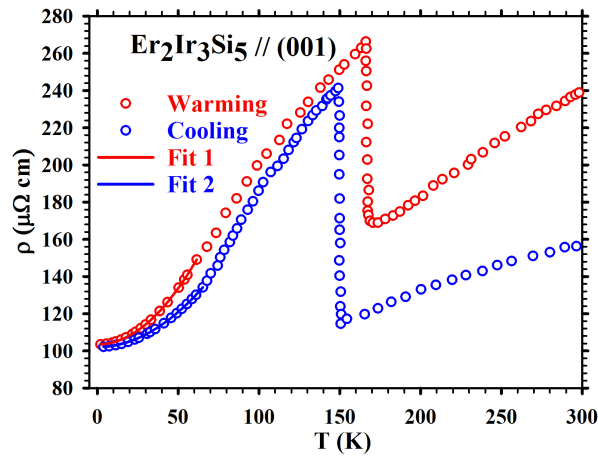


Figure 4.1: (color online) Temperature dependence of the electrical resistivity, ρ , along the \mathbf{c} -axis of $\text{Er}_2\text{Ir}_3\text{Si}_5$, as measured between 1.5 to 300 K, during cooling (blue circles) and heating (red circles) of the sample. The solid lines are fits to the low temperature data (see text).

quality, which indicated a broadened transition (see preliminary reports by one of us [96, 34]). Another important feature is the different values of the electrical resistivity obtained on cooling and subsequent heating of the sample. Similar behavior has been observed for ceramic material of $\text{Lu}_2\text{Ir}_3\text{Si}_5$ [26, 91].

It has been explained by variations of pinning of the CDW. Alternatively, it is possible that the large lattice distortions across the CDW transition are responsible for the formation of micro-cracks, a reduction of sizes of mosaic blocks and an increase in texture, which, in turn, would cause an increase of the electrical resistance at each thermal cycle. A mechanism by micro cracks is supported by the observation that the transition temperatures and hysteresis are the same in each thermal cycle. An increase of pinning centers would lead to a lowering of the CDW transition temperature, which is not observed.

It is interesting to note that the electrical resistivity exhibits a T^2 dependence below $T < 50$ K ($\rho(T) = \rho_0 + AT^2$; Fit 1 and Fit 2 in Fig. 4.1), *i.e.* up to much higher temperatures than ~ 10 K for a Fermi liquid, implying dominant contributions from short-range magnetic fluctuations in the absence of magnetic ordering.

The specific heat (C_p) was measured by the thermal relaxation method, using a Physical Property Measuring System (PPMS, Quantum Design, USA). Data obtained during heating of a single crystal of 11 mg from 2 to 250 K exhibit a sharp peak at the temperature of the CDW transition at 163.8(1) K (Fig. 4.2).

We are unable to find a peak in $C_p(T)$ while cooling the crystal. Similar behavior was noted earlier for a crystal of $\text{Lu}_2\text{Ir}_3\text{Si}_5$ [27].

This feature could be the result of the specific method of measurement employed

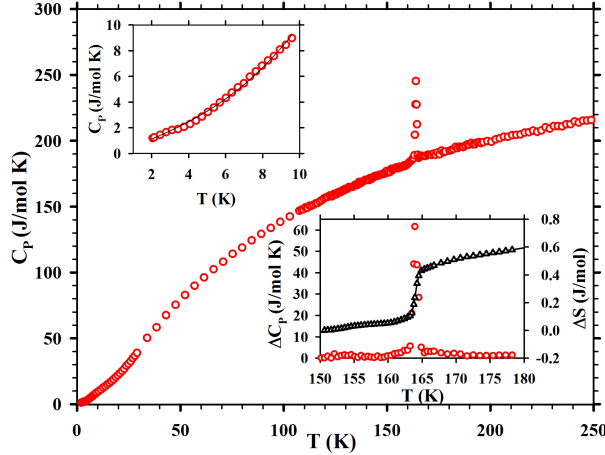


Figure 4.2: The specific heat (C_p) of a single crystal of $\text{Er}_2\text{Ir}_3\text{Si}_5$ upon heating from 2 to 250 K. Upper inset shows the specific heat data below 10 K; the solid line is a fit to the data points (see text). The lower inset provides an expanded view around the phase transition of ΔC_p (see text) and the increase of entropy, ΔS , due to the phase transition.

in the PPMS instrument. In a second experiment, differential scanning calorimetry (DSC) was measured from 120 to 200 K on the same single crystal of $\text{Er}_2\text{Ir}_3\text{Si}_5$. DSC data show sharp peaks in both heating and cooling runs, that appear at similar temperatures as is found for the electrical resistivity, and thus confirm the first-order phase transition (Fig. 4.3).

The transition is even sharper than what was found for $\text{Lu}_2\text{Ir}_3\text{Si}_5$ [27]). This feature might be related to the high quality of the present single crystal (see discussion above). Below 10 K, $C_p(T)$ could be fitted to $\gamma T + \beta T^3$, resulting in a high value of $\gamma = 0.545 \text{ J}/(\text{mol K}^2)$ and a Debye temperature of $\theta_D = 350 \text{ K}$ (upper panel of Fig. 4.2). Along with the T^2 dependence of the electrical resistivity, the high value of γ is in agreement with short-range antiferromagnetic correlations of the magnetic moments of Er^{3+} .

The lattice contribution to the specific heat was determined from a fit to the data far away from the transition. Subtraction of the lattice contribution resulted in $\Delta C_p(T)$ (Fig. 4.2). The change of entropy at the transition, $\Delta S(T)$, has been determined by integration of $\Delta C_p(T)/T$ over temperature (lower inset in Fig. 4.2). The resulting value of $\Delta S = 0.06 R$ is comparable to transition entropies obtained for conventional CDW systems, but it is 7–10 times smaller than for $R_5\text{Ir}_4\text{Si}_{10}$ [25] and $\text{Lu}_2\text{Ir}_3\text{Si}_5$ [27]).

On the other hand, the specific heat anomaly indicates a much sharper transition for single crystals of $\text{Er}_2\text{Ir}_3\text{Si}_5$ than for conventional CDW systems, which is in agreement with the first-order character of the transition. Furthermore, the specific

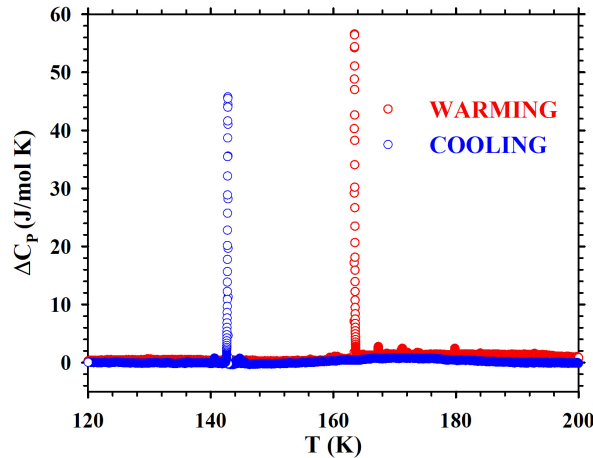


Figure 4.3: Temperature dependence of ΔC_p of $\text{Er}_2\text{Ir}_3\text{Si}_5$, obtained by subtracting a smooth background from the measured DSC data. A peak is found at $T = 142.8(1)$ K upon cooling (blue circles), an at $T = 163.6(1)$ K upon heating (red circles).

heat anomaly with $\Delta C_p(\text{max}) = 61.65(5)$ J/(mol K) at $T = 163.6(1)$ K is much larger than for conventional CDW systems, such as $\text{K}_{0.3}\text{MoO}_3$ ($\Delta C_p(\text{max}) = 8$ J/(mol K); $\Delta S = 0.18R$) [97, 98, 99] and NbSe_3 ($\Delta C_p(\text{max}) \approx 9$ J/(mol K); $\Delta S = 0.08R$) [100].

Large values of $\Delta C_p(\text{max})$ have also been found for $\text{Lu}_5\text{Ir}_4\text{Si}_{10}$ [95] and $\text{Lu}_2\text{Ir}_3\text{Si}_5$ [27]). It is in agreement with substantial lattice distortions accompanying the CDW transition (see below). The temperature dependent magnetic susceptibility, $\chi(T)$, was measured with a commercial SQUID magnetometer (MPMS 7, Quantum Design, USA) along the \mathbf{c} direction of a single crystal during cooling and during heating of the sample between 2 and 300 K, and employing a magnetic field of 0.1 mT (Fig. 4.4).

In a second experiment, $\chi(T)$ was measured with a custom built setup for temperatures between 0.1 and 10 K, again employing a magnetic field of 0.1 mT (lower inset in Fig. 4.4). The data show the absence of magnetic order down to 0.1 K.

The most interesting feature of the temperature dependent magnetic susceptibility is the sudden increase of $\chi(T)$ at 144.0(1) K upon cooling through the CDW transition. The observed effect cannot be explained by a change of Pauli susceptibility at the transition, because the estimated magnitude of the Pauli susceptibility is at least two orders of magnitude smaller than the observed jump of the susceptibility. Furthermore, one would expect a smaller Pauli susceptibility in the CDW phase, whereas we observe an increase of the susceptibility when cooling through the transition.

The same transition is found at 164(1) K upon heating. The observed hysteresis is in good agreement with the hysteresis found in the electrical resistivity and DSC

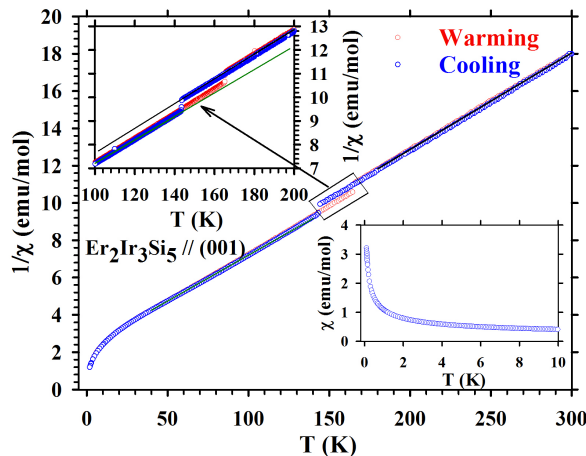


Figure 4.4: Temperature dependence of the magnetic susceptibility, χ , along \mathbf{c} of a single crystal of $\text{Er}_2\text{Ir}_3\text{Si}_5$. The main panel shows $\frac{1}{\chi}$ for cooling (blue circles) and heating (red circles) of the sample between 2 and 300 K. The upper inset gives an enlarged view of the hysteresis observed around the CDW transition, with solid lines describing the results of a Curie-Weiss fit to data for 180–300 K and a Curie-Weiss fit to data for 40–140 K (see text). The lower inset gives $\chi(T)$ at low temperatures, and clearly indicates the absence of magnetic ordering down 0.1 K.

measurements. A Curie-Weiss fit to the data at 180–300 K results in a Curie constant $C = 19.29(1)$ emu/mol K and an antiferromagnetic Weiss temperature of $\theta = -48.2(1)$ K. A Curie-Weiss fit to the low-temperature paramagnetic regime 40–140 K results in $C = 20.34(1)$ emu/mol K and $\theta = -46.4(1)$ K. The different Curie constants correspond to different effective magnetic moments on Er^{3+} of 8.78 and 9.02 μ_B , respectively.

$\text{Er}_2\text{Ir}_3\text{Si}_5$ is an exceptional case, in showing an effect of the CDW transition on the magnetic susceptibility. Usually, compounds containing magnetic rare earth elements do not show any anomaly in the paramagnetic susceptibility at the high-temperature CDW transitions. For example, $\text{Er}_5\text{Ir}_4\text{Si}_{10}$ is paramagnetic for at least 3–300 K without any anomalies in the magnetic susceptibility at its CDW transition [47]. For this compound, the Curie-Weiss fit resulted in a magnetic moment on Er^{3+} of 9.7 μ_B , which represents the theoretical value of free Er^{3+} ions [47].

Furthermore, the interaction between magnetic moments appears to be much weaker in $\text{Er}_5\text{Ir}_4\text{Si}_{10}$ (fitted value $\theta = -3.0$ K) than in $\text{Er}_2\text{Ir}_3\text{Si}_5$. The coexistence of antiferromagnetic order ($T_N = 2.8$ K) and CDW in $\text{Er}_5\text{Ir}_4\text{Si}_{10}$ might be related to the presence of weakly coupled independent 4*f* electrons of Er^{3+} ions [101], while for $\text{Er}_2\text{Ir}_3\text{Si}_5$ the reduced magnitude of the magnetic moments and strong coupling suggest participation of the 4*f* electrons in the conduction bands.

It is not clear at this moment, whether the small but distinct change of Er^{3+}

moment ($8.78 \mu_B$ vs $9.02 \mu_B$) across the CDW transition in a single crystal of $\text{Er}_2\text{Ir}_3\text{Si}_5$ could be responsible for absence of magnetic ordering of Er^{3+} moments in the crystal down to 0.1 K. Single-crystal X-ray diffraction (SXR) indicates a strong monoclinic lattice distortion with $\beta = 91.695(2)$ deg at $T = 75$ K in the CDW phase (Table B3 in the Appendix). The lattice distortion is accompanied by superlattice reflections that can be indexed by incommensurate modulation wave vectors (Eq. B1 in the Appendix)

$$\begin{aligned}\mathbf{q}^1 &= (0.2495(2), 0.4973(1), 0.2483(1)) \\ \mathbf{q}^3 &= (0.2495(2), -0.4973(1), 0.2483(1))\end{aligned}\quad (4.1)$$

Related \mathbf{q} -vectors describe satellite reflections from the other domains. The modulation wave vectors resemble those observed in ED on $\text{Lu}_2\text{Ir}_3\text{Si}_5$, while the monoclinic lattice distortion was not noticed in ED, because it cannot be visualized in the $[1\ 0\ 1]$ zone diffraction patterns studied in [44].

Based on the observed lattice distortion, two monoclinic structure models can be devised for the CDW phase. The first model preserves the I center of the lattice and it has a 2D modulation, involving both modulation wave vectors (Eq. 4.1). The second model assumes the second component of each wave vector to be exactly $\pm 1/2$; then $\mathbf{q}^1 - \mathbf{q}^3 = (0, 1, 0)$ and the I center is lost. The CDW superstructure would become a mixture of a commensurate supercell (loss of I -center corresponds to doubling of the unit cell) and a 1D incommensurate modulation according to \mathbf{q}^1 .

However, neither of these two models is compatible with the diffraction data (Table B5 in the Appendix). Instead, the CDW crystal structure is triclinic, preserves the I center and has a 1D incommensurate modulation according to the superspace group $I\bar{1}(\alpha\ \beta\ \gamma)0$ (No. 2.1.1.1 with standard setting $P\bar{1}(\alpha'\ \beta'\ \gamma')0$ [79]) with modulation wave vector $\mathbf{q}^1 = (0.2495(2), 0.4973(1), 0.2483(1))$ and lattice parameters $a = 9.8498(3)$, $b = 11.4863(3)$, $c = 5.7268(2)$ Å, and $\alpha = 90.079(1)$, $\beta = 91.695(2)$ and $\gamma = 90.051(1)$ deg at $T = 75$ K (Table B3 in the Appendix).

The large monoclinic lattice distortion accompanying the incommensurate CDW transition makes $\text{Er}_2\text{Ir}_3\text{Si}_5$ a unique CDW system without a counterpart in the literature. Both aspects, the lattice distortion and the 1D incommensurate modulation appear to be important for the formation of the CDW. The orthorhombic $Ibam$ crystal structure, stable above T_{CDW} , has six crystallographically independent atoms, Er1, Ir1, Ir2, Si1, Si2 and Si3 (Table B7 in the Appendix). The triclinic basic structure has ten independent atoms in the unit cell (Table B8 in the Appendix). In particular, Ir1 atoms form a regular zigzag chain along \mathbf{c} in $Ibam$ with distance $d[\text{Ir1}-\text{Ir1}] = 3.666(1)$ Å. In $I\bar{1}$, Ir1 splits into Ir1a and Ir1b sites, with the zigzag chain described as $(\text{Ir1a}, \text{Ir1b})_\infty$ (Fig. 4.5).

The lattice distortion is responsible for the formation of a dimerized zigzag chain with alternating distances $d[\text{Ir1a}-\text{Ir1b}] = 3.390(6)$ and $3.763(6)$ Å. It then is the shorter distance of these two, which is mostly affected by the incommensurate mod-

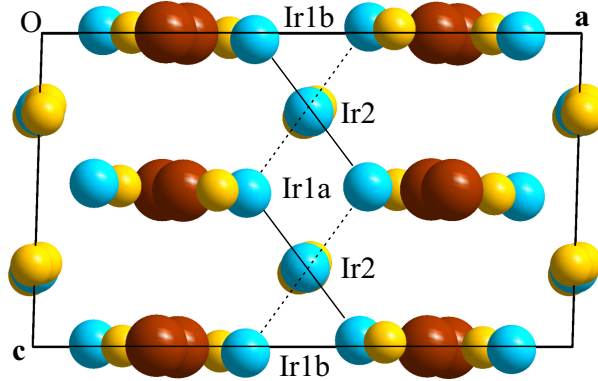


Figure 4.5: (Color online) The crystal structure of $\text{Er}_2\text{Ir}_3\text{Si}_5$ at 75 K projected onto the (\mathbf{a}, \mathbf{c}) -plane. Large red spheres correspond to Er atoms; blue spheres of intermediate size correspond to Ir atoms; small yellow spheres are Si atoms. Ir1a–Ir1b atoms are at a basic-structure distance of $3.763(6)$ Å for the dashed lines and of $3.390(6)$ Å for the solid lines.

ulation (Fig. 4.6).

The result is a strong modulation along the zigzag chain of Ir1, with one distance nearly constant at 3.76 Å and the other distance varying between 3.1 and 3.8 Å. These features strongly suggest that the zigzag chains of Ir1 atoms along \mathbf{c} are responsible for the CDW. Er1 atoms also are arranged in zigzag chains along \mathbf{c} . However, distances Er1–Er1 are around 4 Å and they exhibit a much smaller modulation than the short Ir1a–Ir1b distance. Direct participation of Er1 in the CDW thus is not expected.

In conclusion, we have described in full detail the incommensurately modulated crystal structure of the CDW phase of $\text{Er}_2\text{Ir}_3\text{Si}_5$. As we have shown, the incommensurate CDW is accompanied by a strong lattice distortion, both of which are important for the modulation of interatomic distances on zigzag chains of iridium atoms along \mathbf{c} . These features are in agreement with the CDW being supported by these zigzag chains. A presumed role of Er atoms could be excluded.

A combination of a lattice distortion and incommensurate modulation was previously found for $\text{Er}_5\text{Ir}_4\text{Si}_{10}$ [102]. This suggests similarities between the mechanisms for CDW formation in these two compounds. Nevertheless, the change of entropy at the CDW transition in $\text{Er}_2\text{Ir}_3\text{Si}_5$ is similar to typical CDW systems, while it is much smaller than in the 3D CDW system $\text{Er}_5\text{Ir}_4\text{Si}_{10}$ (Fig. 4.2 and [25]).

The large lattice distortion explains the sluggish character and large hysteresis of the transition, as they are apparent in the temperature dependencies of the electrical resistivity, DSC and magnetic susceptibility. A unique feature of compounds $R_2\text{Ir}_3\text{Si}_5$ is the extreme sensitivity of the phase transitions on crystalline order. The present single crystals of high perfection undergo a CDW transition,

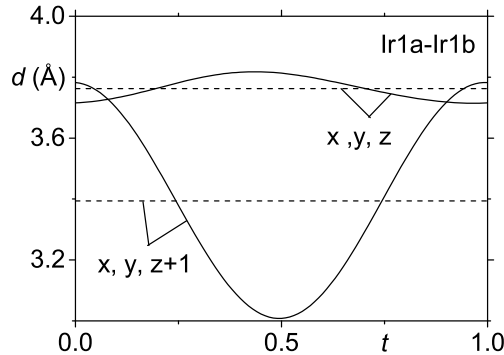


Figure 4.6: t -Plot of the interatomic distances between atoms Ir1a and Ir1b (x, y, z) and between Ir1a and Ir1b at ($x, y, z + 1$) for the crystal structure at $T = 75$ K. Dashed lines give the distances in the basic structure, with values of $3.763(6)$ and $3.390(6)$ Å.

while magnetic order is suppressed down to at least 0.1 K. Previous experiments on polycrystalline material have observed a broader CDW transition, while magnetic order appears below $T_N = 2.1$ K [46, 33]. This is qualitatively different from $\text{Lu}_2\text{Ir}_3\text{Si}_5$, for which superconductivity is weakly affected by the crystal perfection [27]. It demonstrates an intimate competition between CDW and magnetic order, presumably both interactions employing the same part of the Fermi surface, which is not the case in $\text{Er}_5\text{Ir}_4\text{Si}_{10}$, where Er spins are not affected by the CDW ordering. Accordingly, $\text{Er}_2\text{Ir}_3\text{Si}_5$ provides a new test bed for studies towards the competition between CDW and magnetism of the Er spins and the influence of disorder on these phase transitions.

We thank Mr. D. D. Buddikot for his help in measuring the heat capacity. Mr. L. Eiter is thanked for his assistance with preliminary X-ray diffraction experiments. X-ray diffraction experiments with synchrotron radiation were performed at station EH2 of beamline P24 of PETRA-III at DESY in Hamburg, Germany. This research has been funded by the Deutsche Forschungsgemeinschaft (DFG, German Research Foundation)—265092781, and by the Alexander-von-Humboldt foundation within their research-group linkage program.

Chapter 5

Unusual magnetic behavior of crystalline $\text{Ni}_{0.89}\text{V}_{2.11}\text{Se}_4$ with site disorder

1

We report temperature dependent electronic and magnetic properties of single-crystalline site-disordered $\text{Ni}_{0.89}\text{V}_{2.11}\text{Se}_4$. $(\text{Ni}_{1-x}\text{V}_x)\text{V}_2\text{Se}_4$ is found to crystallize in the monoclinic Cr_3S_4 structure type with space group $I2/m$. The electrical resistivity ($\rho(T)$) shows metallic behavior with a broad anomaly around 150–200 K; the magnetic susceptibility displays paramagnetic behavior which deviates from Curie-Weiss behavior below 150 K. These anomalies indicate a change of state of the material below 150 K. Indeed, between 15 and 150 K, $\rho(T)$ is found to exhibit an anomalous $T^{3/2}$ dependence, and below 15 K it exhibits a T^2 dependence down to 1.5 K. The analysis of the low temperature specific heat data shows the existence of magnetic fluctuations as well as an enhanced value of the Sommerfeld coefficient $\gamma = 104.0(1) \text{ mJ/mol}\cdot\text{K}^2$, suggesting strong electron-electron correlations in this system. We believe that the system exhibits a Non-Fermi-liquid to a Fermi-liquid transition under ambient pressure. The presence of magnetic fluctuations (borderline magnetism) and quenched disorder on the Ni/V sites could be the cause for this phenomenon.

¹This chapter has been yet to be published as: Sitaram Ramakrishnan, Shidaling Mathepanavar, Arumugam Thamizhavel, Srinivasan Ramakrishnan and Sander van Smaalen. Unusual magnetic behavior of crystalline $\text{Ni}_{0.89}\text{V}_{2.11}\text{Se}_4$ with site disorder

5.1 Introduction

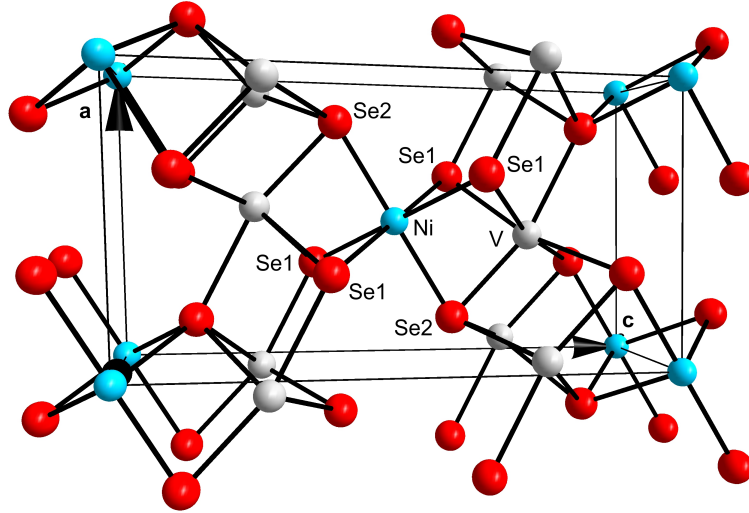


Figure 5.1: The crystal structure of NiV_2Se_4 at 100 K. Perspective view approximately along **b**. The shortest distances between metal atoms form an unbounded network on the (101) plane; $d(\text{Ni}-\text{V}) = 2.988(1) \text{ \AA}$ and $d(\text{V}-\text{V}) = 3.033(1) \text{ \AA}$. The next shortest distance is $b = 3.416 \text{ \AA}$ along $[0, 1, 0]$.

It is now well known that site disorder leads to unusual magnetic phenomena in many Cerium based intermetallic compounds [103, 104, 105]. This is due to fact that the crystal structures of these compound permit multiple inequivalent sites for Ce consisting of both magnetic Ce^{3+} and non-magnetic Ce^{4+} ions. Such an occurrence of magnetic ordering observed in metallic systems having these two different valence states of Ce is rare. Here we report even more unusual transport and magnetic properties of site disordered $\text{Ni}_{0.89}\text{V}_{2.11}\text{Se}_4$. The presence of site disorder is a natural occurrence in compounds AT_2X_4 (A and T are transition metals; X is chalcogenide), which display exotic electronic and magnetic properties. Cubic thiospinels of transition metal chalcogenides of the type AT_2S_4 (A = Cu, Ni; T = V, Rh, Ir) have always attracted attention due to the unusual ground states exhibited by them [106, 107, 108, 109, 110, 111]. For instance, superconductivity (e.g. in CuRh_2S_4) [106], magnetic order in insulators (CuIr_2S_4) [107, 108], and charge density waves (CDWs; CuV_2S_4) [109, 110] have been found to exist in this class of compounds. In addition, structural studies have shown that phase transitions are accompanied by charge ordering and spin dimerization [111]. The occurrence of spin dimerization in a three dimensional compound, like CuIr_2S_4 , is unique and not understood at present.

Apart from these cubic spinel compounds, there exists more than 50 chalcogenides with the same stoichiometry AT_2X_4 (A = Y, Cr, Fe, Co, Ni; T = Ti, Y,

Cr; X = S, Se, Te), but crystallizing in the monoclinic defect NiAs structure type (Fig. 5.1) [112], where little investigations have been made. In considering the band structure of compounds with the defect NiAs structure, only octahedral site ions are involved. Unlike spinels, all metal ions are on octahedral sites and, therefore, the t_{2g} levels have the lowest energy. The metallic behavior for the AT_2X_4 compounds can be ascribed to partially filled bands formed as a result of T–T overlap.

The NiAs structure is also known as the Cr_3S_4 structure (space group $I2/m$) with two nonequivalent crystallographic sites for Cr. Chromium atoms occupy Wyckoff positions 2a and 4i, with two and four atoms per unit cell, respectively. These sites can be occupied by different element [113, 114, 115, 116, 117, 118, 119, 120, 121]. A study on polycrystalline NiV_2S_4 has indicated a CDW transition at 165 K [48], while another study on NiV_2Se_4 reported a small anomaly in the resistivity around 160 K [49]. We have obtained by the vapour transport method a site disordered single crystal of composition $Ni_{0.89}V_{2.11}Se_4$, which has the same crystal structure as NiV_2Se_4 . We report detailed studies on physical properties of the $Ni_{0.89}V_{2.11}Se_4$ single crystal, and discuss an unusual electronic ground state of this disordered material.

5.2 Results and discussion

Single-crystal X-ray diffraction has been measured on a Mar345dtb image plate diffractometer with Ag- $K\alpha$ radiation from a rotating anode generator. A crystal of dimensions $0.1 \times 0.1 \times 0.1 \text{ mm}^3$ was selected from a different batch than that contained the large crystal for physical properties measurements. Complete sets of diffraction images have been measured at 293 K and 100 K, employing an exposure time such that the strongest Bragg reflection was close to saturation of the detector. A second run was measured with an offset of 30 deg in 2θ for obtaining data at high resolution, and employing an eight times longer exposure time, resulting in over exposed strong reflections but allowing for detection of weak scattering effects. All diffraction maxima could be indexed by a single unit cell similar to the published unit cell of NiV_2Se_4 [122]. Superlattice reflections could not be detected, in agreement with the absence of a CDW at 100 K. A structure analysis on the basis of the nominal composition NiV_2Se_4 lead to a good fit to the diffraction data with $R = 0.0380$, employing the Cr_3S_4 structure type. A much improved fit was obtained at $R = 0.0224$ after refinement of Ni/V disorder on the A-site [123]. Disorder on the T site did not lead to significant deviations from full occupancy by vanadium.

The refined composition is $(Ni_{0.306(11)}V_{0.694})V_{2.000}Se_4$. Apparently, the small crystal contains even less nickel than the large crystal does. It shows, however, that Ni is partly replaced by V, but that Ni does not enter the T site. The formation of nickel-deficient compounds NiV_2Se_4 is in agreement with similar findings in the

literature, where attempted compositions AV_2Se_4 ($A = \text{transition metal}$) tend to produce crystals that contain more vanadium than given by the stoichiometry [49, 124]. All the bulk measurements reported here are done on the large crystal of composition $(\text{Ni}_{0.89}\text{V}_{0.11})\text{V}_2\text{Se}_4$ (see above).

The electrical resistivity, $\rho(T)$, of $\text{Ni}_{0.89}\text{V}_{2.11}\text{Se}_4$ monotonously decreases upon cooling from room temperature down to 1.6 K (Fig. 5.2).

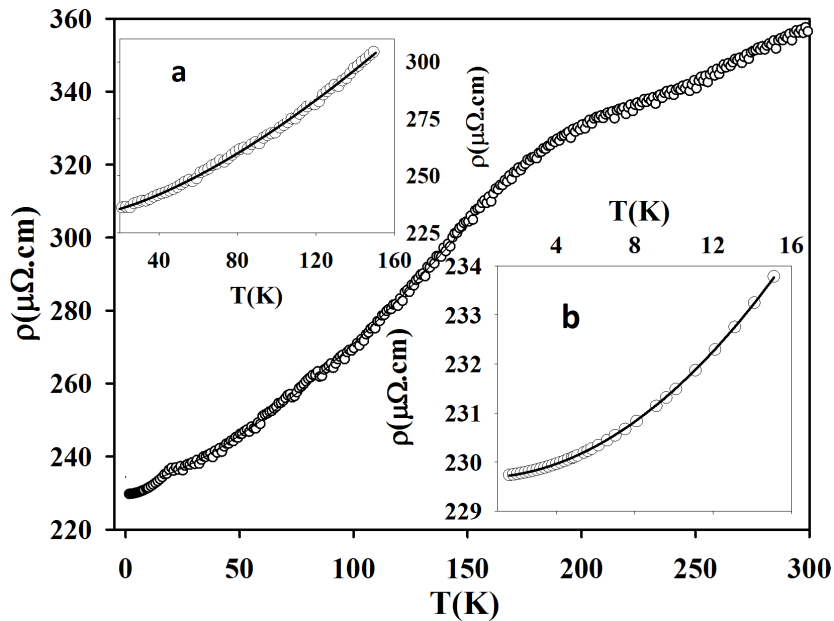


Figure 5.2: Temperature dependent electrical resistivity of $\text{Ni}_{0.89}\text{V}_{2.11}\text{Se}_4$. The upper inset (a) provides an expanded view of 15–150 K; the solid line is a fit to a $T^{3/2}$ dependence (Eq. 5.1), with $\rho_{0,1} = 231.600(1) \mu\Omega \text{ cm}$ and $a_1 = 0.038(1) \mu\Omega \text{ cm}/\text{K}^{3/2}$. The lower inset (b) gives an expanded view of 1.5–15 K; the solid line is a fit to a T^2 dependence (Eq. 5.2), with $\rho_{0,2} = 229.982(1) \mu\Omega \text{ cm}$ and $a_2 = 0.017(1) \mu\Omega \text{ cm}/\text{K}^2$.

One can see that $\rho(T)$ exhibits metallic behavior with a broad hump between 150–200 K. The metallic behavior is consistent with other polycrystalline materials of the defect-NiAs structure, which were reported earlier [113, 114, 115, 116, 117, 118, 119, 120, 121, 48].

In particular, the observed broad anomaly also agrees with Bouchard et. al. (1966) [49], who first reported an anomaly at about 160 K in $\rho(T)$ of a polycrystalline sample of NiV_2Se_4 . They suggested that the observed anomaly may be due to either a crystallographic or a magnetic transition. However, we find that the broad anomaly between 150–200 K cannot be ascribed to a CDW or another major structural transition, since our diffraction studies did not find any evidence of a structural transition [123]. Contributions to this anomaly of magnetic origin

cannot be ruled out (see below).

It is noticed that below the broad hump, $\rho(T)$ exhibits an unusual $T^{3/2}$ dependence in the temperature region 15–150 K. Such a behavior is generally observed in spin glasses and amorphous ferromagnets, where a $T^{3/2}$ dependence in $\rho(T)$ is explained by a diffusive motion of the charge carriers [125, 126]. Most theories suggest an explanation of the anomalous resistivity by an inhomogeneous magnetic state, through comparison with the resistivity of spin glasses [127]. Since $\text{Ni}_{0.89}\text{V}_{2.11}\text{Se}_4$ is a single crystal, the diffusive carrier motion has to be intrinsic somewhat similar to the behavior observed in MnSi under pressure [128].

It is well established that the electronic properties of metals on the border of magnetic phase transitions at low temperatures are often found to exhibit temperature dependencies that differ from the predictions of Fermi liquid theory. Early attempts to explore such non-Fermi-liquid behavior have been based on mean-field treatments of the effects of enhanced magnetic fluctuations, as in the self-consistent renormalization (SCR) model [129]. The SCR model seems to explain the temperature dependence of the resistivity of Ni_3Al under high pressure, where its ferromagnetism is suppressed leading to negligible magnetic correlation vector $\kappa(T)$. In the idealized limit $\kappa \rightarrow 0$ and $T \rightarrow 0$, the SCR model predicts that in 3D, the quasiparticle scattering rate $(\tau_{qp})^{-1}$ varies linearly with the quasiparticle excitation energy, rather than quadratically as in the standard Fermi-liquid picture. This form of $(\tau_{qp})^{-1}$ is similar to that of the marginal Fermi-liquid model, [130] which is normally associated with a linear temperature dependence of the resistivity. However, at the border of ferromagnetism, the relevant fluctuations responsible for quasiparticle scattering are of long wavelength and, thus, are ineffective in reducing the current. This leads to a transport relaxation rate $(\tau_{tr})^{-1}$ that differs from $(\tau_{qp})^{-1}$ and varies not as T , but as $T^{5/3}$ which was observed in high pressure studies on Ni_3Al .

For a metal on the border of metallic antiferromagnetism in three dimensions, the SCR model predicts $\rho(T)$ to vary as $T^{3/2}$ in the idealized limit $\kappa \rightarrow 0$, $T \rightarrow 0$, where $\kappa(T)$ now stands for the correlation wave vector for the staggered magnetization. This simple model for the scattering from antiferromagnetic fluctuations assumes that the scattering rate can be averaged over the Fermi surface. Within the SCR model, this procedure would seem to require the presence of a sufficient level of quenched disorder, the latter which might be provided by the chemical disorder at the A-site in $\text{Ni}_{0.89}\text{V}_{2.11}\text{Se}_4$. This quenched disorder is supposed to inhibit the short circuiting caused by the carriers on the cold spots of the Fermi surface, i.e., regions far from the hot spots connected by the antiferromagnetic ordering wave vector and, thus, strongly affected by spin-fluctuation scattering. Such a behavior has been observed in NiSSe [131].

In the case of single crystalline $\text{Ni}_{0.89}\text{V}_{2.11}\text{Se}_4$, the temperature dependence of the electrical resistivity between 15 and 150 K could be fitted by the equation

$$\rho(T) = \rho_{0,1} + a_1 T^{3/2}, \quad (5.1)$$

where ρ_0 is the residual resistivity and the second term is the contribution from the scattering proposed by the SCR model. It is of interest to see that below 15 K, $\rho(T)$ can be fitted to the equation

$$\rho(T) = \rho_{0,2} + a_2 T^2, \quad (5.2)$$

which suggests that the breakdown of NFL behavior below 15 K. The second term here arises from the scattering of electrons due to localized spin fluctuations [132].

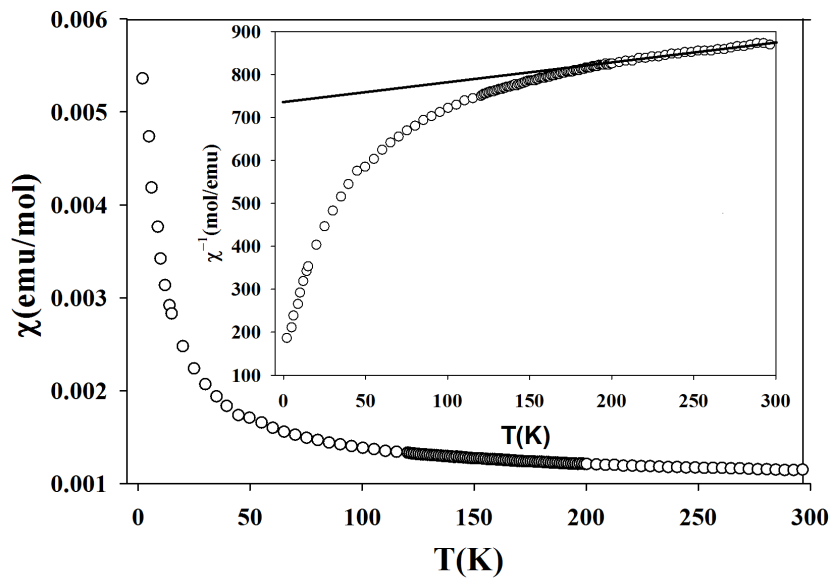


Figure 5.3: Temperature dependent magnetic susceptibility of $\text{Ni}_{0.89}\text{V}_{2.11}\text{Se}_4$. Data measured in a field of 5 T under zero field cooled (ZFC) condition. A measurement under field cooled (FC) conditions produced data coinciding with those shown for ZFC conditions. The inset provides the inverse susceptibility; the solid line is the $(T+\theta)/C$ part of a fit of the modified Curie-Weiss law (Eq. 5.3), with $\chi_0 = 1.01(1) \times 10^{-3}$ emu/mol, $C = 0.040(1)$ emu/mol·K, $\mu_{eff} = 0.57(1) \mu_B$ and $\theta = 4.8(1)$ K.

The temperature dependence of the magnetic susceptibility clearly shows paramagnetic behavior (Fig. 5.3) at high temperatures (150 to 300 K). However, below 150 K, it does deviate from a simple Curie-Weiss behaviour as discussed below. Magnetization measurements performed under field cooled (FC; not shown) and zero-field cooled (ZFC; Fig. 5.3) conditions produced identical results, implying that spin glass phenomena can be ruled out in the case of $\text{Ni}_{0.89}\text{V}_{2.11}\text{Se}_4$. The high temperature (150–300 K) data can be described by a modified Curie-Weiss law,

$$\chi = \chi_0 + C/(T + \theta). \quad (5.3)$$

where χ_0 includes the diamagnetic and temperature-independent paramagnetic contributions. From the value of the Curie constant C , the effective magnetic moment is estimated as $\mu_{eff} = 0.57(1) \mu_B$ per formula unit. Usually, the Ni ion does not have a magnetic moment in metallic compounds of the type AB_2X_4 , since all valence electrons of Ni are completely delocalized in a fully ordered crystal structures. Apparently, this scenario breaks down in $Ni_{0.89}V_{2.11}Se_4$, which again might be related to the Ni/V chemical disorder. The Weiss temperature is found to be $\theta = 4.8(1)$ K, indicative of weak antiferromagnetic exchange interactions. Finally, the inset in Fig. 5.3 clearly shows that below 150 K, χ significantly deviates from Curie-Weiss behavior. All these features are in agreement with the interpretation of the electrical resistivity data.

Isothermal magnetization (M–H) curves have been measured at selected temperatures within the range 2–300 K up to magnetic fields of ± 7 T (Fig. 5.4).

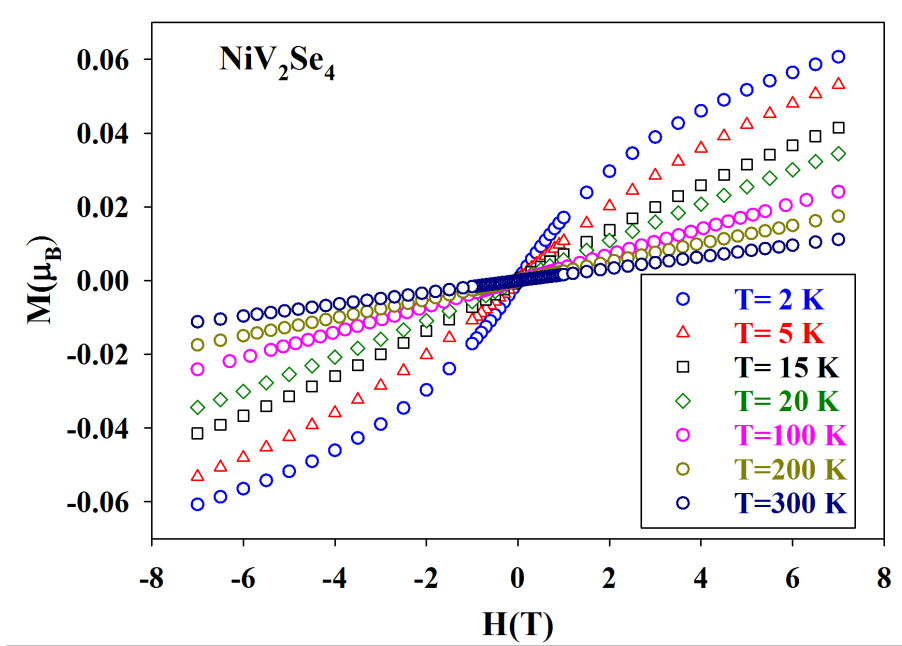


Figure 5.4: Magnetization (M) in dependence on the applied magnetic field (H) at selected temperatures.

Hysteresis is absent at all temperatures, demonstrating that $Ni_{0.89}V_{2.11}Se_4$ does not undergo a magnetic phase transition, but remains in the paramagnetic state down to 2 K. At the lowest measured temperatures, the M–H dependence is S-shaped instead of linear at higher temperatures. This might be related to the fact that lower temperatures allow to reach higher values of H/T , thus bringing the M–H relation outside the linear regime. However, attempts failed to bring all data onto a universal H/T dependence. This seems to imply that the crystal does not

behave like an usual paramagnet below 15 K. The specific heat, $C_p(T)$, decreases monotonically on cooling (Fig. 5.5).

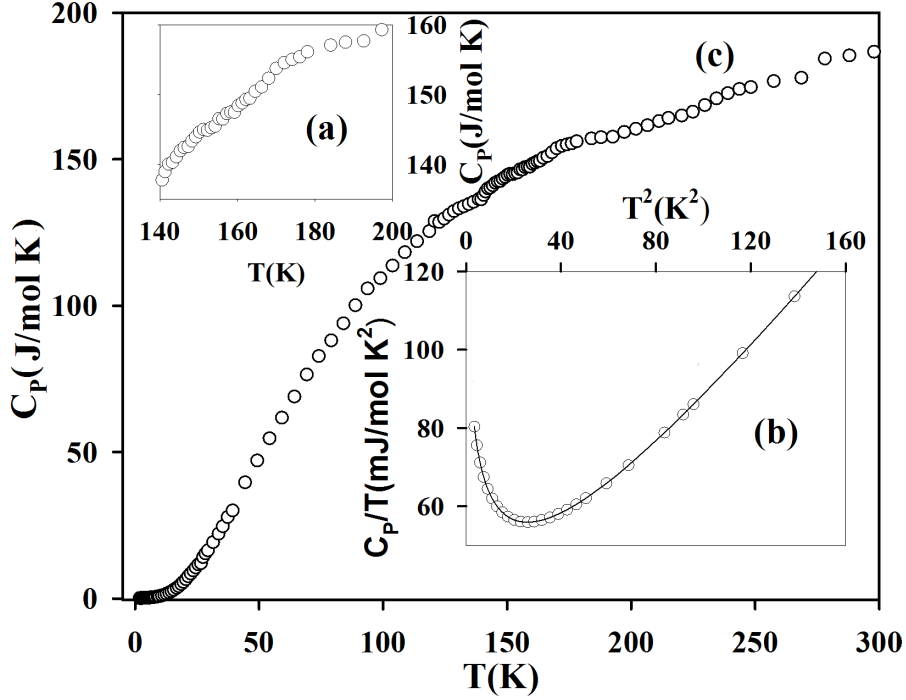


Figure 5.5: Temperature dependence of the specific heat C_p from 2 to 300 K (c). The upper inset (a) provides an expanded view of the region of the anomaly around 160 K. The lower inset (b) displays C_p/T vs T^2 at low temperatures 2–40 K. Contributions from strong spin fluctuations are demonstrated by a fit (solid line) of Eq. 5.4 with $\gamma = 104.0(1)$ mJ/mol·K², $\beta = 0.84(1)$ mJ/mol·K⁴, $\theta_D = 252.9(1)$ K, $a = 42.42(1)$ and $T^* = 1.00(1)$ K.

A broad small anomaly at $T = 150$ – 170 K rules out a possible structural phase transition, which is in agreement with our single-crystal X-ray diffraction studies. However, the presence of this anomaly in the heat capacity data is in agreement with the anomalies observed in resistivity and magnetic properties. The origin of this anomaly is not understood at this juncture. It is important to specify here, the NFL starts below this transition. The low temperature data can be fitted with the model, given by [133],

$$C_p/T = \gamma + \beta T^2 + a \ln(T^*/T). \quad (5.4)$$

The first term is the contribution due to conduction electrons, the second term is the contribution from the lattice, and the third term is the contribution from spin fluctuations due to site disorder. This model was successfully employed to explain a

similar heat capacity anomaly in $\text{Fe}_{1-x}\text{V}_{2+x}\text{Al}$ in another context [133]. The fitting yields $\gamma = 104.0(1)$ mJ/mol·K² and the Debye temperature $\theta_D = 252.9(1)$ K. The existence of magnetic fluctuations below 15 K has been corroborated by the isothermal magnetization data, as explained earlier. The presence of such magnetic fluctuations seems to change the NFL behavior below 15 K.

5.3 Conclusions

The perfectly ordered structure of NiV_2Se_4 does not have a magnetic moment on Ni. However, our attempted growth of single crystals of NiV_2Se_4 has resulted in Ni-deficient crystals, where the crystallographic Ni site is disorderly occupied by Ni and V, but full chemical order is preserved at the V and the two Se sites of the AT_2Se_4 monoclinic structure type. This observation is in agreement with reports in the literature of crystallization attempts, where part or all of the transition metal A is replaced by V [49, 124]. We have found that a single crystal of composition $(\text{Ni}_{0.894(6)}\text{V}_{0.106})\text{V}_2\text{Se}_4$ exhibits anomalies or cross-over in its physical properties at temperatures around 150 K. All properties, including low-temperature X-ray diffraction data, are in agreement with the absence of phase transitions down to $T = 2$ K in the absence of a magnetic field. The temperature dependence of the electrical resistivity demonstrates that $\text{Ni}_{0.89}\text{V}_{2.11}\text{Se}_4$ is in a non-Fermi liquid state for 15–150 K, while Fermi liquid behavior is present below 15 K. These features, together with deviations from Curie-Weiss behavior of the magnetic susceptibility below 150 K can be explained by the gradual build-up of antiferromagnetic fluctuations upon cooling. Isothermal magnetization curves confirm the absence of bulk magnetic order down to 2 K but suggests build up of antiferromagnetic correlations. There are a large number of studies which show the emergence of non-Fermi liquid (NFL) behavior from a Fermi liquid behavior at some critical value of the external parameter like, pressure, magnetic field etc (see for instance [134, 135]). In this work, we show an emergence of a Fermi liquid like state from an NFL start at ambient pressure and in the absence of magnetic field. After a weak anomaly at 160 K, the system attains an NFL state (150 to 15 K) and that changes below 15 K due to the build-up of short range antiferromagnetic correlations. We believe that $\text{Ni}_{0.89}\text{V}_{2.11}\text{Se}_4$ is a correlated system that displays unusual electronic properties which warrant more investigations, notably on the nature of the phase transition around 160 K.

5.4 Methods

5.4.1 Crystal growth

$\text{Ni}_{0.89}\text{V}_{2.11}\text{Se}_4$ has been prepared by reaction of the elements in evacuated quartz-glass tubes at a temperature of $T = 1153$ K, employing stoichiometric amounts of the elements obtained from Alfa Aesar: nickel (99.996% purity), vanadium (99.5%), and selenium (99.999%). Single crystals of nominal composition NiV_2Se_4 have been grown by vapor transport in evacuated quartz-glass tubes, employing iodine as transport agent and a temperature gradient of $T = 1033 / 973$ K over 200 mm. Different experiments have been performed for growing large single crystals for physical properties measurements and for growing small crystals for x-ray diffraction.

5.4.2 Chemical composition

The chemical composition has been determined by energy dispersive x-ray spectroscopy (EDX) applied to a flat, as-grown surface of the large single crystal as used for the physical-properties measurements. Normalized to four Se atoms, EDX gave the composition $\text{Ni}_{0.899(6)}\text{V}_{2.118(7)}\text{Se}_4$, resulting in 3.017(9) metal atoms (Ni + V) per formula unit. This number deviates less than two standard uncertainties from the stoichiometric composition. Therefore, we will assume fully occupied atomic sites of the monoclinic AT_2X_4 crystal structure. The measured composition, however, implies that $\sim 11\%$ of the Ni atoms are replaced by V, resulting in composition $(\text{Ni}_{0.894(6)}\text{V}_{0.106})\text{V}_2\text{Se}_4$. The latter interpretation is in agreement with the results of X-ray diffraction.

5.4.3 Physical properties measurements

The electrical resistivity $\rho(T)$ has been measured on cooling from 300 down to 1.5 K in a standard four-probe configuration, employing a cryostat and a LR-700 (Linear Research, USA) bridge with 5 mA current of small AC frequency of 16 Hz. Electrical contacts have been made using silver paste and gold wires (40 μm diameter).

The magnetic susceptibility $\chi(T)$ has been measured for temperatures 2–300 K, using a commercial SQUID magnetometer (MPMS5 by Quantum Design, USA). Measurements have been repeated in both zero-field-cooled (ZFC) and field-cooled (FC) conditions for magnetic fields of different strength.

The isothermal magnetization has been measured for magnetic fields from -7 to $+7$ Tesla at a few selected temperatures. The heat capacity $C_p(T)$ has been measured from 2 to 300 K by the thermal relaxation method using a Physical property measuring system (PPMS, Quantum Design, USA).

5.5 Acknowledgements

Single crystals have been grown by Kerstin Küspert at the Laboratory of Crystallography in Bayreuth. Financial support has been obtained from the German Science Foundation (DFG) under contract No. SM55/25-1, and from the Alexander-von-Humboldt Foundation in their Research Group Linkage Programme. S.M thanks the Tata Institute of Fundamental Research, Mumbai for providing a postdoctoral fellowship.

Appendix A: Structure refinements and models of CuV_2S_4

2

Supplemental material for the incommensurate and lock-in CDW structures of CuV_2S_4 :

- A1. Transformation between I and F centered settings of the lattice.
- A2. Diffraction experiment at beamline P24.
- A3. Data processing for crystal A (annealed).
- A4. Structure refinements and tables of structural parameters for crystal A (annealed).
- A5. Diffraction experiment at beamline SNBL.
- A6. Data processing for crystals B–E (as grown).
- A7. Structure refinements and tables of structural parameters for crystals B–E (as grown).

²The appendix has been published as a supplemental material for the manuscript: Sitaram Ramakrishnan, Andreas Schönleber, Christian B. Hübschle, Claudio Eisele, Achim M. Schaller, Toms Rekis, Nguyen Hai An Bui, Florian Feulner, Sander van Smaalen, Biplab Bag, Srinivasan Ramakrishnan, Martin Tolkieln, and Carsten Paulmann. Charge-density-wave and lock-in transitions of CuV_2S_4 . *Phys. Rev. B* **99**, 195140 (2019)

A1 F -centered setting of the I -centered lattice

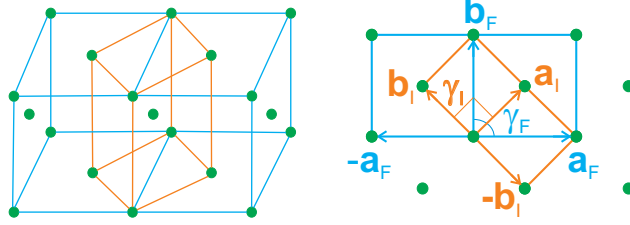


Figure A1: Relation between the F -centered (blue) and I -centered (orange) unit cells for an I -centered, pseudo-tetragonal lattice. Notice that $\gamma_I = 90$ deg and $\gamma_F \neq 90$ deg for the I -centered orthorhombic lattice.

At high temperatures CuV_2S_4 possesses the spinel structure type with a F -centered lattice and the cubic space group $Fd\bar{3}m$ (No. 227 in [78]). The basic structures in the CDW states at low temperatures may have symmetry according to a subgroup of $Fd\bar{3}m$, including $I4_1/amd$, $Fddd$, $Imma$ and $Imm2$. The I -centered setting of the originally F -centered cubic lattice is obtained by the following transformation of basis vectors (Fig. A1):

$$\begin{aligned}
 \mathbf{a}_I &= \frac{1}{2}(\mathbf{a}_F + \mathbf{b}_F) & \mathbf{a}_F &= (\mathbf{a}_I - \mathbf{b}_I) \\
 \mathbf{b}_I &= \frac{1}{2}(-\mathbf{a}_F + \mathbf{b}_F) ; & \mathbf{b}_F &= (\mathbf{a}_I + \mathbf{b}_I) . \\
 \mathbf{c}_I &= \mathbf{c}_F & \mathbf{c}_F &= \mathbf{c}_I
 \end{aligned} \tag{A1}$$

Employing the inverse transformation, one always obtains a F -centered unit cell for an I -centered lattice. The F -centered setting is a valid setting for the I -centered tetragonal lattice, with $a_F = b_F = \sqrt{2}a_I$ and $c_F = c_I$ and angles of 90 deg. For the I -centered orthorhombic lattice we have

$$\begin{aligned}
 a_I &\neq b_I \neq c_I \neq a_I \\
 \alpha_I &= \beta_I = \gamma_I = 90 \text{ deg} .
 \end{aligned} \tag{A2}$$

Employing the definitions $a_F = \sqrt{\mathbf{a}_F \cdot \mathbf{a}_F}$ and $\mathbf{a}_F \cdot \mathbf{b}_F = a_F b_F \cos(\gamma_F)$, and employing $\mathbf{a}_I \cdot \mathbf{b}_I = a_I b_I \cos(\gamma_I) = 0$ the transformation in Eq. A1 then leads to

$$\begin{aligned}
 a_F = b_F &= \sqrt{(a_I)^2 + (b_I)^2} \\
 \cos(\gamma_F) &= \frac{(a_I)^2 - (b_I)^2}{((a_I)^2 + (b_I)^2)} \neq 0 .
 \end{aligned} \tag{A3}$$

This result implies that the orthorhombic character of the I -centered lattice (Eq. A2), *i.e.* $a_I \neq b_I$ translates into $\gamma_F \neq 90$ deg for the F -centered setting. The inverse transformation leads to

$$\begin{aligned}
a_I &= \frac{1}{2} \sqrt{(a_F)^2 + (b_F)^2 + 2a_F b_F \cos \gamma_F} \\
b_I &= \frac{1}{2} \sqrt{(a_F)^2 + (b_F)^2 - 2a_F b_F \cos \gamma_F} \\
c_I &= c_F \\
\alpha_I &= \beta_I = \gamma_I = 90 \text{ deg.}
\end{aligned}
\tag{A4}$$

That is, for $\gamma_F < 90$ deg, the present transformation results in $a_I > b_I$. The CDW phases have been established to possess orthorhombic symmetry with an I -centered lattice as described above. The superspace group is $Imm2(\sigma_1 0 0)000$ (No. 44.1.12.4 with standard setting $I2mm(0 0 \sigma_1)000$ [79]). The modulation wave vector in the I and F centered settings then is (Eq. A1):

$$\begin{aligned}
\mathbf{q}^{(I)} &= (\sigma_1, 0, 0) \\
\mathbf{q}^{(F)} &= (\sigma_1, \sigma_1, 0).
\end{aligned}
\tag{A5}$$

A2 X-ray diffraction at beamline P24 of DESY

Single-crystal X-ray diffraction (SXR) was measured at station EH2 of beamline P24 of PETRA III extension at DESY in Hamburg, Germany, employing radiation of a wave length of $\lambda_{P24} = 0.495935$ Å. Diffracted X rays were detected by a MARCCD165 detector. The temperature of the sample was regulated with a CRY-OCOOL open-flow cryostat, employing helium as cryo gas. The annealed crystal A of dimensions $0.08 \times 0.11 \times 0.09$ mm³ was selected for the SXR experiment at P24. Diffracted intensity was collected on the detector during rotation of the crystal by 1 deg. Each run of data collection comprises 362 of these frames, corresponding to a total rotation of the crystal by 362 deg.

Table A1: Thermal history of crystal A, detailing the measured runs at beamline P24 at DESY, Hamburg. The date and time are given for the start of one run of data collection at the given temperature and for the given attenuator.

Temperature (K)	Phase	Attenuator		Date dd.mm.year	Time hh:mm:ss	Number of hours
		setting	factor			
250	Cubic	0	1.0	17.09.2018	21:44:34	0
80	Incommensurate	16	0.046	18.09.2018	00:46:13	3
80	Incommensurate	6	0.316	18.09.2018	02:32:56	5
80	Incommensurate	0	1.0	18.09.2018	03:30:43	6
20	Incommensurate	14	0.068	18.09.2018	05:54:23	8
20	Mixed	0	1.0	18.09.2018	07:53:43	10
20	Commensurate	4	0.464	18.09.2018	10:24:38	12.5
40	Commensurate	14	0.068	18.09.2018	11:33:23	13
40	Commensurate	4	0.464	18.09.2018	12:37:32	14
40 ^a	Commensurate	0	1.0	18.09.2018	13:38:11	15
60	Incommensurate	16	0.046	18.09.2018	17:50:16	19
60	Incommensurate	6	0.316	18.09.2018	18:47:29	20
60 ^b	Incommensurate	0	1.0	18.09.2018	19:45:01	21
90 ^c	Incommensurate	16	0.046	19.09.2018	05:10:34	-
90	Incommensurate	0	1.0	19.09.2018	06:12:17	-

^aThis run at 40 K was halted after 228 measured frames and resumed at 16:29:45 to complete the remaining frames. ^bCrystal removed and heated to 293 K after this run. ^cSecond time cooling from 293 K.

The time of measurement for one run was about 60 minutes. The crystal-to-detector distance was chosen as 90 mm, resulting in $(\frac{\sin(\theta)}{\lambda})_{max} = 0.7310 \text{ \AA}^{-1}$. Several runs with different attenuators in the primary beam were measured for each of the six selected temperatures (Table A1). An initial data collection at 250 K confirmed the cubic symmetry of CuV_2S_4 (Table A1). Cooling to 80 K brought the crystal into the incommensurate CDW phase. After further cooling to 20 K it required about 4 hours and 30 minutes for the second phase transition (reported to occur at 50 K) to complete (Table A1). After heating to room temperature, a second cooling cycle brought crystal A into the incommensurate CDW phase at 90 K.

A3 Data processing of SXRD data of crystal A

Data processing was performed with the software EVAL15 [50]. Absorption correction was applied by the software SADABS [51]. Each data set consists of 1, 2 or 3 runs. Each run was indexed and integrated separately. Subsequently, the mod-

ule ANY of EVAL15 was used for merging the different runs of one data set. The SXRD data at 250 K could successfully be indexed by the F -centered cubic lattice of CuV_2S_4 , with $a = 9.8203(5)$ Å (Table A2).

Table A2: Crystallographic data of crystal A of batch KK271 of CuV_2S_4 at various temperatures. The modulation wave vector in the F -centered setting is $\mathbf{q} = (\sigma, \sigma, 0)$.

Temperature (K)	250	90	80
Crystal system	Cubic	Orthorhombic	Orthorhombic
(Super)space group No. [79]	227	44.1.12.4	44.1.12.4
(Super)space group	$Fd\bar{3}m$	$Imm2(\sigma 00)000$	$Imm2(\sigma 00)000$
Setting	F -centered	F -centered	F -centered
a (Å)	9.8203(5)	9.7762(2)	9.7711(4)
b (Å)	9.8203	9.7762	9.7711
c (Å)	9.8203	9.7736(4)	9.7664(4)
γ_F (deg)	90	89.984(2)	89.987(2)
Volume (Å ³)	941.87(15)	934.10(6)	932.44(8)
σ	–	0.7595 (3)	0.7517 (2)
Z	8	8	8
Wavelength (Å)	0.495935	0.495935	0.495935
Detector distance (mm)	90	90	90
2θ -offset (deg)	0	0	0
χ -offset (deg)	-60	-60	-60
Rotation per image (deg)	1	1	1
$(\sin(\theta)/\lambda)_{max}$ (Å ⁻¹)	0.71099	0.72136	0.72219
Absorption, μ (mm ⁻¹)	3.505	3.553	3.560
T_{min}, T_{max}	0.1124, 0.3028	0.1694, 0.3268	0.1773, 0.3257
Number of main reflections			
measured	1667	2588	2832
unique (obs/all)	70/84	986/1334	1087/1441
Number of satellites			
measured	–	33092	35224
unique (obs/all)	–	1383/4918	1970/4994
R_{int} main (obs/all)	0.0608/0.0615	0.0349/0.0352	0.0290/0.0291
R_{int} sat (obs/all)	–	0.1046/0.1381	0.1042/0.1488
No. of parameters	8	50	50
R_F main (obs)	0.0327	0.0761	0.0708
R_F sat (obs)	–	0.0664	0.0764
wR_{F^2} main (all)	0.0389	0.0949	0.0903
wR_{F^2} sat (all)	–	0.0856	0.0923
GoF (obs/all)	2.56/2.31	2.65/1.66	2.90/2.05
$\Delta\rho_{min}, \Delta\rho_{max}$ (e Å ⁻³)	-0.75, 0.5	-2.66, 3.37	-2.77, 3.42

For all data sets at 90 K and below, the main reflections were surrounded by

twelve first-order satellite reflections, described by six modulation wave vectors, given in Table A3.

Table A3: Six modulation wave vectors describing the twelve satellite reflections at positions $\pm\mathbf{q}^j$ around the main reflections. The domain number gives the assignment to the orthorhombic domain.

q.no.	Modulation wavevector, q	Domain.no
\mathbf{q}^1	$(\sigma, \sigma, 0)$	1
\mathbf{q}^2	$(-\sigma, \sigma, 0)$	2
\mathbf{q}^3	$(\sigma, 0, \sigma)$	3
\mathbf{q}^4	$(-\sigma, 0, \sigma)$	4
\mathbf{q}^5	$(0, \sigma, \sigma)$	5
\mathbf{q}^6	$(0, -\sigma, \sigma)$	6

Three out of these six vectors are independent, for which we have chosen \mathbf{q}^2 , \mathbf{q}^4 and \mathbf{q}^5 (Table A3). The other three modulation wave vectors are related to the first three by

$$\begin{aligned}
 \mathbf{q}^1 &= \mathbf{q}^5 - \mathbf{q}^4 = (\sigma \mathbf{a}_F^* + \sigma \mathbf{b}_F^* + 0 \mathbf{c}_F^*) \\
 \mathbf{q}^3 &= \mathbf{q}^5 - \mathbf{q}^2 = (\sigma \mathbf{a}_F^* + 0 \mathbf{b}_F^* + \sigma \mathbf{c}_F^*) \\
 \mathbf{q}^6 &= \mathbf{q}^4 - \mathbf{q}^2 = (0 \mathbf{a}_F^* - \sigma \mathbf{b}_F^* + \sigma \mathbf{c}_F^*)
 \end{aligned}
 \tag{A6}$$

Accordingly, all Bragg reflections can be indexed by six integer indices (h, k, l, m_1, m_2, m_3) with respect to

$$\{\mathbf{a}_F^*, \mathbf{b}_F^*, \mathbf{c}_F^*, \mathbf{q}^2, \mathbf{q}^4, \mathbf{q}^5\}.
 \tag{A7}$$

SADABS does not allow to simultaneously handle twinning and an incommensurate modulation. For integration and absorption correction of the intensities of Bragg reflections we have, therefore, employed the incommensurate options in EVAL15 and SADABS [50, 51]. Reflections were indexed with six integers according to the F -centered lattice and three modulation wave vectors (Eq. A7 and Table A4).

Table A4: Indexing of the twelve satellite reflections surrounding one main reflection. Information is given for (i) the cubic indexing (h, k, l, m_1, m_2, m_3) (Eq. A7), and (ii) the orthorhombic indexing (h, k, l, m) .

Sr.no	m, n, p			Modulation wavevector, \mathbf{q}	Type	Domain No.	m'
1	1	0	0	$(-\sigma, \sigma, 0)$	\mathbf{q}^2	2	1
2	0	1	0	$(-\sigma, 0, \sigma)$	\mathbf{q}^4	4	1
3	0	0	1	$(0, \sigma, \sigma)$	\mathbf{q}^5	5	1
4	-1	0	0	$(\sigma, -\sigma, 0)$	$-\mathbf{q}^2$	2	-1
5	0	-1	0	$(\sigma, 0, -\sigma)$	$-\mathbf{q}^4$	4	-1
6	0	0	-1	$(0, -\sigma, -\sigma)$	$-\mathbf{q}^5$	5	-1
7	1	-1	0	$(0, \sigma, -\sigma)$	$-\mathbf{q}^6$	6	-1
8	0	1	-1	$(-\sigma, -\sigma, 0)$	$-\mathbf{q}^1$	1	-1
9	1	0	-1	$(-\sigma, 0, -\sigma)$	$-\mathbf{q}^3$	3	-1
10	-1	1	0	$(0, -\sigma, \sigma)$	\mathbf{q}^6	6	1
11	0	-1	1	$(\sigma, \sigma, 0)$	\mathbf{q}^1	1	1
12	-1	0	1	$(\sigma, 0, \sigma)$	\mathbf{q}^3	3	1

Equivalent reflections for computation of scaling and absorption correction have been defined by point symmetry $\bar{1}$, as this is the symmetry of the diffraction pattern, in the general case of a multiply twinned CDW phase of orthorhombic symmetry.

Under the assumption that the basic structures of the CDW phases will have symmetries according to a subgroup of the cubic space group $Fd\bar{3}m$, the subgroup of highest symmetry (index 3) is tetragonal $I4_1/amd$ (No. 141 in [78]). A tentative symbol for this space group in the F -centered setting is $F4_1/ndm$. Two fundamentally different orthorhombic symmetries exist as subgroups of $I4_1/amd$. $Imma$ (No. 74) and its acentric subgroup $Imm2$ (No. 44) contain mirror planes and rotation axes perpendicular to the face diagonals of the F -centered cubic unit cell, while $Fddd$ (No. 70) contains the mirror planes and rotation axes perpendicular to the axes of the F -centered cubic unit cell. The tetragonal symmetries contain both types of symmetry operators.

In case cubic symmetry would be preserved in the CDW phases, the modulation would be three dimensional (Eq. A7), and reflections are indexed by six integers. Three domains exist in case of tetragonal symmetry, whereby satellite reflections (Table A3) are pairwise assigned to each of the three domains. For example, \mathbf{q}^1 and \mathbf{q}^2 belong to one tetragonal domain. Six domains exist in case of $Imma$ symmetry, whereby each satellite reflection belongs to one domain (Table A4). Further reduction towards non-centrosymmetric $Imm2$ symmetry makes each satellite reflection to have contributions from a pair of inversion domains. Orthorhombic symmetry $Fddd$ is different from those considered above, since each of the six domains contains the same pair of reflections as a tetragonal domain does, while each satellite belongs to two different orthorhombic domains: those two that are related by a

fourfold rotation. Due to the small lattice distortions, all main Bragg reflections have contributions from all domains.

We have tested the point symmetry of the diffraction pattern according to different superspace groups for the CDW phases. Table A5 clearly demonstrates that the true symmetry of the incommensurate CDW phase at 80 K is orthorhombic mmm or $mm2$, while it invalidates tetragonal and cubic symmetries.

Table A5: Averaging diffraction data in orthorhombic and tetragonal point symmetries for data obtained in the incommensurate CDW phase at 80 K. Provided are the values for R_{int} for separate reflection groups of main reflections and of satellite reflections, R_σ and the number of measured and unique reflections.

Superspace group	$I4_1/amd(\sigma 0 0)0000(0 \sigma 0)0000$	$Imm2(\sigma 0 0)000$
Main reflections		
Point symmetry	mmm	$\bar{1}$
Number measured	2616	2832
Number unique (obs/all)	310/362	1089/1441
R_{int}^{obs} (main)	0.0728	0.0291
R_σ^{obs} (main)	0.0134	0.0239
Satellite reflections		
Point symmetry	$4/mmm$	mmm
Number measured	34264	35224
Number unique (obs/all)	1235/2469	1922/4994
R_{int}^{obs} (sat)	0.4870	0.1042
R_σ^{obs} (sat)	0.1821	0.1166

Similar results have been obtained for data measured at other temperatures and data measured for the commensurate phase. This test is not possible for powder diffraction data, but the result of the present test is in agreement with the superspace group proposed by Kawaguchi *et al.* [32].

A4 Structure refinements and crystal structures of the incommensurate and commensurate CDW phases of crystal A

Structure refinements have been performed with Jana2006 [56] for each of the six data sets. The cubic spinel structure of CuV_2S_4 provides an excellent fit to the diffraction data measured at 250 K (Table A2).

The incommensurate CDW exists at 90, 80 and 60 K. We could successfully refine a structure model comprising first-order harmonics for displacive modulation

of all atoms (Tables A2 and A6).

Table A6: Crystallographic data of crystal A of batch KK271 of CuV_2S_4 at temperatures of 20, 40 and 60 K. The modulation wave vector in the F -centered setting is $\mathbf{q} = (\sigma, \sigma, 0)$.

Temperature (K)	60	40	20
Crystal system	Orthorhombic	Orthorhombic	Orthorhombic
(Super)space group No. [79]	44.1.12.4	44.1.12.4	44.1.12.4
(Super)space group	$Imm2(\sigma 00)000$	$Imm2(\sigma 00)000$	$Imm2(\sigma 00)000$
Setting	F -centered	F -centered	F -centered
a (Å)	9.7728(14)	9.7743(3)	9.7592(3)
b (Å)	9.7728	9.7743	9.7592
c (Å)	9.7738(13)	9.7726(5)	9.7576(4)
γ_F (deg)	89.996(4)	90.012(3)	89.993(2)
Volume (Å ³)	933.48(26)	933.63(8)	929.32(6)
σ	0.7370 (3)	0.6702 (4)	0.6733 (3)
Z	8	8	8
Detector distance (mm)	90	90	90
$2\theta_{offset}$ (deg)	0	0	0
χ_{offset} (deg)	-60	-60	-60
Rotation per image (deg)	1	1	1
$(\sin(\theta)/\lambda)_{max}$ (Å ⁻¹)	0.72250	0.72088	0.72139
Absorption, μ (mm ⁻¹)	3.556	3.555	3.572
T_{min}, T_{max}	0.1488, 0.3268	0.1681, 0.3269	0.2693, 0.3254
Wavelength (Å)	0.495935	0.495935	0.495935
Number of main reflections			
measured	2661	2664	2638
Unique (obs/all)	1015/1351	1046/1358	955/1350
R_{int} main (obs/all)	0.0310/0.0311	0.0304/0.0305	0.0400/0.0402
Number of satellites			
measured	32991	33120	32968
unique (obs/all)	2091/4929	2873/4921	1026/4918
R_{int} sat (obs/all)	0.0970/0.1230	0.1111/0.1219	0.2384/0.2842
No. of parameters	50	50	50
R_F main (obs)	0.0755	0.0825	0.0847
R_F sat (obs)	0.0831	0.0461	0.0779
wR_{F^2} main (all)	0.0956	0.1032	0.0931
wR_{F^2} sat (all)	0.1028	0.0572	0.1073
GoF (obs/all)	3.02/2.18	2.81/2.23	2.37/1.36
$\Delta\rho_{min}, \Delta\rho_{max}$ (e Å ⁻³)	-2.55, 3.31	-2.28, 2.11	-2.24, 1.98

The relatively high values of about $R_F \approx 0.07$ are due to a yet unresolved scaling problem at beamline P24. The much better value for the refinement of the cubic structure is the result of averaging many more reflections. Their less than perfect agreement then results in a high value for R_{int} .

The result of indexing the different data sets has resulted in modulations with $\sigma = 0.6702$ or $\sigma = 0.6733$ at 40 and 20 K, clearly different from the incommensurate modulations at 60–90 K, but also significantly different from commensurate $\frac{2}{3}$. However, a stronger test for commensurability is provided by structure refinements, since the calculated intensities of Bragg reflections is different for commensurate and incommensurate modulations with otherwise equal amplitudes. For the data measured at 40 K, these refinements lead to a fit to the satellite reflections that is clearly better for the commensurate model than for the incommensurate model (Table A7).

Table A7: Structure refinements against data measured at 40 K in superspace group $Imm2(\sigma 00)000$. The commensurate model leads to a better fit to the data than the incommensurate model does.

	incommensurate	commensurate
σ	0.6702 (4)	$\frac{2}{3}$
Order of harmonics	1	1
t_0	–	$\frac{1}{6}$
Main reflections		
number (obs/all)	1046/1358	1046/1358
R_F^{obs} (main)	0.0830	0.0825
Satellite reflections		
number (obs/all)	2873/4921	2873/4921
R_F^{obs} (sat)	0.0959	0.0461
wR_{F^2} (all)	0.1063	0.0938

For the data at 60–90 K as well as for the data measured on crystals B–D, the incommensurate model gave a better fit.

The modulation function $\mathbf{u}(\bar{x}_{s4}) = (u_x(\bar{x}_{s4}), u_y(\bar{x}_{s4}), u_z(\bar{x}_{s4}))$ for displacement modulation is defined as

$$u_\alpha(\bar{x}_{s4}) = \sum_{n=1}^{n_{max}} \{A_{n,\alpha} \sin(2\pi n \bar{x}_{s4}) + B_{n,\alpha} \cos(2\pi n \bar{x}_{s4})\}, \quad (\text{A8})$$

for $\alpha = x, y, z$. $n = 1, \dots, n_{max}$ enumerates the harmonics. Kawaguchi *et al.* [32] have proposed a structure model with up to second harmonic modulation functions ($n_{max} = 2$). We can also refine such a model against our SXRD data. Although this leads to a considerable improvement of the fit, second-harmonic modulation

amplitudes ($n = 2$ in Eq. A8) are mostly insignificant in view of their standard uncertainties. This matches the generally accepted rule, that harmonics of modulation functions cannot be refined in a meaningful way for orders that go beyond the highest order of measured satellite reflections. Employing modulated ADPs or anharmonic ADPs did not lead to significant improvements either. It is noticed that the structure model obtained by Rietveld refinement against XRPD data suffers from large standard uncertainties on the modulation parameters [32], that are considerably larger than the present standard uncertainties. The atomic coordinates, ADPs and modulation parameters for the present models with single-harmonic modulation functions ($n_{max} = 1$) are summarized in Tables A8–A10.

Table A8: Structural parameters for the cubic spinel structure of annealed crystal A of CuV_2S_4 at 250 K. Given are the fractional coordinates x , y , z of the atoms, as well as their anisotropic displacement parameters (ADPs) U_{ij} ($i, j = 1, 2, 3$) and the equivalent isotropic displacement parameter U_{iso}^{eq} .

Atom	x	y	z	U_{11}	U_{22}	U_{33}	U_{12}	U_{13}	U_{23}	U_{iso}^{eq}
Cu	0	0	0	0.0208(7)	0.0208	0.0208	0	0	0	0.0208(2)
V	0.625	0.625	0.625	0.0270(6)	0.0270	0.0270	0.0076(6)	0.0076	0.0076	0.0270(2)
S	0.38099(9)	0.38099	0.38099	0.0201(6)	0.0200	0.0200	-0.0010(4)	-0.0010	-0.0010	0.0201(2)

Table A9: Atomic coordinates x , y , z and anisotropic ADPs of the orthorhombic basic structure of annealed crystal A in the incommensurate CDW phase at 90, 80 and 60 K and in the commensurate CDW phase at 40 and 20 K.

Atom	x	y	z	U_{11}	U_{22}	U_{33}	U_{12}	U_{13}	U_{23}	U_{iso}^{eq}
crystal A at $T = 90$ K										
Cu1	0	0	0	0.0098(1)	0.0098	0.0098	0	0	0	0.00983(4)
Cu2	0.25	0.25	0.2514(3)	0.0098	0.0098	0.0098	0	0	0	0.00983
V1	0.1250(4)	-0.1250	0.3750(7)	0.0118	0.0118	0.0118	-0.0030	-0.0030	0.0030	0.01178
V2	0.1281(3)	0.1281	0.6288(5)	0.0118(1)	0.0118	0.0118	0.0030(1)	0.0030	0.0030	0.01178(5)
S1	0.1316(5)	-0.1316	0.1278(7)	0.0105(1)	0.0105	0.0105	-0.0003(1)	0.0003	-0.0003	0.01050(4)
S2	0.1202(4)	-0.1202	0.6156(7)	0.0105	0.0105	0.0105	-0.0003	0.0003	-0.0003	0.01052
S3	0.1168(4)	0.1168	0.3779(7)	0.0105	0.0105	0.0105	0.0003	-0.0003	-0.0003	0.01052
S4	0.3704(4)	0.3704	0.8664(8)	0.0105	0.0105	0.0105	0.0003	0.0003	0.0003	0.01052
crystal A at $T = 80$ K										
Cu1	0	0	0	0.0104(1)	0.0104	0.0104	0	0	0	0.01042(4)
Cu2	0.25	0.25	0.2512(3)	0.0104	0.0104	0.0104	0	0	0	0.01042
V1	0.1249(3)	-0.1249	0.3738(5)	0.0115	0.0115	0.0115	-0.00210	-0.00210	0.00210	0.01145
V2	0.1283(3)	0.1283	0.6289(4)	0.0115(1)	0.0115	0.0115	0.00210(9)	0.00210	0.00210	0.01145(4)
S1	0.1317(3)	-0.1317	0.1265(6)	0.0106(1)	0.0106	0.0106	-0.0002(1)	0.0002	-0.0002	0.01058(4)
S2	0.1200(1)	-0.1200	0.6152(6)	0.0106	0.0106	0.0106	-0.0002	0.0002	-0.0002	0.01058
S3	0.1169(3)	0.1169	0.3790(7)	0.0106	0.0106	0.0106	0.0002	-0.0002	-0.0002	0.01058
S4	0.3708(3)	0.3708	0.8675(7)	0.0106	0.0106	0.0106	0.0002	0.0002	0.0002	0.01058
crystal A at $T = 60$ K										
Cu1	0	0	0	0.0101(1)	0.0101	0.0101	0	0	0	0.01009(5)
Cu2	0.25	0.25	0.2512(4)	0.0101	0.0101	0.0101	0	0	0	0.01009
V1	0.1253(4)	-0.1253	0.3743(7)	0.0111	0.0111	0.0111	-0.00206	-0.00206	0.00206	0.01112
V2	0.1285(3)	0.1285	0.6291(5)	0.0111(1)	0.0111	0.0111	0.00206(9)	0.00206	0.00206	0.01112(4)
S1	0.1313(4)	-0.1313	0.1282(8)	0.0101(1)	0.0101	0.0101	-0.0002(1)	0.0002	-0.0002	0.01007(4)
S2	0.1197(4)	-0.1197	0.6174(7)	0.0101	0.0101	0.0101	-0.0002	0.0002	-0.0002	0.01007
S3	0.1170(4)	0.1170	0.3800(7)	0.0101	0.0101	0.0101	0.0002	-0.0002	-0.0002	0.01007
S4	0.3704(4)	0.3704	0.8686(8)	0.0101	0.0101	0.0101	0.0002	0.0002	0.0002	0.01007
crystal A at $T = 40$ K										
Cu1	0	0	0	0.0100(1)	0.0100	0.0100	0	0	0	0.01026(4)
Cu2	0.25	0.25	0.2503(4)	0.0101	0.0101	0.0101	0	0	0	0.01026
V1	0.1228(2)	-0.1228	0.3767(5)	0.0116	0.0116	0.0116	-0.00216	-0.00216	0.00216	0.01162
V2	0.1246(1)	0.1246	0.6263(4)	0.0116(1)	0.0116	0.0116	0.00216(9)	0.00216	0.00216	0.01162(4)
S1	0.1310(2)	-0.1310	0.1305(6)	0.0102(1)	0.0102	0.0102	0.00028(8)	-0.00028	0.00028	0.01017(4)
S2	0.1188(2)	-0.1188	0.6206(6)	0.0102	0.0102	0.0102	0.00028	-0.00028	0.00028	0.01017
S3	0.1193(2)	0.1193	0.3816(5)	0.0102	0.0102	0.0102	-0.00028	0.00028	0.00028	0.01017
S4	0.3682(2)	0.3682	0.8705(5)	0.0102	0.0102	0.0102	-0.00028	-0.00028	-0.00028	0.01017
crystal A at $T = 20$ K										
Cu1	0	0	0	0.0086(1)	0.0086	0.0086	0	0	0	0.00864(5)
Cu2	0.25	0.25	0.2504(6)	0.0086	0.0086	0.0086	0	0	0	0.00864
V1	0.1230(3)	-0.1230	0.3769(7)	0.0107	0.0107	0.0107	-0.0033	-0.0033	0.0033	0.01072
V2	0.1250(2)	0.1250	0.6265(6)	0.0107(1)	0.0107	0.0107	0.0033(1)	0.0033	0.0033	0.01072(5)
S1	0.1312(3)	-0.1312	0.1312(10)	0.0089(1)	0.0089	0.0089	0.0002(1)	-0.0002	0.0002	0.00891(4)
S2	0.1187(4)	-0.1187	0.6207(10)	0.0089	0.0089	0.0089	0.0002	-0.0002	0.0002	0.00891
S3	0.1195(3)	0.1195	0.3826(9)	0.0089	0.0089	0.0089	-0.0002	0.0002	0.0002	0.00891
S4	0.3691(3)	0.3691	0.8708(8)	0.0089	0.0089	0.0089	-0.0002	-0.0002	-0.0002	0.00891

Table A10: Amplitudes for the displacement modulation of crystal A at 20, 40, 60, 80 and 90 K. Modulation amplitudes are given according to Eq. A8 and they are multiplied by the corresponding lattice parameter to result in values in Å.

Atom	$A_{1,x} a$ (Å)	$A_{1,y} b$ (Å)	$A_{1,z} c$ (Å)	$B_{1,x} a$ (Å)	$B_{1,y} b$ (Å)	$B_{1,z} c$ (Å)
crystal A at $T = 90$ K						
Cu1	-0.0501(23)	-0.0501	0	0	0	0.0578(27)
Cu2	0.0497(23)	0.0497	0	0	0	0.0630(26)
V1	0.0007(28)	0.0007	0	-0.0928(9)	0.0928	0.0878(14)
V2	-0.0320(28)	-0.0320	-0.0488(34)	-0.0761(9)	-0.0761	-0.0877(14)
S1	-0.0376(25)	-0.0376	0	0.0093(34)	-0.0093	0.0457(37)
S2	0.0407(25)	0.0407	0	0.0118(33)	-0.0118	0.0335(37)
S3	0.0375(27)	0.0375	-0.0026(35)	0.0160(30)	0.0160	-0.0325(41)
S4	-0.0414(27)	-0.0414	-0.0024(35)	-0.0299(29)	-0.0299	-0.0435(40)
crystal A at $T = 80$ K						
Cu1	-0.0553(20)	-0.0553	0	0	0	0.0595(23)
Cu2	0.0531(20)	0.0531	0	0	0	0.0677(22)
V1	-0.0005(23)	-0.0005	0	-0.0980(8)	0.0980	0.0915(12)
V2	-0.0342(23)	-0.0342	-0.0495(28)	-0.0802(8)	-0.0802	-0.0924(12)
S1	-0.0422(20)	-0.0422	0	0.0112(28)	-0.0112	0.0497(31)
S2	0.0414(20)	0.0414	0	0.0119(26)	-0.0119	0.0322(31)
S3	0.0396(23)	0.0396	-0.0055(31)	0.0189(26)	0.0189	-0.0340(36)
S4	-0.0441(22)	-0.0441	-0.0018(31)	-0.0291(25)	-0.0291	-0.0480(35)
crystal A at $T = 60$ K						
Cu1	-0.0604(23)	-0.0604	0	0	0	0.0605(28)
Cu2	0.0563(23)	0.0563	0	0	0	0.0682(26)
V1	-0.0029(26)	-0.0029	0	-0.1038(9)	0.1038	0.0943(14)
V2	-0.0376(27)	-0.0376	-0.0518(32)	-0.0838(9)	-0.0838	-0.0963(14)
S1	-0.0421(23)	-0.0421	0	0.0087(33)	-0.0087	0.0482(39)
S2	0.0397(24)	0.0397	0	0.0161(31)	-0.0161	0.0309(39)
S3	0.0399(26)	0.0399	-0.0065(34)	0.0196(32)	0.0196	-0.0354(44)
S4	-0.0468(26)	-0.0468	-0.0016(35)	-0.0309(30)	-0.0309	-0.0528(43)
crystal A at $T = 40$ K						
Cu1	-0.0623(10)	-0.0623	0	0	0	-0.0094(13)
Cu2	0.0727(9)	0.0727	0	0	0	0.1174(13)
V1	0.0143(10)	0.0143	0	-0.1042(8)	0.1042	0.0909(13)
V2	-0.0794(11)	-0.0794	-0.0818(21)	-0.0771(8)	-0.0771	-0.0963(12)
S1	-0.0516(11)	-0.0516	0	-0.0183(13)	0.0183	0.0373(21)
S2	0.0128(11)	0.0128	0	0.0444(13)	-0.0444	0.0327(20)
S3	0.0472(12)	0.0472	-0.0495(20)	0.0220(14)	0.0220	-0.0372(20)
S4	-0.0403(13)	-0.0403	0.0454(24)	-0.0352(14)	-0.0352	-0.0533(19)
crystal A at $T = 20$ K						
Cu1	-0.0575(16)	-0.0575	0	0	0	-0.0049(21)
Cu2	0.0648(15)	0.0648	0	0	0	0.1062(22)
V1	0.0140(18)	0.0140	0	-0.0964(13)	0.0966	0.0841(21)
V2	-0.0707(19)	-0.0707	-0.0765(35)	-0.0716(13)	-0.0718	-0.0931(20)
S1	-0.0473(19)	-0.0473	0	-0.0137(22)	0.0138	0.0353(35)
S2	0.0117(19)	0.0117	0	0.0383(22)	-0.0383	0.0322(33)
S3	0.0453(21)	0.0453	-0.0449(33)	0.0183(23)	0.0183	-0.0350(31)
S4	-0.0377(22)	-0.0377	0.0403(41)	-0.0324(23)	-0.0325	-0.0501(31)

A5 X-ray diffraction at the SNBL of the ESRF

Single-crystal X-ray diffraction (SXRD) of as-grown CuV_2S_4 was measured at station BM01 of the Swiss-Norwegian Beamlines (SNBL) at the European Synchrotron Radiation Facility (ESRF), Grenoble, employing radiation of a wave length of $\lambda_{\text{SNBL}} = 0.67760 \text{ \AA}$. Diffracted X rays were detected by a Pilatus 2M area detector placed perpendicular to the beam and shifted vertically by 80 mm out of the center. The temperature of the sample was regulated with a open-flow nitrogen cryostat (80–295 K) in the first experiment on crystal B, and an open-flow helium cryostat (4–35 K) in the second experiment on crystals C, D and E.

Diffracted intensity was collected on the detector during 0.1 s for a rotation of the crystal by 0.1 deg. Each run of data collection comprises 3640 of these frames, corresponding to a total rotation of the crystal by 364 deg. Each run was repeated up to ten times. The raw data were binned, *i.e.* intensity values were added on a pixel by pixel basis, in time and rotation, resulting in data sets of 360 frames of effectively 1 deg of rotation, that were used for data processing. Several data sets comprise two runs as measured with and without an attenuator in the primary beam.

Crystal B of dimensions $0.12 \times 0.11 \times 0.11 \text{ mm}^3$ was selected from batch KK3 of as-grown crystals of CuV_2S_4 . The first experiment employed an open-flow nitrogen cryostat that limited the lowest temperature to 80 K.

Three more crystals were used for experiments employing an open-flow helium cryostat. Crystal C from batch KK5 has dimensions $0.2 \times 0.2 \times 0.2 \text{ mm}^3$. Crystal D from batch KK5 has dimensions $0.19 \times 0.17 \times 0.19 \text{ mm}^3$. Crystal E, also from batch KK5 has dimensions $0.1 \times 0.075 \times 0.1 \text{ mm}^3$.

The lowest stable temperature was about 5 K, while the highest stable temperature was about 25–35 K, thus leaving a gap between 35 and 80 K that could not be reached in our experiment.

A6 Data processing of SXRD data of crystals B–E

Data processing was performed with the software EVAL15 [50]. Absorption correction was applied by the software SADABS [51]. Each data set consists of 1 or 2 runs with different attenuators in the primary beam. Each run was indexed and integrated separately. Subsequently, the module ANY of EVAL15 was used for merging the different runs of one data set. Indexing and refinement of lattice parameters and components of modulation wave vectors as well as integration of Bragg reflections was performed in complete analogy to the data processing of SXRD measured at beam line P24 on crystal A (Section A3).

The SXRD data of as-grown crystal B at the nine measured temperatures between 85 and 95 K could successfully be indexed by the F -centered cubic lattice of CuV_2S_4 , with $a \approx 9.766$ Å (Table A11).

Table A11: Lattice parameters of the F -centered setting of crystal B at temperatures of 80–95 K. The modulation wave vector in the F -centered setting is $\mathbf{q} = (\sigma, \sigma, 0)$ with satellite reflections observed for 80–84 K only. N_{ref} gives the number of reflections used for indexing

T (K)	N_{ref}	a (Å)	c (Å)	γ_F (deg)	σ	V (Å ³)
80	6566/6579	9.7749(3)	9.7588(5)	89.945(3)	0.7625(2)	932.45(8)
81	6487/6511	9.7748(3)	9.7596(4)	89.961(3)	0.7622(2)	932.50(7)
82	6564/6581	9.7742(3)	9.7596(5)	89.958(3)	0.7625(2)	932.38(8)
83	6412/6432	9.7741(3)	9.7591(5)	89.960(2)	0.7629(2)	932.29(7)
84	6434/6441	9.7715(4)	9.7587(5)	89.959(3)	0.7659(2)	931.79(10)
85	2047/2050	9.7667(4)	9.7654(5)	89.994(3)	–	931.50(7)
87	2048/2049	9.7666(4)	9.7669(5)	90.002(4)	–	931.64(8)
88	2042/2045	9.7680(3)	9.7659(5)	89.994(3)	–	931.81(7)
89	2054/2055	9.7670(2)	9.7653(4)	89.981(3)	–	931.54(5)
91	2062/2063	9.7653(3)	9.7635(5)	89.987(4)	–	931.06(7)
92	2055/2056	9.7650(3)	9.7631(4)	90.003(4)	–	930.96(6)
93	2051/2051	9.7643(3)	9.7636(5)	89.988(3)	–	930.87(8)
94	2052/2055	9.7656(4)	9.7630(4)	89.996(3)	–	931.08(8)
95	2054/2054	9.7655(3)	9.7643(5)	90.009(4)	–	931.19(7)

Crystal B is in the incommensurately modulated phase at temperatures 80–84 K (Table A11). Details of the data processing are summarized in Tables A12–A14.

Table A12: Crystallographic data of crystal B of batch KK3 of CuV_2S_4 at various temperatures. The modulation wave vector in the F centered setting is $\mathbf{q} = (\sigma, \sigma, 0)$.

Temperature (K)	95	85	84
Crystal	B	B	B
Crystal system	Cubic	Cubic	Orthorhombic
(Super)space group No. [79]	227	227	44.1.12.4
(Super)space group	$Fd\bar{3}m$	$Fd\bar{3}m$	$Imm2(\sigma 00)000$
Setting	F -centered	F -centered	F -centered
a (Å)	9.7655(3)	9.7667(4)	9.7715(4)
b (Å)	9.7655	9.7667	9.7715
c (Å)	9.7655	9.7667	9.7587(5)
γ_F (deg)	90	90	89.959(3)
Volume (Å ³)	931.19(7)	931.50(7)	931.79(10)
σ	–	–	0.7659(2)
Z	8	8	8
Wavelength (Å)	0.67760	0.67760	0.67760
Detector distance (mm)	146	146	146
Vertical detector shift (mm)	80	80	80
$2\theta_{offset}$ (deg)	0	0	0
Rotation per image (deg)	0.1	0.1	0.1
No. of raw images	3640	3640	3640
No. of binned images to 1 deg	364	364	364
Exposure time (s)	0.1	0.1	0.1
$(\sin(\theta)/\lambda)_{max}$ (Å ⁻¹)	0.786625	0.786504	0.786375
Absorption, μ (mm ⁻¹)	8.666	8.662	8.660
T_{min}, T_{max}	0.7528, 0.8623	0.7802, 0.8623	0.8303, 0.8623
Number of main reflections			
measured	1360	1252	1282
Unique (obs/all)	85/107	85/101	672/510
Number of satellites			
measured	–	–	15891
Unique (obs/all)	–	–	224/4238
R_{int} main (obs/all)	0.0257/0.0260	0.0216/0.0217	0.0118/0.0119
R_{int} sat (obs/all)	–	–	0.1793/0.2300
No. of parameters	8	8	50
R_F main (obs)	0.0188	0.0150	0.0169
R_F sat (obs)	–	–	0.0620
wR_{F2} main (all)	0.0205	0.0213	0.0230
wR_{F2} sat (all)	–	–	0.0922
GoF (obs/all)	1.40/1.25	1.74/1.58	1.34/0.55
$\Delta\rho_{min}, \Delta\rho_{max}$ (e Å ⁻³)	-0.91, 0.67	-0.30, 0.41	-0.41, 0.43

Table A13: Crystallographic data of crystal B of batch KK3 of CuV_2S_4 at various temperatures. The modulation wave vector in the F -centered setting is $\mathbf{q} = (\sigma, \sigma, 0)$.

Temperature (K)	83	82	81
Crystal	B	B	B
Crystal system	Orthorhombic	Orthorhombic	Orthorhombic
(Super)space group No. [79]	44.1.12.4	44.1.12.4	44.1.12.4
(Super)space group	$Imm2(\sigma 00)000$	$Imm2(\sigma 00)000$	$Imm2(\sigma 00)000$
Setting	F -centered	F -centered	F -centered
a (Å)	9.7741(3)	9.7742(3)	9.7748(3)
b (Å)	9.7741	9.7742	9.7748
c (Å)	9.7591(5)	9.7596(5)	9.7596(4)
γ_F (deg)	89.960(2)	89.958(3)	89.961(3)
Volume (Å ³)	932.29(7)	932.38(8)	932.50(7)
σ	0.7629 (2)	0.7625 (2)	0.7622 (2)
Z	8	8	8
Wavelength (Å)	0.67760	0.67760	0.67760
Detector distance (mm)	146	146	146
Vertical detector shift (mm)	80	80	80
$2\theta_{offset}$ (deg)	0	0	0
Rotation per image (deg)	0.1	0.1	0.1
No. of images	3640	3640	3640
No. of images binned to 1 deg	364	364	364
Exposure time (s)	0.1	0.1	0.1
$(\sin(\theta)/\lambda)_{max}$ (Å ⁻¹)	0.782176	0.771525	0.771522
Absorption, μ (mm ⁻¹)	8.654	8.654	8.653
T_{min}, T_{max}	0.8505, 0.8623	0.8256, 0.8623	0.8302, 0.8623
Number of main reflections			
Measured	1259	1183	1151
Unique (obs/all)	514/661	481/631	472/618
Number of satellite reflections			
Measured	15446	16087	16069
Unique (obs/all)	1150/4129	1186/4277	1366/4273
R_{int} main (obs/all)	0.0090/0.0091	0.0098/0.0099	0.0119/0.0128
R_{int} sat (obs/all)	0.0981/0.1197	0.1018/0.1213	0.1087/0.1246
No. of parameters	50	50	50
R_F main (obs)	0.0164	0.0209	0.0200
R_F sat (obs)	0.0614	0.0670	0.0683
wR_{F2} main (all)	0.0231	0.0342	0.0336
wR_{F2} sat (all)	0.0775	0.0821	0.0827
GoF (obs/all)	1.22/0.80	1.57/0.97	1.55/1.02
$\Delta\rho_{min}, \Delta\rho_{max}$ (e Å ⁻³)	-0.86, -1.01	-1.19, 1.16	-1.47, 1.36

Table A14: Crystallographic data of CuV_2S_4 for crystals B, D and C at the indicated temperatures.

Temperature (K)	80	35	25
Crystal	B	D	C
Crystal system	Orthorhombic	Orthorhombic	Orthorhombic
(Super)space group No. [79]	44.1.12.4	44.1.12.4	44.1.12.4
(Super)space group	<i>Imm2</i> ($\sigma 00$)000	<i>Imm2</i> ($\sigma 00$)000	<i>Imm2</i> ($\sigma 00$)000
Setting	<i>F</i> -centered	<i>F</i> -centered	<i>F</i> -centered
<i>a</i> (Å)	9.7749(3)	9.7796(4)	9.7754(4)
<i>b</i> (Å)	9.7749	9.7796	9.7754
<i>c</i> (Å)	9.7588(5)	9.7641(5)	9.7705(4)
γ_F (deg)	89.945(3)	89.949(2)	89.978(4)
Volume (Å ³)	932.45(8)	933.85(7)	933.12(6)
σ	0.7625 (2)	0.7511 (1)	0.7496 (6)
Z	8	8	8
Wavelength (Å)	0.67760	0.67760	0.67760
Detector distance (mm)	146	146	146
Vertical detector shift (mm)	80	64	64
$2\theta_{offset}$ (deg)	0	0	0
Rotation per image (deg)	0.1	0.1	0.1
No. of images	3640	3640	3640
No. of images binned to 1 deg	364	364	364
Exposure time (s)	0.1	0.1	0.1
$(\sin(\theta)/\lambda)_{max}$ (Å ⁻¹)	0.771403	0.635308	0.630880
Absorption, μ (mm ⁻¹)	8.653	8.640	8.647
T_{min}, T_{max}	0.8094, 0.8623	0.6899, 0.7452	0.6235, 0.7452
Number of main reflections			
Measured	993	536	760
Unique (obs/all)	424/538	205/297	294/415
Number of satellites			
Measured	16039	10670	10630
Unique (obs/all)	1866/4274	733/2860	179/2843
R_{int} main (obs/all)	0.0113/0.0113	0.0398/0.0399	0.0417/0.0419
R_{int} sat (obs/all)	0.1598/0.1667	0.1857/0.1954	0.2346/0.2801
No. of parameters	50	50	50
R_F main (obs)	0.0263	0.0464	0.0491
R_F sat (obs)	0.0738	0.0896	0.0736
wR_{F^2} main (all)	0.0407	0.0827	0.0735
wR_{F^2} sat (all)	0.0866	0.1074	0.1093
GoF (obs/all)	1.76/1.30	2.15/1.24	2.37/0.90
$\Delta\rho_{min}, \Delta\rho_{max}$ (e Å ⁻³)	-1.83, 1.94	-1.24, 1.35	-1.22, 1.03

SXRD on as-grown crystal D was measured at twelve temperatures between 5 and 35 K in the order 35–20–5–16–5²–20–30–5³–18–24–11–8 K. Formation of ice around or at the crystal was a major problem at these temperatures. As a result of ice problems, SXRD data could not be indexed for four temperatures, while reliable intensity data (as required for structure refinements) could not be obtained at five more temperatures. Crystal data on the remaining three temperatures are summarized in Tables A14 and A15.

Table A15: Crystallographic data of CuV_2S_4 for crystals D and C at the indicated temperatures of 5, 16, 4.4 K and 4.2 K.

Temperature (K)	5	16	4.4	4.2
Crystal	D	D	C	C
Crystal system	Orthorhombic	Orthorhombic	Orthorhombic	Orthorhombic
(Super)space group No. [79]	44.1.12.4	44.1.12.4	44.1.12.4	44.1.12.4
(Super)space group	$Imm2(\sigma 00)000$	$Imm2(\sigma 00)000$	$Imm2(\sigma 00)000$	$Imm2(\sigma 00)000$
Setting	F -centered	F -centered	F -centered	F -centered
a (Å)	9.7697(4)	9.7718(4)	9.7672(4)	9.7746(6)
b (Å)	9.7697	9.7718	9.7672	9.7746
c (Å)	9.7627(4)	9.7702(5)	9.7660(6)	9.7752(4)
γ_F (deg)	89.987(2)	89.981(3)	89.989(4)	89.999(3)
Volume (Å ³)	931.82(6)	932.93(8)	931.54(10)	933.96(7)
σ	0.7289 (3)	0.7476 (3)	0.7290(5)	0.7598 (7)
σ_2				0.6593 (8)
Z	8	8	8	8
Wavelength (Å)	0.67760	0.67760	0.67760	0.67760
Detector distance (mm)	146	146	146	146
Vertical detector shift (mm)	64	64	64	64
$2\theta_{offset}$ (deg)	0	0	0	0
Rotation per image (deg)	0.1	0.1	0.1	0.1
No. of images	3640	3640	3640	3640
No. of images binned to 1 deg	364	364	364	364
Exposure time (s)	0.1	0.1	0.1	0.1
$(\sin(\theta)/\lambda)_{max}$ (Å ⁻¹)	0.633606	0.633256	0.633414	0.632453
Absorption, μ (mm ⁻¹)	8.659	8.640	8.661	8.638
T_{min}, T_{max}	0.6735, 0.7452	0.6899, 0.7452	0.6877, 0.7462	0.6895, 0.7438
Number of main reflections				
Measured	804	510	823	1218
Unique (obs/all)	330/430	197/301	327/439	519/969
Number of satellites				
Measured σ	10629	11033	10597	25980
Measured σ_2				25768
Unique σ (obs/all)	896/2708	357/2907	291/2708	45/5467
Unique σ_2 (obs/all)				45/5467
R_{int} main (obs/all)	0.0146/0.0147	0.0677/0.0806	0.0253/0.0266	0.0620/0.0624
R_{int} sat σ (obs/all)	0.1294/0.1412	0.4237/0.4325	0.2444/0.2972	0.6575/0.7741
R_{int} sat σ_2 (obs/all)				0.6575/0.7741
No. of parameters	50	50	50	–
R_F main (obs)	0.0339	0.0659	0.0415	–
R_F sat (obs)	0.0754	0.1228	0.0926	–
wR_{F2} main (all)	0.0497	0.0824	0.0515	–
wR_{F2} sat (all)	0.0976	0.1687	0.1316	–
GoF (obs/all)	1.91/1.27	1.97/0.84	2.12/0.97	–
$\Delta\rho_{min}, \Delta\rho_{max}$ (e Å ⁻³)	-2.05, 2.09	-2.11, 2.22	-1.54, 1.85	–

It is noticed that crystal D is in the incommensurate CDW phase at all measured temperatures.

SXRD on as-grown crystal C was measured at eight temperatures between 5

and 39 K in the order 4.2–35–25–4.4–39–41–35²–25 K. Indexing was successful for six temperatures, while intensity data suitable for structure refinements could be obtained for 25 and 4.4 K only (Tables A14 and A15).

The pristine crystal was initially cooled down to 4.2 K. At this temperature the SXR D showed the presence of satellite reflections corresponding to both the incommensurate and commensurate CDWs (Table A15). Upon heating to 35 K and cooling again, only the incommensurate CDW remained. Unfortunately, the SXR D data were of insufficient quality for structure refinements.

As-grown crystal E was also cooled to 4.2 K. SXR D showed that crystal E had remained in the non-modulated cubic phase at this temperature, as well as at 30 K. Heating to 53 K with subsequent cooling to 45 K brought crystal E into the incommensurate CDW phase. Again, ice problems caused unreliable intensity data not suitable for structure refinements.

A7 Structure refinements and crystal structures of the incommensurate CDW phases of crystals B–D

Structure refinements have been performed with Jana2006 [56] for all data sets (80–95 K) of crystal B, one data set of crystal C and three data sets of crystal D. The cubic spinel structure of CuV_2S_4 provides an excellent fit to the diffraction data measured at 85–95 K. Here we give details for temperatures of 85 and 95 K only (Table A12). It is noticed that excellent R values are obtained for these data. Structural parameters are summarized in Table A16.

Table A16: Structural parameters for the cubic spinel structure of crystal B of CuV_2S_4 at 85 and 95 K. Given are the fractional coordinates x , y , z of the atoms, as well as their anisotropic ADPs U_{ij} ($i, j = 1, 2, 3$) and the equivalent isotropic displacement parameter U_{iso}^{eq} .

Atom	x	y	z	U_{11}	U_{22}	U_{33}	U_{12}	U_{13}	U_{23}	U_{iso}^{eq}
Crystal B at $T = 95$ K										
Cu	0	0	0	0.0038(2)	0.0038	0.0038	0	0	0	0.00384(8)
V	0.625	0.625	0.625	0.0099(2)	0.0099	0.0099	0.0079(3)	0.0079	0.0079	0.00986(8)
S	0.38085(5)	0.38085	0.38083	0.0034(2)	0.0034	0.0034	-0.0004(2)	-0.0004	-0.0004	0.00345(7)
Crystal B at $T = 85$ K										
Cu	0	0	0	0.0041(2)	0.0041	0.0041	0	0	0	0.00406(8)
V	0.625	0.625	0.625	0.0097(2)	0.0097	0.0097	0.0079(2)	0.0079	0.0079	0.00969(8)
S	0.38083(3)	0.38083	0.38083	0.0033(2)	0.0033	0.0033	-0.0002(1)	-0.0002	-0.0002	0.00339(8)

Crystal B is in the incommensurate phase for temperatures 80–84 K. Main reflections lead to excellent values of less than 2% for both R_{int} and R_F , indicating a high quality of the SXRd data as well as providing evidence for the spinel structure as average structure (Tables A12–A14). Atomic coordinates and ADPs of the basic structure are summarized in Table A16. They are virtually equal to the parameters obtained on crystal A (Table A9).

Table A17: Atomic coordinates x , y , z and ADPs of the basic structure of crystal B in the incommensurate CDW phase at 80–84 K.

Atom	x	y	z	U_{11}	U_{22}	U_{33}	U_{12}	U_{13}	U_{23}	U_{iso}^{eq}
Crystal B at $T = 84$ K										
Cu1	0	0	0	0.00369(4)	0.00369	0.00369	0	0	0	0.00369(1)
Cu2	0.25	0.25	0.2506(1)	0.00369	0.00369	0.00369	0	0	0	0.00369
V1	0.1249(2)	-0.1249	0.3747(3)	0.00759	0.00759	0.00759	-0.00589	-0.00589	0.00589	0.00759
V2	0.1279	0.1279	0.6278	0.00759(5)	0.00759	0.00759	0.00589(3)	0.00589	0.00589	0.00759(2)
S1	0.1308(1)	-0.1308	0.1281(3)	0.00334(3)	0.00334	0.00334	0.00011(4)	-0.00011	0.00011	0.00334(1)
S2	0.1189(1)	-0.1189	0.6168(3)	0.00334	0.00334	0.00334	0.00011(4)	-0.00011	0.00011	0.00334
S3	0.1184(1)	0.1184	0.3791(3)	0.00334	0.00334	0.00334	0.00011(4)	-0.00011	0.00011	0.00334
S4	0.3695(1)	0.3695	0.8675(3)	0.00334	0.00334	0.00334	0.00011(4)	-0.00011	0.00011	0.00334
Crystal B at $T = 83$ K										
Cu1	0	0	0	0.00327(5)	0.00327	0.00327	0	0	0	0.00327(2)
Cu2	0.25	0.25	0.2511(1)	0.00327	0.00327	0.00327	0	0	0	0.00327
V1	0.1250(1)	-0.1250	0.3753(2)	0.00594	0.00594	0.00594	-0.00441	-0.00441	0.00441	0.00594
V2	0.1279(1)	0.1279	0.6290(2)	0.00594(6)	0.00594	0.00594	0.00441(3)	0.00441	0.00441	0.00594(2)
S1	0.1307(1)	-0.1307	0.1285(3)	0.00306(4)	0.00306	0.00306	0.00048(4)	-0.00048	0.00048	0.00306(1)
S2	0.1190(1)	-0.1190	0.6170(2)	0.00306	0.00306	0.00306	0.00048	-0.00048	0.00048	0.00306
S3	0.1182(1)	0.1182	0.3795(2)	0.00306	0.00306	0.00306	0.00048	-0.00048	0.00048	0.00306
S4	0.3699(5)	0.3699	0.8679(2)	0.00306	0.00306	0.00306	-0.00048	-0.00048	-0.00048	0.00306
Crystal B at $T = 82$ K										
Cu1	0	0	0	0.00350(6)	0.00350	0.00350	0	0	0	0.00350(2)
Cu2	0.25	0.25	0.2510(2)	0.00350	0.00350	0.00350	0	0	0	0.00350
V1	0.1254(2)	-0.1254	0.3754(3)	0.00604	0.00604	0.00604	-0.00434	-0.00434	-0.00434	0.00604
V2	0.1278(2)	0.1278	0.6294(2)	0.00604(7)	0.00604	0.00604	0.00434(4)	0.00434	0.00434	0.00604 (2)
S1	0.1305(2)	-0.1305	0.1287(3)	0.00345(5)	0.00345	0.00345	0.00064(5)	-0.00064	0.00064	0.00345(2)
S2	0.1190(2)	-0.1190	0.6173(3)	0.00345	0.00345	0.00345	0.00064	-0.00064	0.00064	0.00345
S3	0.1181(2)	0.1181	0.3800(3)	0.00345	0.00345	0.00345	0.00064	-0.00064	0.00064	0.00345
S4	0.3696(2)	0.3696	0.8684(3)	0.00345	0.00345	0.00345	-0.00064	-0.00064	-0.00064	0.00345
Crystal B at $T = 81$ K										
Cu1	0	0	0	0.00323(6)	0.00323	0.00323	0	0	0	0.00323(2)
Cu2	0.25	0.25	0.2509(1)	0.00323	0.00323	0.00323	0	0	0	0.00323
V1	0.1256(2)	-0.1256	0.3755(3)	0.00568	0.00568	0.00568	-0.00413	-0.00413	0.00413	0.00567
V2	0.1279(1)	0.1279	0.6293(2)	0.00568(7)	0.00568	0.00568	0.00413(4)	0.00413	0.00413	0.00567(2)
S1	0.1305(2)	-0.1305	0.1287(3)	0.00324(5)	0.00324	0.00324	0.00061(5)	-0.00061	0.00061	0.00324(2)
S2	0.1191(2)	-0.1191	0.6172(3)	0.00324	0.00324	0.00324	0.00061	-0.00061	0.00061	0.00324
S3	0.1181(1)	0.1181	0.3798(3)	0.00324	0.00324	0.00324	0.00061	-0.00061	0.00061	0.00324
S4	0.3695(2)	0.3695	0.8682(3)	0.00324	0.00324	0.00324	-0.00061	-0.00061	-0.00061	0.00324
Crystal B at $T = 80$ K										
Cu1	0	0	0	0.00215(7)	0.00215	0.00215	0	0	0	0.00215(2)
Cu2	0.25	0.25	0.2511(2)	0.00215	0.00215	0.00215	0	0	0	0.00215
V1	0.1253(2)	-0.1253	0.3757(3)	0.00456	0.00456	0.00456	-0.00401	-0.00401	0.00401	0.00456
V2	0.1277(1)	0.1277	0.6295(2)	0.00456(8)	0.00456	0.00456	0.00401(4)	0.00401	0.00401	0.00456(3)
S1	0.1303(2)	-0.1303	0.1284(3)	0.00240(7)	0.00240	0.00240	0.00064(5)	-0.00064	0.00064	0.00240(2)
S2	0.1192(2)	-0.1192	0.6167(3)	0.00240	0.00240	0.00240	0.00064	-0.00064	0.00064	0.00240
S3	0.1179(2)	0.1179	0.3798(3)	0.00240	0.00240	0.00240	0.00064	-0.00064	0.00064	0.00240
S4	0.3695(2)	0.3695	0.8678(3)	0.00240	0.00240	0.00240	-0.00064	-0.00064	-0.00064	0.00240

R_{int} for satellite reflections is higher, which we attribute to poor crystal quality.

In view of R_{int} of around 10%, the refinements leads to acceptable R_F of around 8%. Nevertheless, the incommensurate modulations of crystal B (80–84 K) and crystal A (60–90 K) are very similar too, with a temperature dependence of the amplitude, while the overall shape remains the same. Generally, the amplitude of the modulation of crystal A is larger than the amplitude of the modulation of crystal B at the same temperature. Modulation parameters for crystal B are given in Table [A18](#).

Table A18: Amplitudes of the modulation functions of of crystal B at 80–84 K. Modulation amplitudes as defined in Eq. A8. They have been multiplied by the corresponding lattice parameter, in order to obtain values in Å.

Atom	$A_{1,x} a$ (Å)	$A_{1,y} b$ (Å)	$A_{1,z} c$ (Å)	$B_{1,x} a$ (Å)	$B_{1,y} b$ (Å)	$B_{1,z} c$ (Å)
Crystal B at $T = 84$ K						
Cu1	-0.0284(14)	-0.0284	0	0	0	0.0327(17)
Cu2	0.0275(14)	0.0275	0	0	0	0.0374(16)
V1	-0.0019(17)	-0.0019	0	-0.0557(5)	0.0557	0.0530(8)
V2	-0.0196(15)	-0.0196	-0.0296(20)	-0.0442(5)	-0.0442	-0.0518(7)
S1	-0.0215(15)	-0.0215	0	0.0012(19)	-0.0012	0.0241(24)
S2	0.0228(14)	0.0228	0	0.0091(19)	-0.0091	0.0219(24)
S3	0.0215(16)	0.0215	-0.0002(21)	0.0118(21)	0.0118	-0.0147(26)
S4	-0.0229(17)	-0.0229	-0.0005(21)	-0.0123(21)	-0.0123	-0.0260(25)
Crystal B at $T = 83$ K						
Cu1	-0.0420(10)	-0.0420	0	0	0	0.0474(12)
Cu2	0.0405(10)	0.0405	0	0	0	0.0531(11)
V1	-0.0010(12)	-0.0010	0	-0.0798(4)	0.0798	0.0757(6)
V2	-0.0285(11)	-0.0285	-0.0433(14)	-0.0636(4)	-0.0636	-0.0743(6)
S1	-0.0329(10)	-0.0329	0	0.0047(14)	-0.0047	0.0397(16)
S2	0.0326(10)	0.0326	0	0.0098(14)	-0.0098	0.0252(16)
S3	0.0318(11)	0.0318	-0.0007(8)	0.0136(14)	0.0136	-0.0248(18)
S4	-0.0336(11)	-0.0336	-0.0047(14)	-0.0220(14)	-0.0220	-0.0359(17)
Crystal B at $T = 82$ K						
Cu1	-0.0431(12)	-0.0431	0	0	0	0.0487(14)
Cu2	0.0420(12)	0.0420	0	0	0	0.0557(14)
V1	-0.0001(15)	-0.0001	0	-0.0827(5)	0.0827	0.0784(7)
V2	-0.0304(14)	-0.0304	-0.0398(17)	-0.0657(5)	-0.0657	-0.0762(7)
S1	-0.0347(13)	-0.0347	0	0.0084(18)	-0.0084	0.0404(19)
S2	0.0331(13)	0.0331	0	0.0084(17)	-0.0084	0.0267(19)
S3	0.0302(14)	0.0302	-0.0048(18)	0.0146(17)	0.0146	-0.0270(22)
S4	-0.0358(14)	-0.0358	0.00001(182)	-0.0231(17)	-0.0231	-0.0357(22)
Crystal B at $T = 81$ K						
Cu1	-0.0440(11)	-0.0440	0	0	0	0.0496(13)
Cu2	0.0431(11)	0.0431	0	0	0	0.0575(12)
V1	-0.0003(14)	-0.0003	0	-0.0846(4)	0.0846	0.0801(7)
V2	-0.0309(13)	-0.0309	-0.0404(16)	-0.0675(4)	-0.0675	-0.0782(7)
S1	-0.0363(12)	-0.0363	0	0.0085(16)	-0.0085	0.0424(18)
S2	0.0334(12)	0.0334	0	0.0089(16)	-0.0089	0.0270(18)
S3	0.0312(13)	0.0312	-0.0051(17)	0.0140(16)	0.0140	-0.0272(20)
S4	-0.0366(13)	-0.0366	0.00006(170)	-0.0247(15)	-0.0247	-0.0373(20)
Crystal B at $T = 80$ K						
Cu1	-0.0450(10)	-0.0450	0	0	0	0.0526(12)
Cu2	0.0439(10)	0.0439	0	0	0	0.0576(11)
V1	0.0003(13)	0.0003	0	-0.0869(4)	0.0869	0.0828(6)
V2	-0.0305(12)	-0.0305	-0.0414(14)	-0.0690(4)	-0.0690	-0.0804(6)
S1	-0.0362(11)	-0.0362	0	0.0086(15)	-0.0086	0.0445(16)
S2	0.0361(11)	0.0361	0	0.0092(15)	-0.0092	0.0270(16)
S3	0.0326(12)	0.0326	-0.0049(15)	0.0152(14)	0.0152	-0.0329(18)
S4	-0.0369(12)	-0.0369	0.0006(15)	-0.0246(14)	-0.0246	-0.0335(18)

Crystals C and D are the incommensurate CDW phase at the measured temperatures below 41 K, except for the first cooling of crystal C, where the incommensurate and commensurate CDWs coexist. We provide details of the structure refinements for temperatures of 5, 16 and 35 K for crystal D, and 4 and 25 K for crystal C (Tables [A14](#) and [A15](#)). The problems with mismatch between intensities of equivalent Bragg reflections is exacerbated as compared to the problems found for crystal B. This is attributed in part to the difficulties (*e.g.* ice problems) with the low-temperature experiment. Nonetheless, refined structures including the modulation functions are similar to the modulated structures found for the incommensurate CDW phases of the other crystals. Atomic coordinates and ADPs of the basic structures are summarized in Table [A19](#). Modulation parameters are given in Table [A20](#).

A7. REFINEMENTS AND CRYSTAL STRUCTURES OF CRYSTALS B–D 125

Table A19: Atomic coordinates x, y, z and ADPs of the basic structure of crystal D at 35, 16 and 5 K and of crystal C at 25 K and 4.4 K.

Atom	x	y	z	U_{11}	U_{22}	U_{33}	U_{12}	U_{13}	U_{23}	U_{iso}^{eq}
Crystal D at $T = 35$ K										
Cu1	0	0	0	0.0022(3)	0.0022	0.0022	0	0	0	0.00217(7)
Cu2	0.25	0.25	0.2503(3)	0.0022	0.0022	0.0022	0	0	0	0.00217
V1	0.1246(3)	-0.1246	0.3776(3)	0.0023	0.0023	0.0023	-0.0011	-0.0011	0.0011	0.00233
V2	0.1296(2)	0.1296	0.6291(4)	0.0023(2)	0.0023	0.0023	-0.0011(1)	-0.0011	0.0011	0.00233
S1	0.1315(3)	-0.1315	0.1321(5)	0.0014(2)	0.0014	0.0014	-0.0001(1)	0.0001	-0.0001	0.00144(6)
S2	0.1190	-0.1190	0.6204	0.0014	0.0014	0.0014	-0.0001	0.0001	-0.0001	0.00144
S3	0.1176	0.1176	0.3797	0.0014	0.0014	0.0014	0.0001	-0.0001	-0.0001	0.00144
S4	0.3708(3)	0.3708	0.8697(6)	0.0014	0.0014	0.0014	0.0001	0.0001	0.0001	0.00144
Crystal C at $T = 25$ K										
Cu1	0	0	0	0.0037(3)	0.0037	0.0037	0	0	0	0.00366(9)
Cu2	0.25	0.25	0.2496(5)	0.0037	0.0037	0.0037	0	0	0	0.00366
V1	0.1257(6)	-0.1257	0.3735(10)	0.0031	0.0031	0.0031	-0.0013	-0.0013	0.0013	0.00311
V2	0.1302(4)	0.1302	0.6277(10)	0.0031(3)	0.0031	0.0031	0.0013(2)	0.0013	0.0013	0.00311(10)
S1	0.1316(5)	-0.1316	0.1250(12)	0.0034(2)	0.0034	0.0034	0.0001(2)	-0.0001	0.0001	0.00339(7)
S2	0.1177(5)	-0.1177	0.6154(11)	0.0034	0.0034	0.0034	0.0001	-0.0001	0.0001	0.00339
S3	0.1167(5)	0.1167	0.3767(11)	0.0034	0.0034	0.0034	-0.0001	0.0001	0.0001	0.00339
S4	0.3707(5)	0.3707	0.8662(11)	0.0034	0.0034	0.0034	-0.0001	-0.0001	-0.0001	0.00339
Crystal D at $T = 5$ K										
Cu1	0	0	0	0.0022(2)	0.0022	0.0022	0	0	0	0.00223(5)
Cu2	0.25	0.25	0.2504(4)	0.0022	0.0022	0.0022	0	0	0	0.00223
V1	0.1249(3)	-0.1249	0.3736(6)	0.0030	0.0030	0.0030	-0.0030	-0.0030	0.0030	0.00297
V2	0.1284(3)	0.1284	0.6293(4)	0.0030(2)	0.0030	0.0030	0.0030(1)	0.0030	0.0030	0.00297
S1	0.1327(4)	-0.1327	0.1253(6)	0.0031(1)	0.0031	0.0031	-0.0005(1)	0.0005	-0.0005	0.00305(5)
S2	0.1202(4)	-0.1202	0.6132(7)	0.0031	0.0031	0.0031	-0.0005	0.0005	-0.0005	0.00305
S3	0.1170(3)	0.1170	0.3769(5)	0.0031	0.0031	0.0031	0.0005	-0.0005	-0.0005	0.00305
S4	0.3710(3)	0.3710	0.8634(7)	0.0031	0.0031	0.0031	0.0005	0.0005	0.0005	0.00305
Crystal D at $T = 16$ K										
Cu1	0	0	0	0.0046(4)	0.0046	0.0046	0	0	0	0.00459(12)
Cu2	0.25	0.25	0.2523(4)	0.0046	0.0046	0.0046	0	0	0	0.00459
V1	0.1247(5)	-0.1247	0.3742(10)	0.0058	0.0058	0.0058	-0.0021	-0.0021	0.0021	0.00580
V2	0.1289(4)	0.1289	0.6291(6)	0.0058(4)	0.0058	0.0058	-0.0021	-0.0021	0.0021	0.00580(12)
S1	0.1310(5)	-0.1310	0.1289(10)	0.0041(3)	0.0041	0.0041	-0.0004(2)	0.0004	-0.0004	0.00408(10)
S2	0.1205(5)	-0.1205	0.6167(12)	0.0041	0.0041	0.0041	-0.0004	0.0004	-0.0004	0.00408
S3	0.1152(4)	0.1152	0.3791(9)	0.0041	0.0041	0.0041	0.0004	-0.0004	-0.0004	0.00408
S4	0.3717(4)	0.3717	0.8676(12)	0.0041	0.0041	0.0041	0.0004	0.0004	0.0004	0.00408
Crystal C at $T = 4.4$ K										
Cu1	0	0	0	0.0042(2)	0.0042	0.0042	0	0	0	0.00415(6)
Cu2	0.25	0.25	0.2506(6)	0.0042	0.0042	0.0042	0	0	0	0.00415
V1	0.1239(4)	-0.1239	0.3734(9)	0.0045	0.0045	0.0045	-0.0032	-0.0032	0.0032	0.00453
V2	0.1286(4)	0.1286	0.6288(7)	0.0045(2)	0.0045	0.0045	-0.0032(1)	-0.0032	0.0032	0.00453(7)
S1	0.1319(5)	-0.1319	0.1248(8)	0.0038(1)	0.0038	0.0038	-0.0006(1)	0.0006	-0.0006	0.00379(4)
S2	0.1203(4)	-0.1203	0.6123(9)	0.0038	0.0038	0.0038	-0.0006	0.0006	-0.0006	0.00379
S3	0.1183(5)	0.1183	0.3784(8)	0.0038	0.0038	0.0038	0.0006	-0.0006	-0.0006	0.00379
S4	0.3704(4)	0.3704	0.8637(10)	0.0038	0.0038	0.0038	0.0006	0.0006	0.0006	0.00379

Table A20: Amplitudes of the modulation functions of of crystals C and D. Modulation amplitudes as defined in Eq. A8

Atom	$A_{1,x} a$ (Å)	$A_{1,y} b$ (Å)	$A_{1,z} c$ (Å)	$B_{1,x} a$ (Å)	$B_{1,y} b$ (Å)	$B_{1,z} c$ (Å)
Crystal D at $T = 35$ K						
Cu1	-0.0684(22)	-0.0684	0	0	0	0.0574(28)
Cu2	0.0489(23)	0.0489	0	0	0	0.0802(26)
V1	-0.0020(26)	-0.0020	0	-0.1048(10)	0.1048	0.0983(14)
V2	-0.0333(23)	-0.0333	0.0447(35)	-0.0860(11)	-0.0860	-0.0959(14)
S1	-0.0471(24)	-0.0471	0	0.0046(33)	-0.0046	0.0578(38)
S2	0.0411(23)	0.0411	0	0.0192(32)	-0.0192	0.0335(37)
S3	0.0404(25)	0.0404	-0.0016(35)	0.0136(30)	0.0136	-0.0244(39)
S4	-0.0465(25)	-0.0465	-0.0093(36)	-0.0349(28)	-0.0349	-0.0617(39)
Crystal C at $T = 25$ K						
Cu1	-0.0701(53)	-0.0701	0	0	0	0.0629(65)
Cu2	0.0483(56)	0.0483	0	0	0	0.0823(61)
V1	-0.0029(62)	-0.0029	0	-0.1094(19)	0.1094	0.1042(30)
V2	-0.0312(46)	-0.0312	-0.0520(79)	-0.0890(21)	-0.0890	-0.1031(30)
S1	-0.0514(58)	-0.0514	0	-0.0040(64)	0.0040	0.0629(88)
S2	0.0480(53)	0.0480	0	0.0315(64)	-0.0315	0.0284(83)
S3	0.0429(57)	0.0429	-0.0155(84)	0.0144(68)	0.0144	-0.0237(86)
S4	-0.0440(57)	-0.0440	-0.0053(85)	-0.0339(64)	-0.0339	-0.0638(84)
Crystal D at $T = 5$ K						
Cu1	-0.0569(20)	-0.0569	0	0	0	0.0522(25)
Cu2	0.0534(21)	0.0534	0	0	0	0.0668(23)
V1	0.0009(24)	0.0009	0	-0.0980(9)	0.0980	0.0871(13)
V2	-0.0344(23)	-0.0344	-0.0474(29)	-0.0753(9)	-0.0753	-0.0894(13)
S1	-0.0364(22)	-0.0364	0	0.0100(30)	-0.0100	0.0519(32)
S2	0.0386(22)	0.0386	0	0.0134(29)	-0.0134	0.0294(32)
S3	0.0431(23)	0.0431	-0.0037(23)	0.0132(27)	0.0132	-0.0406(36)
S4	-0.0412(23)	-0.0412	-0.0014(33)	-0.0366(26)	-0.0366	-0.0498(34)
Crystal D at $T = 16$ K						
Cu1	-0.0577(31)	-0.0577	0	0	0	0.0633(33)
Cu2	0.0549(30)	0.0549	0	0	0	0.0744(31)
V1	0.0051(35)	0.0051	0	-0.0981(12)	0.0981	0.0942(17)
V2	-0.0329(33)	-0.0329	-0.0452(40)	-0.0816(13)	-0.0816	-0.0971(17)
S1	-0.0408(32)	-0.0408	0	0.0054(43)	-0.0054	0.0538(37)
S2	0.0415(35)	0.0415	0	0.0138(42)	-0.0138	0.0287(36)
S3	0.0376(30)	0.0376	-0.0104(42)	0.0228(37)	0.0228	-0.0446(53)
S4	-0.0421(32)	-0.0421	-0.0024(43)	-0.0239(34)	-0.0239	-0.0453(49)
Crystal C at $T = 4.4$ K						
Cu1	-0.0532(37)	-0.0532	0	0	0	0.0494(44)
Cu2	0.0489(38)	0.0489	0	0	0	0.0597(42)
V1	-0.0019(43)	-0.0019	0	-0.0912(14)	0.0912	0.0796(22)
V2	-0.0309(40)	-0.0309	-0.0446(50)	-0.0710(14)	-0.0710	-0.0846(21)
S1	-0.0361(39)	-0.0361	0	0.0035(50)	-0.0035	0.0454(54)
S2	0.0342(38)	0.0342	0	0.0153(47)	-0.0153	0.0315(52)
S3	0.0370(43)	0.0370	-0.00305(50)	0.0152(50)	0.0152	-0.0340(68)
S4	-0.0368(41)	-0.0368	-0.00349(58)	-0.0300(47)	-0.0300	-0.0501(63)

Appendix B: Structure refinements and models of $\text{Er}_2\text{Ir}_3\text{Si}_5$

3

Supplemental material for the incommensurate CDW structure of $\text{Er}_2\text{Ir}_3\text{Si}_5$:

- B1. X-ray diffraction at beamline P24 at DESY.
- B2. Data processing of SXRD data measured at P24.
- B3. Diffraction sketches.
- B4. Choice of symmetry.
- B5. Treatment of partial overlaps.
- B6. Structure refinements and crystal structures of the incommensurate CDW phases of crystal A

B1 X-ray diffraction at beamline P24 at DESY

Small pieces of single-crystalline $\text{Er}_2\text{Ir}_3\text{Si}_5$ were acquired by crushing a large single crystal, from which crystal A of dimensions $0.05 \times 0.08 \times 0.06 \text{ mm}^3$ was selected for a single-crystal X-ray diffraction (SXRD) experiment at beamline P24 of PETRA-III Extension at DESY in Hamburg, Germany.

SXRD was measured at station EH2 of beamline P24, employing radiation of a wave length of $\lambda_{P24} = 0.49994 \text{ \AA}$. Diffracted X rays were detected by a Pilatus 1M CdTe detector. The temperature of the sample was regulated with a CRYOCOOL open-flow cryostat, employing helium as cryo gas. Diffracted intensity was collected

³The appendix has been published as a supplemental material for the manuscript: Sitaram Ramakrishnan, Andreas Schönleber, Toms Rekis, Natalija van Well, Leila Noohinejad, Sander van Smaalen, Martin Tolkiehn, Carsten Paulmann Biplab Bag, Arumugam Thamizhavel, Dilip Pal and Srinivasan Ramakrishnan. Unusual charge density wave transition and absence of magnetic ordering in $\text{Er}_2\text{Ir}_3\text{Si}_5$. *Phys. Rev. B* **101** 060101(R) (2020)

on the detector during rotation of the crystal by 1 deg. Each run of data collection comprises 362 of these frames, corresponding to a total rotation of the crystal by 362 deg. The time of measurement for one run was about 10 minutes. The crystal-to-detector distance was chosen as 110 mm, resulting in a resolution of the SXRD data of approximately $(\sin(\theta)/\lambda)_{max} = 0.684 \text{ \AA}^{-1}$.

Table B1 shows that for each temperature there are multiple runs with different filters. This strategy was chosen especially for the incommensurate phase, in order to capture both weak satellite reflections as well as strong main reflections, given the limited dynamic range of the detector.

Table B1: Single-crystal X-ray diffraction of $\text{Er}_2\text{Ir}_3\text{Si}_5$ at beamline P24 at DESY, Hamburg. For each run is given: temperature of the crystal, phase, setting and attenuation factor of filter in the primary beam, and the number of measured frames that has been processed. Entries are given in chronological order, thus providing the thermal history.

Temperature (K)	Name	Phase	Attenuator		Number of frames
			setting	factor	
150	150f10	Periodic	10	7.11794	362
150	150f24	Periodic	24	111.1111	362
75	75f0	Incommensurate	0	1	362
75	75f10	Incommensurate	10	7.11794	362
75	75f24	Incommensurate	24	111.1111	362
20	20f0	Incommensurate	0	1	362
20	20f10	Incommensurate	10	7.11794	362
20	20f24	Incommensurate	24	111.1111	362
130	130f0	Incommensurate	0	1	362
130	130f10	Incommensurate	10	7.11794	362
130	130f24	Incommensurate	24	111.1111	362
200 ^a	200f10	Periodic	10	7.11794	362
200	200f24	Periodic	24	111.1111	362

^aAlthough the 200f0 with filter factor 1 run has been collected and analyzed, it has not been included in the final refinements as the crystal is periodic at 200 K, and without weak satellite reflections it would not be beneficial to include this overexposed run.

According to Table B1 we started cooling the crystal down to 150 K where it remains periodic. The crystal was cooled further to 75 K and 20 K where it became incommensurate and remained in the incommensurate phase when warmed up to 130 K. The crystal was removed after warming it up to 200 K after collecting the data.

Crystallographic information and instrumental parameters used in the experiment are listed in Tables B2 and B3.

Table B2: Crystallographic data of crystal A of $\text{Er}_2\text{Ir}_3\text{Si}_5$ at temperatures 200 K and 150 K. At these temperatures the crystal structure is periodic.

Temperature (K)	200	150
Crystal system	Orthorhombic	Orthorhombic
Space group	<i>Ibam</i>	<i>Ibam</i>
Space group No.	72	72
<i>a</i> (Å)	9.9075(5)	9.9042(5)
<i>b</i> (Å)	11.3524(4)	11.3432(4)
<i>c</i> (Å)	5.7632(3)	5.7612(3)
Volume (Å ³)	648.21(6)	647.24(5)
<i>Z</i>	4	4
Wavelength (Å)	0.49994	0.49994
Detector distance (mm)	110	110
2 θ -offset (deg)	0	0
χ -offset (deg)	-60	-60
Rotation per image (deg)	1	1
($\sin(\theta)/\lambda$) _{max} (Å ⁻¹)	0.683152	0.683429
Absorption, μ (mm ⁻¹)	35.419	35.472
T_{min} , T_{max}	0.0099, 0.0238	0.0095, 0.0219
Criterion of observability	$I > 1.5\sigma(I)$	$I > 1.5\sigma(I)$
Number of main reflections		
measured	8735	8423
unique (obs/all)	399/474	403/475
R_{int} main (obs/all)	0.0746/0.0768	0.0710/0.0727
No. of parameters	31	31
R_F main (obs)	0.0421	0.0436
wR_F all (all)	0.0428	0.0432
GoF (obs/all)	2.26/2.06	2.27/2.09
$\Delta\rho_{min}$, $\Delta\rho_{max}$ (e Å ⁻³)	-3.71, 3.41	-3.75, 3.74

Table B3: Crystallographic data of crystal A of $\text{Er}_2\text{Ir}_3\text{Si}_5$ at 130 K, 75 K and 20 K. At these temperatures, the material is in the incommensurate CDW phase.

Temperature (K)	130	75	20
Crystal system	Triclinic	Triclinic	Triclinic
Superspace group	$I\bar{1}(\sigma_1 \sigma_2 \sigma_3)0$	$I\bar{1}(\sigma_1 \sigma_2 \sigma_3)0$	$I\bar{1}(\sigma_1 \sigma_2 \sigma_3)0$
Superspace group No. [79]	2.1.1.1	2.1.1.1	2.1.1.1
a (Å)	9.8440(3)	9.8494(3)	9.8387(5)
b (Å)	11.4837(2)	11.4863(3)	11.4681(4)
c (Å)	5.7251(2)	5.7268(2)	5.7188(2)
α (deg)	90.094(1)	90.079(1)	90.075(1)
β (deg)	91.709(2)	91.695(2)	91.701(2)
γ (deg)	90.039(2)	90.051(1)	90.116(2)
Volume (Å ³)	644.90(3)	647.60(5)	644.97(6)
Wavevector \mathbf{q}	(0.2492(1), 0.4983(1), 0.2487(1))	(0.2495(2), 0.4973(1), 0.2483(1))	(0.2492(1), 0.4966(2), 0.2478(1))
Z	4	4	4
Wavelength (Å)	0.49994	0.49994	0.49994
Detector distance (mm)	110	110	110
2θ -offset (deg)	0	0	0
χ -offset (deg)	-60	-60	-60
Rotation per image (deg)	1	1	1
$(\sin(\theta)/\lambda)_{max}$ (Å ⁻¹)	0.683451	0.683251	0.684086
Absorption, μ (mm ⁻¹)	35.490	35.452	35.597
T_{min} , T_{max}	0.0116, 0.0253	0.0677, 0.1034	0.0118, 0.0254
Criterion of observability	$I > 1.5\sigma(I)$	$I > 1.5\sigma(I)$	$I > 1.5\sigma(I)$
Number of main reflections measured	6344	6362	6286
unique (obs/all)	1875/2475	1924/2480	1869/2478
Number of satellites measured	25703	25707	25652
unique (obs/all)	3174/12595	3286/12599	3071/12565
R_{int} main (obs/all)	0.0442/0.0452	0.0360/0.0372	0.0428/0.0442
R_{int} sat (obs/all)	0.0631/0.0841	0.0634/0.0839	0.0667/0.0885
No. of parameters	117	117	117
R_F main (obs)	0.0703	0.0650	0.0758
R_F sat (obs)	0.0624	0.0611	0.0744
wR_F main (all)	0.0845	0.0797	0.0857
wR_F sat (all)	0.0729	0.0731	0.0903
wR_F all (all)	0.0830	0.0788	0.1084
GoF (obs/all)	1.91/1.11	1.81/1.07	1.93/1.11
$\Delta\rho_{min}$, $\Delta\rho_{max}$ (e Å ⁻³)	-5.21, 5.82	-4.60, 5.05	-6.46, 8.24

B2 Data processing of SXRD data measured at P24

Data processing has been done with the EVAL15 suite package [50]. SADABS [51] has been used for the absorption correction.

Each data set consists of multiple runs, that differ in the intensity of the primary beam as regulated by filters (Table B1). They were processed together, thus eventually producing for each temperature a single data set of integrated intensities of Bragg reflections.

The SXRD data at 150 K and 200 K could successfully be indexed on an I -centered orthorhombic lattice described by the space group $Ibam$ (Table B2). The space group and the lattice parameters are in agreement with the literature [33, 96].

At 130 K and lower temperatures, analysis of the images has shown a clear monoclinic lattice distortion indicated by split reflections due to twinning (both possible monoclinic orientations occur as they are allowed by the transition from the orthorhombic high-temperature structure). Furthermore, the main reflections are surrounded by weaker, incommensurate satellite reflections of first order. Finally, the analysis has shown that the true symmetry of the CDW phase is triclinic (see Section B4 below). Therefore, there are four domains, arranged in two pairs of pseudomerohedric twinning of the main reflections, but each domain with its own set of satellite reflections.

Accurate values for lattice parameters and modulation wave vectors have been obtained by the simultaneous treatment of twinning and satellite reflections in EVAL15. Such a combined treatment is not possible in SADABS. Accurate values for integrated intensities of Bragg reflections have thus been obtained by a separate integration and absorption correction of each pair of pseudomerohedric domains. The intensities of Bragg reflections were obtained for the combination of domain I and domain III by employing five integer indices (h, k, l, m, n) for indexing all reflections on an I -centered, pseudo-monoclinic lattice

$$\{\mathbf{a}_I^*, \mathbf{b}_I^*, \mathbf{c}_I^*, \mathbf{q}^1, \mathbf{q}^3\}. \quad (\text{B1})$$

Main reflections $(h, k, l, 0, 0)$ are common to domains I and III. Satellite reflections $(h, k, l, m, 0)$ belong to domain I, and satellite reflections $(h, k, l, 0, n)$ belong to domain III. Domain I and domain III are related by a mirror plane perpendicular to the \mathbf{b} -axis. Modulation wave vectors are therefore

$$\begin{aligned} \mathbf{q}^1 &= (\sigma_1 \mathbf{a}_I^* + \sigma_2 \mathbf{b}_I^* + \sigma_3 \mathbf{c}_I^*) \\ \mathbf{q}^3 &= (\sigma_1 \mathbf{a}_I^* - \sigma_2 \mathbf{b}_I^* + \sigma_3 \mathbf{c}_I^*). \end{aligned} \quad (\text{B2})$$

Non-merohedral twinning exists between domains I and III on the one hand and

domains II and IV on the other hand. A similar integration was performed for domain II and domain IV. The five-integer indexing (h, k, l, m, n) now refers to the I -centered, pseudo-monoclinic lattice defined by

$$\{\mathbf{a}_{II}^*, \mathbf{b}_{II}^*, \mathbf{c}_{II}^*, \mathbf{q}^2, \mathbf{q}^4\}. \quad (\text{B3})$$

Domain II and domain IV are again related by a mirror plane perpendicular to the \mathbf{b} -axis. Modulation wave vectors possess components with respect to the second reciprocal lattice according to

$$\begin{aligned} \mathbf{q}^2 &= (\sigma_1 \mathbf{a}_{II}^* + \sigma_2 \mathbf{b}_{II}^* + \sigma_3 \mathbf{c}_{II}^*) \\ \mathbf{q}^4 &= (\sigma_1 \mathbf{a}_{II}^* - \sigma_2 \mathbf{b}_{II}^* + \sigma_3 \mathbf{c}_{II}^*). \end{aligned} \quad (\text{B4})$$

It is stressed that σ_1, σ_2 and σ_3 will have the same numerical values for all four modulation wave vectors (Eqs. B2 and B4), due to the twinning relations.

Table B4 shows the assignment of observed satellite reflections in relation to the domain and the satellite index m' for the one-dimensional (1D) modulation. After integrating and absorption correction, employing five indices (h, k, l, m, n) , a Fortran program was used to transform the reflection file to a file with a four-integer indexing (h, k, l, m') .

Table B4: Indexing of the four satellite reflections surrounding one main reflection belonging to both domains I and III. Information is given for the five-integer indexing (h, k, l, m, n) and the four-integer indexing (h, k, l, m') , reflecting the (3+1)-dimensional character of the modulation of a single domain. Treatment of domains II and IV is analogous.

No.	m	n	Modulation wavevector	Type	Domain No.	m'
1	1	0	$(\sigma_1, \sigma_2, \sigma_3)$	\mathbf{q}^1	I	1
2	0	1	$(\sigma_1, -\sigma_2, \sigma_3)$	\mathbf{q}^3	III	1
3	-1	0	$(-\sigma_1, -\sigma_2, -\sigma_3)$	$-\mathbf{q}^1$	I	-1
4	0	-1	$(-\sigma_1, \sigma_2, -\sigma_3)$	$-\mathbf{q}^3$	III	-1

Using SADABS equivalent reflections for computation of scaling and absorption correction have been defined by point symmetry $\bar{1}$, as this is the symmetry of the diffraction pattern.

B3 Diffraction sketches

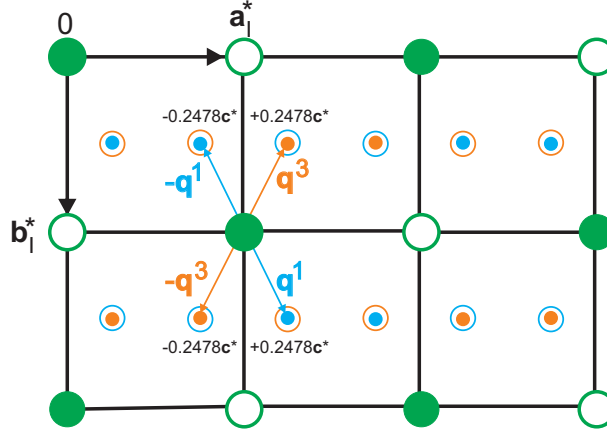


Figure B1: Sketch of the $(\mathbf{a}_I^*, \mathbf{b}_I^*)$ reciprocal lattice plane of $\text{Er}_2\text{Ir}_3\text{Si}_5$ in the triclinic phase at 20 K. Green circles are the main reflections, blue circles are the \mathbf{q}^1 satellites, and orange circles indicate the \mathbf{q}^3 satellites. Main reflections are in the plane of the drawing, while satellite reflections are projected onto it. Open circles indicate systematic absences.

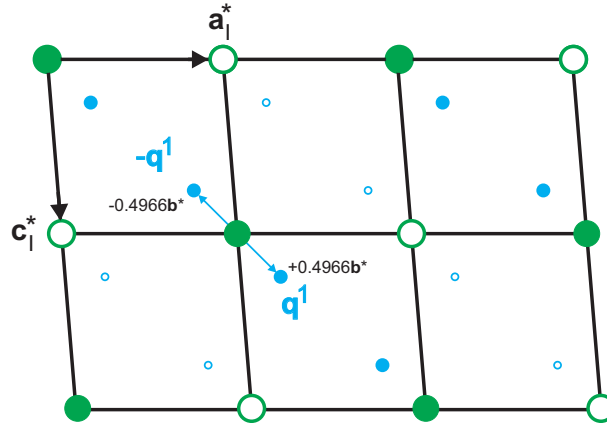


Figure B2: Sketch of the $(\mathbf{a}_I^*, \mathbf{c}_I^*)$ reciprocal lattice plane of $\text{Er}_2\text{Ir}_3\text{Si}_5$ in the triclinic phase at 20 K. Green circles are the main reflections and blue circles are the \mathbf{q}^1 satellites. Main reflections are in the plane of the drawing, while satellite reflections are projected onto it. \mathbf{q}^3 satellites are not shown, because they appear directly behind the \mathbf{q}^1 satellites. Note that the lattice distortion has been exaggerated, in order to make it visible.

At room temperature the symmetry of $\text{Er}_2\text{Ir}_3\text{Si}_5$ is orthorhombic $Ibam$ [33, 96]. Upon cooling the crystal to 130 K and at lower temperatures, we observed

superlattice reflections along with a distortion of the lattice. Although the distortion appears monoclinic, triclinic symmetry is favoured due to the high R_{int} of 50% for monoclinic symmetry, as explained in Section B4 and Table B5. Due to the loss of symmetry the crystal becomes twinned with four twin domains.

In Figure B1 we show the $(\mathbf{a}_I^*, \mathbf{b}_I^*)$ reciprocal lattice plane of domain I. (which coincides with that of domain III.) The I -centering is reflected by open circles for extinct reflections and full circles for the allowed Bragg reflections. Main reflections coincide for domains I and III. Satellites of domain I are defined by \mathbf{q}^1 , and clearly appear at different positions than satellites of domain III, which are defined by \mathbf{q}^3 . At $T = 20$ K the two wave vectors have irrational components

$$\begin{aligned}\mathbf{q}^1 &= (0.2492(1), 0.4966(2), 0.2478(1)) \\ \mathbf{q}^3 &= (0.2492(1), -0.4966(2), 0.2478(1)).\end{aligned}\tag{B5}$$

On inspection of the figure, one would see that the satellites are not along a straight line in the direction \mathbf{a}_I^* , but rather form a zigzag line. This is because the σ_2 components of the wave vectors are not rational.

We have not included into this sketch the satellites of domains II and IV, since they correspond to other domains. For example, consider the \mathbf{q}^2 satellites with components $(0.2492, 0.4966, 0.2478)$ with respect to the second reciprocal lattice (Eq. B3). With respect to the first reciprocal basis of domain I (Eq. B1), its components are

$$\mathbf{q}^2 = (0.2492(1), -0.4966(2), -0.2556(1))_I.\tag{B6}$$

Notice that due to the non-merohedral twin law the magnitude of σ_3 component of the wave vector is slightly changed.

Figure B2 shows the $(\mathbf{a}_I^*, \mathbf{c}_I^*)$ reciprocal lattice plane of domain I. This projection reveals the lattice distortion where $\beta \neq 90$ deg. In this representation, satellite reflections \mathbf{q}^3 of domain III appear directly below satellite reflections \mathbf{q}^1 of domain I.

B4 Choice of symmetry

In the room-temperature phase, $\text{Er}_2\text{Ir}_3\text{Si}_5$ is orthorhombic $Ibam$ (Table B2). a low value for R_{int} indicates diffraction symmetry mmm and a low value for R_F obtained after structure refinement confirms the orthorhombic structure.

Below the CDW phase transition, the lattice of the average structure appears monoclinic, with $\beta = 91.70$ deg far away from 90 deg (Table B3). Nevertheless, the symmetry of crystal structure is triclinic instead of monoclinic. This is shown by the following analysis.

Two different models are possible when assuming monoclinic symmetry. The

first monoclinic model respects the I centering and the incommensurate values of the modulation wave vector. Then \mathbf{q}^1 and \mathbf{q}^3 are equivalent by symmetry and the CDW would involve a two-dimensional (2D) modulation. Previously triclinic domains I and III become a single monoclinic domain I. The analysis in $(3+2)$ -dimensional superspace, employing a five-integer indexing (h, k, l, m, n) then results in a very high value of 50.4% for R_{int} computed for the satellites, while a low value is obtained for R_{int} on the main reflections (Table B5). First, this implies that monoclinic $I2/c(\sigma_1, \sigma_2, \sigma_3)00(\sigma_1, -\sigma_2, \sigma_3)00$ is not the correct symmetry for the CDW phase. Secondly, it implies that the atomic positions in the average structure resemble those in the orthorhombic high-temperature structure, while the triclinic distortion is the result of the modulation.

The second monoclinic model assumes that the second component of the modulation wave vector would be exactly 0.5. This assumption implies a one-dimensional modulation with $\mathbf{q}^1 = (\sigma_1, 1/2, \sigma_3)$. But $\mathbf{q}^1 - \mathbf{q}^3 = (0, 1, 0)$ violates the I -centering. This choice thus implies a loss of I -centering and the $(3+1)$ -dimensional superspace group is $P2/a(\sigma_1, 0.5, \sigma_3)0s$. Again, averaging apparent equivalent satellite reflections results in $R_{int} = 49\%$ and thus invalidates this choice of symmetry too (Table B5).

Assuming triclinic symmetry results in four domains, and averaging equivalent reflections gives the expected low values for R_{int} (Table B5).

Table B5: Results of indexing and integration of the diffraction data of $\text{Er}_2\text{Ir}_3\text{Si}_5$ at $T = 75$ K, assuming alternatively monoclinic and triclinic symmetries. Only the run with the highest intensity (attenuator 0) was used for this analysis.

Superspace group	$I2/c(\sigma_1, \sigma_2, \sigma_3)00(\sigma_1, -\sigma_2, \sigma_3)00$	$P2/a(\sigma_1, 0.5, \sigma_3)0s$	$I1(\sigma_1, \sigma_2, \sigma_3)0$
a (Å)	9.8482(3)	9.8483(3)	9.8493(2)
b (Å)	11.4876(4)	11.4801(3)	11.4811(2)
c (Å)	5.7262(2)	5.7254(2)	5.7253(2)
α (deg)	90	90	90.022(1)
β (deg)	91.774(1)	91.770(1)	91.775(1)
γ (deg)	90	90	90.061(2)
V (Å ³)	647.17(4)	647.14(4)	647.11(3)
Wave vector	(0.2493, 0.4971, 0.2471) (0.2493, -0.4971, 0.2471)	(0.2492, 0.5, 0.2474)	(0.2492, 0.4972, 0.2482)
Reflections (EVAL15)	28605	34303	17112
Reflections (SADABS)	15760	18996	9443
R_{int} (SADABS) (%)	6.26	6.28	6.24
Measured main	2787	5951	2987
Measured satellites	12874	12891	6456
R_{exp} main obs/all (%)	4.04/4.54	2.63/3.47	5.05/6.04
R_{exp} sat obs/all (%)	15.83/40.28	12.73/25.48	16.45/43.98
R_{int} main (obs/all) (%)	4.15/4.18	4.08/4.14	3.46/3.48
R_{int} sat (obs/all) (%)	50.40/49.44	49.01/48.86	5.73/6.72
Unique main (obs/all)	643/857	1174/2043	1028/1575
Unique sat (obs/all)	690/3458	1328/5205	564/3269

B5 Treatment of partial overlaps

Domains I and II possess non-coinciding lattices and reciprocal lattices in relation to $\beta \neq 90$ deg. Nevertheless, these two domains have a common $(h, k, 0, 0)$ reciprocal lattice plane. Reflections with $l \neq 0$ appear as double or split reflections, because the two domains have reflections at slightly different positions. The splitting increases with increasing index l and it is larger for larger deviations from 90 deg of the angle β .

For the common reciprocal lattice plane and for reflections with a sufficiently small splitting, EVAL15 obtains an integrated intensity that is the sum of the intensities of both domains. For large splittings, EVAL15 obtains the integrated intensity of a reflection belonging to a single domain. For partial overlap or insufficient splitting, the result of EVAL15 is unpredictable and different from the two desired cases above. Refinement software Jana2006 can handle both overlapped and split reflections, but not the intermediate case [56]. Accordingly, two parameters are available in Jana2006 for defining usable reflections. The smaller value "Maximal angular difference for twin overlap" gives an upper boundary for overlapping reflections. The larger value "Minimal angular difference for full separation" gives a lower boundary for fully split reflections. Reflections with split angles in between these two values are not used in the refinement. Structure refinements have been performed for several values of these parameters. Based on the results in Table B6 the values $L1 = 0.1$ and $L2 = 0.27$ have been chosen for the upper and lower boundaries.

Table B6: Results of structure refinements with Jana2006 of the 75 K data measured with attenuator 0. "Maximal angular difference for twin overlap" (L1) and "Minimal angular difference for full separation" (L2).

R_F (main) (%)	R_F (sat) (%)	wR (all) (%)	Unique main (obs/all)	Unique sat (obs/all)	Comments	L1 (deg)	L2 (deg)
5.94	6.84	7.90	1022/1572	1097/13042	D1(main) + all sat	0.1	0.1
5.72	5.20	6.66	769/1249	1025/12496	D1(main) + all sat	0.1	0.27
6.08	8.02	7.46	1022/0	1097/0	D1(main) + all sat	0.1	0.1
5.74	5.21	6.33	769/0	1025/0	D1(main) + all sat	0.1	0.27
14.15	8.03	20.21	866/1513	1097/13042	D2(main)+ all sat	0.1	0.1
5.84	5.23	6.64	1022/1572	720/6527	D1(main) + D1 and D3(sat)	0.1	0.1
14.36	12.81	21.13	866/1513	377/6515	D2(main)+ D2 and D4(sat)	0.1	0.1
9.40	7.23	16.17	1839/2997	1097/13042	All	0.1	0.1
6.51	5.27	7.68	1190/2098	966/11521	All No NPD	0.1	0.4
6.56	5.24	7.94	1395/2394	979/11892	All No NPD	0.1	0.35
6.56	5.22	7.94	1395/2394	1002/12220	All No NPD	0.1	0.3
6.56	5.28	7.96	1395/2394	1025/12496	All No NPD	0.1	0.27
6.62	5.28	7.78	1395/0	1025/0	All	0.1	0.27
7.64	5.50	11.16	1623/2691	1025/12496	All	0.1	0.26
7.64	5.50	11.16	1623/2691	1025/12496	All	0.1	0.25

B6 Structure refinements and crystal structures of the incommensurate CDW phases of crystal A

Structure refinements have been performed with Jana2006 [56] for each of the data sets. The orthorhombic structure of $\text{Er}_2\text{Ir}_3\text{Si}_5$ provides a good fit to the diffraction data measured at 200 K and 150 K (Table B2). Structure parameters are given in Table B7.

Table B7: Structural parameters for the orthorhombic structure of crystal A of $\text{Er}_2\text{Ir}_3\text{Si}_5$ at 150 and 200 K. Given are the fractional coordinates x , y , z of the atoms, their anisotropic displacement parameters (ADPs) U_{ij} ($i, j = 1, 2, 3$) and the equivalent isotropic displacement parameter U_{iso}^{eq} .

Atom	x	y	z	U_{11}	U_{22}	U_{33}	U_{12}	U_{13}	U_{23}	U_{iso}^{eq}
Crystal A at $T = 200$ K										
Er1	0.2710(1)	0.3691(1)	0	0.0171(7)	0.0121(6)	0.0173(8)	-0.0001(5)	0	0	0.0155(4)
Ir1	0.1142(1)	0.1402(1)	0	0.0175(5)	0.0118(5)	0.0165(6)	0.0007(4)	0	0	0.0153(3)
Ir2	0.5	0	0.25	0.0175(7)	0.0157(7)	0.0148(9)	0	0	0	0.0160(4)
Si1	0	0	0.25	0.0165(51)	0.0254(53)	0.0149(62)	0	0	0	0.0190(32)
Si2	0	0.2753(6)	0.25	0.0257(38)	0.0052(28)	0.0194(44)	0	-0.0020(37)	0	0.0168(21)
Si3	0.3424(8)	0.1034(7)	0	0.0153(39)	0.0199(39)	0.0194(49)	0.0035(32)	0	0	0.0182(25)
Crystal A at $T = 150$ K										
Er1	0.2710(1)	0.3692(1)	0	0.0159(7)	0.0117(6)	0.0174(8)	-0.0002(5)	0	0	0.0150(4)
Ir1	0.1144(1)	0.1402(1)	0	0.0163(5)	0.0116(5)	0.0163(6)	0.0006(4)	0	0	0.0147(3)
Ir2	0.5	0	0.25	0.0171(7)	0.0149(7)	0.0149(9)	0	0	0	0.0156(4)
Si1	0	0	0.25	0.0166(51)	0.0198(51)	0.0179(64)	0	0	0	0.0181(32)
Si2	0	0.2754(6)	0.25	0.0220(36)	0.0091(31)	0.0189(44)	0	-0.0019(36)	0	0.0167(22)
Si3	0.3427(8)	0.1045(7)	0	0.0164(39)	0.0204(40)	0.0179(49)	0.0023(32)	0	0	0.0182(25)

The incommensurate CDW exists at 130 K, 75 K and 20 K. We could successfully refine a structure model comprising first-order harmonics for displacive modulation of all atoms (Table B3). The relatively high values of $R_F \approx 0.07$ are due to a yet unresolved scaling problem at beamline P24. The much better values for the refinement of the orthorhombic structure is the result of averaging reflections in a higher point symmetry. Their less than perfect agreement then results in a higher value for R_{int} .

The modulation function for displacement modulation,

$$\mathbf{u}(\bar{x}_{s4}) = (u_x(\bar{x}_{s4}), u_y(\bar{x}_{s4}), u_z(\bar{x}_{s4})), \quad (\text{B7})$$

is defined as

$$u_\alpha(\bar{x}_{s4}) = \sum_{n=1}^{n_{max}} \{A_{n,\alpha} \sin(2\pi n \bar{x}_{s4}) + B_{n,\alpha} \cos(2\pi n \bar{x}_{s4})\}, \quad (\text{B8})$$

where we have used $n_{max} = 1$ (first-order harmonics). Structural parameters are summarized in Tables B8 and B9.

Table B8: Atomic coordinates x , y , z and ADPs of the basic structure of crystal A in the incommensurate CDW phase.

Atom	x	y	z	U_{11}	U_{22}	U_{33}	U_{12}	U_{13}	U_{23}	U_{iso}^{eq}
Crystal A at $T = 130$ K										
Er1a	0.2699(1)	0.3679(1)	0.0018(2)	0.0109(2)	0.0155(2)	0.0203(2)	-0.0001(2)	0	0	0.0156(1)
Er1b	-0.2670(1)	0.3672(1)	0.4978(2)	0.0109	0.0155	0.0203	-0.0001	0	0	0.0156
Ir1a	0.1086(1)	0.1404(1)	-0.0146(2)	0.0102(2)	0.0150(2)	0.0196(2)	0.0006(1)	0	0	0.0150(1)
Ir1b	-0.1087(1)	0.1407(1)	0.5144(2)	0.0102	0.0158	0.0196	-0.0006	0	0	0.0150
Ir2	0.4993(1)	-0.0012(1)	0.2497(2)	0.0114(2)	0.0170(2)	0.0205(3)	0	0	0	0.0163(1)
Si1	-0.0024(7)	0.0081(3)	0.2501(12)	0.0180(16)	0.0137(17)	0.0019(15)	0	0	0	0.0112(9)
Si2a	-0.0013(7)	0.2715(3)	0.2521(15)	0.0115(10)	0.0189(12)	0.0200(14)	0	0.0024(10)	0	0.0168(7)
Si2b	-0.0013(7)	-0.2823(4)	0.2475(15)	0.0115	0.0189	0.0200	0	0.0024	0	0.0168
Si3a	0.3412(5)	0.1080(5)	0.0030(2)	0.0158(13)	0.0193(12)	0.0051(12)	0.0011(10)	0	0	0.0134(7)
Si3b	-0.3378(5)	0.1038(5)	0.4961(10)	0.0158	0.0193	0.0051	-0.0011	0	0	0.0134
Crystal A at $T = 75$ K										
Er1a	0.2696(1)	0.3679(1)	0.0021(2)	0.0113(2)	0.0153(2)	0.0193(2)	0.0001(1)	0	0	0.0153(1)
Er1b	-0.2701(1)	0.3671(1)	0.4981(2)	0.0113	0.0153	0.0193	-0.0001	0	0	0.0153
Ir1a	0.1088(1)	0.1403(1)	-0.0147(1)	0.0106(2)	0.0149(2)	0.0189(2)	0.0005(1)	0	0	0.0148(1)
Ir1b	-0.1086(1)	0.1408(1)	0.5144(1)	0.0106	0.0149	0.0189	-0.0005	0	0	0.0148
Ir2	0.4998(1)	-0.0012(1)	0.2499(2)	0.0111(2)	0.0169(2)	0.0202(3)	0	0	0	0.0161(1)
Si1	-0.0004(6)	0.0083(3)	0.2501(12)	0.0169(15)	0.0126(16)	0.0076(16)	0	0	0	0.0124(9)
Si2a	0.0004(6)	0.2718(3)	0.2519(13)	0.0126(10)	0.0128(10)	0.0218(13)	0	0.0015(9)	0	0.0157(7)
Si2b	-0.0009(6)	-0.2833(3)	0.2497(13)	0.0126	0.0128	0.0218	0	0.0015	0	0.0157
Si3a	0.3417(5)	0.1066(5)	0.0001(10)	0.0151(12)	0.0234(13)	0.0116(13)	0.0055(10)	0	0	0.0167(7)
Si3b	-0.3376(5)	0.1030(5)	0.4981(10)	0.0151	0.0234	0.0116	-0.0055	0	0	0.0167
Crystal A at $T = 20$ K										
Er1a	0.2697(1)	0.3677(1)	0.0019(2)	0.0113(2)	0.0151(2)	0.0201(3)	0.0003(2)	0	0	0.0155(1)
Er1b	-0.2702(1)	0.3673(1)	0.4980(2)	0.0113	0.0151	0.0201	0.0003	0	0	0.0155
Ir1a	0.1089(1)	0.1404(1)	-0.0146(2)	0.0097(2)	0.0158(2)	0.0204(2)	0.0005(1)	0	0	0.0159(1)
Ir1b	-0.1088(1)	0.1405(1)	0.5138(2)	0.0097	0.0158	0.0204	-0.0005	0	0	0.0159
Ir2	0.4996(1)	-0.0012(1)	0.2497(2)	0.0099(3)	0.0168(2)	0.0222(3)	0	0	0	0.0163(1)
Si1	-0.0011(7)	0.0087(3)	0.2467(13)	0.0173(16)	0.0110(16)	0.0151(16)	0	0	0	0.0010(9)
Si2a	-0.0020(7)	0.2708(4)	0.2533(15)	0.0127(12)	0.0186(12)	0.0168(14)	0	0.0034(10)	0	0.0160(7)
Si2b	-0.0002(7)	-0.2838(4)	0.2461(15)	0.0127	0.0186	0.0168	0	0.0034	0	0.0160
Si3a	0.3408(5)	0.1069(5)	0.0001(11)	0.0108(13)	0.0185(13)	0.0091(13)	0.0026(10)	0	0	0.0128(7)
Si3b	-0.3376(6)	0.1044(5)	0.4978(11)	0.00108	0.0185	0.0091	-0.0026	0	0	0.0128

Table B9: Amplitudes of the modulation functions of crystal A. Values according to Eq. B8 have been multiplied by the corresponding lattice parameter, in order to obtain values in Å.

Atom	$A_{1,x} a$ (Å)	$A_{1,y} b$ (Å)	$A_{1,z} c$ (Å)	$B_{1,x} a$ (Å)	$B_{1,y} b$ (Å)	$B_{1,z} c$ (Å)
Crystal A at $T = 130$ K						
Er1a	0.0330(13)	-0.0982(13)	0.0578(16)	0.0244(13)	0.0033(13)	-0.0176(17)
Er1b	0.0554(14)	-0.0687(13)	0.0518(16)	-0.0328(13)	0.0202(13)	0.0145(16)
Ir1a	0.0718(12)	-0.0577(11)	0.1187(15)	0.0921(12)	-0.0370(11)	0.1003(15)
Ir1b	0.0994(12)	-0.0897(11)	0.1056(15)	-0.0951(12)	0.0014(11)	-0.1163(15)
Ir2	0.1027(11)	-0.0894(10)	0.0491(13)	0.0214(12)	0.0092(12)	0.0076(14)
Si1	0.0615(84)	-0.1081(75)	0.0554(90)	0.0160(96)	-0.1067(84)	0.099(101)
Si2a	0.0773(81)	-0.0824(77)	0.0643(97)	-0.0034(87)	-0.0093(82)	-0.0163(102)
Si2b	0.0820(81)	-0.1244(80)	-0.0235(98)	0.0046(89)	0.1446(83)	-0.0256(106)
Si3a	0.0944(81)	-0.0921(82)	0.0522(91)	0.0529(81)	0.0058(71)	0.0106(91)
Si3b	0.1220(83)	-0.0697(83)	0.0375(90)	-0.0315(81)	0.0134(81)	-0.0008(90)
Crystal A at $T = 75$ K						
Er1a	0.0336(12)	-0.0992(12)	0.0568(15)	0.0243(13)	0.0032(12)	-0.0180(16)
Er1b	0.0567(13)	-0.0707(12)	0.0524(15)	-0.0331(13)	0.0207(12)	0.0154(15)
Ir1a	0.0732(12)	-0.0587(10)	0.1199(14)	0.0929(12)	-0.0376(11)	0.1006(14)
Ir1b	0.1001(12)	-0.0902(11)	0.1046(14)	-0.0966(12)	0.0007(10)	-0.1171(14)
Ir2	0.1052(13)	-0.0905(10)	0.0491(12)	0.0212(11)	0.0010(11)	0.0075(13)
Si1	0.0566(79)	-0.1130(76)	0.0627(92)	0.0111(92)	-0.1076(85)	0.0147(102)
Si2a	0.0932(78)	-0.0832(74)	0.0726(96)	-0.0051(83)	-0.0085(79)	-0.0139(101)
Si2b	0.0742(79)	-0.1063(78)	-0.0219(97)	0.0073(87)	0.1321(80)	-0.0332(106)
Si3a	0.0894(81)	-0.1014(79)	0.0565(94)	0.0567(80)	0.0092(79)	0.0120(93)
Si3b	0.1289(84)	-0.0799(81)	0.0340(94)	-0.0362(83)	0.0154(79)	0.0009(94)
Crystal A at $T = 20$ K						
Er1a	0.0337(15)	-0.0971(15)	0.0534(18)	0.0242(15)	0.0029(15)	-0.0154(19)
Er1b	0.0579(16)	-0.0679(15)	0.0495(18)	-0.0322(15)	0.0191(14)	0.0147(19)
Ir1a	0.0731(14)	-0.0568(13)	0.1181(17)	0.0925(14)	-0.0367(13)	0.0987(17)
Ir1b	0.0991(14)	-0.0890(11)	0.1035(17)	-0.0959(14)	-0.0002(13)	-0.1155(17)
Ir2	0.1026(13)	-0.0875(12)	0.0471(15)	0.0196(14)	0.0010(14)	0.0065(16)
Si1	0.0578(98)	-0.1070(87)	0.0596(101)	0.0196(112)	-0.0985(97)	0.0150(111)
Si2a	0.0889(94)	-0.0871(90)	0.0572(110)	-0.0008(100)	-0.0123(96)	-0.0077(115)
Si2b	0.0774(95)	-0.1216(96)	-0.0285(111)	0.0100(105)	0.1429(98)	-0.0202(120)
Si3a	0.0892(94)	-0.0945(94)	0.0496(104)	0.0501(94)	0.0076(94)	0.0099(104)
Si3b	0.1152(96)	-0.0654(95)	0.0305(103)	-0.0341(93)	0.0123(92)	0.0004(102)

Two projections of the basic structure are provided in Fig. B3. Furthermore, a series of figures is given providing t plots of interatomic distances and of atomic modulation functions (Figs. B4–B30).

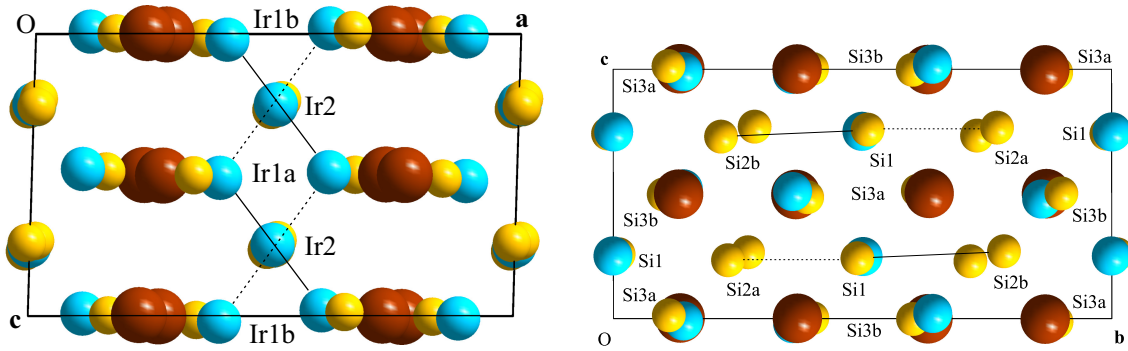


Figure B3: The crystal structure of $\text{Er}_2\text{Ir}_3\text{Si}_5$ at 75 K projected onto (left:) the (\mathbf{a}, \mathbf{c}) -plane and (right:) the (\mathbf{a}, \mathbf{b}) -plane. Large red spheres correspond to Er atoms; blue spheres of intermediate size correspond to Ir atoms; small yellow spheres are Si atoms. Ir1a–Ir1b atoms are at a basic-structure distance of $3.763(6) \text{ \AA}$ for the dashed lines and of $3.390(6) \text{ \AA}$ for the solid lines.

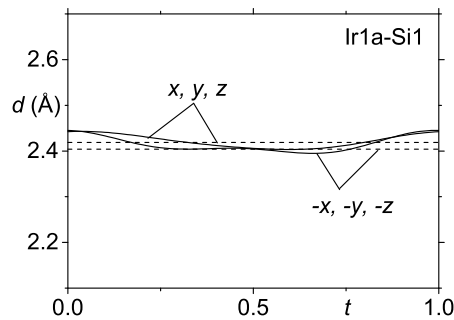


Figure B4: t -Plot of interatomic distances d (\AA) of Ir1a–Si1 at 75 K, where Ir1a is the central atom and Si1 is the neighbor.

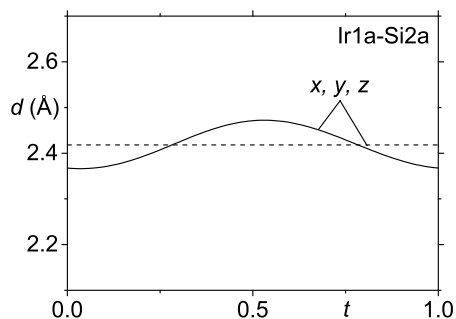


Figure B5: t -Plot of interatomic distances d (Å) of Ir1a-Si2a at 75 K, where Ir1a is the central atom and Si2a is the neighbor.

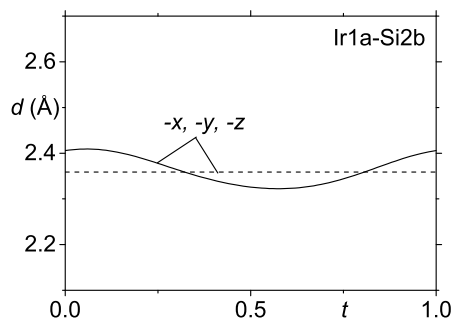


Figure B6: t -Plot of interatomic distances d (Å) of Ir1a-Si2b at 75 K, where Ir1a is the central atom and Si2b is the neighbor.

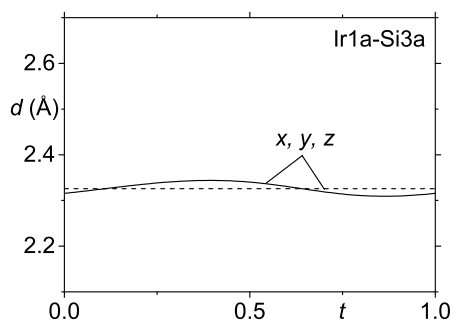


Figure B7: t -Plot of interatomic distances d (Å) of Ir1a-Si3a at 75 K, where Ir1a is the central atom and Si3a is the neighbor.

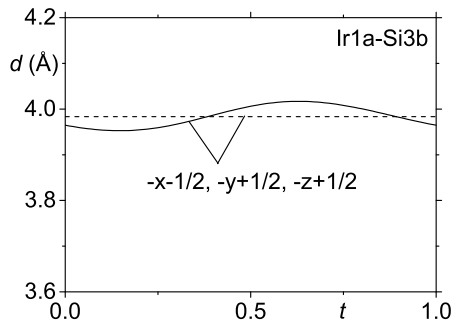


Figure B8: t -Plot of interatomic distances d (Å) of Ir1a-Si3b at 75 K, where Ir1a is the central atom and Si3b is the neighbor.

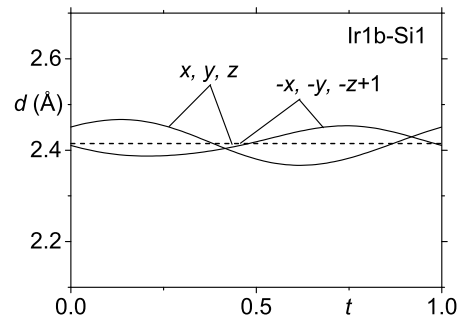


Figure B9: t -Plot of interatomic distances d (Å) of Ir1b-Si1 at 75 K, where Ir1b is the central atom and Si1 is the neighbor.

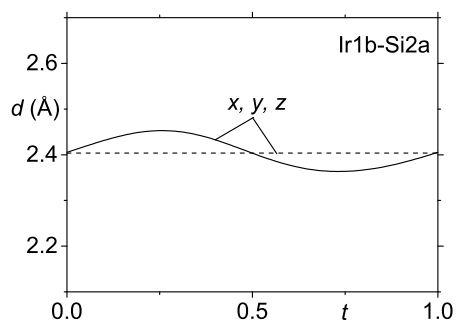


Figure B10: t -Plot of interatomic distances d (Å) of Ir1b-Si2a at 75 K, where Ir1b is the central atom and Si2a is the neighbor.

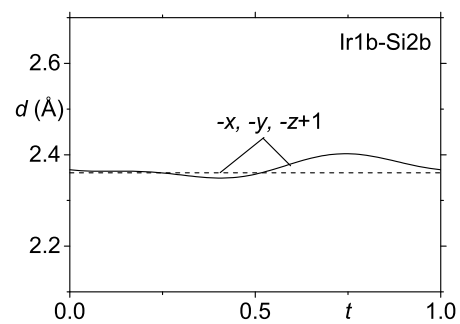


Figure B11: t -Plot of interatomic distances d (Å) of Ir1b-Si2b at 75 K, where Ir1b is the central atom and Si2b is the neighbor.

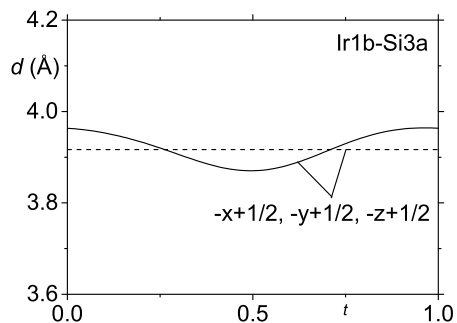


Figure B12: t -Plot of interatomic distances d (Å) of Ir1b-Si3a at 75 K, where Ir1b is the central atom and Si3a is the neighbor.

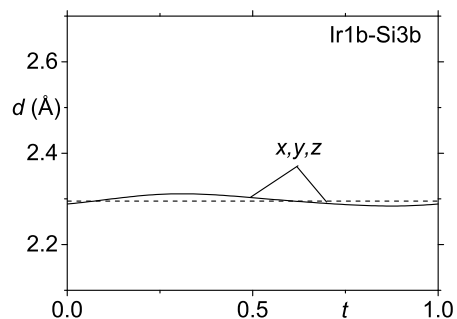


Figure B13: t -Plot of interatomic distances d (Å) of Ir1b-Si3b at 75 K, where Ir1b is the central atom and Si3b is the neighbor.

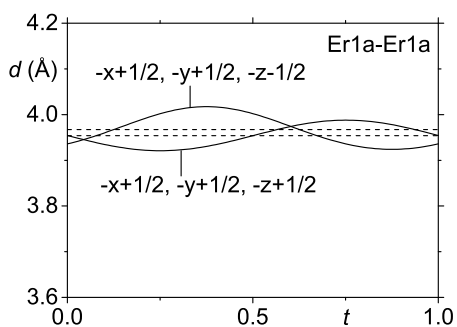


Figure B14: t -Plot of interatomic distances d (Å) of Er1a-Er1a at 75 K.

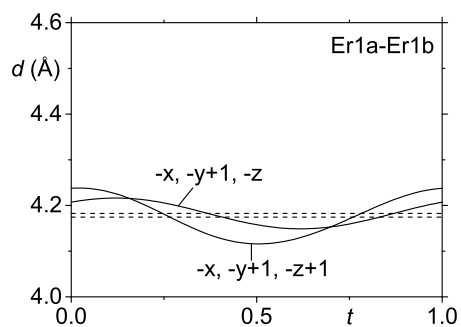


Figure B15: t -Plot of interatomic distances d (Å) of Er1a-Er1b at 75 K, where Er1a is the central atom and Er1b is the neighbor.

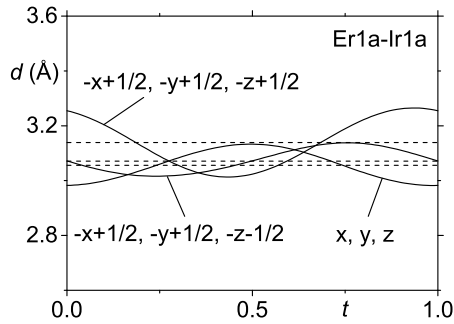


Figure B16: t -Plot of interatomic distances d (Å) of Er1a-Ir1a at 75 K, where Er1a is the central atom and Ir1a is the neighbor.

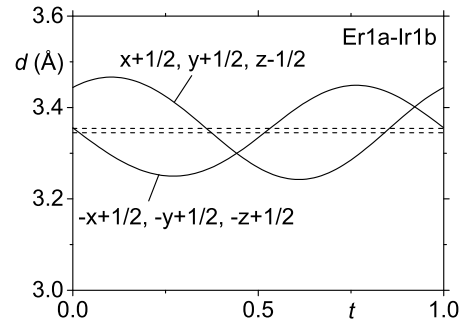


Figure B17: t -Plot of interatomic distances d (Å) of Er1a-Ir1b at 75 K, where Er1a is the central atom and Ir1b is the neighbor.

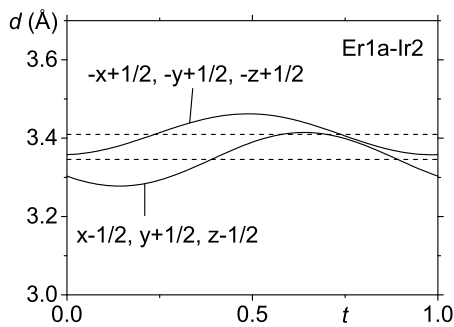


Figure B18: t -Plot of interatomic distances d (Å) of Er1a-Ir2 at 75 K, where Er1a is the central atom and Ir2 is the neighbor.

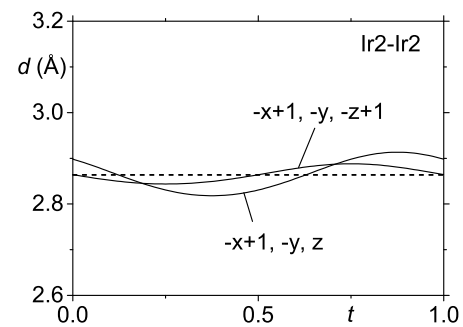


Figure B19: t -Plot of interatomic distances d (Å) of Ir2-Ir2 at 75 K.

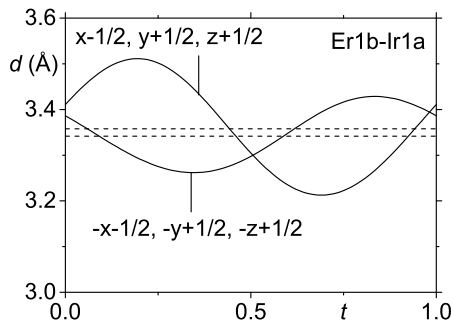


Figure B20: t -Plot of interatomic distances d (Å) of Er1b–Ir1a at 75 K, where Er1b is the central atom and Ir1a is the neighbor.

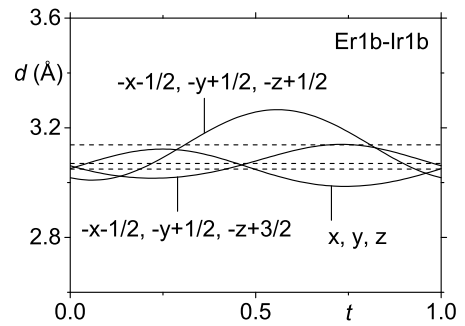


Figure B21: t -Plot of interatomic distances d (Å) of Er1b–Ir1b at 75 K, where Er1b is the central atom and Ir1b is the neighbor.

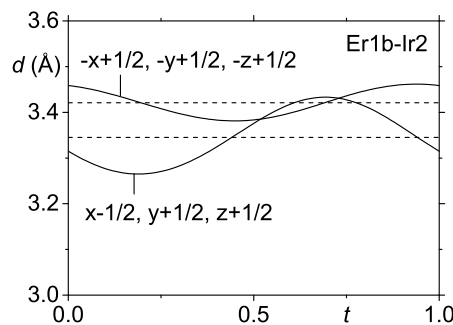


Figure B22: t -Plot of interatomic distances d (Å) of Er1b–Ir2 at 75 K, where Er1b is the central atom and Ir2 is the neighbor.

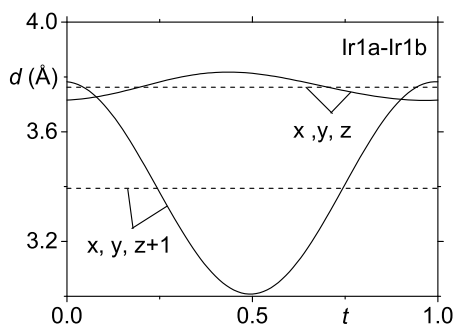


Figure B23: t -Plot of interatomic distances d (Å) of Ir1a-Ir1b at 75 K, where Ir1a is the central atom and Ir1b is the neighbor.

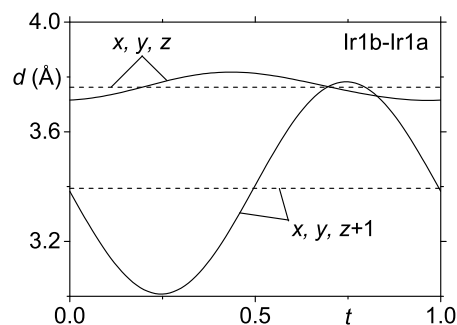


Figure B24: t -Plot of interatomic distances d (Å) of Ir1b-Ir1a at 75 K, where Ir1b is the central atom and Ir1a is the neighbor.

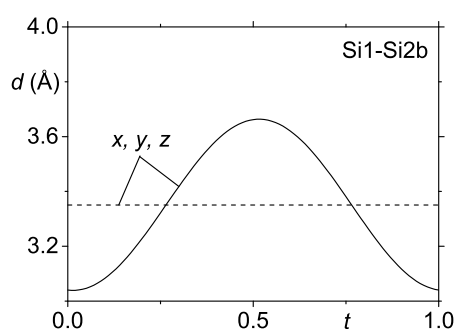
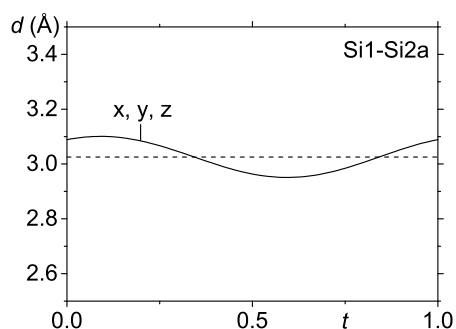


Figure B25: t -Plot of interatomic distances d (Å) of Si1-Si2a and of Si1-Si2b at 75 K, where Si1 is the central atom and Si2a and Si2b are neighbors.

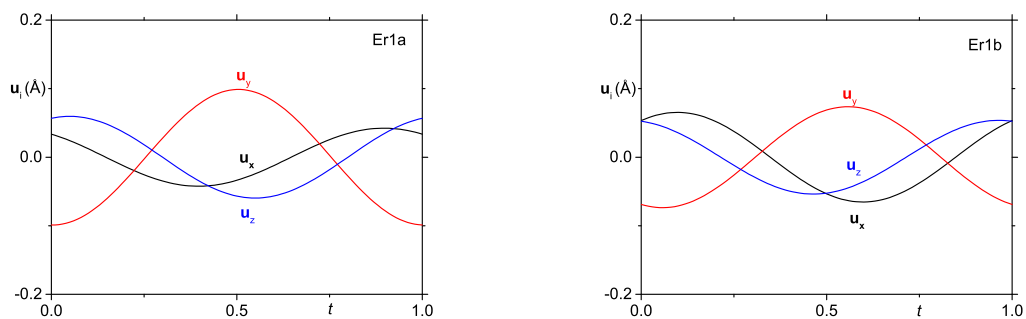


Figure B26: t -Plot of displacement modulation of Er1a and Er1b at 75 K.

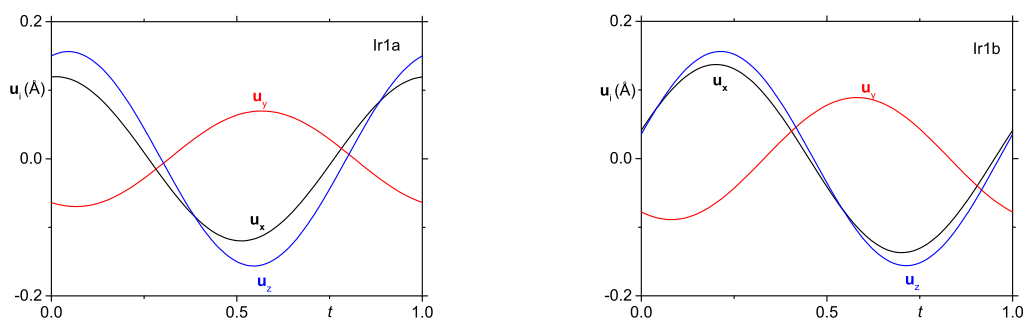


Figure B27: t -Plot of displacement modulation of Ir1a and Ir1b at 75 K.

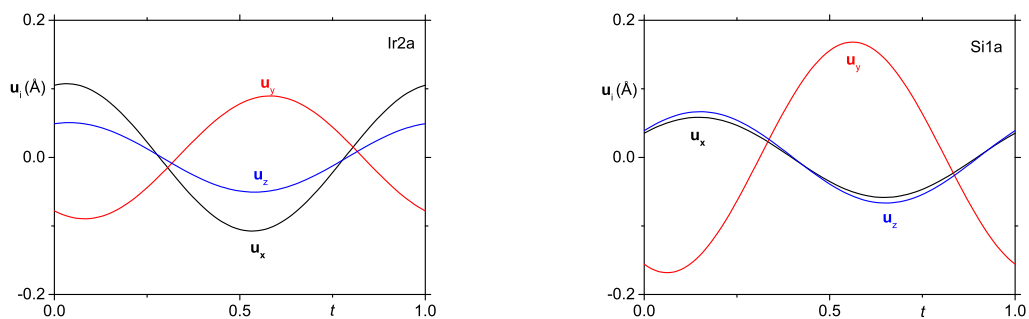
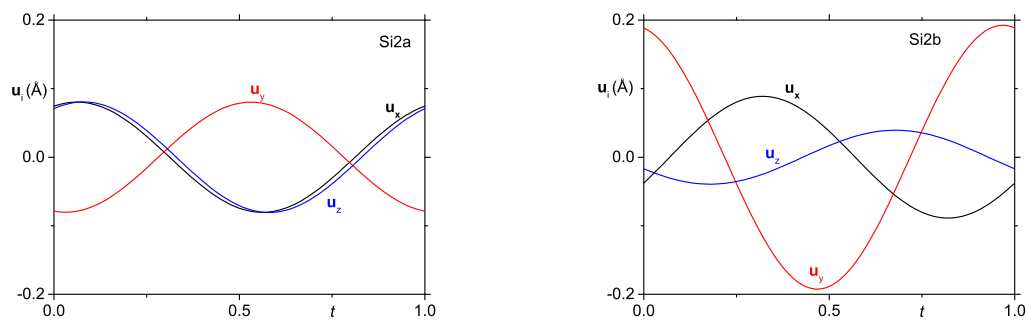
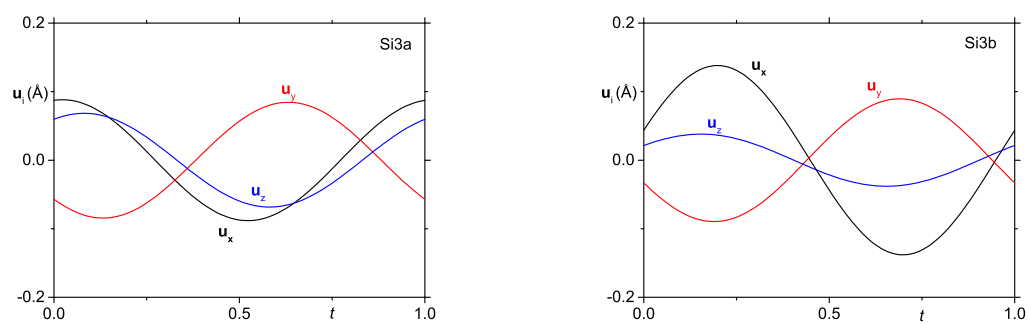


Figure B28: t -Plot of displacement modulation of Ir2 and Si1 at 75 K.

Figure B29: t -Plot of displacement modulation of Si2a and Si2b at 75 K.Figure B30: t -Plot of displacement modulation of Si3a and Si3b at 75 K.

Bibliography

- [1] Charles Kittel. *Introduction to solid state physics, 8th Edition*. Wiley, Berkley, California, 2004. (Cited in pages: 11)
- [2] Pierre Monceau. Electronic crystals: an experimental overview. *Adv. Phys.*, **61**(4):325–581, 2012. (Cited in pages: 11, 54)
- [3] George Gruner. *Density waves in solids*. Addison–Wesley, Reading, Massachusetts, 1994. (Cited in pages: 11, 54)
- [4] Brent Fultz. *Phase Transitions in Materials*. Cambridge University Press, 2014. (Cited in pages: 12)
- [5] Donald W. Rogers. *Concise Physical Chemistry*. Wiley, Hoboken, New Jersey, 2011. (Cited in pages: 13)
- [6] P. Monceau, N. P. Ong, A. M. Portis, A. Meerschaut, and J. Rouxel. Electric field breakdown of charge-density-wave—induced anomalies in NbSe₃. *Phys. Rev. Lett.*, **37**:602–606, 1976. (Cited in pages: 13, 17)
- [7] H Ando, T Yokoya, K Ishizaka, S Tsuda, T Kiss, S Shin, T Eguchi, M Nohara, and H Takagi. Angle-resolved photoemission study of K_{0.3}MoO₃: direct observation of temperature-dependent fermi surface across the peierls transition. *Journal of Physics: Condensed Matter*, **17**(32):4935–4940, 2005. (Cited in pages: 13, 18)
- [8] H. J. Bernstein and A. P. Hammersley. Chapter 1 introduction to highly conducting quasi-one-dimensional organic crystals. In E. M. Conwell, editor, *Semiconductors and Semimetals*, volume 27, pages 1–27. 1988. (Cited in pages: 14)
- [9] Chih-Wei Chen, Jesse Choe, and E. Morosan. Charge density waves in strongly correlated electron systems. *Rep. Prog. Phys.*, **79**(8):084505, 2016. (Cited in pages: 14, 54)

- [10] Xuetao Zhu, Jiandong Guo, Jiandi Zhang, and E. W. Plummer. Misconceptions associated with the origin of charge density waves. *Advances in Physics: X*, **2**(3):622–640, 2017. (Cited in pages: 14, 15, 19)
- [11] W. Kohn. Image of the Fermi surface in the vibration spectrum of a metal. *Phys. Rev. Lett.*, **2**:393–394, 1959. (Cited in pages: 14)
- [12] S K Chan and V Heine. Spin density wave and soft phonon mode from nesting fermi surfaces. *Journal of Physics F: Metal Physics*, **3**(4):795–809, 1973. (Cited in pages: 15)
- [13] S. A. Kivelson, I. P. Bindloss, E. Fradkin, V. Oganesyan, J. M. Tranquada, A. Kapitulnik, and C. Howald. How to detect fluctuating stripes in the high-temperature superconductors. *Rev. Mod. Phys.*, **75**:1201–1241, 2003. (Cited in pages: 15)
- [14] R. E. Peierls. *Quantum Theory of Solids*. Oxford University, New York, 1955. (Cited in pages: 15)
- [15] Sander van Smaalen. The Peierls transition in low-dimensional electronic crystals. *Acta Crystallographica Section A*, **61**(1):51–61, 2005. (Cited in pages: 16)
- [16] J. L. Hodeau, M. Marezio, C. Roucau, R. Ayroles, A. Meerschaut, J. Rouxel and P. Monceau. Charge-density waves in NbSe₃ at 145 K: crystal structures, X-ray and electron diffraction studies. *Journal of Physics C: Solid State Physics*, **11**(20):4117–4134, 1978. (Cited in pages: 18)
- [17] Diamond Crystal and Molecular Structure Visualization. Crystal Impact- Dr. H. Putz and Dr. K. Brandenburg Gbr, Kreuzherrenstr. 102, 53227 Bonn, Germany. <http://www.crystalimpact.com/diamond>. (Cited in pages: 18, 20, 21, 29)
- [18] H. Bartl, D. Schuster, F. A Schroeder. Verfeinerung der Kristallstruktur der blauen Kalium Molybdaen-bronze, K_{0.3}MoO₃, durch Roentgenbeugung. *Zeitschrift für Kristallographie (149,1979-)*, **149**:127–128, 1979. (Cited in pages: 18)
- [19] J. A. Wilson, F. J. Di Salvo, and S. Mahajan. Charge-density waves and superlattices in the metallic layered transition metal dichalcogenides. *Advances in Physics*, **24**(2):117–201, 1975. (Cited in pages: 19)
- [20] Xuetao Zhu, Yanwei Cao, Jiandi Zhang, E W Plummer, and Jiandong Guo. Classification of charge density waves based on their nature. *Proc. Natl. Acad. Sci. U. S. A.*, **112**(8):2367–2371, 2015. (Cited in pages: 19, 54)

- [21] Michio Naito and Shoji Tanaka. Electrical transport properties in 2H-NbS₂, -NbSe₂, -TaS₂ and -TaSe₂. *Journal of the Physical Society of Japan*, **51**:219–227, 1982. (Cited in pages: 19)
- [22] C. M. Varma and A. L. Simons. Strong-coupling theory of charge-density-wave transitions. *Phys. Rev. Lett.*, **51**:138–141, 1983. (Cited in pages: 19)
- [23] Koichi Momma and Fujio Izumi. *VESTA3* for three-dimensional visualization of crystal, volumetric and morphology data. *Journal of Applied Crystallography*, **44**(6):1272–1276, 2011. (Cited in pages: 19)
- [24] K. Selte and A. Kjekshus. On the Structural Properties of the Nb_{1+x}Se₂ phase. *Acta Chemica Scandinavica 1947 - 1999*, **18**:697–706, 1964. (Cited in pages: 19)
- [25] S. Ramakrishnan and Sander van Smaalen. *Rep. Prog. Phys.*, **80**:116501, 2017. (Cited in pages: 20, 78, 81, 85)
- [26] Yogesh Singh, Dilip Pal, S. Ramakrishnan, A. M. Awasthi, and S. K. Malik. Phase transitions in Lu₂Ir₃Si₅. *Phys. Rev. B*, **71**(4):045109, 2005. (Cited in pages: 20, 78, 79, 80)
- [27] N. S. Sangeetha, A. Thamizhavel, C. V. Tomy, Saurabh Basu, A. M. Awasthi, Piu Rajak, Somnath Bhattacharyya, S. Ramakrishnan, and D. Pal. Multiple charge density wave transitions in single-crystalline Lu₂Ir₃Si₅. *Phys. Rev. B*, **91**:205131, 2015. (Cited in pages: 20, 79, 80, 81, 82, 86)
- [28] E. DiMasi, B. Foran, M. C. Aronson, and S. Lee. *Phys. Rev. B.*, **54**(19):13587–13596, 1996. (Cited in pages: 20, 78)
- [29] E. DiMasi, M. C. Aronson, J. F. Mansfield, B. Foran, and S. Lee. *Phys. Rev. B.*, **52**(20):14516–14531, 1995. (Cited in pages: 20, 78)
- [30] Kefeng Wang and C. Petrovic. Ca₃Ir₄Sn₁₃: A weakly correlated nodeless superconductor. *Phys. Rev. B*, **86**:024522, 2012. (Cited in pages: 20)
- [31] R. M. Fleming, F. J. DiSalvo, R. J. Cava, and J. V. Waszczak. Observation of charge-density waves in the cubic spinel structure CuV₂S₄. *Phys. Rev. B*, **24**:2850–2853, 1981. (Cited in pages: 20, 26, 34, 54, 55, 59, 65, 78, 155)
- [32] Shogo Kawaguchi, Hiroki Ishibashi, Naruki Tsuji, Jungeun Kim, Kenichi Kato, Masaki Takata, and Yoshiki Kubota. Structural properties in incommensurately modulated spinel compound CuV₂S₄. *J. Phys. Soc. Jpn*, **82**(6):064603, 2013. (Cited in pages: 21, 26, 27, 55, 65, 66, 69, 70, 71, 72, 75, 107, 109, 110)

- [33] R. Padam, A. Thamizhavel, S. Ravi, S. Ramakrishnan, and D. Pal. *AIP Conference Proceedings*, **1447**:1007–1008, 2012. (Cited in pages: 21, 27, 34, 78, 86, 131, 133)
- [34] P. C. Lalngilneia, A. Thamizhavel, S. Ramakrishnan, and D. Pal. Coupling of rare earth moment and charge density wave ordering in a single crystal $\text{Er}_2\text{Ir}_3\text{Si}_5$. *J. Phys.: Conf. Ser.*, **592**:012094, 2015. (Cited in pages: 21, 27, 34, 78, 80)
- [35] C. Giacovazzo, H. Monaco, G. Artioli, D. Viterbo, G. Ferraris, G. Gilli, G. Zan-noti, and M. Catti. *Fundamentals of Crystallography*. Oxford University Press, Oxford, 2011. (Cited in pages: 22)
- [36] Rob Lavinsky iRocks.com. Crystal twinning. Link to image: <https://commons.wikimedia.org/wiki/File:Quartz-rhqtz-109b.jpg>. Accessed: 09.02.2020. Link to licence: (Attribution- CC BY-SA): <https://creativecommons.org/licenses/by-sa/3.0>. (Cited in pages: 22)
- [37] Simon Parsons. Introduction to twinning. *Acta Crystallographica Section D*, **59**(11):1995–2003, 2003. (Cited in pages: 23, 24)
- [38] Massimo Nespolo. Link to page: <http://www.crystallography.fr/mathcryst/twins.htm>, 2009. Accessed: 14.02.2020. (Cited in pages: 24)
- [39] P. Locher. *Z. Angew. Phys.*, **24**(277), 1968. (Cited in pages: 26)
- [40] N. Le Nagard, A. Katty, G. Collin, O. Gorochov, and A. Willig. Elaboration, Structure Crystalline et Proprietes Physiques (transport, susceptibilite magnetique et R.M.N) de Spinelle CuV_2S_4 . *J. Solid State Chem.*, **27**(267), 1979. (Cited in pages: 26)
- [41] Hironari Okada, Keiichi Koyama, and Kazuo Watanabe. Two-step structural modulations and Fermi liquid state in spinel compound CuV_2S_4 . *J. Phys. Soc. Jpn*, **73**(12):3227–3230, 2004. (Cited in pages: 26, 55, 60, 69)
- [42] Robert Horny. *Struktur und Transporteigenschaften des elektronisch korrelierten Thiospinells CuV_2S_4* . PhD thesis, University of Augsburg, Augsburg, Germany, 2005. (Cited in pages: 26, 54, 55, 56, 58, 59, 75)
- [43] G. Venturini, M. Méot-Meyer, J. F. Marêché, B. Malaman, B. Roques. De nouveaux isotopes de $\text{U}_2\text{Co}_3\text{Si}_5$ ou $\text{Lu}_2\text{Co}_3\text{Si}_5$ dans les systems R-T-Ge (R = elements des terres rares; T = Ru, Co, Rh, Ir). supraconductivite de $\text{Y}_2\text{Ir}_3\text{Ge}_5$. *Mat. Res. Bull*, **21**(1):33 – 39, 1985. (Cited in pages: 27)

- [44] M. H. Lee, C. H. Chen, M.-W. Chu, C. S. Lue, and Y. K. Kuo. Electronically phase-separated charge-density waves in $\text{Lu}_2\text{Ir}_3\text{Si}_5$. *Phys. Rev. B*, **83**(15):155121, 2011. (Cited in pages: 28, 78, 84)
- [45] Sander van Smaalen. *Incommensurate Crystallography*. Oxford University Press, Oxford, 2012. (Cited in pages: 28)
- [46] Yogesh Singh, D. Pal, and S. Ramakrishnan. Low-temperature studies of the magnetic and superconducting properties of the $R_2\text{Ir}_3\text{Si}_5$ ($R = \text{Y, La, Ce-Nd, Gd-Tm}$) system. *Phys. Rev. B*, **70**(6):064403, 2004. (Cited in pages: 29, 78, 79, 86)
- [47] F. Galli, R. Feyerherm, R. W. A. Hendrikx, S. Ramakrishnan, G. J. Nieuwenhuys, and J. A. Mydosh. Magnetic structure of the Er^{3+} moments in the charge-density-wave compound $\text{Er}_5\text{Ir}_4\text{Si}_{10}$. *Phys. Rev. B*, **62**:13840–13843, 2000. (Cited in pages: 29, 83)
- [48] Y. K. Kuo, K. M. Sivakumar, J. Y. Lin, C. N. Kuo, and C. S. Lue. First-order phase transition in the ternary sulfide NiV_2S_4 . *J. Phys.: Condens. Matter*, **19**:216210, 2007. (Cited in pages: 29, 54, 89, 90)
- [49] R. J. Bouchard and A. Wold. Structural and electrical properties of some monoclinic ternary sulfides. *J. Phys. Chem. Solids*, **27**:591–595, 1966. (Cited in pages: 29, 89, 90, 95)
- [50] Antoine M. M. Schreurs, Xinyi Xian, and Loes M. J. Kroon-Batenburg. EVAL15: a diffraction data integration method based on ab initio predicted profiles. *J. Appl. Crystallogr.*, **43**:70–82, 2010. (Cited in pages: 33, 102, 105, 113, 131, 160)
- [51] G. M. Sheldrick. *SADABS, Version 2008/1*. Göttingen: University of Göttingen, 2008. (Cited in pages: 33, 37, 43, 102, 105, 113, 131)
- [52] Vadim Dyadkin, Philip Pattison, Vladimir Dmitriev, and Dmitry Chernyshov. A new multipurpose diffractometer PILATUS@SNBL. *J. Synchrotron Rad.*, **23**(3):825–829, 2016. (Cited in pages: 34, 56)
- [53] Christian Brönnimann and Peter Trüb. *Hybrid Pixel Photon Counting X-Ray Detectors for Synchrotron Radiation*, pages 995–1027. Springer International Publishing, 2016. (Cited in pages: 34)
- [54] Ch. Broennimann, E. F. Eikenberry, B. Henrich, R. Horisberger, G. Huelsen, E. Pohl, B. Schmitt, C. Schulze-Briesse, M. Suzuki, T. Tomizaki, H. Toyokawa, and A. Wagner. The PILATUS 1M detector. *Journal of Synchrotron Radiation*, **13**(2):120–130, Mar 2006. (Cited in pages: 34)

- [55] H. J. Bernstein and A. P. Hammersley. Specification of the crystallographic binary file (cbf/imgcif). In S. Hall and B. McMahon, editors, *International Tables for Crystallography Vol. G*, pages 37–43. 2005. (Cited in pages: 35)
- [56] V. Petricek, M. Dusek, and L. Palatinus. Crystallographic computing system JANA2006: general features. *Z. Kristallogr.*, **229**:345–352, 2014. (Cited in pages: 44, 47, 51, 69, 107, 120, 136, 137, 160)
- [57] C. Schlenker, J. Dumas, M. Greenblatt, and S. van Smaalen, editors. *Physics and chemistry of low-dimensional inorganic conductors*, volume 354 of *NATO ASI Series B: Physics*. Plenum Press, New York, 1996. (Cited in pages: 54)
- [58] J. Chaussy, P. Haen, J. C. Lasjaunias, P. Monceau, G. Waysand, A. Waintal, A. Meerschaut, P. Molinie, and J. Rouxel. Phase transitions in NbSe₃. *Sol. State Commun.*, **20**:759–763, 1976. (Cited in pages: 54)
- [59] M. D. Johannes and I. I. Mazin. Fermi surface nesting and the origin of charge density waves in metals. *Phys. Rev. B*, **77**(16):165135, 2008. (Cited in pages: 54)
- [60] T. Ritschel, J. Trinckauf, K. Koepf, B. Buchner, M. v. Zimmermann, H. Berger, Y. I. Joe, P. Abbamonte, and J. Geck. Orbital textures and charge density waves: towards orbitronics in transition metal dichalcogenides. *Nat. Phys.*, **11**(april):328–331, 2015. (Cited in pages: 54)
- [61] S. Ramakrishnan and Sander van Smaalen. Unusual ground states in $R_5T_4X_{10}$ (R = rare earth; T = Rh, Ir; and X = Si, Ge, Sn): a review. *Rep. Prog. Phys.*, **80**(11):116501, 2017. (Cited in pages: 54)
- [62] S. Shimomura, C. Hayashi, G. Asaka, N. Wakabayashi, M. Mizumaki, and H. Onodera. Charge-density-wave destruction and ferromagnetic order in SmNiC₂. *Phys. Rev. Lett.*, **102**(07):076404, 2009. (Cited in pages: 54)
- [63] S. Shimomura, C. Hayashi, N. Hanasaki, K. Ohnuma, Y. Kobayashi, H. Nakao, M. Mizumaki, and H. Onodera. Multiple charge density wave transitions in the antiferromagnets RNiC₂ (R = Gd, Tb). *Phys. Rev. B*, **93**:165108, Apr 2016. (Cited in pages: 54, 78)
- [64] Kamil K. Kolincio, Marta Roman, Michal J. Winiarski, Judyta Strychalska-Nowak, and Tomasz Klimczuk. Magnetism and charge density waves in RNiC₂ (R = Ce, Pr, Nd). *Phys. Rev. B*, **95**(23):235156, 2017. (Cited in pages: 54)
- [65] Marta Roman, Judyta Strychalska-Nowak, Tomasz Klimczuk, and Kamil K. Kolincio. Extended phase diagram of RNiC₂ family: Linear scaling of the

- Peierls temperature. *Phys. Rev. B*, **97**(4):041103(R), 2018. (Cited in pages: 54, 77, 78)
- [66] Yuka Otomo, Kazuaki Iwasa, Kazuya Suyama, Keisuke Tomiyasu, Hajime Sagayama, Ryoko Sagayama, Hironori Nakao, Reiji Kumai, and Youichi Murakami. Chiral crystal-structure transformation of $R_3Co_4Sn_{13}$ ($R = La$ and Ce). *Phys. Rev. B*, **94**(7):075109, 2016. (Cited in pages: 54)
- [67] C. N. Kuo, C. W. Tseng, C. M. Wang, C. Y. Wang, Y. R. Chen, L. M. Wang, C. F. Lin, K. K. Wu, Y. K. Kuo, and C. S. Lue. Lattice distortion associated with Fermi-surface reconstruction in $Sr_3Rh_4Sn_{13}$. *Phys. Rev. B*, **91**(16):165141, 2015. (Cited in pages: 54)
- [68] H. T. Wang, M. K. Srivastava, C. C. Wu, S. H. Hsieh, Y. F. Wang, Y. C. Shao, Y. H. Liang, C. H. Du, J. W. Chiou, C. M. Cheng, J. L. Chen, C. W. Pao, J. F. Lee, C. N. Kuo, C. S. Lue, M. K. Wu, and W. F. Pong. Electronic and atomic structures of the $Sr_3Ir_4Sn_{13}$ single crystal: A possible charge density wave material. *Sci. Rep.*, **7**:40886, 2017. (Cited in pages: 54)
- [69] R. N. Shelton, L. S. Hausermann-Berg, P. Klavins, H. D. Yang, M. S. Anderson, and C. A. Swenson. Electronic phase transition and partially gapped Fermi surface in superconducting $Lu_5Ir_4Si_{10}$. *Phys. Rev. B*, **34**:4590–4594, 1986. (Cited in pages: 54)
- [70] E. Morosan, H. W. Zandbergen, B. S. Dennis, J. W. G. Bos, Y. Onose, T. Klimczuk, A. P. Ramirez, N. P. Ong, and R. J. Cava. Superconductivity in Cu_xTiSe_2 . *Nature Physics*, **2**:544–550, 2006. (Cited in pages: 54)
- [71] F. J. DiSalvo and J. V. Waszczak. Magnetic properties of copper chalcogenide spinels. *Phys. Rev. B*, **26**(5):2501–2506, 1982. (Cited in pages: 54)
- [72] Fleming *et al.* [31] incorrectly report "reduced" modulation wave vectors $\mathbf{q}_F = (\frac{1}{4} - \delta)(1, 1, 0)$ and $\mathbf{q}'_F = (\frac{1}{3} - \delta')(1, 1, 0)$, which are not equivalent to $\mathbf{q} = (1, 1, 0) - \mathbf{q}_F$ and $\mathbf{q}' = (1, 1, 0) - \mathbf{q}'_F$, because $(1, 1, 0)$ is a forbidden reflection of the F-centered lattice. (Cited in pages: 55)
- [73] Hironari Okada, Keiichi Koyama, and Kazuo Watanabe. Specific heat measurement of the spinel compound CuV_2S_4 . *AIP Conference Proceedings*, **850**(1):1317–1318, 2006. (Cited in pages: 55)
- [74] J. Mahy, D. Colaitis, D. van Dyck, and S. Amelinckx. Electron diffraction evidence for domain structures in the low-temperature incommensurate phase in CuV_2S_4 . *J. Sol. State Chem.*, **68**:320–329, 1987. (Cited in pages: 55)

- [75] R. Horny, S. Klimm, M. Klemm, S. Ebbinghaus, G. Eickerling, and S. Horn. Electronic transport and structural properties of electronically correlated CuV_2S_4 . *J. Magn. Magn. Mater.*, **272-276**:E307–E309, 2004. (Cited in pages: 55, 59, 63, 75)
- [76] C. Mujica, G. Carvajal, J. Llanos, and O. Wittke. Redetermination of the crystal structure of copper(I) tetrathiovanadate (sulfanite), Cu_3VS_4 . *Z. Kristallogr. NCS*, **213**:12–12, 1998. (Cited in pages: 56)
- [77] Peter van der Linden, Hugo Vitoux, Ricardo Steinmann, Beatrice Vallone, and Chiara Ardiccioni. An open flow helium cryostat for synchrotron x-ray diffraction experiments. *J. Phys.: Conf. Ser.*, **425**(1):012015, 2013. (Cited in pages: 57)
- [78] Th. Hahn, editor. *International Tables for Crystallography Vol. A, fifth edition*. Kluwer Academic Publishers, Dordrecht, 2002. (Cited in pages: 66, 100, 106)
- [79] H. T. Stokes, B. J. Campbell, and S. van Smaalen. Generation of $(3 + d)$ -dimensional superspace groups for describing the symmetry of modulated crystalline structures. *Acta Crystallogr. A*, **67**:45–55, 2011. (Cited in pages: 66, 84, 101, 104, 108, 115, 116, 117, 118, 130)
- [80] A. G. Jackson. *Handbook of Crystallography*. Springer-Verlag, New York, 1991. (Cited in pages: 68)
- [81] Z. W. Lu, B. M. Klein, E. Z. Kurmaev, V. M. Cherkashenko, V. R. Galakhov, S. N. Shamin, Yu. M. Yarmoshenko, V. A. Trofimova, St. Uhlenbrock, M. Neumann, T. Furubayashi, T. Hagino, and S. Nagata. Electronic structure of CuV_2S_4 . *Phys. Rev. B*, **53**:9626–9633, 1996. (Cited in pages: 71, 75)
- [82] J. Matsuno, A. Fujimori, L. F. Mattheiss, R. Endoh, and S. Nagata. Photoemission and band-calculation studies of the charge-density wave in CuV_2S_4 . *Phys. Rev. B*, **64**(11):115116, 2001. (Cited in pages: 71, 75)
- [83] Alexander Wölfel, Liang Li, Susumu Shimomura, Hideya Onodera, and Sander van Smaalen. Commensurate charge-density wave with frustrated interchain coupling in SmNiC_2 . *Phys. Rev. B*, **82**:054120, 2010. (Cited in pages: 72, 78)
- [84] George Grüner. *Charge Density Waves in Solids*. Addison-Wesley, Reading, Massachusetts, 1994. (Cited in pages: 77)
- [85] Peter Rogl. In K. A. Jr. Gschneidner and L. Eyring, editors, *Handbook of Physics and Chemistry of Rare Earths, Vol. 7*, pages 1–264. North-Holland, Amsterdam, 1984. (Cited in pages: 77)

- [86] Janusz Leciejewicz and Andrzej Szytula. In K. A. Jr. Gschneidner and L. Eyring, editors, *Handbook of Physics and Chemistry of Rare Earths, Vol. 12*, pages 133–211. North-Holland, Amsterdam, 1989. (Cited in pages: 77)
- [87] Hans F. Braun. *J. Less Common Metals*, **100**:105–124, 1984. (Cited in pages: 77)
- [88] J. C. Marmeggi, A. Delapalme, G. H. Lander, C. Vettier, and N. Lehner. Atomic displacements in the incommensurable charge-density wave in alpha-uranium. *Sol. Stat. Commun.*, **43**(7):577–581, 1982. (Cited in pages: 78)
- [89] S. Shimomura, C. Hayashi, G. Asaka, N. Wakabayashi, M. Mizumaki, and H. Onodera. *Phys. Rev. Lett.*, **102**:076404, 2009. (Cited in pages: 78)
- [90] Kamil K. Kolincio, Marta Roman, Michal J. Winiarski, Judyta Strychalska-Nowak, and Tomasz Klimczuk. Magnetism and charge density waves in $R\text{NiC}_2$ ($R = \text{Ce}, \text{Pr}, \text{Nd}$). *Phys. Rev. B*, **95**(23):235156, 2017. (Cited in pages: 78)
- [91] Y. K. Kuo, K. M. Sivakumar, T. H. Su, and C. S. Lue. Phase transitions in $\text{Lu}_2\text{Ir}_3\text{Si}_5$: An experimental investigation by transport measurements. *Phys. Rev. B*, **74**(4):045115, 2006. (Cited in pages: 78, 79, 80)
- [92] Masaki Murase, Aya Tobo, Hideya Onodera, Yukiko Hrano, Tadaaki Hosaka, Susumu Shimomura, and Nobuyoshi Wakabayashi. Lattice constants, electrical resistivity and specific heat of $R\text{NiC}_2$. *J. Phys. Soc. Jpn*, **73**(10):2790–2794, 2004. (Cited in pages: 78)
- [93] G. H. Gweon, J. D. Denlinger, J. A. Clack, J. W. Allen, C. G. Olson, E. DiMasi, M. C. Aronson, B. Foran, and S. Lee. *Phys. Rev. Lett.*, **81**(4):886–889, 1998. (Cited in pages: 78)
- [94] Jean Laugier and Bernard Bochu. *LMGP-Suite Suite of Programs for the interpretation of X-ray Experiments*. ENSP/Laboratoire des Matériaux et du Génie Physique, Saint Martin d’Hères, France, 2004. (Cited in pages: 79)
- [95] B. Becker, N. G. Patil, S. Ramakrishnan, A. A. Menovsky, G. J. Nieuwenhuys, J. A. Mydosh, M. Kohgi, and K. Iwasa. Strongly coupled charge-density wave transition in single-crystal $\text{Lu}_5\text{Ir}_4\text{Si}_{10}$. *Phys. Rev. B*, **59**:7266–7269, 1999. (Cited in pages: 79, 82)
- [96] P. C. Lalngilneia, A. Thamizhavel, S. Ramakrishnan, and D. Pal. Charge density wave in $\text{Er}_2\text{Ir}_3\text{Si}_5$ single crystal. *AIP Conf. Proc.*, **1591**:113–114, 2014. (Cited in pages: 80, 131, 133)

- [97] J. W. Brill, M. Chung, Y.-K. Kuo, X. Zhan, E. Figueroa, and G. Mozurkewich. *Phys. Rev. Lett.*, **74**:1182–1185, 1995. (Cited in pages: 82)
- [98] R. S. Kwok and S. E. Brown. *Phys. Rev. Lett.*, **63**:895–898, 1989. (Cited in pages: 82)
- [99] R. S. Kwok, G. Gruner, and S. E. Brown. *Phys. Rev. Lett.*, **65**:365–368, 1990. (Cited in pages: 82)
- [100] S. Tomić, K. Biljaković, D. Djurek, J.R. Cooper, P. Monceau, and A. Meerschaut. *Solid State Commun.*, **38**:109–112, 1981. (Cited in pages: 82)
- [101] F. Galli, R. Feyerherm, R. W. A. Hendriks, E. Dudzik, G. J. Nieuwenhuys, S. Ramakrishnan, S. D. Brown, S. van Smaalen, and J. A. Mydosh. Coexistence of charge density wave and antiferromagnetism in $\text{Er}_5\text{Ir}_4\text{Si}_{10}$. *J. Phys.: Condens. Matter*, **14**:5067–5075, 2002. (Cited in pages: 83)
- [102] F. Galli, S. Ramakrishnan, T. Taniguchi, G. J. Nieuwenhuys, J. A. Mydosh, S. Geupel, J. Ludecke, and S. van Smaalen. Charge-density-wave transitions in the local-moment magnet $\text{Er}_5\text{Ir}_4\text{Si}_{10}$. *Phys. Rev. Lett.*, **85**:158–161, 2000. (Cited in pages: 85)
- [103] K. Ghosh, S. Ramakrishnan, S. K. Dhar, S. K. Malik, G. Chandra, V. K. Pecharsky, K. A. Gschneidner, Z. Hu, and W. B. Yelon. Crystal structures and low-temperature behaviors of the heavy-fermion compounds CeRuGe_3 and $\text{Ce}_3\text{Ru}_4\text{Ge}_{13}$ containing both trivalent and tetravalent cerium. *Phys. Rev. B*, **52**:7267–7277, 1995. (Cited in pages: 88)
- [104] R. Feyerherm, E. Dudzik, S. Valencia, J. A. Mydosh, Y.-K. Huang, W. Hermes, and R. Pöttgen. Complex charge ordering in CeRuSn . *Phys. Rev. B*, **85**:085120, 2012. (Cited in pages: 88)
- [105] Om Prakash, A. Thamizhavel, and S. Ramakrishnan. Ferromagnetic ordering of minority Ce^{3+} spins in a quasi-skutterudite $\text{Ce}_3\text{Os}_4\text{Ge}_{13}$ single crystal. *Phys. Rev. B*, **93**:064427, 2016. (Cited in pages: 88)
- [106] Takatsugu Hagino, Yoshitaka Seki, Nobuo Wada, Seigo Tsuji, Takashi Shirane, Ken-ichi Kumagai, and Shoichi Nagata. Superconductivity in spinel-type compounds CuRh_2S_4 and CuRh_2Se_4 . *Phys. Rev. B*, **51**(18):12673–12684, 1995. (Cited in pages: 88)
- [107] Shoichi Nagata, Takatsugu Hagino, Yoshitaka Seki, and Teruo Bitoh. Metal-insulator transition in thiospinel CuRh_2S_4 . *Physica B*, **194-196**:1077–1078, 1994. (Cited in pages: 88)

- [108] Takao Furubayashi, Takehiko Matsumoto, Takatsugu Hagino, and Shoichi Nagata. Structural and magnetic studies of metal-insulator transition in thiospinel CuIr_2S_4 . *J. Phys. Soc. Jpn.*, **63**(9):3333–3339, 1994. (Cited in pages: 88)
- [109] Tomoyuki Sekine, Kunimitsu Uchinokura, Haruo Iimura, Ryozo Yoshizaki, and Etsuyuki Matsuura. Electrical and thermal properties in CuV_2S_4 . *Sol. Stat. Commun.*, **51**(4):187–189, 1984. (Cited in pages: 88)
- [110] J. Mahy, D. Colatis, D. Van Dyck, and S. Amelinck. *J. Solid State Chem.*, **68**:320, 1987. (Cited in pages: 88)
- [111] P. G. Radaelli, Y. Horibe, M. J. Gutmann, M. Ishibashi, C. H. Chen, R. M. Ibberson, M. Koyama, Y. S. Hor, V. Kiryukhin, and S. W. Cheong. Formation of isomorphous Ir^{3+} and Ir^{4+} octamers and spin dimerization in the spinel CuIr_2S_4 . *Nature*, **416**:155–158, 2002. (Cited in pages: 88)
- [112] Aaron Wold and Kirby Dwight. *Solid State Chemistry: synthesis, structure, and properties of selected oxides and sulfides*, pages 227–234. Chapman & Hall, New York, 1993. (Cited in pages: 89)
- [113] R. J. Bouchard. Crystal structure and transport properties of NiRh_2Se_4 . *Inorg. chem.*, **8**:850–856, 1969. (Cited in pages: 89, 90)
- [114] F. Jellinek. The structures of the chromium sulphides. *Acta Crystallogr.*, **10**:620, 1957. (Cited in pages: 89, 90)
- [115] Anthony V. Powell, Douglas C. Colgan, and Clemens Ritter. A powder neutron diffraction study of structure and magnetism in NiCr_2S_4 . *J. Solid State Chem.*, **134**:110–119, 1997. (Cited in pages: 89, 90)
- [116] Anthony V. Powell, Clemens Ritter, and Paz Vaqueiro. A powder neutron diffraction study of the magnetic structure of FeV_2S_4 . *J. Solid State Chem.*, **144**:372–378, 1999. (Cited in pages: 89, 90)
- [117] P. Vaqueiro, A. V. Powell, A. I. Coldea, C. A. Steer, I. M. Marshall, S. J. Blundell, J. Singleton, and T. Ohtani. Colossal magnetoresistance in the layered chromium sulfide $\text{Cr}_2\text{S}_{3-x}$ ($x = 0.08$). *Phys. Rev. B*, **64**:132402, 2001. (Cited in pages: 89, 90)
- [118] R. H. Plovnick, D. S. Perloff, M. Vlasse, and A. Wold. Electrical and structural properties of some ternary chalcogenides of titanium. *J. Phys. Chem. Solids*, **29**:1935–1940, 1968. (Cited in pages: 89, 90)

- [119] B. L. Morris, P. Russo, and A. Wold. Magnetic properties of ACr_2Se_4 ($A = \text{Fe, Co, Ni}$) and NiCr_2S_4 . *J. Phys. Chem. Solids*, **31**:635–638, 1970. (Cited in pages: 89, 90)
- [120] B. L. Morris, R. H. Plovnick, and A. Wold. Magnetic susceptibility of some transition metal chalcogenides having the Cr_3S_4 structure. *Sol. Stat. Commun.*, **7**(2):291–293, 1969. (Cited in pages: 89, 90)
- [121] Paz Vaquero, Markus Bold, Anthony V. Powell, and Clemens Ritter. Structural, magnetic, and electronic properties of vanadium-substituted nickel chromium sulfide. *Chem. Mater.*, **12**:1034–1041, 2000. (Cited in pages: 89, 90)
- [122] Robert J. Bouchard, Ward T. Robinson, and Aaron Wold. Structure and properties of nickel vanadium selenide, NiV_2Se_4 . *Inorg. Chem.*, **5**:977–980, 1966. (Cited in pages: 89)
- [123] Details of the crystal structure refinement. single-crystal x-ray diffraction data were measured by ϕ scans of 1° per image on the crystal at $t = 100$ k. data were processed by eval15[50] and sadabs[136] crystal structure refinements were done with jana2006.[56] lattice parameters were obtained as $a = 6.1281(5)$, $b = 3.4155(4)$, $c = 11.5488(13)$ Å, $\beta = 91.706(12)^\circ$, and $v = 241.62(3)$ Å³. structure refinements with space group $i2/m$ against 990 bragg reflections (812 observed) up to $(\sin(\theta)/\lambda)_{max} = 1.0$ Å⁻¹ resulted in an excellent fit with $r = 0.0224$ and structure model with $(\text{ni}_{0.306}\text{V}_{0.694})$ at $(0, 0, 0)$, v at $(-0.04543(9), 0, 0.25593(4))$, se1 at $(0.33732(5), 0, 0.36393(2))$ and se2 at $(0.33783(5), 0, 0.89302(2))$. (Cited in pages: 89, 90)
- [124] K. Kallel and H. Boller. A single-crystal structure refinement of V_3Se_4 . *J. Less-Common Met.*, **102**:213–217, 1984. (Cited in pages: 90, 95)
- [125] J. A. Hertz. Quantum critical phenomena. *Phys. Rev. B*, **14**:1165, 1976. (Cited in pages: 91)
- [126] A. J. Millis. Effect of a nonzero temperature on quantum critical points in itinerant fermion systems. *Phys. Rev. B*, **48**:7183, 1993. (Cited in pages: 91)
- [127] J. A. Mydosh. *Spin glasses: an experimental introduction*. Taylor and Francis, London, 1993. (Cited in pages: 91)
- [128] C. Pfeleiderer, G. J. McMullan, S. R. Julian, and G. G. Lonzarich. Magnetic quantum phase transition in MnSi under hydrostatic pressure. *Phys. Rev. B*, **55**:8330–8338, 1997. (Cited in pages: 91)

- [129] P. G. Niklowitz, F. Beckers, G. G. Lonzarich, G. Knebel, B. Salce, J. Thomason, N. Bernhoeft, D. Braithwaite, and J. Flouquet. Spin-fluctuation-dominated electrical transport of Ni_3Al at high pressure. *Phys. Rev. B*, **72**:024424, 2005. (Cited in pages: 91)
- [130] C. M. Varma, P. B. Littlewood, S. Schmitt-Rink, E. Abrahams, and A. E. Ruckenstein. Phenomenology of the normal state of Cu-O high-temperature superconductors. *Phys. Rev. Lett.*, **63**:1996, 1989. (Cited in pages: 91)
- [131] S. Miyasaka, H. Takagi, Y. Sekine, H. Takahashi, N. Mori, and R. J. Cava. Metal-insulator transition and itinerant antiferromagnetism in $\text{NiS}_{2-x}\text{Se}_x$ pyrite. *J. Phys. Soc. Jpn*, **69**:3166, 2000. (Cited in pages: 91)
- [132] A.B. Kaiser. Effect of spin fluctuations on resistivity. *Phil. Mag. B*, **65**:1197–1206, 1992. (Cited in pages: 92)
- [133] A. T. Lonchakov, V. V. Marchenkov, V. I. Okulov, K. A. Okulova, T. E. Govorkova, S. M. Podgornykh, and H. W. Weber. Anomalous low-temperature specific heat of $\text{Fe}_{2-x}\text{V}_{1+x}\text{Al}$ ($x=0; 0.1$) alloys. *J. Phys.: Conf. Series*, **568**:052018, 2014. (Cited in pages: 94, 95)
- [134] P. G. Niklowitz, F. Beckers, G. G. Lonzarich, G. Knebel, B. Salce, J. Thomason, N. Bernhoeft, D. Braithwaite, and J. Flouquet. Spin-fluctuation-dominated electrical transport of Ni_3Al at high pressure. *Phys. Rev. B*, **72**:024424, 2005. (Cited in pages: 95)
- [135] P. G. Niklowitz, P. L. Alireza, M. J. Steiner, G. G. Lonzarich, D. Braithwaite, G. Knebel, J. Flouquet, and J. A. Wilson. Unconventional resistivity at the border of metallic antiferromagnetism in NiS_2 . *Phys. Rev. B*, **77**:115315, 2008. (Cited in pages: 95)
- [136] G. M. Sheldrick. *Sadabs*. University of Goettingen, Göttingen, Germany, 1996. (Cited in pages: 160)

List of Publications

Publications that are part of the thesis:

1. Chapter 3 has been published as: S. Ramakrishnan, A. Schönleber, C. B. Hübschle, C. Eisele, A. M. Schaller, T. Rekiş, N. H. A. Bui, F. Feulner, S. van Smaalen, B. Bag, S. Ramakrishnan, M. Tolkiehn, and C. Paulmann. Charge-density-wave and lock-in transitions of CuV_2S_4 . *Phys. Rev. B* **99** 195140, (2019).
2. Chapter 4 has been published as: S. Ramakrishnan, A. Schönleber, T. Rekiş, N. van Well, L. Noohinejad, S. van Smaalen, M. Tolkiehn, C. Paulmann, B. Bag, A. Thamizhavel, D. Pal and S. Ramakrishnan. Unusual charge density wave transition and absence of magnetic ordering in $\text{Er}_2\text{Ir}_3\text{Si}_5$. *Phys. Rev. B* **101** 060101(R) (2020).
3. Chapter 5 has yet to be submitted as: S. Ramakrishnan, S. Matteppanavar, A. Thamizhavel, S. Ramakrishnan and S. van Smaalen. Unusual magnetic behavior of crystalline $\text{Ni}_{0.89}\text{V}_{2.11}\text{Se}_4$ with site disorder. (2020).

Other Publications:

1. N. van Well, C. Eisele, S. Ramakrishnan, T. Shang, M. Medarde, A. Cervellino, M. Skoulatos, R. Georgii and S. van Smaalen. Tetragonal mixed system $\text{Cs}_2\text{CuCl}_{(4-x)}\text{Br}_x$ complemented by the tetragonal phase realisation of Cs_2CuCl_4 . *Cryst. Growth Des*, (2019).

2. J. Welsch, S. Ramakrishnan, C. Eisele, N. van Well, A. Schönleber, S. van Smaalen, S. Mattheppanavar, A. Thamizhavel, M. Tolkiehn, C. Paulmann and S. Ramakrishnan. Second order CDW transition in single crystals of $\text{La}_3\text{Co}_4\text{Sn}_{13}$. *Phys. Rev. Mater* **3**, 125003, (2019).

3. N. van Well, S. Ramakrishnan, K. Beauvois, N. Qureshi, E. Ressouche, M. Skoulatos, R. Georgii, O. Zaharko, Ch. Rüegg, S. van Smaalen Magnetic field-controlled quantum critical points in the triangular antiferromagnetic $\text{Cs}_2\text{CuCl}_{(4-x)}\text{Br}_x$ mixed system (Submitted to *Advanced Materials*) (2020).

Acknowledgements

Firstly, I would like to give my thanks and gratitude to my 'Doctorvater' Prof. Dr. Sander van Smaalen, who has given me a position in his Laboratory of Crystallography. During these five years Sander has shared his wealth of knowledge not only to better understand on tackling complex aperiodic crystal structures but also, changed my approach and thinking towards scientific problems for the better. Sander was extremely patient and understanding in mentoring me throughout my Phd.

PD. Dr. Andreas Schönleber is involved in many of my projects and has also helped in understanding on how to use different softwares and handling data of complex aperiodic structures. I also reminisce the interesting talks we had outside the topic of crystallography.

I would like thank Dr. Christian Hübschle for introducing me to Fortran programming and helping me write programs required for the processing of my data. Christian has also helped me personally when he had to accompany me to the hospital during my surgery for my left hand.

The secretary of our department Denise Kelk-Huth has been instrumental in helping me handle administration procedures and translating documents. Our chemist Kerstin Küspert is a maestro at single-crystal growth, without her this project would have never come into fruition. She spent long hours and painstakingly synthesised high quality single-crystals of CuV_2S_4 with which we could measure and collect our data. She also helped me to apply for 'Arbeitsamt' and other administrative and medical work. Along with Denise she has also organized trips/hikes which was an excellent opportunity to explore more of Germany.

Franz Fischer our technician has worked hard to keep our in-house diffractometer running which is important as we collect our data and test crystals before taking it to synchrotron. He has also been very helpful in helping me to deal with hardware and software problems regarding the instruments and also my working computer in the office.

I had the pleasure of working with Dr. Natalija van well in several of her neutron diffraction experiments and thank her for broadening my knowledge. I thank Dr. Somnath Dey for the long hours we spent in discussing and understanding on how to tackle the problem of twinning. Dr. Leila Noonhinjead has been very helpful in discussions regarding Jana 2006 and EVAL15.

Dr. Maxim Bykov and Dr. Elena Bykova introduced me to the first synchrotron experiment in May 2015 at P02. Thanks to them, I acquired some basic knowledge of High-pressure crystallography. My friend and colleague Mr. Claudio Eisele has been very helpful in handling administrative procedures, translations, and accompanying me to the doctor when my hand was broken. He is a very dependable person and an excellent friend. I thank Mr. Achim Schaller and Dr. Toms Rekis who have helped me to collect the data at the synchrotron and for fruitful discussions, be it crystallography or other topics. I also thank our newcomers, Mr. Surya Kotla and Dr. Jinke Bao for their inputs and suggestions.

Lastly, I would like to thank my brother Santosh Ramakrishnan, my father Prof. Dr. Srinivasan Ramakrishnan for his moral and scientific support, carrying out physical property measurements for the various compounds whose crystal structure I have analyzed, and my mother Shyamala Ramakrishnan for her invaluable support in guiding me to complete my odyssey.

Declaration

Hiermit versichere ich an Eides statt, dass ich die vorliegende Arbeit selbstständig verfasst und keine anderen als die von mir angegebenen Quellen und Hilfsmittel verwendet habe.

Weiterhin erkläre ich, dass ich die Hilfe von gewerblichen Promotionsberatern bzw. -vermittlern oder ähnlichen Dienstleistern weder bisher in Anspruch genommen habe, noch künftig in Anspruch nehmen werde.

Zusätzlich erkläre ich hiermit, dass ich keinerlei frühere Promotionsversuche unternommen habe.

Bayreuth 2020,

Sitaram Ramakrishnan

